UNIVERSITÀ DEGLI STUDI DI TRIESTE

Department of Physics

Ph.D. in Physics, cycle XXXV

Precision cosmology with galaxy clusters: preparing for *Euclid*

Ph.D. student:

Alessandra Fumagalli

Supervisor:

prof. Alexandro Saro

Co-supervisor:

prof. Stefano Borgani

Academic Year 2022/2023

Abstract

The flat ΛCDM cosmological model has been demonstrated to provide a good description of the observed properties of the Universe. However, several unanswered questions and tensions on cosmological parameters indicate that our knowledge of the Universe still needs to be investigated. Galaxy clusters, as tracers of the large-scale structure geometry end evolution, are well-known powerful cosmological probes, sensitive to the properties of the initial density field of the Universe, to the nature of dark matter and dark energy, and to the laws of gravity on large scales. In particular, mass abundance (i.e., number counts) and spatial distribution (i.e., clustering) of such objects are sensitive to changes in several cosmological parameters, mainly the amplitude of density fluctuations (σ_8) and the matter content of the Universe (Ω_m).

Current cosmological constraints from cluster surveys are limited in redshift ($z \lesssim 1$) and statistics ($N_{cl} \sim 10^3$). This scenario will drastically change with the advent of the next generation of wide-field photometric surveys. Among them, the future ESA space mission Euclid (Laureijs et al. 2011) will produce cluster catalogs with $\sim 10^5$ objects up to redshift $z \simeq 2$, allowing the cosmological parameters to be constrained with unprecedented precision. In this scenario, cosmological constraints from galaxy clusters will be almost entirely limited by systematic uncertainties, related to both observational and theoretical aspects.

The goal of this Ph.D. thesis is to characterize the theoretical systematics of cluster cosmology experiments, allowing for the full cosmological exploitation of the upcoming Euclid cluster survey. By analyzing 1000 Euclid-like simulated light cones, produced with the PINOCCHIO code (Monaco et al. 2002b), we validate analytical models for the covariance matrix of cluster number counts and real-space cluster clustering. We demonstrate that the analytical models achieve an accuracy within 10 percent for both number counts and clustering covariance matrices, and this translates to negligible impact on the figure of merit of the cosmological parameters Ω_m and σ_8.

The resulting models allow us to study the response of the likelihood analysis to variations of the covariance, and in particular to assess the relevance of the cosmology dependence of the covariance matrix. Our results indicate that a Gaussian likelihood with full cosmology-dependent covariance provides an unbiased inference of cosmological parameters for number counts analyses. Also, we find that a simple Gaussian model with Poissonian shot-noise does not correctly predict the clustering covariance, but the inaccuracy can be mitigated with the help of few additional parameters fitted from simulations. Furthermore, we show that both the mass dependence of the halo bias, and the cosmology dependence of the covariance help to improve the constraining power of cluster clustering.

The final part of this work is aimed at studying the combined analysis of cluster number counts and cluster clustering for richness-selected clusters. After showing that the two statistics exhibit negligible cross-correlation, we quantify the improvement in their joint cosmological constraints, as a function of scaling relation priors' amplitude. Our analyses show that the addition of cluster clustering brings a 20 to 90 percent improvement on parameter constraints when compared with the analysis of number counts alone, depending on the uncertainty on the scaling relation. Finally, we apply the framework validated in this work to the analysis of the SDSS redMaPPer cluster catalog (Rozo et al. 2015), confirming that

also in real observing conditions cluster clustering yields relevant information to improve the cosmological constraints obtained from number counts.

Contents

Introduction

Galaxy clusters are the most massive gravitationally bound systems in the Universe, formed through the gravitational collapse of initial perturbations of the matter density field, through a hierarchical process of accretion and merging of small objects into increasingly massive systems (Kravtsov & Borgani 2012). Therefore galaxy clusters have several properties that contain cosmological information on the geometry and the evolution of the large-scale structure of the Universe. In particular, their abundance and spatial distribution are powerful tools to constrain the amplitude of matter fluctuations on $8\,h^{-1}$ Mpc scales (σ_8) and the matter content of the Universe (Ω_m). Moreover, clusters are observed at low redshift (out to redshift $z \sim 2$), thus sampling the cosmic epochs during which the effect of dark energy begins to dominate the expansion of the Universe; as such, the evolution of the statistical properties of galaxy clusters allow us to place constraints on the dark energy equation of state, and investigate possible deviations of dark energy from a simple cosmological constant (e.g., Sartoris et al. 2012). Finally, such observables can be used to constrain neutrino masses (e.g. Costanzi et al. 2013; Mantz et al. 2015; Costanzi et al. 2019; Bocquet et al. 2019), the Gaussianity of initial conditions (e.g. Sartoris et al. 2010; Mana et al. 2013) and the behavior of gravity on cosmological scales (e.g. Cataneo & Rapetti 2018; Bocquet et al. 2015).

A crucial aspect for such observables to be turned into stringent cosmological constraints concerns the accurate description of all the sources of uncertainties that characterize a cluster cosmology experiment. First, cluster masses are not directly observed but must be inferred through other measurable properties of clusters, e.g., properties of their galaxy population (i.e. richness, velocity dispersion) or of the intracluster gas (i.g., total gas mass, temperature, pressure). The relationships between these observables and clusters masses, called *scaling relations*, provide a statistical estimate of masses, but require an accurate calibration in order to correctly relate the mass proxies with the actual cluster mass. Furthermore, even if accurately calibrated, scaling relations only describe cluster masses in a statistical sense due to the combined effect of baryonic physics processes and of the different formation history of individual clusters. As such, they are characterized by an intrinsic scatter between the true cluster mass and mass proxies, that complicates the calibration process (Kravtsov & Borgani 2012; Pratt et al. 2019). Other measurement errors are related to the estimation of redshifts and the selection function (Allen et al. 2011). In addition to these observational sources of systematics, there may be theoretical systematics linked to the modeling of the statistical errors: *shot-noise*, the uncertainty due to the discrete nature of data, and *sample variance*, the uncertainty due to the finite size of the survey. Finally, analytical models describing the observed distributions, such as the mass function and halo bias, have to be carefully calibrated, to avoid introducing further systematics (e.g. Sheth & Tormen 2002; Tinker et al. 2008, 2010; Bocquet et al. 2016; Despali et al. 2016; Castro et al. 2020).

To account for all these potential sources of systematics that can bias the cosmological

results, it is required an accurate description of the uncertainties affecting the observables, which are given in the form of covariance matrices. The simplest but computationally expensive way to compute a covariance matrix is from measurements in a large set of simulations. The computational costs can be reduced by generating mocks with approximate methods instead of full N-body simulations (Monaco 2016) or with mixed methods such as the shrinkage technique (Pope & Szapudi 2008). However, the resulting matrix will still be noisy unless a large number of mocks realizations are generated. If the covariance is considered cosmology dependent, the cost will inevitably increase as many more simulations are required to explore the high-dimensional space of cosmological parameters with such simulations. An alternative approach is to estimate covariances from the data itself by means of bootstrap or jackknife techniques: these methods have the advantage of providing matrices evaluated at the true cosmology of the Universe, but the resampling methods tend to overestimate the true covariance, especially for 2-point statistics (Norberg et al. 2009; Friedrich et al. 2016; Lacasa & Kunz 2017; Mohammad & Percival 2021). A third method consists in the analytic calculation of the covariance matrix (e.g. Feldman et al. 1994; Scoccimarro et al. 1999; Meiksin & White 1999; Hu & Kravtsov 2003; Takada & Hu 2013), which provides noise-free, cosmology-dependent matrices without requiring expensive computational resources. The limitation of this method lies in the difficulty of describing analytically all the contributions to the covariance (e.g. non-linearities, non-Gaussianities, ...). Moreover, it is straightforward to include a treatment of systematic errors by imposing a realistic selection function to mock catalogs, while in the case of an analytical model this is more challenging and likely to require significant approximations. Therefore, such models have to be validated against simulations, in order to determine which contributions are relevant at the required level of statistics. Moreover, in some cases, this validation process may indicate that an analytical description is not sufficient to correctly describe the covariance matrix, and it is thus necessary to calibrate model parameters that cannot be determined from first principles (Xu et al. 2012; O'Connell et al. 2016; Fumagalli et al. 2022).

Both for computing numerical covariances and for validating analytical or semi-analytical models, a fundamental requirement is the use of a large set of simulations. The dimension of such set depends on the size of the data vector (i.e. the total number of bins) and the desired accuracy. Typically, order of 10^3 or higher number of simulated catalogs are required (Taylor et al. 2013; Dodelson & Schneider 2013). For this purpose, catalogs generated with N-body simulations are hardly obtainable, due to their high computational cost. Instead, large sets of mock data can be produced in a simpler and faster way by using approximate methods based on perturbative theories. Although less accurate than full N-body simulations in reproducing observables, these methods are able to accurately estimate covariances requiring fewer resources and far less computational time (Sahni & Coles 1995; Monaco 2016; Lippich et al. 2019; Blot et al. 2019; Colavincenzo et al. 2019).

The study and the control of these uncertainties is critical for future cluster surveys, as they will provide extremely large samples of clusters associated therefore with very small statistical errors. In this sense, only a comprehensive characterization of systematics will allow us to thus fully constrain cosmological parameters to the precision level allowed by these surveys. One of the main forthcoming surveys is the European Space Agency (ESA) mission *Euclid*[1], planned for 2023, which will map $\sim 15\,000$ deg^2 of the extragalactic sky in

[1] http://www.euclid-ec.org

order to investigate the nature of dark energy, dark matter and gravity. Galaxy clusters are among the cosmological probes that will be used by *Euclid*: the mission is expected to yield a sample of $\sim 10^5$ clusters up to redshift $z = 2$, using photometric and spectroscopic data and through gravitational lensing (Laureijs et al. 2011).

In this thesis we present the validation of models of covariance for number counts and clustering of galaxy clusters, evaluating the impact of sample variance, lightcone geometry, and high-order terms, at the level of accuracy expected for the future *Euclid* survey. The resulting models allow us to study the response of the likelihood analysis to variations of the covariance and to provide forecasts to predict the impact of such uncertainties in the recovered cosmological parameters for the upcoming *Euclid* cluster survey.

In Chapter 1, we introduce the statistical quantities relevant to the analysis of the evolution and geometry of the large-scale structure of the Universe, such as the halo mass function, 2-point correlation function, and linear halo bias. We will then present the observational and theoretical systematics that can affect the cosmological parameter inference. The former are mainly related to the cluster mass estimation and to the modeling of selection functions, while the latter can arise from a wrong treatment of statistical uncertainties, such as sample variance and shot-noise. We also give an overview of the state-of-the-art of cluster cosmology: first, we describe the standard cosmological model, the so-called flat ΛCDM, and the cosmological probes most frequently used to constraint the parameter values. Afterwards, the use of galaxy clusters as cosmological probes will be described in more detail, highlighting their dependence on cosmological parameters and the characteristics that make these objects extremely advantageous observables in the cosmological as well as astrophysical domain. Finally, we will summarize some of the most recent results concerning the cosmological analysis of galaxy clusters, and we will present the properties of the upcoming *Euclid* mission, which will represent an important advance for investigating the cosmological model and, in particular, for cluster cosmology.

In Chapter 2, we present the topic of numerical simulations used to describe the evolution of cosmic structures beyond the strictly linear regime. After a brief introduction to N-body simulations, the focus will shift to the approximate methods used to produce a large number of catalogs relevant for the analysis of systematics. These methods are less accurate, but also computationally less expensive than N-body simulations, thanks to the use of perturbative theories such as the *Lagrangian Perturbation Theory* or its first-order development, the *Zel'dovich approximation*, which will be described in the chapter. Finally, we will present the PINOCCHIO algorithm and the catalogs used in this work both for the covariance validation and for the likelihood forecasts.

In Chapter 3, we describe the methodology adopted for validating the covariance models and for the likelihood analysis. We first describe the Bayesian inference process, focusing on the likelihood functions that will be taken into account in this work, Then, we introduce the concept of covariance matrix and its numerical estimation. Finally, we describe a likelihood-based method for fitting semi-analytic covariance models from a small number of numerical simulations (Fumagalli et al. 2022). We first describe the method and present the mathematical reasoning behind it. Then, we apply the method in two examples, one based on the 2PCF and the other on the bispectrum (i.e., 3PCF in Fourier space), and present the results.

In Chapter 4, we describe the results of the number counts analysis presented in Euclid Collaboration: Fumagalli et al. (2021). After describing the analytical model for the number counts covariance, we validate it by comparison with the numerical matrix from simulations.

We analyze the effect of the mass and redshift binning on the estimation of parameters, and we compare the effect on the parameter posteriors of different likelihood models. We also assess the impact of assuming a wrong cosmology in the covariance, as well as the effect of adopting a cosmology-depended matrix. While this work is focused on the analysis of a cluster survey similar in sky coverage and depth to the *Euclid* one, for completeness we also provide results relevant for present and ongoing surveys.

In Chapter 5, we describe the results of the cluster clustering analysis presented in Euclid Collaboration: Fumagalli et al. (2022). We introduce the analytical formalism to describe the 2PCF and its covariance, as well as the measurements of the 2PCF and the associated numerical covariance. Then, we present the results of our analysis: we define the best binning in radial separation and redshift to extract the cosmological information, and we compare the analytical and numerical matrices, introducing additional parameters to improve the agreement between the two covariances. Then, we study the impact of the non-Gaussian term, and we evaluate the improvement obtained from the mass dependence of the halo bias. As for number counts, we investigate the effect of a wrong-cosmology and a cosmology-dependent matrix.

In Chapter 6, we present the validation of the covariance models in observable space, i.e., for richness-selected clusters. First, we demonstrate the validity of our modeling also for richness-selected clusters. We then use the analytical covariances for computing likelihood forecasts. We first establish that the cross-covariance between number counts and cluster clustering is negligible, allowing us to treat the two statistics as independent quantities in the combined analysis. Then, we study the impact of the uncertainty of mass-observable relation parameters on the cosmological posteriors, by varying the amplitude of Gaussian priors in the likelihood analysis. We also assess the impact of cosmology-dependent covariances, with respect to the the broadening of posteriors in observable space. Finally, we show some application of the method validated in this work, with particular attention to the application of the joint number counts and clustering analysis to real data, i.e., the redMaPPer catalog from the Sloan Digital Sky Survey (Rozo et al. 2015).

Finally, in Chapter 7 we discuss our conclusions.

Chapter 1

Cluster cosmology

In this chapter we introduce the theoretical framework needed to model cluster number counts and cluster clustering. After a brief introduction of the observables used to constrain the cosmological parameters, the treatment of galaxy clusters will be explored in depth, with a focus on the main systematics that affect such observables. We also give an overview of the state of the art of parameter estimation, presenting the open issues and the future perspectives of cluster cosmology, related in particular to the future *Euclid* space mission.

1.1 Large-scale structure of the Universe

The large-scale structure of the Universe (LSS) is defined as the distribution of matter on scales larger than galaxies, formed by the collapse of fluctuations of the initial matter density field, driven by the gravitational field of dark matter (Kravtsov & Borgani 2012). The left panel of Fig. 1.1 shows the dark matter distribution in a simulated cubical volume of side $500\,h^{-1}$ Mpc at redshift $z = 0$ [1]. Dark matter is arranged in high-density halos of comoving size of $\sim 1-3\,h^{-1}$ Mpc, connected by a network of low-density filaments of length $> 10\,h^{-1}$ Mpc, that surround large void regions of size $> 20\,h^{-1}$ Mpc. Baryonic matter, i.e. stars, galaxies and gas, follows the distribution of dark matter along the filaments and inside halos, contributing to form galaxy clusters.

Galaxy clusters are the most massive gravitationally bound systems in the Universe ($M \sim 10^{14} - 10^{15}\,\mathrm{M}_\odot$) and they are composed of dark matter for 85 per cent, hot ionized gas ($T \sim 10^7 - 10^8$ K) for 12 percent and stars for 3 percent (Pratt et al. 2019). These massive structures are formed by the gravitational collapse of initial perturbations of the matter density field, through a hierarchical process of accretion and merging of small objects into increasingly massive systems (Kravtsov & Borgani 2012).

To describe the evolution of perturbations that generate galaxy clusters and characterize their statistics, we express the matter density field in terms of density contrast δ, defined as

$$\delta(\mathbf{x}, t) = \frac{\rho(\mathbf{x}, t) - \overline{\rho}(t)}{\overline{\rho}(t)}, \tag{1.1}$$

where $\rho(\mathbf{x}, t)$ is the density at the comoving position $\mathbf{x}$ at time t, and $\overline{\rho}(t)$ is the mean density at time t. The initial density contrast $\delta_0(\mathbf{x})$ originates from quantum fluctuations in the energy

[1] https://wwwmpa.mpa-garching.mpg.de/galform/virgo/millennium/

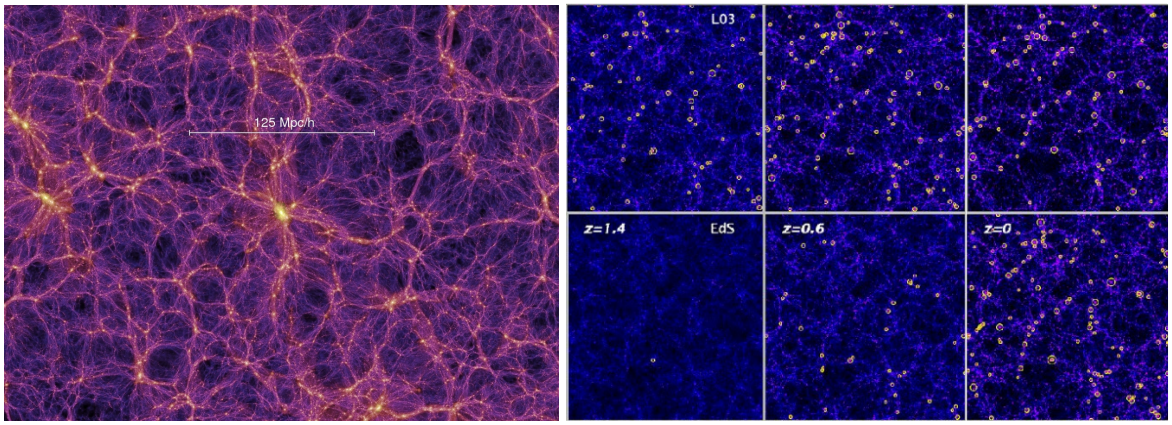

Figure 1.1: *Left panel:* Large-scale structure of the Universe. The "cosmic web" of dark matter is shown in purple, with high density regions represented in yellow, where galaxy clusters form. Image produced by *Millennium simulation* (Springel et al. 2005). *Right panel:*Redshift evolution of the LSS in two different cosmological models, obtained from N-body simulations. The distribution of matter is represented in blue, while the yellow circles identify galaxy clusters. The normalization is chosen to have the same distribution at $z = 0$. The top panels describe a flat Universe with $\Omega_m = 0.3$ and $\Omega_\Lambda = 0.7$, in the bottom panels $\Omega_m = 1$ and $\Omega_\Lambda = 0$. Image taken from Borgani & Guzzo (2001).

density, which are amplified during the inflationary epoch and become classical fluctuations in the density of matter. This initial field is described as an isotropic, homogeneous Gaussian random field, whose evolution is affected by pre-recombination processes and, later, by non-linear processes. The evolution of cosmic structures can be divided into three phases:

- linear evolution ($\delta \ll 1$), that can be described analytically;
- quasi-linear evolution ($\delta \sim 1$), that can be described by perturbative theories;
- non-linear evolution ($\delta \gg 1$), that can only be analyzed through the use of simulations.

The formation of virialised structures takes place during the last phase. Within dark matter halos, dissipative baryon physics processes occur, such as star formation and feedback from AGN (active galactic nuclei) and supernovae, leading to the formation of galaxy clusters (Kravtsov & Borgani 2012). However, to describe the large-scale properties of the Universe, it is sufficient, as a first approximation, to study the properties of dark matter halos. This makes it possible to neglect the complex processes of non-linear and baryon physics that characterize galaxy clusters. Therefore, in the following text, the terms *galaxy cluster* and *dark matter halo* will generally be considered as synonyms.

Galaxy clusters, as tracers of the matter density field, are useful tools for deriving properties on the geometry and evolution of the LSS, which strongly depend on the value of cosmological parameters and contain information for determining the correct cosmological model. The right panel of Fig. 1.1 shows the redshift evolution of the matter distribution simulated according to two different cosmological models: flat ΛCDM model (Sect. 1.3.1) in the top panels, and Einstein de Sitter model (i.e., flat Universe with $\Omega_m = 1$) in the bottom panels. The two simulations are normalized to obtain the same matter distribution at the present time (redshift $z = 0$, right panels). It can be seen that the Universe model strongly influences

the evolution of clusters (yellow circles), which constitute a fundamental resource for determining the value of cosmological parameters. In order to be exploited, the information from galaxy clusters must be compressed into some summary statistics. In this work, the mass abundance and spatial distribution of the clusters are considered, respectively described by the halo mass function and the 2-point correlation function.

1.1.1 Halo mass function

The halo mass function $\mathrm{d}n(M,z)$ is defined as the comoving volume number density of collapsed objects at redshift z with masses between M and $M+\mathrm{d}M$ (Press & Schechter 1974; Bond et al. 1991; Lacey & Cole 1993),

$$\frac{\mathrm{d}n(M,z)}{\mathrm{d}\ln M} = \frac{\overline{\rho}}{M}\,\nu f(\nu)\,\frac{\mathrm{d}\ln\nu}{\mathrm{d}\ln M}\,, \tag{1.2}$$

where $\overline{\rho}/M$ is the inverse of the Lagrangian volume of a halo of mass M, and $\nu = \delta_\mathrm{c}/\sigma(R,z)$ is the *peak height*, defined in terms of the variance of the linear density field smoothed on scale R,

$$\sigma^2(R,z) = \frac{1}{2\pi^2}\int \mathrm{d}k\, k^2\, P(k,z)\, W_R^2(k)\,, \tag{1.3}$$

where R is the radius enclosing the mass $M = 4\pi/3\;\overline{\rho}\,R^3$, $P(k,z)$ the matter power spectrum, linearly extrapolated to redshift z, and $W_R(k)$ is the filtering function; the latter usually takes the form of a top-hat function in Fourier space:

$$W_R(k) = 3\frac{\sin(kR) - kR\cos(kR)}{(kR)^3}\,. \tag{1.4}$$

The term δ_c represents the critical linear overdensity for the spherical collapse and contains a weak dependence on cosmology and redshift that can be expressed as (Kitayama & Suto 1996)

$$\delta_\mathrm{c}(z) = \frac{3}{20}(12\pi)^{2/3}[1 + 0.012299\log_{10}\Omega_\mathrm{m}(z)]\,. \tag{1.5}$$

The function $\nu f(\nu)$ is called multiplicity function, whose analytical expression was first derived by Press & Schechter (1974), basing on the hypothesis of spherical collapse and Gaussian initial conditions. The normalization of such expression was found to be wrong by a factor of 2, as if only half of the mass of the Universe is contained in collapsed objects, in contrast to the predictions of the hierarchical model. A more accurate derivation has been proposed by Bond et al. (1991) with the *excursion set* ansatz, who derived an expression for the halo mass function with a k-space top-hat window, that properly solves the normalization problem. One of the main characteristics of the multiplicity function is that its shape is universal, meaning that it can be described in terms of a single variable, i.e. the peak-height ν, and with the same parameters for all the redshifts and cosmological models (Sheth & Tormen 2002). A number of parametrizations have been derived by fitting the mass distribution from N-body simulations, in order to describe such universality with the highest possible accuracy. In reality, the analysis performed by White (2002) using N-body simulations shows that the universality of the mass function is only approximate and depends on the estimator used to define the mass.

In fact, halos can be defined in different ways; the main definitions are based on the Friends-of-Friends (FoF, Davis et al. 1985) and Spherical Overdensity (SO, Lacey & Cole 1993; White 2001) algorithms. The former consists of selecting pairs of particles with a separation shorter than a certain linking length b and defining a halo considering that the "friends-of-friends" will all be part of the same group. This method has the advantage of having a single free parameter (b) and of making no assumptions regarding the center or shape of the clusters, but it is practically impossible to compare the groups identified in the simulations with the observed clusters. Moreover, several clusters can be erroneously merged if characterized by a few pairs in common. The second method, on the other hand, defines the halo as a sphere with radius containing the overdensity $\Delta\rho$ and center at a fixed point. In this way, it is necessary to impose the center of the cluster, but the resulting object can be in principle compared more closely with observations. Ambiguity in the mass definition, due to both the use of different methods and the choice of different overdensities Δ or linking lengths b, can create ambiguities in the calibration of analytical models, such as the halo mass function.

According to White (2002), the best result is achieved by identifying halos using the FoF method with linking-length $b = 0.2$, in agreement with the results of Jenkins et al. (2001). Also according to Watson et al. (2013) the mass function turns out to be universal only for FoF halos, while for SO halos it presents an evolution with redshift. A further proof of the non-universality of SO halos comes from Tinker et al. (2008), which find that the universality is not respected within the level of accuracy of the proposed parameterisation ($\leq 5\,\%$): the shape of the mass function presents a dependence on both redshift and the overdensity used to identify the halos. The model proposed by Despali et al. (2016), on the other hand, turns out to be valid independently of redshift and cosmological model for halos identified by SO method at the virial overdensity, presenting a universal shape of the virial mass function. As the overdensity varies, some redshift dependence has to be introduced to rescale the parameters of the model. Finally, some works as Crocce et al. (2010) and Courtin et al. (2011) show non-universality even for FoF halos, which present redshift dependent deviations from a universal behavior.

Since deviations from universality become more and more apparent, also because of the increase in precision required to describe the halo properties, some works have focused on the characterization of this non-universal mass function, demonstrating that a more complex parametrization is able to better describe the abundance of halos (Ondaro-Mallea et al. 2021; Euclid Collaboration: Castro et al. 2022). The difference between various parametrizations of the multiplicity function can be observed in the left panel of Fig. 1.2, which shows some of the models mentioned above. Non-negligible differences can be noted not only with the Press-Schechter simple model, but also between the different models fitted on simulations. The need to improve the accuracy and precision of the mass function calibration is revealed by the impact that an incorrect parameterisation has on the estimation of cosmological parameters, in particular for future surveys such as *Euclid* (Salvati et al. 2020; Artis et al. 2021).

Another way to predict the abundance of halos is the use of emulators, built by fitting the mass function from simulations as a function of cosmology; such emulators are able to reproduce the mass function within few percent accuracy (Heitmann et al. 2016; McClintock et al. 2019; Bocquet et al. 2020). The description of the cluster mass function is further complicated by the presence of baryons, which have to be taken into account when analyzing the observational data; their effect must therefore be included in the calibration of the model

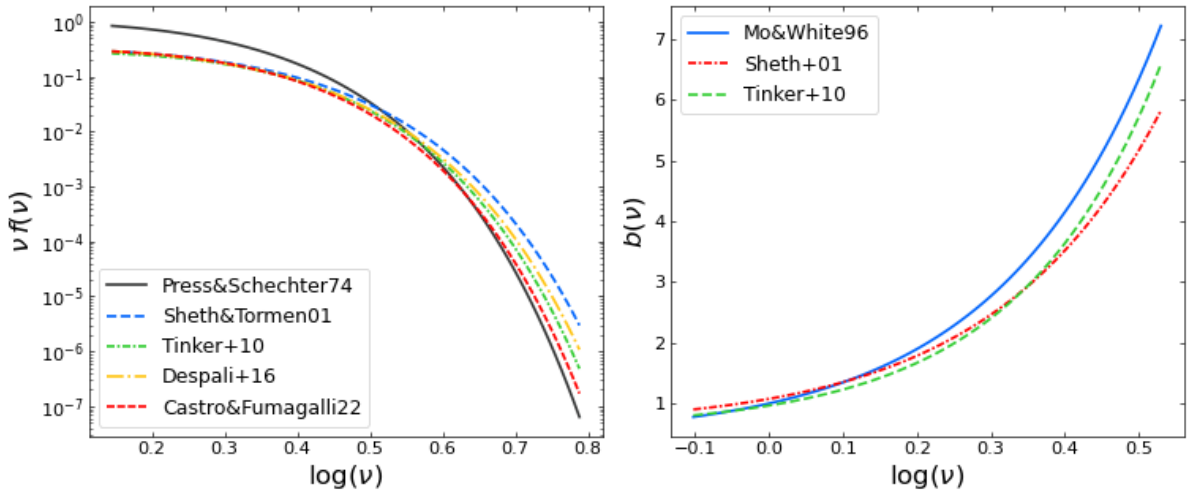

Figure 1.2: *Left panel:* virial multiplicity function as predicted by: Press & Schechter (1974), Sheth & Tormen (2002), Tinker et al. (2010), Despali et al. (2016), and Euclid Collaboration: Castro et al. (2022). *Right panel:* halo bias from peak-background split and spherical collapse (Eq.1.23, Mo & White 1996), peak-background split and ellipsoidal collapse (Sheth et al. 2001), and model by Tinker et al. (2010).

(e.g. Cui et al. 2014; Velliscig et al. 2014; Bocquet et al. 2016; Castro et al. 2020).

1.1.2 Power spectrum and correlation functions

The density field of perturbations $\delta(\mathbf{x}, t)$ is a random field representing one of the many possible realisations of the Universe. Its properties can be described by statistical quantities, given by the *ensemble* average over a set of realisations. However, since we have access only to a single realization of the Universe, the ensemble average cannot be calculated from observational data and is replaced by a spatial average: on the basis of the ergodic theorem, the two definitions are equivalent and it is therefore possible to study the density field by averaging the observed properties in different spatial regions. On the other hand, the ensemble mean and the sample variance can be calculated theoretically through the use of numerical simulations, which make it possible to produce different realisations of the same Universe by changing the phases and amplitudes of the $\delta_{\mathbf{k}}$, to vary the fluctuations of the initial density field. In this way, theoretical predictions can be made and compared with observations.

By definition, a Gaussian random field is fully specified by its 2-point correlation function

$$\xi(r) = \langle \delta(\mathbf{x}) \delta(\mathbf{x}+\mathbf{r}) \rangle \,. \tag{1.6}$$

The definition given by Eq. 1.6 is valid for a continuous field. To define the correlation function of a discrete distribution of points, such as dark matter halos, we divide the space into volumes ΔV such that each of them contains at most one particle, i.e., the occupation number of a cell in $\mathbf{x}$ can be $\mathcal{N}(\mathbf{x}) = 0, 1$. Such a sampling is called Poissonian and is completely specified by the probability of finding an object in the cell centred in $\mathbf{x}$

$$p^{(1)}(\mathbf{x}) = \langle \mathcal{N}(\mathbf{x}) \rangle_p = [1 + \delta(\mathbf{x})] \, \overline{n} \, \Delta V \,, \tag{1.7}$$

where $\langle\rangle_p$ denotes the average over the Poissonian samplings and $\overline{n}$ is the mean number density. The joint probability of having an object in $\mathbf{x}$ and an object in $\mathbf{x}+\mathbf{r}$ is thus given by

$$\mathrm{d}^2P = \langle p^{(1)}(\mathbf{x})\, p^{(1)}(\mathbf{x}+\mathbf{r})\rangle\,, \tag{1.8}$$

where $\langle\rangle$ denotes the ensemble average. By inserting Eqs. (1.7) and (1.6), Eq. (1.8) becomes

$$\mathrm{d}^2P = (\overline{n}\Delta V)^2[1+\xi(r)]\,, \tag{1.9}$$

where ξ only depends on the modulus of the separation vector r due to assumption of homogeneity and isotropy of the Universe. From this equation it appears clear that $\xi(r)$ quantifies the excess probability of finding a pair of objects at comoving separation r, with respect to a random distribution.

Equivalently, the Gaussian random field can be totally specified by its power spectrum $P(k)$, which describes the power assigned to the fluctuations as a function of the Fourier modes k (at a fixed time) and is defined as

$$P(k) = V_u\langle|\delta_{\mathbf{k}}|^2\rangle\,, \tag{1.10}$$

where V_u is the volume over which the perturbation field is assumed to be periodic, and $\delta_{\mathbf{k}}$ is the Fourier transform of the density field defined in Eq. (1.1). As for the correlation function, also the power spectrum only depends on the modulus of the scale k.

The 2-point correlation function represents the Fourier transform of the power spectrum and the two quantities can be written as

$$\xi(r) = \frac{1}{(2\pi)^3}\int \mathrm{d}k^3\, P(k)\, e^{i\mathbf{k}\cdot\mathbf{r}} = \frac{1}{2\pi^2}\int_0^\infty \mathrm{d}k\; k^2\, P(k)\,\frac{\sin(kr)}{kr}\,, \tag{1.11}$$

$$P(k) = \int \mathrm{d}^3r\; \xi(r) e^{-i\mathbf{k}\cdot\mathbf{r}} = 4\pi\int_0^\infty \mathrm{d}r\, r^2\, \xi(r)\frac{\sin(kr)}{kr}\,. \tag{1.12}$$

Figure 1.4 shows an example of the linear matter power spectrum and 2-point correlation function, respectively in the left and right panel. In both the two quantities one can observe the Baryon Acoustic Oscillations (BAO, Eisenstein et al. 2005; Cole et al. 2005), i.e., the trace of the fluctuations in the pre-recombination baryon-photon fluid. Such feature is imprinted in the matter power spectrum as oscillations around the scale $k \sim 0.1\,h\,\mathrm{Mpc}^{-1}$, as well as in the matter 2-point correlation function as a peak around the scale $r \sim 110\,h^{-1}\,\mathrm{Mpc}$. Although considering linear quantities, the BAO signal is subject to a non-linear damping produced by large-scale bulk flows. This produces a broadening and a shift of the BAO peak in the 2-point correlation function (Eisenstein et al. 2007), or a damping in the oscillations of the power spectrum. This effect can be modelled by the Infrared Resummation (IR, Senatore & Zaldarriaga 2015; Baldauf et al. 2015): at the lowest order, the matter power spectrum is corrected as

$$P_{\mathrm{m}}(k,z) \simeq P_{\mathrm{nw}}(k,z) + e^{-k^2\Sigma^2(z)}P_{\mathrm{w}}(k,z)\,, \tag{1.13}$$

where P_{w} and P_{nw} are, respectively, the wiggle and non-wiggle parts of the linear power spectrum, and

$$\Sigma^2(z) = \int_0^{k_s}\frac{\mathrm{d}q}{6\pi^2}\,P_{\mathrm{nw}}(q,z)\,[1 - j_0(q\,r_{\mathrm{BAO}}) + 2\,j_2(q\,r_{\mathrm{BAO}})]\,, \tag{1.14}$$

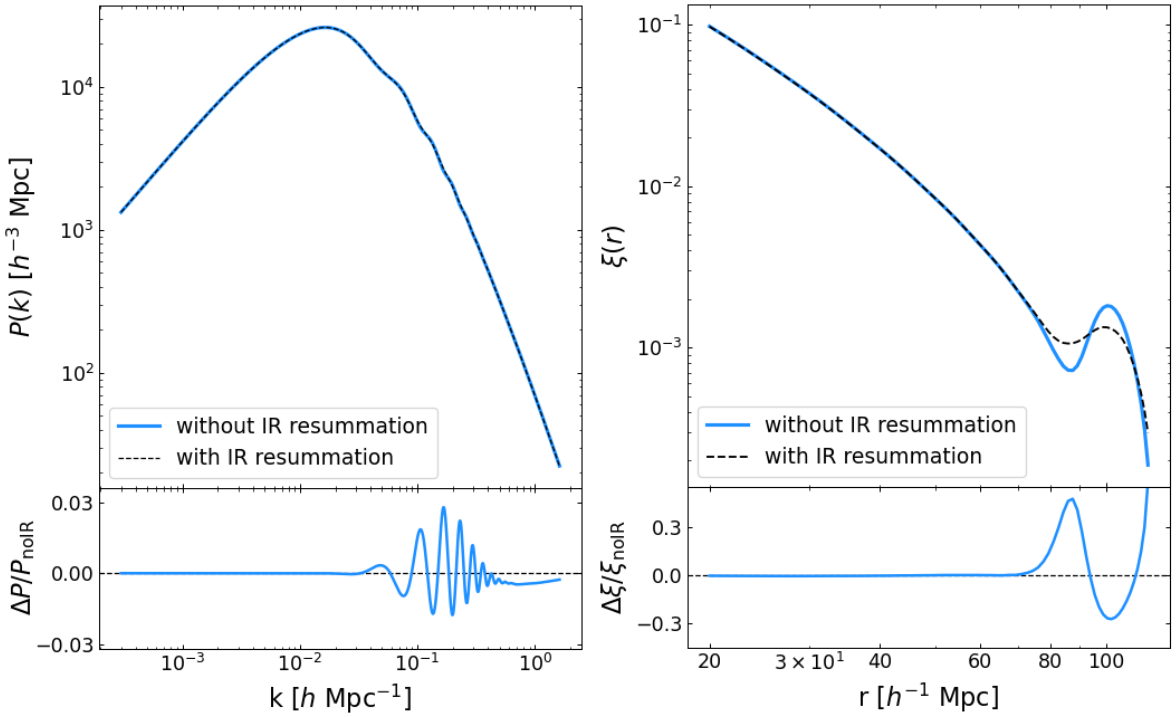

Figure 1.3: Power spectrum (left) and 2-point correlation function (right) of the matter density field at redshift $z = 0$, without (blue solid lines) and with (black dashed lines) the IR resummation. In the bottom panels, residuals between the two quantities.

where j_0 and j_2 are, respectively, the 0-th and 2-nd order spherical Bessel function. The corrected 2-point correlation function is given by the Fourier transform of Eq. (1.13). As shown in Fig. 1.4 (black dashed lines), this damping is smaller in the power spectrum (percent level), while it has an effect about ten times larger in the 2-point correlation function.

The given description of clustering statistics is based on the assumption that there is not a preferred direction in the coordinate system. Although this is essentially true on the basis of homogeneity and isotropy of the Universe, from an observational point of view the assumption ceases to be valid. In fact, the radial distance is obtained indirectly through the measurement of redshift; since galaxies have their own motion, peculiar velocities produce an additional Doppler effect that adds to the true redshift of the object, generating distortions on the observed distribution of galaxies, i.e., *redshift-space distortions* (RSD). More specifically, virialized velocities on small scales produce elongations in the radial direction, the so-called "Fingers of God", while at large scales the galaxy distribution flattens in the radial direction due to dynamical infall (Kaiser 1987).

The redshift-space matter power spectrum can be related to the real-space matter power spectrum as

$$P^{(s)}(k,\mu_{\mathbf{k}}) = \left(1 + f\mu_k^2\right)^2 P(k)\,, \tag{1.15}$$

where $\mu_{\mathbf{k}} = k_z/k$ and $f \sim \Omega_{\rm m}(z)^{0.545}$ is the linear growth rate. The redshift-space power spectrum can also be expanded in harmonics of $\mu_{\mathbf{k}}$, as

$$P^{(s)}(k,\mu_{\mathbf{k}}) = \sum_\ell P_\ell^{(s)}(k)\ \mathcal{P}_\ell(\mu_{\mathbf{k}})\,, \tag{1.16}$$

where $\mathcal{P}_l$ are the Legendre polynomials, and $P_\ell^{(s)}$ are the power spectrum multipoles. In linear regime and under the plane-parallel approximation, we can find an analytical expression for the monopole, quadrupole and exadecapole terms, respectively given by

$$P_0^{(s)}(k) = \left(1 + \frac{2}{3}f + \frac{1}{5}f^2\right) P(k), \tag{1.17}$$

$$P_2^{(s)}(k) = \left(\frac{4}{3}f + \frac{4}{7}f^2\right) P(k), \tag{1.18}$$

$$P_4^{(s)}(k) = \frac{8}{35}f^2 P(k). \tag{1.19}$$

Similar expressions are obtained for the redshift-space 2-point correlation function.

In addition to the dynamical distortions, also a geometric distortion can be introduced when assuming a wrong cosmology to convert redshifts to comoving distances (Alcock & Paczynski 1979). This geometric distortion can be modeled by multiplying the radial scale by a factor

$$\alpha = \frac{D_V}{r_s}\frac{r_s^{\rm fid}}{D_V^{\rm fid}} \tag{1.20}$$

where D_V is the isotropic volume distance and r_s is the position of the sound horizon at decoupling (Veropalumbo et al. 2014).

1.1.3 Halo bias

The distribution of galaxy clusters does not represent a Poissonian sampling of the matter density field, since clusters correspond to dark matter halos, which are expected to arise from the collapse of density peaks in the linear field, exceeding a certain threshold. The distribution of such objects is therefore affected by a bias, which in the linear regime can be described through the parameter b. Equation (1.7) is modified as

$$p^{(1)}(\mathbf{x}) = [1 + b\delta(\mathbf{x})]\,\overline{n}\,\Delta V. \tag{1.21}$$

Defining the halo density field as $\delta_{\rm h}(\mathbf{x}) = b\delta(\mathbf{x})$, we find

$$b^2 = \frac{P_{\rm h}(k)}{P_{\rm m}(k)} = \frac{\xi_{\rm h}(r)}{\xi_{\rm m}(r)}, \tag{1.22}$$

where subscripts h and m denote halos and matter, respectively.

As long as it is measured in linear regime ($k \lesssim 0.05\,h\,{\rm Mpc}^{-1}$ or $r \gtrsim 30\,h^{-1}\,{\rm Mpc}$), the halo bias of a Gaussian density field is independent of the scale, but depends on the mass and, weakly, on the redshift. A theoretical model to describe the halo bias as a function of mass and redshift can be derived from the halo mass function through the *peak-background split* (Cole & Kaiser 1989; Mo & White 1996). Such formalism is based on the assumption that the large-scale density fluctuations acts as "background" enhancement of the probability of forming a "peak", meaning that the halo bias depends on the relative abundance of halos in different large-scale regions. Being related to the halo mass function, also the halo bias has a nearly universal form if expressed in terms of peak height.

By applying the peak-background split to the Press & Schechter (1974) halo mass function, Mo & White (1996) derived an expression for the halo bias with spherical collapse

$$b(\nu) = 1 + \frac{\nu^2 + 1}{\delta_c}. \tag{1.23}$$

Since the Press-Schechter halo mass function is incorrect, also the corresponding halo bias does not agree with the simulations. A more accurate expression for the halo bias has been derived by Sheth et al. (2001), that applied the peak-background split with moving barrier for describing the ellipsoidal collapse to the Sheth & Tormen (2002) halo mass function model. Tinker et al. (2010) showed that the peak-background split prediction is, however, only 20 percent accurate. In order to increase this accuracy, the bias function can be calibrated from simulations in the same way of the halo mass function. Tinker et al. (2010) proposed a parameterization accurate to about 5 percent with simulations, and showed that FoF halos with linking length 0.2 are systematically less biased by about a 10 percent with respect SO halos at $\delta = 200$. Right panel of Fig. 1.2 shows the comparison between the three bias models, highlighting the presence of significant differences.

1.2 Cosmology with galaxy clusters

As previously stated, galaxy clusters represent a powerful tool to investigate the large-scale properties of the Universe, as they reside in dark matter halos tracing the large-scale structure's geometry and evolution. The first step in the cluster cosmology process consists in the cluster detection and the subsequent mass estimation; in fact, cluster masses are not directly observed but must be inferred through other measurable properties of clusters. From an observational point of view, clusters are detectable across the entire electromagnetic spectrum: stars composing galaxies emit light in the optical and infrared bands, while intracluster gas is observable in the X-band; in addition, such objects are visible through the Sunyaev-Zel'dovich effect (millimeter band) and they can produce gravitational lensing.

In the optical/near-IR band, clusters are seen as enhancements of the background galaxy density, and they are mainly identified by counting the number of galaxies in these overdense regions, i.e., through the optical richness. Richness correlates with cluster mass, but the intrinsic scatter of such relation is wide, also suffering from projection effects that lead to wrongly assign field galaxies along the line of sight to the cluster. To decrease such uncertainty, richness measurements can be correlated with photometric properties of galaxies. For instance, galaxy clusters are dominated by elliptical and lenticular galaxies, which lie along a sequence in the color-magnitude diagram, called red-sequence (Bower et al. 1992). Such tight relation can be exploited to obtain an unbiased identification of clusters. An example of red-sequence based identification is given by the redMaPPer detection algorithm (Rykoff et al. 2014). Another photometric property that can be used for cluster detection is the luminosity profile: as performed by the AMICO detection algorithm (Bellagamba et al. 2018), the expected galaxy distribution can be modeled by combining the information from the luminosity function and the radial density profile, assigning the appropriate weights to the galaxies in the clusters. Finally, also spectroscopic data can provide useful observables, such as the galaxy velocity dispersion, which is related to the cluster mass under the assumption of virial equilibrium.

The X-ray emission is provided by the intracluster gas that, heated to $T \sim 10^7 - 10^8$ K by the deep potential well of dark matter halos, emits light through free-free (bremsstrahlung), free-bound (recombination), and bound-bound (line emissions) interactions, whose emissivity is proportional to the square of the electron density. The X-ray band offers the most powerful way for cluster detection. In fact, clusters represent the only spatially extended extragalactic X-ray sources, clearly distinguishable from the background point-like sources, making their selection not affected by projection effects. Moreover, X-ray luminosity is well correlated with the cluster mass, with a lower dispersion with respect to the optical observables.

The Sunyaev-Zel'dovich effect (SZ, Birkinshaw 1999) is an effect that introduces secondary anisotropies into the CMB, due to the propagation of photons through clouds of ionized gas. Photons are absorbed by the high-energy electrons in the gas and re-emitted via inverse Compton effect in a different band. This mechanism produces shadows on the CMB due to the unobserved scattered photons, and bright regions in the bands where photons are re-emitted. Since gas clouds are generally found within galaxy clusters, the SZ effect can be used to detect clusters. The magnitude of the effect is proportional to the line of sight integral of the product of the gas density and temperature, and the main observable for quantifying the SZ signal is represented by $Y_{\rm SZ} = M_{\rm g}\, T$. This effect is independent on redshift, allowing for an optimal detection of high-redshift clusters, and it is insensitive to projection effects. As a disadvantage, it suffers from contamination by radio and infrared sources (Sehgal et al. 2010).

The gravitational lensing effect consists in the deflection of light by the gravitational field of massive objects (Narayan & Bartelmann 1996; Bartelmann & Schneider 2001). As such, the presence of a clusters on the line of sight can coherently distort and magnify the shape of background galaxies, producing the so-called weak lensing effect that offers a way to detect clusters and infer their masses. The advantage of gravitational lensing is that the effect depends on the total mass of the system, and does not rely on any assumption on the physical state of the cluster. Although cluster masses can be estimated only for a limited sample of objects, the information can be statistically exploited to calibrate the mass-observable relations (MoR).

All these multi-wavelength measurements make it possible to analyze various properties of clusters, such as the fraction of baryons, the mass abundance of clusters and their spatial clustering. Galaxy clusters are therefore useful as both cosmological and astrophysical observables.

1.2.1 Statistical quantities

The statistical quantities considered in this analysis are cluster abundance and cluster clustering. Mass abundance is described by the number counts, namely the mass function (Eq. 1.2) integrated over over the observed volume,

$$N_{ai} = \Omega_{\rm sky} \int_{\Delta z_a} {\rm d}z \, \frac{{\rm d}V}{{\rm d}z\, {\rm d}\Omega} \int_{\Delta M_i} {\rm d}M \, \frac{{\rm d}n}{{\rm d}M}(M, z)\,, \tag{1.24}$$

where Δz_a and ΔM_i represent, respectively, the redshift and mass bins, $\Omega_{\rm sky} = 2\pi(1 - \cos\theta)$, with θ field-of-view angle of the light cone, ${\rm d}n/{\rm d}M$ is the halo mass function, and ${\rm d}V/{\rm d}z\,{\rm d}\Omega$ is the comoving volume element per unit redshift and solid angle.

Figure 1.4: Images of the Abell 1835 cluster (z = 0.25) from X-ray, optical and SZ observations (from left to right, respectively). The images are centered on the X-ray peak position and have a side of $\sim 1.2\,\mathrm{Mpc}$. Figure from Allen et al. (2011, and references therein).

The mass function depends on cosmology through the variance (contained in the definition of ν),

$$\sigma(M,z) = \sigma(M,0)\,D(z) \sim \sigma_8 \left(\frac{M}{M_8}\right)^{-1/3} D(z), \tag{1.25}$$

where M_8 is the mass enclosed within a top-hat sphere of radius $R = 8\,h^{-1}\,\mathrm{Mpc}$. For large-mass halos the dependence on the amplitude of the fluctuations is exponential, that means that for high values of σ_8 there is a high formation of high redshift objects. Instead, the time evolution is related to the linear growth factor of the perturbations $D(z)$, which depends on Ω_m through the relation

$$D(z) = \frac{5}{2}\Omega_\mathrm{m}\,E(z) \int_z^\infty \mathrm{d}z' \frac{1+z'}{E(z')^3}, \tag{1.26}$$

where $E(z)$ is the normalized expansion rate, which for a flat ΛCDM Universe (see Sect. 1.3.1) is given by

$$E(z) = \frac{H(z)}{H_0} = \left[\Omega_\mathrm{m}(1+z)^{-3} + \Omega_\Lambda + \Omega_k(1+z)^2\right]^{1/2}, \tag{1.27}$$

where Ω_k is the curvature parameter; for a flat ΛCDM Universe $\Omega_k = 0$ and $\Omega_\Lambda = 1 - \Omega_\mathrm{m}$.

Furthermore, cluster number counts present an additional dependence on cosmology through the volume element

$$\frac{\mathrm{d}V}{\mathrm{d}\Omega\,\mathrm{d}z} = \frac{c}{H(z)}\chi^2(z), \tag{1.28}$$

where $\chi(z)$ is the comoving distance and $H(z) = H_0\,E(z)$ is the Hubble parameter.

The clustering of cluster is described by the 2-point correlation function integrated in redshift and separation bins:

$$\xi_{aj} = \int \frac{\mathrm{d}k\,k^2}{2\pi^2} \left\langle \bar{b}^2\,P_\mathrm{m}(k)\right\rangle_a W_j(k), \tag{1.29}$$

where $W_j(k)$ is the spherical-shell window function for the j-th separation bin, and $\left\langle \bar{b}^2\,P_\mathrm{m}(k)\right\rangle_a$ is the halo power spectrum averaged on the a-th redshift bin; the 2PCF will be better described in Sect. 5.1.2.

Cluster clustering also shows a strong dependence on the cosmological parameters Ω_m and σ_8: Ω_m is found, again, in the linear growth factor describing the temporal evolution of the power spectrum $P(k,z) = D^2(z)\,P_m(k,0)$, while, by definition, σ_8 is related to the normalization of the power spectrum through Eq. (1.3). Moreover, also the halo bias contains a cosmology dependence, as described in Sect. 1.1.3.

Clusters of galaxies are therefore extremely sensitive to the matter content of the Universe (Ω_m) and to the amplitude of the power spectrum (σ_8); in particular, abundance and clustering constitute two complementary probes, the combination of which helps to break the degeneracy between such two cosmological parameters.

A third observable widely used in cluster cosmology is the weak-lensing signal, which allows us to probe the projected mass distribution of clusters. Being very massive objects, galaxy clusters deflect light crossing their gravitational filed, causing a slight tangential alignment of background galaxies. This coherent image distortion allows us to detect clusters and reconstruct their mass independently of their dynamical state or through assumptions on complex baryonic physics (e.g., Bartelmann & Schneider 2001; Schneider 2006; Hoekstra et al. 2013). Mass estimation via weak lensing, either through individual cluster estimates or through stacked analyses, is extremely relevant for calibrating scaling relations (see, e.g., Johnston et al. 2007; Murata et al. 2018; Simet et al. 2017; Melchior et al. 2017; Costanzi et al. 2019). In addition, weak lensing masses contain a dependence on cosmological parameters, depending on the angular diameter distance to the sources and the mean matter density at the redshift of the clusters. For a flat ΛCDM cosmology, log-masses scale as a linear function in the matter density Ω_m, and can be modeled as (Costanzi et al. 2019)

$$\log_{10}\hat{M}_{WL}(\Omega_m) = \log_{10}\hat{M}_{WL}\big|_{\Omega_m=0.3} + \frac{d\log_{10}M_{WL}}{d\Omega_m}(\Omega_m - 0.3)\,. \tag{1.30}$$

Although we do not deal with weak lensing masses in most of this work, being focused on the characterization of theoretical systematics, in Sect. 6.5 we will consider this observable in combination with number counts and clustering, when applying the analysis to real data.

1.2.2 Systematics

The main obstacle in using clusters as cosmological probes lies in the proper calibration of systematic uncertainties that characterize the analyses of statistical quantities.

First, cluster masses must be inferred through measurable properties of clusters; the main *mass proxies* are the temperature T, mass M_g and luminosity (bolometric or X-band) of the intracluster gas, richness, velocity dispersion of galaxies, and the quantity $Y_{SZ} = M_g T$. The relationships between these observables and clusters masses, called *scaling relations*, provide a statistical measurement of cluster masses. As a first approximation, baryonic matter is exclusively subject to the dark matter gravity, which does not have a preferred scale. Under this assumption, and assuming that clusters are in virial equilibrium and formed from the gravitational collapse of initial density peaks in an Einstein de-Sitter Universe ($\Omega_m = 1$), we can expect clusters to follow a self-similar model (Kaiser 1986), meaning that perturbations has not a preferred scale and clusters are identical objects when scaled by their mass (Kravtsov & Borgani 2012). This allows the relation between the observed quantities and the cluster mass to be expressed as a power law $Q = A(z)\,M_\Delta^\alpha$, where M_Δ represents the total mass at

the overdensity Δ, and the time evolution factor depends on the evolution of the density field $A(z) \propto \overline{\rho}_{\rm g}(z) \propto E^2(z)$.

In reality, baryon physics is characterized also by non-gravitational effects, such as gas cooling and feedback from supernovae and AGN, which introduce characteristic scales into the problem, thus requiring an extension of the self-similar model. Moreover, scaling relations can be affected by intrinsic scatter due to the properties of individual clusters and baryonic physics effects that further complicate their characterization. Therefore, scaling relations must be calibrated to determine their normalization, slope, scatter and evolution (Kravtsov & Borgani 2012; Pratt et al. 2019). A first step is carried out by means of N-body simulations, which allow the calibration of parameters that strictly depend on gravity. Regarding the factors related to gas physics, since the simulation of baryonic physics is difficult and often inaccurate, an internal calibration through observational data is required. Such a calibration can be performed with the help of weak lensing mass estimates, by fitting the gravitational shear profile (Hoekstra et al. 2013). Although potentially very useful, this method still suffers from biases and uncertainties that must be removed for a proper cosmological analysis. Finally, mass proxies and observed redshifts are affected by measurement uncertainties that must be taken into account through an accurate calibration of the relations between the "true" and the observed quantities.

Another issue that requires particular attention is the cluster detection: clusters are detected by exploiting different observable properties (e.g., geometrical distribution, colors, luminosities, and density profiles for optical surveys, flux and spatial extent for X-ray surveys, and CMB distortions for SZ detection). Matching cluster detections to halos can be complex, as two halos along the same line of sight may be identified as a single cluster, or a single halo may be fragmented into more than one cluster. The cluster detection algorithm should be chosen appropriately to ensure the best final catalog's completeness and purity, which means, respectively, that it must not miss clusters that should be identified and must not identify spurious clusters not associated with any halo (White & Kochanek 2002; Aguena & Lima 2018). For this purpose, it is important to properly choose the survey selection function, i.e., the function describing the probability of an object to be observed and included in the catalog. The incorrect description of the selection function can introduce errors in the calibration of the scaling relations, as shown with an illustrative example in Fig. 1.5: black dots represent the observed objects with a value of the observable on which cluster identification is based (luminosity in this case) above the threshold set by the selection function (blue horizontal line). These are not correctly described by the mass-brightness relation represented in red, which is calibrated considering also the objects excluded from the sample (green dots). If the selection function is not considered in the calibration process, the relationship would be affected by a bias due to the absence of low-luminosity objects.

While these are the systematics related to observational processes, cluster cosmology is also affected by theoretical systematics. First, the incorrect parameterisation of the analytical models describing the observed distributions, such as mass function and bias, can introduce systematics into the analyses. As described in Sect. 1.1.1, part of the problem is associated with the ambiguity in the definition of masses due to both the use of different methods (e.g. FoF or SO) and the choice of different overdensities Δ or linking lengths b, that can create problems in the calibration of such models. It is therefore necessary to accurately study these quantities, again through the use of numerical simulations. Furthermore, the description of the cluster mass function is complicated by the presence of baryons, which have to be

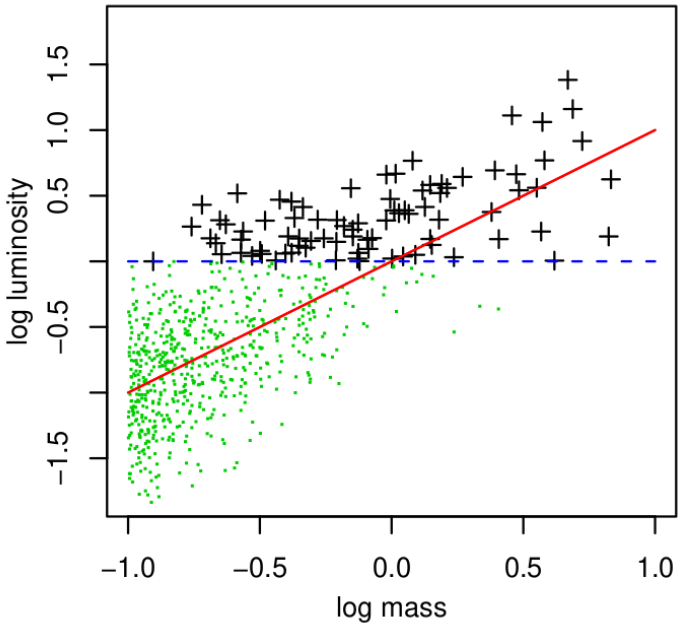

Figure 1.5: Effect of selection function in the calibration of the mass-luminosity relation. Black dots represent the observed clusters, the blue dotted line represents the brightness threshold imposed by the selection function and green dots are the clusters not observed due to the selection function. The red line is the mass-luminosity relation, calibrated considering all points. Image from Allen et al. (2011).

included in the calibration of the model.

Figure 1.2 represents different models of halo mass function (left) and bias (right), obtained through the use of simulations. It can be seen how the various parameterisations differ from each other; the choice of a model to describe the data is therefore a fundamental step in the analysis of observational catalogs.

Second, there may be theoretical systematics linked to the modeling of statistical errors associated to those quantities, which require to be properly included in the form of covariance matrices. For number counts, the main sources of statistical errors are represented by shot-noise and sample variance. Shot-noise is the error arising from the discrete nature of the data and describes the fluctuations in the number of objects observed around the expected value. In the case of a Poissonian distribution, shot-noise is given by

$$\sigma_{\rm sn} = \sqrt{N}, \tag{1.31}$$

where N is the number of objects counted in a bin. Shot-noise is relevant when the number of counts is low, while it becomes negligible as N increases. Sample variance derives from the fact that the Universe is isotropic and homogeneous on a large scale, but on smaller scales it presents inhomogeneities resulting from random processes; in order to "cancel" the effect of these fluctuations it is necessary to observe a sufficiently large volume that is representative of the entire Universe. Observing finite volumes, instead, introduces an uncertainty that, unlike shot-noise, only depends on the size and the shape of the sampled volume. Similarly to shot-noise, the sample variance contribution can be expressed, in terms of the number of counts N

as

$$\sigma^2_{\rm sv} = \frac{\langle N^2\rangle - \langle N\rangle^2}{\langle N\rangle^2} - \frac{1}{\langle N\rangle}\,, \tag{1.32}$$

where the first term is the variance of counts in random spheres and the second term is the Poissonian contribution, and brackets indicate the ensemble average. Sample variance introduces correlation between different mass and redshift ranges, while shot-noise only affects objects in the same bin. In the past, surveys were characterized by low numbers of counts and consequently the main contribution to the error came from shot-noise, while the sample variance term was usually neglected (e.g. Mantz et al. 2015; Bocquet et al. 2019). Nevertheless, the most recent and upcoming surveys provide catalogs with a larger number of objects, making sample variance comparable, or even greater, than the shot-noise level (Hu & Kravtsov 2003). An example is provided by the DES analyses, where the sample variance contribution is already taken into account when analyzing cluster number counts (Abbott et al. 2020; Costanzi et al. 2021).

For cluster clustering the treatment of theoretical systematic is non-trivial to be modeled. Several works have developed models for the covariance of galaxy correlation functions, both in configuration and Fourier space (see, for instance, Scoccimarro et al. 1999; Meiksin & White 1999; Takada & Hu 2013; Wadekar & Scoccimarro 2020; Philcox & Eisenstein 2019; Li et al. 2019). Galaxy clustering is characterized by a Gaussian covariance, representing the main contribution at large scales, plus a non-Gaussian term arising from nonlinear gravitational instability, galaxy/halo bias and redshift-space distortions, which dominates at small scales. In addition, the coupling between short-wavelengths modes with perturbations larger than the survey size, also induced by non-Gaussianities, namely super-sample covariance, contributes to the error budget on small scales. Lastly, the shape of the observed volume can also have an impact on the covariance, requiring a convolution of the power spectrum with the window function of the survey. Because of these non-Gaussian contributes, the error associated with the 2-point function is described through the use of high-order statistics, i.e., 3- and 4-point functions. For cluster clustering the situation is in principle simpler, as the scales involved are larger and mostly linear. This feature makes it possible to ignore highly nonlinear effects, such as super-sample covariance, since it dominates the non-Gaussian errors in the weakly or deeply nonlinear regime (Takada & Hu 2013). However, the lower densities characterizing these objects produce a different weight of the various contributions (e.g. shot noise, Paech et al. 2017) to the covariance, compared to the case of galaxies, and this could make non-Gaussian terms relevant even in the linear regime. Up to now, the analytical covariance for cluster clustering has rarely been studied (Valageas et al. 2011; To et al. 2021b), preferring instead numerical methods or internal estimates.

1.3 Cosmological parameter estimation

1.3.1 ΛCMD model

The model that better seems to describe the observed properties of the Universe is the so-called "flat ΛCD" model, which predicts a flat Universe in accelerated expansion, composed by baryonic matter ($\sim 4\%$), dark matter ($\sim 26\%$) and dark energy ($\sim 70\,\%$), plus small fractions of other components, as radiation ($\sim 0.01\,\%$) and neutrinos ($\sim 0.1\,\%$) (Planck Collabo-

ration VI. 2020). While baryonic matter interacts with electromagnetic radiation and can be easily detected, the "dark" components are much more complicated to observe, so that their nature is still unknown. According to the model, dark matter behaves like a cold collisionless fluid, i.e., it is composed by particles that were not relativistic at the time of their decoupling from the other components of the Universe, and that is only subject to gravitational interactions. Dark energy is described as a negative-pressure fluid, consistent with being a term of pure cosmological constant (Λ) and responsible for the accelerated expansion. Moreover, such model assumes that general relativity is still valid on cosmological scales and that the initial matter fluctuations have been generated as a random Gaussian field during Inflation, i.e., a period of accelerated expansion in the primordial Universe.

Such model is defined through six parameters:

- Ω_b and Ω_c, respectively the baryon and dark matter density parameters, such that their sum provides the total matter density parameter $\Omega_\mathrm{m} = \Omega_\mathrm{b} + \Omega_\mathrm{c}$;
- cosmological constant density parameter Ω_Λ, which for a flat Universe is such that $\Omega_\Lambda + \Omega_\mathrm{m} = 1$;
- the Hubble constant H_0, usually expressed in terms of dimensionless parameter $h = H_0/(100\,\mathrm{Km\,s^{-1}\,Mpc^{-1}})$;
- normalization and slope of the matter power spectrum, respectively A_s and n_s. Alternatively, the normalization can be described by σ_8, i.e. the r.m.s. of matter fluctuations on scale of $8\,h^{-1}\,\mathrm{Mpc}$, derived through the definition of variance σ_R^2 (Eq. 1.3) and the relation $P_\mathrm{m}(k) = A_s k^{n_s} T(k)^2$, where $T(k)$ is the transfer function.

The standard model can eventually be extended, with the addition of some parameters:

- w_0 and w_a, to describe an evolving dark energy equation of state (Chevallier & Polarski 2001)
$$P = [w_0 + w_a(1-a)]\rho\,,$$
where a is the scale factor, and $w_0 = -1$, $w_a = 0$ correspond to the cosmological constant case;
- f_NL, describing non-Gaussian initial condition of the matter density field. According to Salopek & Bond (1990), the gravitational potential fluctuations can be parametrised as
$$\Phi = \Phi_\mathrm{G} + f_\mathrm{NL}(\Phi_\mathrm{G}^2 - \langle\Phi_\mathrm{G}^2\rangle)\,,$$
where Φ is the gauge-invariant Bardeen potential of the primordial fluctuations, and Φ_G is the Gaussian component. Setting $f_\mathrm{NL} = 0$ recovers the standard case;
- γ, describing possible deviations from general relativity (Linder 2005), such that the growth of perturbations follows
$$\frac{\mathrm{d}\ln D(a)}{\mathrm{d}\ln a} = \Omega_\mathrm{m}(a)^\gamma\,,$$
where $D(a)$ is the linear growth factor as function of the scale factor. For general relativity $\gamma \simeq 0.55$, with a weak dependence on cosmological parameters;

- Ω_ν, i.e. the neutrino density parameter, linked to the total neutrino mass $\sum m_\nu$ by

$$\Omega_\nu = \frac{\rho_\nu}{\rho_c} = \frac{\sum m_\nu}{93.14\,h^2\,\mathrm{eV}},$$

  where ρ_c i the critical density of the Universe. The standard model predicts three neutrino flavors, with still unknown masses; neutrino oscillation experiments allows a minimum value of $\sum m_\nu = 0.06\,\mathrm{eV}$, to which corresponds $\Omega_\nu = 0.0016$ (Lattanzi & Gerbino 2018), while cosmological observations can provide an upper limit (see left panel of Table 1.1).

Parameter estimation can be carried out through the use of different observables, which are sensitive to variations of different parameters. One of the most important cosmological probes is the *Cosmic Microwave Background* (CMB, Hu & Dodelson 2002), which represents the radiation density field immediately after the decoupling with matter ($z \simeq 1100$), when photons began to propagate without interacting with baryonic particles anymore. This observable reflects the initial conditions of baryonic fluctuations, which until the time of decoupling oscillated together with radiation. Once decoupled, baryonic matter continued to evolve following the gravitational field of dark matter, independent of radiation. CMB therefore describes the density field of radiation, which has remained unchanged since the epoch of recombination (except for the expansion of the Universe), and allows us to extract information regarding baryonic fluctuations at the time of decoupling, but not their subsequent evolution.

Another widely used observable is gravitational lensing (Narayan & Bartelmann 1996; Bartelmann & Schneider 2001), consisting in the deflection of light by the gravitational field of massive objects, such as galaxy clusters. In particular, *cosmic shear* represents the differential distortion due to the propagation of light through the LSS and is therefore sensitive to the distribution of matter. The study of this effect is particularly advantageous because it provides direct information regarding the distribution of both dark and baryonic matter, as it is only generated by gravity. Unlike CMB, gravitational lensing provides information about the density field of matter at low redshift ($z < 10$) and is sensitive to the evolution of structures.

Other useful observables are the Baryon Acoustic Oscillations (BAO, Eisenstein et al. 2007; Cole et al. 2005), the redshift-space distortions (RSD, Kaiser 1987; Hamilton 1997), supernovae Ia (SNIa, Perlmutter et al. 1999) and galaxy clusters (see, e.g., Allen et al. 2011). BAO represent the trace of the acoustic oscillations of the pre-recombination baryon – photon fluid, and are observed in both the matter, through galaxy clustering, and CMB radiation power spectra on a scale of $\sim 110\,h^{-1}\,\mathrm{Mpc}$. Due to their fixed size, BAO are used as standard rulers in calculating the distances and expansion of the Universe. RSD are the distortions of the galaxy distribution produced by the peculiar velocities of galaxies along the line of sight. Being related to the dynamics of galaxies, such distortions contain information about the cosmic mass distribution, probing the growth rate of cosmic structures and gravity. SNIa are supernovae originated from the explosion of a white dwarf in a binary system: the white dwarf accretes mass from its companion star (or merge with anther white dwarf) until it reaches the Chandrasekhar limit, beyond which the electron degeneracy pressure cannot compensate for the gravitational force of the star, leading to the collapse and explosion of the system. Since the explosion always occurs under the same conditions, all SNIa have the same peak brightness, making them standard candles useful for estimating distances and the rate of

expansion of the local Universe. Being sensitive to different parameters, all these observables can be combined together to break degeneracies and obtain more stringent constraints.

Left panel of Table 1.1 shows the values of the standard model cosmological parameters measured by Planck Collaboration VI. (2020). The reported values were obtained by combining CMB measurements made by the Planck satellite with BAO and gravitational lensing measurements. It can be seen that the uncertainties on the parameters are extremely small, partly due to the combination of multiple observables. Right panel of Table 1.1 reports values for the extensions of the standard model, measured by Planck Collaboration VI. (2020) through CMB, BAO and gravitational lensing, Planck Collaboration IX. (2020) from combined temperature and polarization CMB data, and Mana et al. (2013) through CMB and cluster data.

Table 1.1: *Left panel:* Best-fit values of parameters and 1σ uncertainties for the flat ΛCDM model, measured by Planck Collaboration VI. (2020) through combination of CMB, BAO and lensing. *Right panel:* Best-fit values of parameters and 1σ uncertainties for the extensions of flat ΛCDM model. $w_a, w_0, \sum m_\nu$ are measured by Planck Collaboration VI. (2020), while γ and f_{NL} are obtained, respectively, by Planck Collaboration IX. (2020) from CMB data and Mana et al. (2013) from galaxy cluster and CMB data.

flat ΛCDM model	
parameter	value
$\Omega_b h^2$	0.02242 ± 0.00014
$\Omega_c h^2$	0.11933 ± 0.00091
Ω_m	0.3111 ± 0.0056
Ω_Λ	0.6889 ± 0.0056
h	0.6766 ± 0.0042
n_s	0.9665 ± 0.0038
$\ln(10^{10} A_s)$	3.047 ± 0.014
σ_8	0.8102 ± 0.0060

flat ΛCDM model extensions	
parameter	value
w_0	-0.961 ± 0.077
w_a	$-0.28^{+0.31}_{-0.27}$
$\sum m_\nu$	$< 0.12\ eV$
γ	0.58 ± 0.12
$f_{\rm NL}$	-0.9 ± 5.1

1.3.2 State of the art of cluster cosmology

Regarding the state-of-the-art of cluster cosmology, number counts constitute the most widely used observable. Some of the most recent results in the optical band have been obtained from Costanzi et al. (2019) and Abbott et al. (2020), respectively analyzing cluster data from the *Sloan Digital Sky Survey*[2] (SDSS) and the *Dark Energy Survey*[3] (DES). Another recent result is proposed by Bocquet et al. (2019), who analyzed a sample of SZ-selected clusters by the *South Pole Telescope*[4] (SPT). In all these cases the relationship between cluster masses and observables are calibrated via weak lensing observations and a flat ΛCDM model with massive neutrinos is assumed. Costanzi et al. (2021), instead, derived cosmological and scaling relation constraints from the combination of DES cluster abundance data and SPT follow-up

[2] https://www.sdss.org/
[3] https://www.darkenergysurvey.org/
[4] https://pole.uchicago.edu/

Table 1.2: Constraints for the cosmological parameters Ω_m and σ_8 from cluster number counts (NC), alone and combined with other cosmological probes

	probes	Ω_m	σ_8
Schellenberger & Reiprich (2017)	NC	$0.217^{+0.073}_{-0.054}$	$0.894^{+0.098}_{-0.095}$
	NC + f_{gas} + WMAP9	0.297 ± 0.008	$0.822^{+0.016}_{-0.014}$
Costanzi et al. (2019)	NC + WL	$0.22^{+0.05}_{-0.04}$	$0.91^{+0.11}_{-0.10}$
	NC + WL + Planck + BAO	$0.316^{+0.010}_{-0.008}$	0.81 ± 0.02
Bocquet et al. (2019)	NC + WL	0.285 ± 0.047	0.763 ± 0.037
	NC + WL + Y_X + Planck	0.353 ± 0.027	0.761 ± 0.033
Abbott et al. (2020)	NC + WL	$0.179^{+0.031}_{-0.038}$	$0.85^{+0.04}_{-0.06}$
Costanzi et al. (2021)	DES-NC + SPT-OMR	$0.264^{+0.047}_{-0.073}$	$0.795^{+0.045}_{-0.059}$
Salvati et al. (2022)	NC + Planck	$0.29^{+0.04}_{-0.03}$	$0.76^{+0.03}_{-0.04}$

data, constraining the mass-observable relation with multi-wavelength data. Another example is provided by Salvati et al. (2022), who provided the first combination of Planck and SPT cluster catalogs. An example of an X-band result is instead provided by Schellenberger & Reiprich (2017), through the analysis of the *HIghest X-ray FLUx Galaxy Cluster Sample* (HIFLUGCS) catalog produced from the data of *ROSAT All Sky Survey*[5] (RASS). Table 1.2 shows the constraints for the parameters σ_8 and Ω_m obtained from all the groups, either by analyzing cluster abundances alone or by combining them with other data. Comparing the results, it can be seen that the values obtained from the abundance analyses are compatible with each other. However, the analysis of number counts from optical surveys combined with weak-lensing masses usually presents lower values of Ω_m with respect the standard values; this topic will be further discussed in Sect. 1.3.3. Also, these results show that the combination with other complementary observables allows the level of precision to be increased, reducing the error bars of the number counts results.

For further comparison, Fig. 1.6 shows the values of σ_8 at $\Omega_m = 0.3$ found by several authors, including those mentioned above. Blue points represent the results from number counts, green points are the values obtained from weak lensing/cosmic shear and galaxy clustering analyses, and red points show the constraints from CMB. The blue bands represent the standard error (0.012, dark region) and standard deviation (0.033, light region) around the mean (0.789), calculated from the values found from the cluster analyses. It can be seen that all the values obtained from number counts are in good agreement with each other and with the cosmic shear/galaxy clustering results, as well as with the CMB results obtained from WMAP; the parameters found by Planck, on the other hand, prefer somewhat larger values of σ_8, with values that are barely contained in 1σ region.

Although still poorly exploited due to the lack of statistics, also the cluster clustering is a powerful tool to extract cosmological information. Derivation of cosmological constraints from the clustering of galaxy clusters was first studied by Borgani et al. (1999), in which the 2-point correlation function of clusters in the *X-ray Brightest Abell-type Cluster sample* catalog

[5] https://heasarc.gsfc.nasa.gov/docs/rosat/rass.html

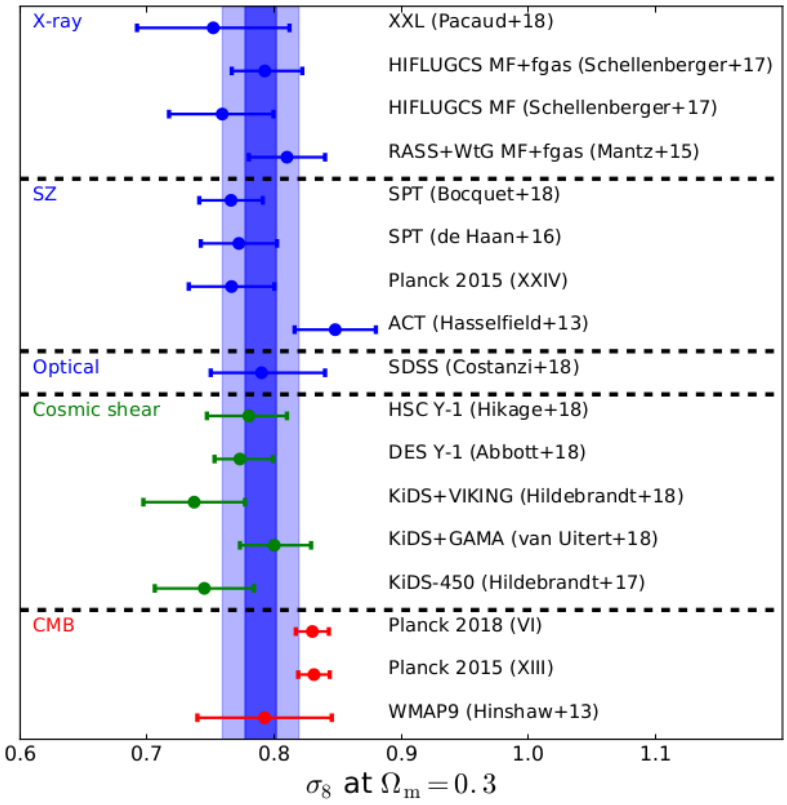

Figure 1.6: Best-fit values and 1σ uncertainties for σ_8 at $\Omega_m = 0.3$ found by various authors with different observables: cluster number counts in blue, cosmic shear/galaxy clustering in green, and CMB in red. Blue bands represents the standard error (dark) and standard deviation (light) with respect to the cluster results average. Image from Pratt et al. (2019).

(XBACs) was analyzed to find constraints on σ_8. The result, corresponding to $0.8 < \sigma_8 < 2.0$ for $\Omega_m = 0.3$, is in agreement with what was found by the abundance analysis, although characterized by less stringent constraints.

The clustering of clusters presents some advantages with respect to the clustering of galaxies. Rising from the highest density peaks of the density field, galaxy clusters are a highly biased tracer of the large-scale structure, i.e., with a larger clustering signal easily detectable also at large scales. Cluster clustering can be observed on large scales, where linear theory is still suitable for describing its properties (i.e., $k \lesssim 0.05\,h\,\mathrm{Mpc}^{-1}$ or $r \gtrsim 30\,h^{-1}\,\mathrm{Mpc}$). Also, bias is primarily a function of the halo mass and can be calibrated using multi-wavelength observations. Moreover, cosmology enters in the relation between bias and mass/redshift, increasing the constraining power of cluster clustering (Mo & White 1996; Tinker et al. 2010). Finally, Castro et al. (2020) showed that the net effect of baryons is to change the mass of clusters with negligible impact on the clustering of matched objects in dark matter and hydro simulations.

Although clustering analysis of clusters does not provide results as accurate as those of other observables, cluster clustering is especially useful when combined with other probes, such as number counts or weak gravitational lensing, for two main reasons. First, having a different cosmology dependence, it makes it possible to break the degeneracies on parameters and improve the constraining power of these observables (Schuecker et al. 2003; Sereno

et al. 2015; Sartoris et al. 2016). Second, one of the main limitations in the cosmological exploitation of galaxy clusters lies in the fact that cluster masses have to be indirectly inferred through observable properties, such as the cluster richness, velocity dispersion, X-ray temperature or Sunyaev-Zeldovich signal. The calibration of such mass-observable scaling relations is affected by systematic biases and observational uncertainties (e.g. Kravtsov & Borgani 2012; Pratt et al. 2019). Cluster clustering, presenting different degeneracies on parameters with respect to cluster number counts, can help to calibrate such relations, reducing the uncertainties in the mass estimation and further improving the constraints on cosmological parameters (Majumdar & Mohr 2004; Mana et al. 2013; To et al. 2021a; Lesci et al. 2022). The correlation function of galaxy clusters has also been used to identify the Baryonic Acoustic Oscillations (BAO) in a CMB-independent way (Miller et al. 2001; Angulo et al. 2005; Huetsi 2010; Veropalumbo et al. 2014; Moresco et al. 2021).

The simultaneous analysis of abundances and clustering was first proposed by Schuecker et al. (2003), through the analysis of the cluster catalog *ROSAT ESO Flux-Limited X-ray* (REFLEX). The constraints on Ω_m were found to have error bars reduced by a factor of 2, and by a factor of 8.6 for σ_8, compared to the analysis of abundances alone. Cluster clustering has also been combined with other data by Mana et al. (2013): by analyzing the *maxBCG catalogue* produced from SDSS photometric data, they showed that the joint analysis of power spectrum and cluster counts provides an improvement on the accuracy on the constraints of σ_8 and Ω_m by about 50% compared to the analysis of abundances alone, which can be further increased by including CMB data. The left panel of Fig. 1.7 shows the confidence levels on the parameters σ_8 and Ω_m, found through abundance, clustering and CMB analysis. From this plot, one can see the different degeneracy presented by number counts (blue contours) and clustering (yellow contours) in the plane $\sigma_8 - \Omega_m$ and how this decreases by combining the analysis of the two observables (green contours). A third result has been presented by Sereno et al. (2015), who constrained σ_8 through a combined analysis of stacked gravitational lensing and clustering of galaxy clusters, finding that such combination allows to constrain σ_8 without any knowledge of scaling relations, selection function, or modeling of the bias. A further result has been obtained by To et al. (2021a), who performed a joint analysis of cluster abundances, three cluster cross-correlations (including cluster clustering), and auto correlations of galaxy density. The results are consistent with the DES-Y1 galaxy clustering and weak lensing analysis, and show an improvement in the constraints on both cosmological and observable–mass scaling relation parameters. Finally, Lesci et al. (2022) analyzed the KiDS-DR3 data (Maturi et al. 2019), showing how the cluster clustering can successfully constrain cosmological parameters and the normalization of the mass-observable relation, if combined with the prior information from number counts and weak lensing. Table 1.3 shows the constraints on Ω_m and σ_8 obtained by the mentioned works.

1.3.3 Open issues

Although the ΛCDM model successfully explains most of the observational constraints on cosmic expansion and growth of structures, it still suffers from some tensions between the values of some parameters, estimated from different probes. The main examples are the value of the Hubble constant H_0 (see, e.g., Verde et al. 2019), and the value of $S_8 = \sigma_8 \sqrt{\Omega_m/0.3}$ (see, e.g., Battye et al. 2015). The former is characterized by different results from late-time probes, such as SNIa, which measure values around $73\,\mathrm{km\,s^{-1}\,Mpc^{-1}}$, and CMB, measuring

Table 1.3: Constraints for the cosmological parameters Ω_m and σ_8 from cluster clustering (CL), combined or combined with other cosmological probes

	probes	Ω_m	σ_8
Schuecker et al. (2003)	CL+NC	$0.341^{+0.031}_{-0.028}$	$0.711^{+0.039}_{-0.031}$
Mana et al. (2013)	CL+NC	0.215 ± 0.022	0.84 ± 0.04
Sereno et al. (2015)	CL+WL	-	0.79 ± 0.16
To et al. (2021a)	6x2pt+N	$0.305^{+0.055}_{-0.038}$	$0.783^{+0.064}_{-0.054}$
Lesci et al. (2022)	CL+prior from NC+WL	$0.28^{+0.05}_{-0.04}$	$0.82^{+0.14}_{-0.12}$

the early Universe and its growth rate, which prefers values around $67\,\mathrm{km\,s^{-1}\,Mpc^{-1}}$. The discrepancy between early and local measurements is about 5σ. The latter refers to a $\sim 2\sigma$ tension between measurements of the amplitude of the matter power spectrum inferred from CMB ($S_8 \sim 0.83$), and directly measured by LSS probes, such as lensing and galaxy clustering, clusters, and redshift space distortions ($S_8 \sim 0.75$).

Besides these two main tensions, there are other inconsistencies that specifically concern galaxy clusters. As the analyses of the DES cluster catalogs show, the cosmological constraints from cluster counts lead to particularly low values of the matter density parameter ($\Omega_m = 0.179^{+0.031}_{-0.038}$, Abbott et al. 2020), in sharp contrast with the values found by the other observables ($\Omega_m \sim 0.3$). Unlike the H_0 and S_8 tensions, which might indicate the incompleteness of the ΛCDM model and the need to introduce new physics, these values are most likely caused by the incorrect or incomplete treatment of the systematics affecting the cosmological analysis of DES clusters. More specifically, cluster counts results are limited by the accuracy of the cluster mass calibration. In fact, the weak lensing mass estimate can be biased by the wrong treatment of selection and projection effects affecting the optical observables such as richness (Sunayama et al. 2020; Zhang & Annis 2022; Wu et al. 2022). In particular, the weak lensing mass estimates for richness $\lambda < 30$ drive the tension with other cosmological results, including the constraints inferred through different observables from the DES data (Abbott et al. 2020).

1.3.4 The Euclid mission

The study and the control of the uncertainties described in Sect. 1.2.2 are fundamental for future surveys, which will provide large cluster samples that will allow us to constrain cosmological parameters with a level of precision much higher than that obtained so far. One of the main forthcoming surveys is the European Space Agency (ESA) mission *Euclid* [6] which will observe a large portion of the extragalactic sky in optical and infrared band, identifying about 10^5 galaxy clusters up to redshift $z = 2$ by photometric, spectroscopic and gravitational lensing (Laureijs et al. 2011; Euclid Collaboration: Scaramella et al. 2022). Three-dimensional maps of the distribution of dark and luminous matter in the Universe over the last 10 billion years, corresponding to the period when dark energy produces the accelerated expansion, will thus be constructed. The satellite is scheduled for launch in 2023 and the nominal mission will last six years, during which four photometric surveys will be carried out: a "Euclid

[6] http://www.euclid-ec.org

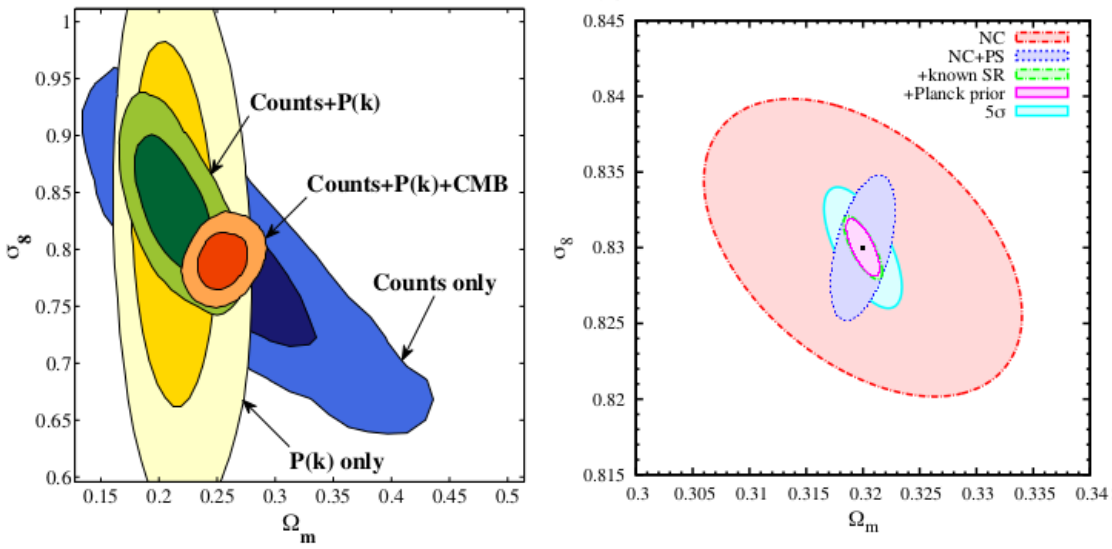

Figure 1.7: *Left panel:* Contours at 68% and 95% confidence level on the parameters σ_8 and Ω_m, from analysis of cluster abundances (Counts), cluster clustering ($P(k)$), and CMB. Image from Mana et al. (2013). *Right panel:* forecasts on the constraints at the 68% confidence level on the parameters σ_8 and Ω_m from: (i) number counts (NC), (ii) number counts and clustering (NC+PS), (iii) NC+PS+ known SR, i.e., assuming full knowledge of the nuisance parameters, (iv) NC+PS+ known SR + Planck, i.e., with priors from Planck data, (v) same as the previous case but with more stringent selection function. Image from Sartoris et al. (2016).

Wide Survey", which will cover 15 000 deg^2 of sky uncontaminated by light from the Galaxy and observe clusters with magnitudes up to 24.5 *mag* in the visible band and 24 *mag* in the infrared band, and three "Euclid Deep Fields" of about 2 magnitudes deeper than the wide survey, which will observe 40 deg^2 of the sky. Photometric observations will also be complemented by spectroscopic surveys that will cover the same areas of sky and provide the redshifts of tens of millions of galaxies.

Catalogs produced by *Euclid* will allow cosmological parameters to be constrained with unprecedented precision, in order to determine the nature and properties of dark energy, dark matter and gravity, and to acquire information on the initial conditions for the formation of cosmic structures and the mass of neutrinos. The mission is optimised to determine the expansion rate of the Universe and the growth rate of cosmic structures. The observables most sensitive to these quantities are weak gravitational lensing and galaxy clustering (BAO and RSD). In addition, other independent observables such as galaxy clusters, dark matter density profiles and supernovae will be analyzed.

Cluster catalogs will be constructed by selecting objects with two detection algorithms: the Adaptive Matched Identifier of Clustered Objects (AMICO, Bellagamba et al. 2018) code, based on matched filtering, and the PZWav (Gonzalez 2014) code, based on an adaptive wavelet approach. Their performance has been tested, along with other four independent detection algorithms, and the two codes have been chosen to be implemented in the *Euclid* pipeline, having achieved more than 80% completeness for a mean purity of 80% down to masses of $10^{14}\,M_\odot$ and up to redshift $z = 2$ (Adam et al. 2019).

A forecast of the capability of the *Euclid* cluster survey has been performed by Sartoris et al. (2016), which shows the effect of the photometric selection function on the number of

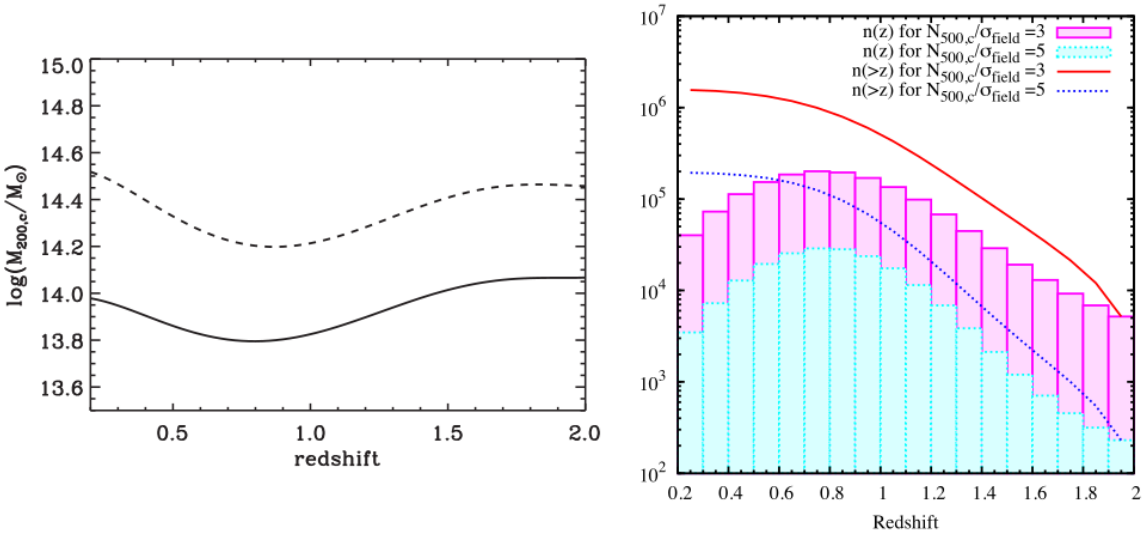

Figure 1.8: *Left panel:* cluster mass selection function for the survey *Euclid*. The solid line corresponds to the threshold $N_{500,c}/\sigma_{\rm field} = 3$, while the dashed line to $N_{500,c}/\sigma_{\rm field} = 5$. *Right panel*: Counts (histograms) and cumulative distributions (lines) of observable clusters as a function of redshift, with bin of $\Delta z = 0.1$, for the two selection functions. Images from Sartoris et al. (2016).

detected objects and the consequent cosmological constraints for different cosmological models. An estimate of the selection function for the photometric survey is shown in the left panel of Fig 1.8, representing the minimum observable mass (measured at $\Delta_c = 200$) as a function of redshift. The two lines refer to the cases $N_{500,c}/\sigma_{\rm field} = 3$ and 5, where $N_{500,c}$ is the number of clusters in a sphere of radius $r_{500,c}$ and $\sigma_{\rm field}$ is the standard deviation of galaxy counts in the field, which takes into account shot-noise and sample variance. The non-constant trend is due to the relative contribution of these terms, such that cosmic variance modifies the trend of the function for $z \leq 0.5$, while shot-noise prevails at higher redshift. The right panel of the same figure shows the expected number of objects as a function of redshift (histograms) and the corresponding cumulative distributions (lines) for the two selection functions. It should be noted that, given the large statistics of galaxy clusters expected from the *Euclid* wide survey, an accurate description of the possible theoretical systematics is necessary. Regarding the forecasts for the parameters constraints, the estimated confidence levels for the parameters σ_8 and $\Omega_{\rm m}$ are shown in the right panel of Fig. 1.7. It can be seen that the posteriors of cluster abundance analysis are significantly improved when number counts are combined with the clustering analysis. The contours are further reduced by introducing priors from CMB or by neglecting measurement uncertainties. We can also note that the constraints are more stringent than those in the left panel of the figure, as the catalogs that will be produced by *Euclid* will have higher statistics than those already available.

Finally, Köhlinger et al. (2015) show that the weak lensing systematics in the mass calibration are under control for *Euclid*, which will be limited by the cluster samples themselves.

Chapter 2

Cosmological simulations

In this chapter, we describe the topic of numerical simulations. In order to perform an accurate statistical analysis, simulations produced with approximate methods are more suitable than N-body simulations; this statement will be motivated in the following. We will give a quick presentation of approximate methods and Lagrangian Perturbation Theory, which provide the basis for generating this type of simulations. After that, we will describe the "PINOCCHIO" algorithm used to produce the catalogs analyzed in this thesis work. Finally, we will present the dataset used in this work, both for the validation of covariance models and for cosmological forecasts, and the mass calibration process required before starting the analysis.

2.1 Numerical simulations

Numerical simulations are the main tool for accurately studying the non-linear evolution of cosmic structures. Over the years, N-body and hydrodynamic simulations made it possible to verify and confirm several theoretical predictions in cosmology and astrophysics, such as the formation of clusters and their clustering (Jenkins et al. 1998), the properties of intracluster gas (Evrard 1990) and the density profiles of dark matter halos (Navarro, Frenk, & White 1996). Moreover, as described in the previous section, N-body simulations are fundamental tools for the calibration of analytical models and scaling relations.

N-body simulations describe the evolution of dark matter under the effect of gravity, calculating the forces acting on the particles, thus determining their orbits (see, e.g., Bertschinger 1998; Vogelsberger et al. 2020). In few words, initial conditions are set by imposing perturbations on an initially uniform distribution of particles, at some early time ($z \sim 100$); these constitute the initial linear density fluctuation field evolving in a homogeneous expanding background. Then, the forces acting on each particle are computed by integrating the equation of motion at each time step. The motion of dark matter particles is described by the collisionless Boltzmann equation

$$\frac{\mathrm{d}f}{\mathrm{d}t} = \frac{\partial f}{\partial t} + \mathbf{v}\frac{\partial f}{\partial \mathbf{r}} - \frac{\partial \Phi}{\partial \mathbf{r}}\frac{\partial f}{\partial \mathbf{v}} = 0\,, \tag{2.1}$$

where $f(\mathbf{r}, \mathbf{v}, t)$ is the phase-space density function of dark matter, and Φ is the collective

gravitational potential satisfying the Poisson equation

$$\nabla^2\Phi = 4\pi G \int f \mathrm{d}\mathbf{v}\,. \tag{2.2}$$

Equations (2.1) and (2.2) have to be solved in an expanding Universe, and the relativistic gravity description can be approximately substituted by Newtonian gravity. Given a system of N particles, the problem consists of a set of $2N$ coupled partial differential equations, which cannot be solved by applying standard discretization techniques because of the high dimensionality of the system. The equations are therefore solved numerically by integrating them into a set of finite time steps, computing the force acting on each particle. To this purposes, different methods can be applied (e.g., Particle-Particle code, Tree code, Particle-Mesh code). Once forces are computed, the positions and velocities of the particles are evolved forward in time. The accuracy and efficiency of a simulation depend on the resolution of mass and force and the choice of time step. Firstly, particles do not represent individual astrophysical objects (e.g. galaxies), but rather fluid elements; consequently the mass of the particles determines the resolution of the simulation, since only objects with mass much large than the mass of a particle can be meaningfully described in a simulation. In addition, a too high force resolution or a too small time step can result in considerably high computational costs, and must therefore be optimized.

The state-of-the-art of N-body cosmological simulations is continuously evolving as computational resources and algorithms improve. The recent simulations have reached an unprecedented level of detail and accuracy; among them, the Abacus Summit, is a recent example of a large-scale N-body simulation that was run on the Summit supercomputer at Oak Ridge National Laboratory (Maksimova et al. 2021). It was able to simulate the distribution of dark matter, galaxies, and other structures in 150 cubical boxes of side of $2\,h^{-1}\,\mathrm{Gpc}$, using more than 10^{12} particles. Other examples are given by the IllustrisTNG simulations (Nelson et al. 2018), which simulate the large-scale structure of the universe including the distribution of dark matter and the formation of galaxies, in volumes of 50, 100, and 300 Mpc side length, using more than 10^{10} particles, the Quijote simulations (Villaescusa-Navarro et al. 2020), a set of 44 100 full N-body simulations spanning more than 7000 cosmological models, designed to provide enough data to train machine-learning algorithms, the OuterRim simulations (Heitmann et al. 2019), covering a volume of side of 4225 Mpc and evolving more than 10^{12} particles, and the Uchuu simulations (Ishiyama et al. 2021), a set of large high-resolution cosmological N-body simulations where the largest simulation consists of more than 10^{12} dark matter particles in a box of side-length $2\,h^{-1}\,\mathrm{Gpc}$. These simulations are becoming essential tools in the field of cosmology, providing the predictions that can be tested with the upcoming high precision surveys and experiments.

N-body simulations are usually generated for describing systems that can exceed 10^{12} particles and can therefore be extremely expensive, from a computational point of view. A further complication occurs when the baryonic component has to be included, as it must be reproduced through the use of hydrodynamic simulations that are even more expensive. In fact, not only is baryonic matter composed of collisional particles that require solving more complex equations, but they are also subject to gas cooling, star formation, and AGN and supernovae feedback, which further complicates the problem (Borgani & Kravtsov 2011). Consequently, although numerical simulations provide accurate results and are indispensable for describing the nonlinear evolution of cosmological systems, they are not the ideal tool for

the study of systematics. Indeed, the use of large sets of simulations is a fundamental requirement for the accurate estimation of covariance matrices, which requires large statistics rather than high accuracy. The dimension of such sets depends on the size of the data vector (i.e., the number of bins) and on the accuracy to be achieved, and typically the required number of catalogs is around 10^3 or even more (Dodelson & Schneider 2013; Taylor et al. 2013). For this purpose, approximate methods represent a valid alternative to N-body simulations: although less accurate than full N-body simulations in reproducing the observables, these methods are able to accurately estimate covariances requiring fewer resources and far less computational time.

2.2 Approximate methods for catalog generation

Approximate methods (Monaco 2016; Sahni & Coles 1995) describe the evolution of dark matter by solving the Vlasov equations via perturbative theories. The advantage in using these methods lies in the fact that N-body simulations require a large number of time-steps to calculate particle displacements, as these depend on time-varying forces. Approximate methods, instead, allow the displacement to be calculated only once, basing on the assumption that the final position of particles depends only on the configuration of the potential under the initial conditions.

Methods for catalog generation can be classified into two categories: *Lagrangian* methods and *biased-based* methods. The former involves the application of a perturbative field to a grid of particles; thus, the particles that constitute the halos are determined, and their displacement from the initial (Lagrangian) to the final (Eulerian) position is computed. These methods are computationally advantageous compared with N-body simulations, but they require a parameter calibration in order to correctly reproduce the quantities predicted by N-bodies. To this class belong algorithms such as PINOCCHIO (Monaco et al. 2002a), PTHalos (Scoccimarro & Sheth 2002), and COLA (Tassev et al. 2013). The second class consists of generating a quasi-linear density field via perturbative theory, and populating it with halos by assuming mass function and bias models. Although they are preferable in terms of computational cost over Lagrangian methods, these methods have lower predictive power and require several calibrations through simulations. Algorithms belonging to this class include PATCHY (Kitaura et al. 2014) and EZmocks (Chuang et al. 2015). In the following, only Lagrangian methods will be discussed.

2.2.1 Lagrangian perturbation theory

The linear evolution of the density field can be described by perturbative theory, by means of two different approaches: the *Eulerian* and the *Lagrangian* approach. The first method, known as Eulerian Perturbation Theory (EPT, Bernardeau et al. 2002), describes the time evolution of the density field $\delta(\mathbf{x},t)$ at a certain position $\mathbf{x}$, assuming $\delta \ll 1$ and that the particle displacement from the initial position is negligible with respect to the scale R, corresponding to the size of the smallest perturbation for which we want to follow the linear evolution. In other words, $vt \ll R$, where v is the velocity of the mass element at time t. Although appropriate for describing the evolution of perturbations in the linear regime, EPT becomes inaccurate as particle displacement increases, and stops to be valid when the limit $\delta \sim 1$ is reached, so

that it does not allow the evolution of perturbations to be described outside the strictly linear regime. The second approach, called Lagrangian Perturbation Theory (LPT, Moutarde et al. 1991; Buchert 1992; Bouchet et al. 1995), follows the displacement of the fluid element with initial position $\mathbf{q}$, which moves along the trajectory $\mathbf{x}(\mathbf{q},t) = \mathbf{q} + \mathbf{S}(\mathbf{q},t)$, where the displacement $\mathbf{S}$ represents a map between the Lagrangian coordinate $\mathbf{q}$ and Eulerian coordinate $\mathbf{x}$. This description is analogous to EPT, except that the condition for the perturbative expansion is set by the displacement parameter, i.e. $\mathbf{S} \ll 1$. The advantage of this second approach is that it is also valid in the quasi-linear regime and thus allows us to describe the formation and structure of the Universe.

The first-order LPT theory is called Zel'dovich approximation (Zeldovich 1970). It consists in defining the linear displacement of the fluid element, $\mathbf{S}(\mathbf{q},t) = b(t)\,\mathbf{p}(\mathbf{q})$, thus writing the position of the element at time t as

$$\mathbf{r}(\mathbf{q},t) = a(t)\,\mathbf{x}(\mathbf{q},t) = a(t)\,[\mathbf{q} + b(t)\,\mathbf{p}(\mathbf{q})]\,, \tag{2.3}$$

where $\mathbf{r}$ and $\mathbf{x}$ are, respectively, the proper and comoving coordinates. Imposing the mass conservation condition $\rho_0(\mathbf{q})\,\mathrm{d}^3\mathbf{q} = \rho(\mathbf{r},t)\,\mathrm{d}^3\mathbf{r}$ and setting $\mathbf{S} \ll 1$, we find the first-order Lagrangian density contrast

$$\delta(\mathbf{q},t) \simeq -b(t)\,\boldsymbol{\nabla}_q\,\mathbf{p}(\mathbf{q})\,. \tag{2.4}$$

Given that the description must be equivalent to the EPT, which defines $\delta(\mathbf{q},t) = D(t)\,\delta_0(\mathbf{q})$ with $D(t)$ linear growth rate, and imposing the initial density contrast to follow the Poisson equation for the gravitational potential $\delta_0(\mathbf{q}) = \nabla_q^2\,\Phi_0(\mathbf{q})$, we find the trajectory of the fluid element,

$$\mathbf{x}(\mathbf{q},t) = \mathbf{q} - D(t)\nabla_q\,\Phi_0(\mathbf{q})\,, \tag{2.5}$$

that is, the fluid elements has a laminar linear motion with respect to the time variable $D(t)$ with speed $-\boldsymbol{\nabla}_q\,\Phi_0(\mathbf{q})$. The structure formation occurs when the trajectories of several particles cross each other (*shell-crossing* regime): when two elements $\mathbf{q}_1$ and $\mathbf{q}_2$ are in the same Eulerian position $\mathbf{x}$, the displacement $\mathbf{S}$ no longer constitutes a biunivocal map between the coordinates $\mathbf{q}$ and $\mathbf{x}$ and the approximation ceases to be valid. From a physical point of view, in such a regime the two elements should interact gravitationally with each other, whereas the Zel'dovich approximation predicts that their motion is only determined by the initial conditions and is therefore unable to describe the interaction between the particles. To describe the shell-crossing phase, we consider the deformation tensor $\partial S_i/\partial q_j$ that, being real and symmetric, can be written in a diagonal coordinate system. Then let the three eigenvalues α,β,γ be such that $\alpha \le \beta \le \gamma$; the density contrast becomes

$$1 + \delta(\mathbf{q},t) = \left|\frac{\partial S_i}{\partial q_j}\right|^{-1} = \frac{1}{[1 - D(t)\alpha(\mathbf{q})][1 - D(t)\beta(\mathbf{q})][1 - D(t)\gamma(\mathbf{q})]}\,. \tag{2.6}$$

Since $D(t)$ grows with time, at some point it will be $[1 - D(t)\alpha(\mathbf{q})] = 0$, meaning $\delta \to \infty$. The singularity can be of three kinds:

- if $\alpha < \beta < \gamma$ the collapse occurs along one direction, producing a sheet-like structure called "pancake";
- if $\alpha = \beta < \gamma$ the collapse is linear and consists in a 1D singularity named "filament";

- if $\alpha = \beta = \gamma$ the collape occurs along the three directions and forms a punctual singolarity called “node”.

Pancakes, filaments and nodes represent the large-scale structure matter distribution.

To describe the evolution of structures beyond this point, it is necessary to extend the approximation to higher levels, e.g. second- or third-order LPT (Bouchet et al. 1995).

2.2.2 PINOCCHIO

PINOCCHIO (PINpointing Orbit-Crossing Collapsed HIerarchical Objects) (Monaco et al. 2002a; Munari et al. 2017) is an algorithm that generates dark matter halo catalogs through LPT and ellipsoidal collapse (e.g. Bond & Myers 1996; Eisenstein & Loeb 1995), up to third order. The code simulates cubic boxes with periodic boundary conditions, starting from a regular grid on which an initial density field is generated in the same way as in N-body simulations. The procedure consists of two steps: first the collapse times of the mass elements are calculated, and then the collapsed elements are assigned to individual halos. Initially, a linear density field is generated on a cubic grid, at the vertices of which the mass elements (or ”particles”) are placed. The field is then filtered on different scales by convolution with a Gaussian window function; about 20 logarithmically equispaced filtering scales are used. Then, for each particle at position $\mathbf{q}$ and for each filtering scale, the collapse time is computed by ellipsoidal collapse, solved analytically by third-order truncated LPT (3LPT, Monaco 1997): the collapse of the mass element, i.e. the *orbit-crossing*, is defined as the instant at which one of the axes of the ellipsoid describing the mass element becomes zero. For each particle, the minimum collapse time and the corresponding filtering scale are then determined. This first step takes most of the computational time, producing a collapsed medium that must be ”fragmented” to form structures.

This second step simulates the process of forming structures by accretion of matter and merging of halos. It is carried out in a way similar to the FoF method used in N-body simulations: first, the centers of the halos are identified, considering the particles with the shortest collapse times. All the other particles can belong to a halo only if it already contains one of their Lagrangian neighbors, i.e. one of the first neighbors of the particle in the initial configuration (consisting of a cubic grid, where each node has six first neighbors). The condition for a mass element to belong to the selected halo is that the distance from its center, calculated by LPT at the instant of collapse, is $d < d_{\mathrm{th},a} = f_a R_{\mathrm{M}}$ where $f_a \sim 1$ is a parameter analogous to the linking-length used to identify FoF halos and $R_{\mathrm{M}} \simeq M^{1/3}$ is the radius of a halo with mass M. If a particle satisfies the condition for more than one halo, it is assigned to the one with the lowest value of d/R_{M}, while all particles not contained in any halo constitute filaments. The resulting halos can then grow by accretion or merging processes; this occurs if the particle-halo or halo-halo distance is such that $d < d_{\mathrm{th},m}$, where the threshold distance $d_{\mathrm{th},m} \sim R_{\mathrm{M}}$ is defined similarly to $d_{\mathrm{th},a}$, but with different parameters. Such distance must be calibrated so that the mass function reproduces that of N-body simulations. LPT is applied both to move particles and halos during the formation process, and to compute their final positions in order to write the catalog. In the first version of the code (Monaco et al. 2002b,a), both displacements were computed using ZA, later replaced with 2LPT and 3LPT in later versions (Monaco et al. 2013; Munari et al. 2017).

The code is also able to build past-light cones (PLC), by replicating the periodic boxes through an “on-the-fly” process that selects only the halos causally connected with an ob-

server at the present time, once the position of the observer and the survey sky area are fixed. The position of the observer is randomly chosen within the box, while the semi-aperture of the cone is defined by an angle θ. The observed volume is given by the volume of a cone with radius θ, calculated between the redshifts $z_{\rm start}$ and $z_{\rm stop}$. The box is then periodically replicated so as to fill the entire volume. The properties of a halo, such as mass and velocity, are recorded at the instant when that object passes through the light cone, which is found by solving the equation

$$|\mathbf{x}_{\rm halo}(z) - \mathbf{x}_{\rm ob}| = r(z)\,,$$

where $\mathbf{x}_{\rm halo}(z)$ is the trajectory of the halo, calculated by LPT, $\mathbf{x}_{\rm ob}$ is the center of the light cone (i.e. the observer position), and $r(z)$ is the proper distance at redshift z. This method permits the generation of PLC in a continuous way, i.e. avoiding "piling-up" snapshots at a discrete set of redshifts. Figure 2.1 shows an example of light cone (in section) with aperture $\theta = 60°$ between redshift $z_{\rm start} = 1.5$ and $z_{\rm stop} = 0$, containing the redshift-space distribution of halos with masses $M > 6.9 \times 10^{12}\, h^{-1}\, M_\odot$.

Finally, PINOCCHIO also allows the reconstruction of merger histories, describing all the merger processes that lead to the formation of a halo over time and are recorded directly during the fragmentation and construction of the halos.

The PINOCCHIO algorithm is significantly faster than N-body simulations (by a factor of $\sim 10^3$, Monaco 2016), thanks to the application of perturbation theory and the fact that the description of the orbits of the particles inside the halos is ignored. In this way, the information about the internal structure of the halos is lost, but this does not affect the evolution of structures on large scales. Catalogs simulated with PINOCCHIO reproduce within $5-10$ percent accuracy the 2-point statistics on large scales ($k < 0.4\, h\,{\rm Mpc}^{-1}$), the linear bias and the mass function of halos derived from full N-body simulations once code parameters are suitably tuned (Munari et al. 2017). The comparison between the PINOCCHIO mass function, computed at different orders of LPT, and that obtained by N-body simulation is shown in the left panel of Fig. 2.2. The analytical prediction by Crocce et al. (2010) is also shown. The lower panel shows the deviations between the simulated mass functions and the analytical model, where the black horizontal lines mark the region at ± 5% from the analytical prediction. At small masses and between $z = 0$ and $z = 1$ all the three orders of LPT present and agreement within the percent level. The agreement slightly decreases with increasing mass, especially at high redshift.

Right panel of Fig. 2.2 shows the comparison of the 2-point correlation function of the halos simulated by PINOCCHIO and N-body simulations, at redshift $z = 1$. The monopole (red), quadrupole (blue) and exadecapole (green) terms from PINOCCHIO are obtained by averaging over 300 boxes, while black lines represent the average measurements obtained from 100 N-body Minerva simulations. It can be seen that in all the cases PINOCCHIO reproduces the correlation of halos with good accuracy, especially the monopole term, and that the differences are mainly due to sample variance.

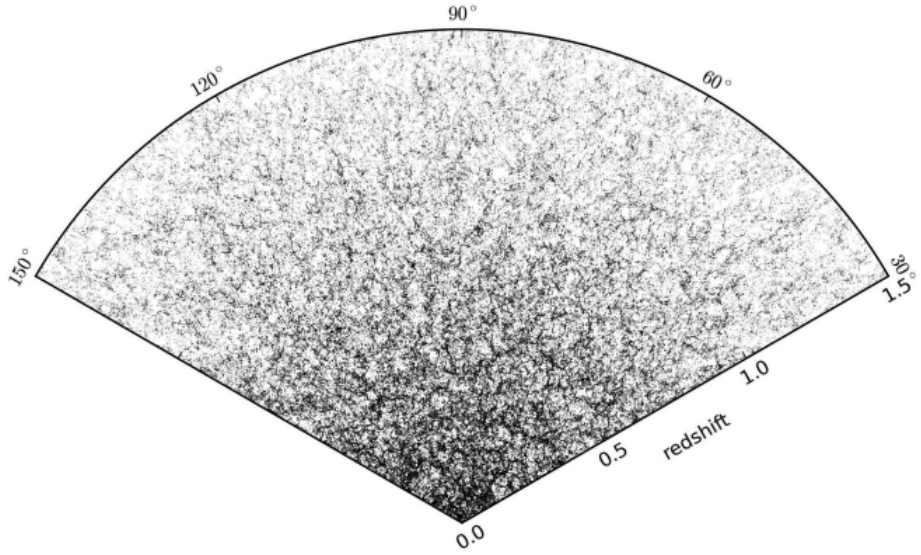

Figure 2.1: PINOCCHIO light cone. Section of thickness 0.5° of a light cone of semi-aperture $\theta = 60°$ and redshift range $z \in [0, 1.5]$, representing the redshift-space distribution of halos with mass $M > 6.9 \times 10^{12}\, h^{-1}\, M_\odot$. Image from Munari et al. (2017).

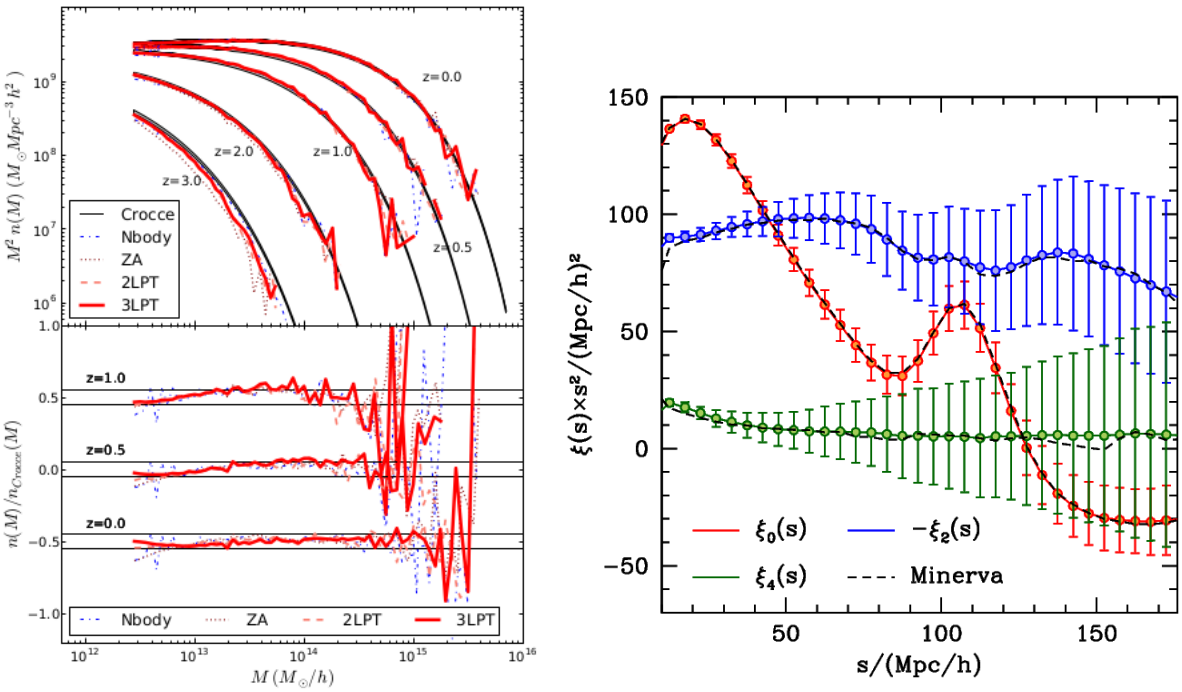

Figure 2.2: *Left panel:* Halo mass function $M^2\, n(M)$ from N-body simulation (blue) and PINOCCHIO (red) at different LPT orders: dotted lines for ZA, dashed lines for 2LPT, and solid lines for 3LPT. Black lines represent the analytical fit of Crocce et al. (2010). The lower panel shows the residuals with respect to the analytical fit, and the the ±5% region around the fit. Figure from Munari et al. (2017). *Right panel:* Monopole (red), quadrupole (blue), and exadecapole (green) of the 2-point correlation function of PINOCCHIO, averaged over 300 boxes of size $1.5\, h^{-1}$ Gpc at $z = 1$. error bars are given by the standard deviation. Black lines represent the average results from 100 Minerva N-body simulations. Additional information in Lippich et al. (2019)

2.3 Simulated data and mass calibration

In this work, the data set consists of 1000 past-light cones produced by the PINOCCHIO alghorithm [1], each covering an area of 10 313 deg^2 and redshift range $z = 0 - 2.5$ [2]. The light cones contain halos with virial masses above $3.61 \times 10^{13}\, M_\odot$, sampled with more than 50 particles. The cosmology assumed in the simulations is the flat ΛCDM one with parameters fixed according to Planck Collaboration XVI. (2014) (Table 5, "Planck+WP+highL+BAO" case): $\Omega_\mathrm{m} = 0.30711$ for the total matter density parameter, $\Omega_\mathrm{b} = 0.048254$ for the corresponding contribution from baryons, $h = 0.6777$ for the Hubble parameter expressed in units of 100 km s^{-1} Mpc^{-1}, $n_\mathrm{s} = 0.96$ for the primordial spectral index, $A_\mathrm{s} = 2.21 \times 10^{-9}$ for the power spectrum normalization, and $\sigma_8 = 0.8288$ for the RMS density fluctuation at $z = 0$ within a top-hat sphere of $8\, h^{-1}$ Mpc radius.

We also use 1000 periodic cubical boxes of side 3870 h^{-1} Mpc for 16 constant redshifts fixed between $z = 0$ and $z = 2$, from which the light cones described above are extracted. Although such boxes are not suitable for realistic analyses, they are useful for carrying out tests where the description of complex geometry or redshift evolution has to be avoided.

To describe the mass distribution of the simulated halos we assume the halo mass function model by Despali et al. (2016) (hereafter D16) [3],

$$\nu f(\nu) = 2A \left(1 + \frac{1}{\nu'^p}\right) \left(\frac{\nu'}{2\pi}\right)^{1/2} \mathrm{e}^{-\nu'/2}, \tag{2.7}$$

with $\nu' = a\nu^2$. The values of the parameters are: $A = 0.3298$, $a = 0.7663$, $p = 0.2579$ ("*All z - Planck cosmology*" case in the reference paper). Comparisons with numerical simulations show departures from the universality described by this model of the order of 5 – 8%, provided that halo masses are computed within the virial overdensity, as predicted by the spherical collapse model.

To avoid complications linked to the modeling of the halo mass function, we rescale masses to the D16 prediction. This step is required both because the PINOCCHIO accuracy in reproducing the halo mass function is "only" 5 percent, and because its calibration has been performed by considering a universal FoF halo mass function, while D16 define halos based on spherical overdensity within the virial radius, demonstrating that the resulting mass function is much nearer to a universal evolution than that of FoF halos.

Masses have been rescaled by matching the mean halo mass function of the PINOCCHIO catalogs to the analytical model of D16. More in detail, we predicted the value for each single mass M_i by using the cumulative mass function, i.e., Eq. (1.24) where the integral above mass bins is replaced by an integration above a mass threshold M_i:

$$N(> M_i) = \Omega_\mathrm{sky} \int_{\Delta z} \mathrm{d}z \, \frac{\mathrm{d}V}{\mathrm{d}z\, \mathrm{d}\Omega} \int_{M_i}^{\infty} \mathrm{d}M \, \frac{\mathrm{d}n}{\mathrm{d}M}(M, z) = i, \tag{2.8}$$

Here $i = 1, 2, 3, ...$ and we assign such values to the simulated halos, previously sorted by preserving the mass order ranking. During this process, all the thousand catalogs are stacked

[1] http://adlibitum.oats.inaf.it/monaco/mocks.html; the light cones analyzed are the ones labeled "NewClusterMocks".

[2] Note that our light cones are covering slightly smaller areas than the expected *Euclid* catalogs (~ 10000 vs. ~ 15000 deg^2); also, the survey will cover two separate patches of the sky. For the purpose of this work, we expect that these differences impact the results in a negligible way.

[3] In D16 the peak height is defined as $\nu = \delta_\mathrm{c}^2 / \sigma^2(R, z)$; in such case the factor "2" in Eq. (2.7) disappears.

together, which is equivalent to use a 1000 times larger volume: the mean distribution obtained in this way contains fluctuations due to shot-noise and sample variance that are reduced by a factor $\sqrt{1000}$ and can thus be properly compared with the theoretical one, preserving the fluctuations in each rescaled catalog. Otherwise, if the mass function from each single realization was directly compared with the model, the shot-noise and sample variance effects would have been washed away. The masses in the original periodic boxes have been rescaled in a similar way.

In our analyses, we considered objects in the mass range $M_{\rm vir} = 10^{14} - 10^{16}\,M_\odot$ and redshift range $z = 0-2$; in this interval, each rescaled light cone contains $\sim 3\times10^5$ halos. We note that this simple constant mass-cut at $10^{14}\,M_\odot$ provides a reasonable approximation to a more refined computation of the mass selection function expected for the *Euclid* photometric survey of galaxy clusters (see Fig. 2 of Sartoris et al. (2016); see also Adam et al. (2019)).

In the left panel of Fig. 2.3 we show the comparison between the calibrated and non-calibrated mass function of the light cones, averaged over the 1000 catalogs, in the redshift bin $z = 0.1-0.2$. For a better comparison, in the bottom panel we show the percent residuals between the two mass functions from simulations and the one of D16: while the original distribution differs from the analytical prediction, with differences of up to about 50 percent, the calibrated mass function matches the model over the entire mass range, except for some small fluctuations in the high-mass end where the number of objects per bin is low.

We describe the halo bias with the analytical model by Tinker et al. (2010, hereafter T10)

$$b(\nu) = 1 + A\frac{\nu^a}{\nu^a + \delta_c^a} + B\,\nu^b + C\,\nu^c \tag{2.9}$$

with parameters presented in Table 2 of the reference paper.

We tested the model of T10 to verify if the analytical prediction is in agreement with the bias from the rescaled catalogs. To avoid complications linked to the redshift evolution or the geometry of the light cones, we performed this test on the cubical boxes. The bias from simulation is measured by applying the definition

$$\hat{b}(z|M) = \left[\frac{\hat{\xi}_{\rm h}(r,z|M)}{\xi_{\rm m}(r,z)}\right]^{1/2}, \tag{2.10}$$

where $\xi_{\rm m}$ is the linear matter 2PCF calculated with the `CAMB` code (Lewis et al. 2000), and $\hat{\xi}_{\rm h}$ is the measured 2PCF for halos with masses above a threshold M, averaged over the 1000 simulations. We use 10 mass thresholds in the range $M = 10^{14} - 10^{15}\,M_\odot$. We compute the correlation functions in the range of separations $r = 30 - 70\,h^{-1}$ Mpc, where the approximation of scale-independent bias is valid (Manera et al. 2010). Since the bias from simulations refers to halos with mass above M, the comparison with the T10 model must be made with an effective bias prediction, i.e., the linear halo bias integrated above the mass threshold M

$$\overline{b}(z\,|\,M) = \frac{1}{\overline{n}(z\,|\,M)}\int_M^\infty {\rm d}M'\,\frac{{\rm d}n}{{\rm d}M}(M',z)\,b(M',z), \tag{2.11}$$

where ${\rm d}n/{\rm d}M$ is the halo mass function and $\overline{n}(z\,|\,M)$ is the mean number density of objects above a mass threshold

$$\overline{n}(z\,|\,M) = \int_M^\infty {\rm d}M'\,\frac{{\rm d}n}{{\rm d}M}(M',z). \tag{2.12}$$

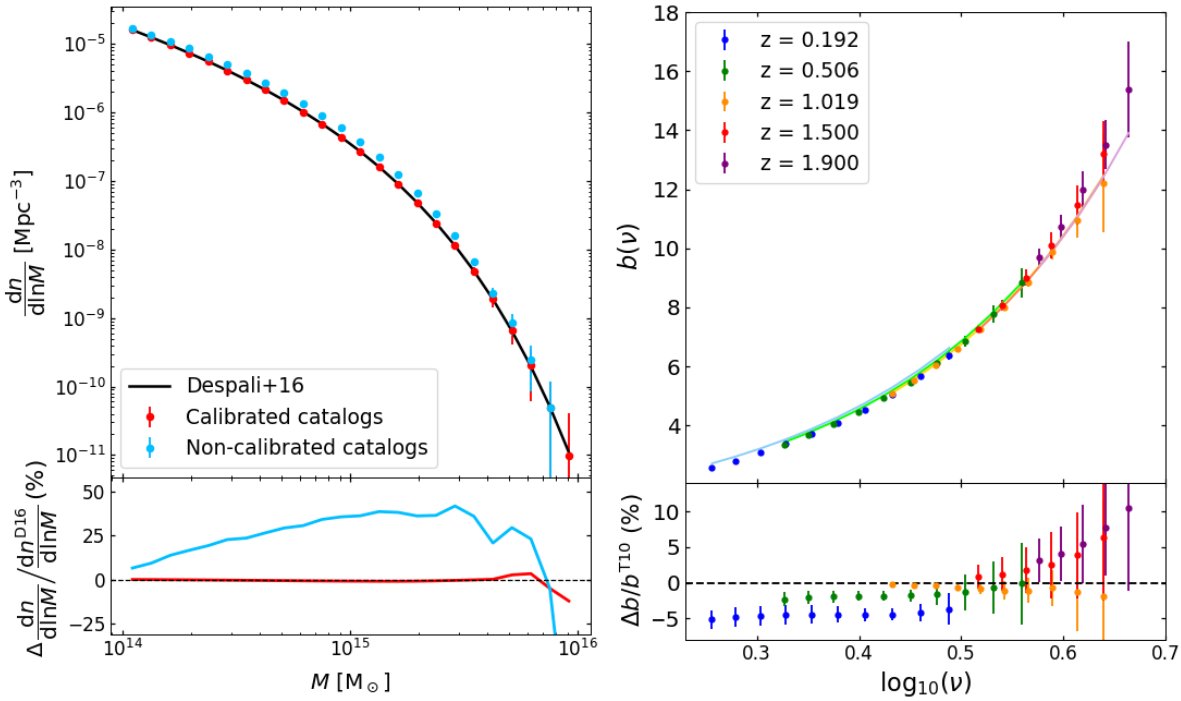

Figure 2.3: *Left panel:* Comparison between the halo mass function from the calibrated (red) and the non-calibrated (blue) light cones, averaged over the 1000 catalogs, in the redshift bin $z = 0.1 - 0.2$. Error bars represent the standard error on the mean. The black line is the D16 mass function. In the bottom panel, percent residuals between the mass function from simulations and the one of D16. *Right panel:* Halo bias from simulations at different redshifts (colored dots), compared to the analytical model of T10 (lighter solid lines). In the bottom panel, percent residuals between the bias from simulations and the one of T10.

The comparison is shown in the right panel of Fig. (2.3), representing the effective bias from boxes (dots) at various redshifts and the corresponding analytical model (lines), as a function of the peak height. We notice that the T10 model slightly overestimates/underestimates the simulated data at low/high masses and redshifts: the difference is below the 5 percent level over the whole ν range, except for high-ν halos, where the discrepancy is of about 10 per cent. At low redshift, this difference is not compatible with the error on the measurements; however, such errors underestimate the real uncertainty, as they do not take into account the correlation between radial bins. We conclude that, to first approximation, the T10 model can provide a sufficiently accurate description for the halo bias of our simulations.

The calibrated light cones are used in this work both to compute the numerical covariance matrices used to validate the analytical models, and to perform the likelihood analysis, to forecast the impact of covariances on the cosmological posteriors. The calibrated boxes, on the other hand, are used to perform tests where the complex effects given by redshift evolution and light cone geometry are to be avoided.

Chapter 3

Methodology

In this chapter we describe the methodology for the covariance matrix validation and the likelihood forecasts that will be applied throughout this work, to obtain the results described in Chapters 4, 5, and 6. First, in Sect. 3.1, we introduce the Bayesian inference method used for constraining cosmological parameters, and we describe the likelihood functions that will be adopted in this work. In Sect. 3.2, we describe the estimator and properties of the numerical matrix, that will be used as a reference for the validation of analytical models. Finally, in Sect. 3.3, we propose a method for fitting additional parameters to the analytical covariance model, and present the tests performed to show the validity of such a method. The results are presented in Fumagalli et al. (2022).

3.1 Bayesian inference for parameter estimation

The procedure generally used to derive constraints on cosmological parameters is called *Bayesian inference* and takes its name from Bayes theorem, according to which the conditional probability of observing data $\mathbf{d}$, once a theoretical model $\mathbf{m}$ characterized by a set of parameters $\boldsymbol{\theta}$ is assumed, is given by

$$p(\boldsymbol{\theta}|\mathbf{d}) = \frac{\mathcal{L}(\mathbf{d}|\mathbf{m}(\boldsymbol{\theta})) \cdot p(\boldsymbol{\theta})}{p(\mathbf{d})}, \tag{3.1}$$

where:

- $p(\boldsymbol{\theta}|\mathbf{d})$ is the *posterior* probability of finding a set of parameters $\boldsymbol{\theta}$, having observed the data $\mathbf{d}$;
- $p(\boldsymbol{\theta})$ is the *prior* probability of the set of parameters $\boldsymbol{\theta}$;
- $\mathcal{L}(\mathbf{d}|\mathbf{m}(\boldsymbol{\theta}))$ is the *likelihood* function, i.e., the probability of observing the data $\mathbf{d}$, assuming a valid model with parameters $\boldsymbol{\theta}$;
- $p(\mathbf{d})$ is the probability distribution of the observed data (*evidence*), which constitutes a normalization factor.

The estimation of the cosmological posteriors consists of comparing an observed quantity with the respective theoretical model, calculated by allowing some parameters to vary. The

latter will be determined by maximizing the logarithm of the likelihood function. The likelihood function can take various forms, depending on the distribution of the data. The most common shapes are the Poissonian and Gaussian likelihood.

In addition to the cosmological parameters that are to be determined, the likelihood function can contain some nuisance parameters, which are related to measurement uncertainties, e.g. scaling relation parameters. Since the nuisance parameters are not of direct interest in the estimation of cosmological posteriors, a "marginalisation" is performed, i.e., the likelihood is maximized by summing over all possible values of these parameters:

$$p(\boldsymbol{\theta}|\mathbf{d}) = \int \mathrm{d}\boldsymbol{\alpha}\, p(\boldsymbol{\theta}, \boldsymbol{\alpha}|\mathbf{d}), \tag{3.2}$$

where $\boldsymbol{\theta}$ and $\boldsymbol{\alpha}$ are, respectively, the cosmological and nuisance parameters.

Priors can be defined as uninformative priors, i.e., flat distributions spanning wide intervals, or they can be based on the results obtained from other observables; this allows us to combine different information in order to obtain more accurate constraints.

In principle, the likelihood maximization process is performed by defining a grid in the parameter space and estimating the function at each point. The procedure thus defined is slow and inefficient for a large number of parameters, since the number of points grows exponentially as the dimension of the parameter space increases. In order to make the posterior estimation more efficient, the parameter space is sampled by considering only those points where the likelihood function assumes high values. One of the most widely used methods is called *Monte Carlo Markov Chain* (MCMC, Heavens 2009): points are selected by a random walk through the parameter space, with probability distribution proportional to that of the posteriors. In this way, the number of points selected scales linearly with the number of parameters and the procedure is considerably faster.

In this work, we explore the posterior distribution with a MCMC approach; we use the *python* wrapper for the nested sampling `PyMultiNest` (Feroz et al. 2009; Buchner et al. 2014), with the exception of Sect. 6.4.2 where we use `zeus` (Karamanis et al. 2021), and Sect. 6.5 where we use `PolyChord` (Handley et al. 2015). Both `MultiNest` and `PolyChord` are based on the nested sampling algorithm, which is a method for exploring the parameter space and estimating the marginal likelihood of the model. The algorithm starts with an initial set of live points, which are sampled from the prior distribution of the parameters. Then, for each iteration of the algorithm, the worst-performing live point is removed from the set and replaced with a new point that is sampled from the prior. The new point is accepted with a probability that is calculated based on the likelihood ratio and the prior ratio, and this acceptance probability is used to ensure that the samples are distributed according to the posterior distribution of the parameters. This process continues until a stopping criterion is met. The algorithm can be used both to estimate the posterior distribution of the model parameters, by considering the set of points that have been generated during the sampling process, and to compute the evidence, by using the distribution of likelihoods of the final set of points to estimate the integral of the likelihood over the prior. The nested sampling algorithm is designed to be more efficient than traditional MCMC methods for exploring high-dimensional, complex, or multi-modal parameter spaces. Instead, `zeus` is a *python* implementation of the Ensemble Slice Sampling, a method for Bayesian inference that combines elements of both slice sampling and ensemble sampling. Slice sampling defines a "heigh" parameter and generates a random sample from the target distribution, called the "current state". Then, it

generates a slice by sampling uniformly from the region above the current state's density up to the chosen height. The method generates new samples by proposing new states within the slice, and accepting or rejecting them based on the target distribution. Ensemble sampling, on the other hand, uses a group of "walkers" that move in the parameter space simultaneously. Each walker samples the target distribution independently, and the final set of samples is obtained by combining the samples from all the walkers. Ensemble slice sampling combines both methods by introducing a set of walkers that move through the parameter space and generate slices independently.

Regarding the choice of likelihood function, in this work we test different likelihood functions for the number counts case: the likelihood commonly adopted in the literature for number counts analyses is the Poissonian one, which takes into account only the shot-noise term. To add the sample variance contribution, the simplest way is to use a Gaussian likelihood. More specifically, we considered the following likelihood functions:

- Poissonian:

$$\mathcal{L}(\mathbf{d}\,|\,\mathbf{m}(\boldsymbol{\theta})) = \prod_{a=1}^{N_z}\prod_{i=1}^{N_M} \frac{m_{ia}^{d_{ia}}\,\mathrm{e}^{-m_{ia}}}{d_{ia}!}\,, \tag{3.3}$$

  where $\mathbf{d} = \{d_{ia}\}$ and $\mathbf{m}(\boldsymbol{\theta})) = \{m_{ia}\}$ are, respectively, the observed and expected number counts in the i-th mass bin and a-th redshift bin. Here the bins are not correlated, since shot-noise does not produce cross-correlation, and the likelihoods are simply multiplied;

- Gaussian with shot-noise only:

$$\mathcal{L}(\mathbf{d}\,|\,\mathbf{m}(\boldsymbol{\theta}), \sigma) = \prod_{a=1}^{N_z}\prod_{i=1}^{N_M} \frac{\exp\left\{-\frac{1}{2}(d_{ia}-m_{ia})^2/\sigma_{ia}^2\right\}}{\sqrt{2\pi\sigma_{ia}^2}}\,, \tag{3.4}$$

  where $\sigma_{ia}^2 = m_{ia}$ is the shot-noise variance. This function represents the limit of the Poissonian case for large occupancy numbers;

- Gaussian with full covariance:

$$\mathcal{L}(\mathbf{d}\,|\,\mathbf{m}(\boldsymbol{\theta}), C) = \frac{\exp\left\{-\frac{1}{2}[\mathbf{d}-\mathbf{m}(\boldsymbol{\theta})]^T C^{-1}[\mathbf{d}-\mathbf{m}(\boldsymbol{\theta})]\right\}}{\sqrt{(2\pi)^N |C|}}\,, \tag{3.5}$$

  where C is the covariance matrix, which may also depend on cosmological parameters. In this case, the sample covariance introduces correlations between different bins, so the individual likelihoods are no longer simply multiplied by each other.

In Sect. 4.2.2 the three likelihoods will be compared, to determine the impact of sample variance on the cosmological constraints from the cluster number counts analysis.

On the contrary, for cluster clustering the sample variance is already known to produce non-negligible diagonal terms, and therefore a Gaussian likelihood with full covariance is necessary to properly include the uncertainties affecting the observable.

Another consideration regarding the likelihood analysis is that each simulation represents a random realization of the Universe. As such, the posteriors obtained for each light cone will

be randomly shifted around the values of the input cosmology of the simulations. This effect, known as cosmic variance, makes it difficult to detect any systematics in the analysis, which can also appear as small, but sizeable shifts in the cosmological posteriors with respect to the input parameter values. To remove the cosmic variance effect, we perform the MCMC analysis by maximizing the log-likelihood function averaged over all the N_S simulated catalogs

$$\ln \mathcal{L}^{\rm tot} = \frac{1}{N_S} \sum_{a=1}^{N_S} \ln \mathcal{L}^{(a)} \,. \tag{3.6}$$

If no systematics are present, posteriors obtained in this way will be perfectly centered on the input parameters.

We quantify the accuracy of our covariance (error) estimates in terms of the effect on the figure of merit (FoM, Albrecht et al. 2006) for two parameters θ_1 and θ_2, defined as

$$\mathrm{FoM}(\theta_1, \theta_2) = |\mathrm{C}(\theta_1, \theta_2)|^{-1/2} \,, \tag{3.7}$$

where $C(\theta_1, \theta_2)$ is the parameter covariance computed from the sampled posteriors. The FoM is proportional to the inverse of the area enclosed by the 68 percent confidence level ellipse; therefore, in general, a higher FoM indicates more accurate evaluation of parameters. For the covariance comparison, however, a larger FoM could indicate an underestimation of the posteriors amplitude, resulting from a wrong estimation of the uncertainties on the statistical quantities entering the likelihood. We should therefore point out that we are not interested in the absolute value of the FoM, but rather in the difference between the various cases.

We consider the cosmological parameters on which cluster number counts and cluster clustering are more sensitive, i.e., $\Omega_{\rm m}$ and σ_8, or equivalently A_s. We assume flat uninformative priors $\Omega_{\rm m} \in [0.2, 0.4]$ and $\log_{10} A_s \in [-9.0, -8.0]$, and then we derive the value of σ_8 through the relation $P_{\rm m}(k) = A_s\, k^{n_s}\, T^2(k)$, where $T(k)$ is the transfer function, and the definition of variance $\sigma^2(R)$ (Eq. 1.3). We are interested in evaluating the variations in the FoM in the $\Omega_{\rm m} - \sigma_8$ plane and the possible biases in the posteriors with respect to the input cosmology. The former case means that not all the relevant sources of error are taken into account, while the latter indicates the presence of systematics due to an incorrect analysis.

3.2 Covariance matrix

The validation of the analytical covariance model is performed by comparison with a reference covariance, computed numerically from a large set of simulations, as motivated in Chapter 2. To compute the numerical covariance matrix, we use the estimator

$$\hat{C}_{ij} = \frac{1}{N_S - 1} \sum_{s=1}^{N_S} \left(\hat{O}_i^{(s)} - \langle \hat{O} \rangle_i \right) \left(\hat{O}_j^{(s)} - \langle \hat{O} \rangle_j \right) , \tag{3.8}$$

where N_S is the number of simulations, $\hat{O}_i^{(s)}$ is the observable (number counts or 2PCF in our case) in the i-th bin measured from the s-th mock, and $\langle \hat{O} \rangle_i$ is the corresponding average value. Note that the number of indices can vary according to the binning scheme of the observable. The uncertainty on the numerical covariance is given by (Taylor et al. 2013)

$$\sigma^2(\hat{C}_{ij}) = \frac{1}{N_S - 1} \left(\hat{C}_{ij}^2 + \hat{C}_{ii}\, \hat{C}_{jj} \right) . \tag{3.9}$$

We perform a first validation of the model by directly comparing the analytical covariance to the numerical matrix, element by element. We assume a reasonable level of agreement if the main terms of the matrices (diagonal and firsts off-diagonal terms) have a relative difference of less than 10 percent. Once this level of agreement has been achieved, we compare the matrices by means of likelihood analysis, to assess the impact of these differences on the cosmological posteriors at the level of accuracy expected for *Euclid*.

For this test, we consider the results obtained from the numerical matrix as reference, to be compared with the posteriors from the analytical matrix. Due to the noise present in the former, arising from the limited number of mocks, we need to take into account a couple of considerations. First, the inverse of the numerical matrix entering the likelihood (see Sect. 3.1) requires to be corrected as (Anderson 2003; Hartlap et al. 2007)

$$\hat{C}^{-1}_{\rm unbiased} = \frac{N_{\rm S} - N_{\rm D} - 2}{N_{\rm S} - 1}\,\hat{C}^{-1}\,, \tag{3.10}$$

where $N_{\rm D}$ is the dimension of the data vector. Second, while this correction removes the bias in the numerical inverse covariance, sampling noise propagates to the parameter covariance inducing an increase of error bars by a factor (Taylor et al. 2013; Dodelson & Schneider 2013)

$$f = 1 + \frac{(N_{\rm S} - N_{\rm D} - 2)}{(N_{\rm S} - N_{\rm D} - 1)(N_{\rm S} - N_{\rm D} - 4)}(N_{\rm D} - N_{\rm P})\,, \tag{3.11}$$

where $N_{\rm P}$ is the number of (cosmological + nuisance) parameters. This correction results from a frequentist style approach concerned with results after repeated trials; for corrections suitable for a Bayesian analysis the proper approach is described by the work of Sellentin & Heavens (2016); Percival et al. (2022). However, this can be avoided by making the numerical results as accurate as possible ($f \sim 1$). To this purpose, the difference between the number of simulations $N_{\rm S}$ and the number of bins $N_{\rm D}$ must be maximized. This can be done, for example, by using the minimum number of bins that properly allows all the information to be extracted. Also, this factor can be reduced by manually setting to zero the noise-dominated elements.

3.3 Fitting covariance matrix models to simulations

Data analysis in cosmology requires reliable covariance matrices. As stated in the previous chapters, covariance matrices derived from numerical simulations often require a very large number of realizations to be accurate. On the other hand, analytical models do not require such high costs, but given the complexity of the problem, sometimes such models depend on nuisance parameters to be determined by proper fits to numerical results. We write a likelihood-based method for performing such a fit. We demonstrate how a model covariance matrix can be tested by examining the appropriate χ^2 distributions from simulations. We show that if model covariance has amplitude freedom, the expectation value of second moment of χ^2 distribution with a wrong covariance matrix will always be larger than one using the true covariance matrix. By combining these steps together, we provide a way of producing reliable covariances without ever requiring running a large number of simulations. We demonstrate our method on two examples. First, we measure the 2-point correlation function of halos from a large set of 10000 mock halo catalogs. We build a model covariance with 2 free parameters,

which we fit using our procedure. The resulting best-fit model covariance obtained from just 100 simulation realizations proves to be as reliable as the numerical covariance matrix built from the full 10000 set. We also test our method on a setup where the covariance matrix is large by measuring the halo bispectrum for thousands of triangles for the same set of mocks. We build a block diagonal model covariance with 2 free parameters as an improvement over the diagonal Gaussian covariance. Our model covariance passes the χ^2 test only partially in this case, signaling that the model is insufficient even using free parameters, but significantly improves over the Gaussian one.

3.3.1 Covariance estimation

In this section, we discuss a hybrid approach, which builds up on recent techniques, with the goal of obtaining covariance matrices that are simultaneously reliable and based on few simulations. There are two insights our result is based on. The first one is that the covariance matrix estimation is, fundamentally, an estimate of 2-point correlations of realizations of the data vector. This is a problem that has been solved many times in various fields and for which an exact likelihood can be written and evaluated. It can be shown that the naively calculated numerical matrix contains all the information needed to evaluate the likelihood of a theoretical model of the same covariance matrix. Previous work has exploited this insight to fit a model covariance to mock simulations for the Baryon Acoustic Oscillations (BAO) analysis of SDSS DR7 (Xu et al. 2012) and the 2-point correlation function (O'Connell et al. 2016), the bispectrum (Slepian et al. 2017) and the power spectrum (Pearson & Samushia 2016) of BOSS data. In particular, O'Connell et al. (2016) and Pearson & Samushia (2016) have used these fits to reduce the number of mocks needed to build a reliable covariance.

The second insight is that, ultimately, any covariance matrix is used to compare some data with a model. The fundamental quantity of interest is therefore the χ^2 distribution. A good covariance matrix produces χ^2-distributed values when presented with realizations of data vectors. A biased or inappropriate covariance matrix produces χ^2 values that are not drawn from the correct distribution. This then tells us how to test a given covariance matrix. Applications of this idea have been investigated recently (Hall & Taylor 2019; Friedrich et al. 2021). Essentially, we propose to combine these two insights into a single algorithm to produce reliable and cheap covariance matrices. Assuming we have 50 realizations of a data vector of size 100, therefore corresponding to a covariance matrix of size 100×100, we are unable to estimate the covariance with precision, but we can both i) test candidate covariance matrices (i.e. 50 χ^2 values are sufficient to show compatibility with the correct distribution) and ii) fit a few parameter model covariance matrices.

Covariance Matrix Estimation is Covariance Estimation

Let us assume we are interested in the covariance matrix for a quantity that can be represented by an N dimensional vector. An example might be a measurement of the power spectrum of galaxies in N bins, or the measurement of a bispectrum, or both.

Ultimately, we want to run a Bayesian analysis, comparing a measurement vector $\mathbf{m}$ (of size N) with a theory prediction $\mathbf{t}(\theta_m)$, where θ_m are the parameters of the model for the

expectation value of $\mathbf{m}$. Assuming a Gaussian likelihood, we have

$$P(\theta_m|\mathbf{m}) \propto P(\mathbf{m}|\theta_m) = (2\pi)^{-N/2} |\mathrm{C}|^{-1/2} \exp\left\{-\frac{1}{2}[\mathbf{m}-\mathbf{t}(\theta_m)]^{\mathrm{T}} \mathrm{C}^{-1} [\mathbf{m}-\mathbf{t}(\theta_m)]\right\}. \quad (3.12)$$

In principle, the matrix C depends as well on the parameters θ_m. If such dependence is significant, our method can be straightforwardly extended to accommodate it as well. For now, we assume that this is not the case.

Suppose we have N_{sims} simulations providing as many realizations of the measurements $\mathbf{m}_i$, where $i = 1 \ldots N_{\mathrm{sims}}$. We assume that these simulations are drawn from the same underlying theory and that the output varies only because of a different realization of the cosmic structure and noise. In practical terms, they are identical runs except for the random seed. By construction, the ensemble mean value of those realizations is $\langle m_i \rangle \equiv \mathbf{m}(\theta_{m,\mathrm{sim}})$ where $\theta_{m,\mathrm{sim}}$ are the fiducial values of the parameters adopted to create the simulations. These are assumed to be the same for all realizations. Defining $\mathbf{d}_i = \mathbf{m}_i - \mathbf{m}(\theta_{m,\mathrm{sim}})$, we see that the d_i are normally distributed around zero with covariance C.

We can write the numerical matrix estimator

$$\mathrm{C}_n = \frac{1}{N_{\mathrm{sims}}} \sum_{i=1\ldots N_{\mathrm{sims}}} \mathbf{d}_i \mathbf{d}_i^{\mathrm{T}}. \quad (3.13)$$

Now, let us assume that we have a theoretical model for C depending on some model parameters θ, i.e. $\mathrm{C} = \mathrm{C}(\theta)$. That is, for a given set of θs, we can predict all values of C. Note that parameters θ cannot contain θ_m, since we have just assumed that these do not affect C.

The model for C can be either physical, based on theoretical expectation about C, but it can also be purely phenomenological, e.g. assuming C has a Toeplitz form, or that the off-diagonal terms beyond the second diagonal vanish. In any case, we can now use the Bayesian theorem to write a likelihood for the covariance parameters θ as:

$$P(\theta|\mathbf{d}) \propto P(\mathbf{d}|\theta)\Pi(\theta), \quad (3.14)$$

where we can put any prior information in $\Pi(\theta)$ and which we assume to be unity and where

$$\mathcal{L} = P(\mathbf{d}|\theta) \propto \prod_{i=1\ldots N_{\mathrm{sims}}} |\mathrm{C}(\theta)|^{-1/2} \exp\left[-\frac{1}{2}\mathbf{d}_i^{\mathrm{T}} \mathrm{C}^{-1}(\theta)\mathbf{d}_i\right]. \quad (3.15)$$

For the classically educated cosmologist, this equation looks quite familiar. It is the equation representing the likelihood a Gaussian field. The log-likelihood function $L \equiv \log \mathcal{L}$ equals up to a constant to

$$L(\mathbf{d}|\theta) = -\frac{N_{\mathrm{sims}}}{2} \log|\mathrm{C}(\theta)| - \frac{1}{2}\sum_i \mathbf{d}_i^{\mathrm{T}} \mathrm{C}^{-1}(\theta)\mathbf{d}_i = -\frac{N_{\mathrm{sims}}}{2}\left[\log|C(\theta)| + \mathrm{Tr}(\mathrm{C}^{-1}(\theta)\mathrm{C}_n)\right]. \quad (3.16)$$

This is the form of the equation that we use in what follows. This equation appears in this form already in O'Connell et al. (2016); Slepian et al. (2017), but in the context of very concrete models for the covariance matrix. In this paper, we stress that this form is general and that it can be applied to any model for covariance matrix and for observables beyond 2-point correlation function, as we will do in Section 3.3.3. The most interesting aspect is that

the likelihood can be rewritten in a form that depends only on the numerical covariance matrix C_n. In other words, we can compress the results of $N_{\rm sims}$ simulations into a single $N \times N$ matrix. If $N_{\rm sims} > N$ this form offers useful information compression. It is also true if $N_{\rm sims} < N$, i.e. C_n can in principle be even non-invertible and still contain all the available information at the 2-point level from the simulation suite. Given a sufficient number of simulations that the uncertainty on θ is negligible compared to the measurement noise on $\mathbf{m}$, it suffices to find the maximum likelihood point in the θ space and use the resulting matrix.

In what follows we demonstrate this technique in practice with two examples.

Goodness of fit for covariance matrix model

After deriving the best-fit parameters for a given model of the covariance matrix, we would like to determine if the result is indeed a useful covariance matrix. Note that this is not a model comparison exercise, but a problem of goodness-of-fit: is the resulting covariance matrix actually fit for purpose?

A common use of the covariance matrix is the evaluation of the χ^2 for a cosmological model likelihood. Under the assumption of Gaussianity, a good covariance matrix is the one providing correctly distributed χ^2 values. A simple test on the inverse can be done by verifying that the residuals $\mathbf{d}_i = \mathbf{m}_i - \mathbf{m}(\theta_{m,\rm sim})$ are χ^2-distributed with the right number of degrees of freedom,

$$\chi^2_i = [\mathbf{m}_i - \mathbf{m}(\theta_{m,\rm sim})]\, \mathrm{C}^{-1}\, [\mathbf{m}_i - \mathbf{m}(\theta_{m,\rm sim})]^T. \tag{3.17}$$

While one would ideally have a separate set of simulations, this test can also be performed on the *same* simulations that were used to infer the parameters. This is equivalent to fitting a theory to data and then using the same data to check the resulting χ^2 *without subtracting the model degrees of freedom*. This is a valid procedure where the number of simulations is much larger than the number of free parameters in the theory. When this condition is violated, the only safe thing to do is to split simulations into a "training" and "testing" subsets.

We will now consider how do the moments of χ^2 distribution respond to being tested with a wrong covariance matrix. First consider a simple model where we simply fit for the covariance matrix amplitude, i.e.

$$C(\theta_A) = \theta_A C_0. \tag{3.18}$$

At this point, we make no claims of whether C_0 is a good or poor approximation of the true covariance matrix, it is simply a matrix. We have $|C(\theta_A)| = \theta_A^N |C_0|$ and $C^{-1}(\theta_A) = \theta_A^{-1} C_0^{-1}$. Plugging these expressions into Equation 3.16 we find that the maximum likelihood point is given by

$$\theta_A = \frac{\mathrm{Tr}(\mathrm{C}_0^{-1}\mathrm{C}_n)}{N}. \tag{3.19}$$

For the simulation realization i, the χ^2 is given by $\chi^2_i = \mathbf{d}_i^T C^{-1} \mathbf{d}$ (for some covariance matrix C) and so the mean over the set of simulations is given by

$$\mathrm{Mean}\,\chi^2 = \frac{1}{N_{\rm sims}} \sum_{i=1}^{N_{\rm sims}} \chi^2_i = \mathrm{Tr}(\mathrm{C}^{-1}(\theta)\mathrm{C}_n) = N, \tag{3.20}$$

$$\mathrm{Var}\,\chi^2 = \frac{1}{N_{\rm sims}} \sum_{i}^{N_{\rm sims}} (\chi^2_i)^2 - \left(\mathrm{Mean}\,\chi^2\right)^2 = \sum_{i}^{N_{\rm sims}} (\mathbf{d}_i^T C^{-1} \mathbf{d})^2 - N^2, \tag{3.21}$$

The last equality of equation 3.20 comes from using solution of Equation 3.19 and doing some straightforward manipulation. Even if C_0 is a completely wrong, the terms containing trace of $C_0^{-1}C_n$ cancel exactly and so one always has Mean $\chi^2 = N$. In other words, if our model for covariance matrix has a freedom to adjust the amplitude, then the maximum likelihood is such that the first moment of χ^2 matches the theoretical expectation. Note that in general, our model for C will have many more parameters, but as long as there is a subspace of the model which corresponds to a simple amplitude rescaling, this statement will be true.

There is no such simplification for variance. In this case we can calculate the expectation value and find after some simplifications that:

$$\left\langle \mathrm{Var}\,\chi^2 \right\rangle = 2\mathrm{Tr}(\mathrm{C}^{-1}(\theta)\mathrm{C}_{\rm true}\mathrm{C}^{-1}(\theta)\mathrm{C}_{\rm true}), \tag{3.22}$$

where $\mathrm{C}_{\rm true}$ is the true covariance matrix, i.e. the one from which vectors $\mathbf{d}$ are drawn. If $\mathrm{C}(\theta) = \mathrm{C}_{\rm true}$, i.e. if our model covariance matrix is indeed true, we find the standard moment of χ^2 distribution, i.e. $\left\langle \mathrm{Var}\,\chi^2 \right\rangle = 2\mathrm{Tr}(\mathrm{I}) = 2N$.

Next let us assume $\mathrm{C}(\theta)$ is different from $\mathrm{C}_{\rm true}$, so that its inverse is given by $\mathrm{C}^{-1}(\theta) = \mathrm{C}_{\rm true}^{-1} + \mathrm{X}$. Additionally, let us assume that the first moment is correctly recovered as will always happen when the model has the freedom to rescale the matrix. In this case we find that

$$\mathrm{Tr}(\mathrm{C}_{\rm true}\mathrm{X}) = \mathrm{Tr}(\mathrm{C}_{\rm true}C^{-1}(\theta)) - \mathrm{Tr}(\mathrm{C}_{\rm true}\mathrm{C}_{\rm true}^{-1}) = \left\langle \chi^2 \right\rangle - N = 0. \tag{3.23}$$

Therefore

$$\left\langle \mathrm{Var}\,\chi^2 \right\rangle = 2N + 2\mathrm{Tr}(\mathrm{C}_{\rm true}\mathrm{X}\mathrm{C}_{\rm true}\mathrm{X}) > 2\mathrm{N} \tag{3.24}$$

To show the second line inequality, we note that $\mathrm{C}_{\rm true}$ is a positive definite matrix and we can always rotate it into the frame $\mathrm{C}'_{\rm true}$ where it is diagonal with its eigen values λ_i on the diagonal. In this frame X becomes X′ and the second term becomes $2\mathrm{Tr}(\mathrm{C}'_{\rm true}\mathrm{X}'\mathrm{C}'_{\rm true}\mathrm{X}') = \sum_{\rm ij}\lambda_{\rm i}\lambda_{\rm j}\mathrm{X}'^2_{\rm ij} > 0$.

Finally, let's consider the error on the χ^2 on a given data vector, which appears as a result of using the wrong covariance matrix. For a given $\mathbf{d}$

$$\Delta\chi^2(\mathbf{d}) = \mathbf{d}^T\mathrm{C}(\theta)^{-1}\mathbf{d} - \mathbf{d}^T\mathrm{C}^{-1}\mathbf{d} = \mathbf{d}^T\mathrm{X}\mathbf{d} \tag{3.25}$$

Using the same assumption as above it is easy to show that the first and second moment of this quantity are

$$\left\langle \Delta\chi^2 \right\rangle = 0 \tag{3.26}$$

$$\left\langle \mathrm{Var}\,\Delta\chi^2 \right\rangle = 2\mathrm{Tr}(\mathrm{CXCX}) \tag{3.27}$$

In other words, for data vectors drawn from the true covariance matrix, using the wrong covariance matrix produces additional scatter around true χ^2 values. This additional scatter has zero mean and variance given by Eq. 3.27. Since variances add, this results in a distribution of χ^2 values that is broader by the same amount.

To recap, we have shown three simple but powerful results. If the model covariance matrix has freedom to vary in amplitude, the maximum likelihood will adjust its value so that the expectation value of χ^2 is the correct value. In that limit, the values of individual χ^2 computed with a wrong covariance matrix scatter around their true values: some of them are

lower and some of them are higher than what they should be. Because variances add, this results in a second moment of χ^2 distribution that is larger that $2N$, with equality holding when $\mathrm{C}(\theta)$ is the correct covariance matrix.

This gives us a direct handle on accuracy of covariance matrix. If we are unwilling to tolerate more than $\Delta\chi^2 = 1$ in χ^2 error, then we should really find a model in which both the first and the second moment are reproduced to this accuracy. In practice, we might find that a significantly more relaxed χ^2 can still produce essentially unchanged constraints.

3.3.2 Test 1: 2-point correlation function

For the first test of our method, we consider the 2-point correlation function as observable, measured from a very large number $N_{\rm sims} = 10000$ of mock halo catalogs. Let us assume as original problem a test of the 2-point correlation function model based on the correct recovery of the cosmological parameters of the simulations. For the sake of simplicity, we only consider Ω_m and σ_8. Such test requires the knowledge of the covariance matrix. Given the large number of mocks, we can build a reliable numerical covariance matrix, C_n. Using the method presented in Section 3.3.1, we show how we can obtain an equally reliable covariance matrix using only a fraction of the $N_{\rm sims}$ simulations available.

The 2-point correlation function and its covariance

The basic ingredients of this test involve a model for the 2-point correlation function of halos corresponding to $\mathbf{t}(\theta_m)$ in the previous section and the model for covariance matrix corresponding to $\mathrm{C}(\theta)$.

For the purpose of testing our covariance fitting technique, we take a simple linear model for the halo power spectrum including shot noise,

$$P_{\rm h}(k) = b^2 P_{\rm m}(k) + \frac{1+\alpha}{\bar{n}}, \tag{3.28}$$

where b is the linear bias, $P_{\rm m}$ is the linear matter power spectrum, $\bar{n}$ is the halo number density and α parameterises deviations from Poissonian shot noise, $1/\bar{n}$. The corresponding 2-point correlation function is given by,

$$\xi_{\rm h}(r) = b^2 \xi_{\rm m}(r), \tag{3.29}$$

where $\xi_{\rm m}$ is the Fourier transform of $P_{\rm m}$. When comparing to simulations, we fit the linear bias to the measurements of the 2-point correlation function. In order to compute the covariance for Eq. (3.29), we Fourier transform the leading[1] term of the power spectrum covariance

$$\mathrm{C}(b,\alpha) \simeq \frac{2}{V}\int \frac{\mathrm{d}k\,k^2}{2\pi^2}\left(b^2 P_{\rm m}(k) + \frac{(1+\alpha)}{\bar{n}}\right)^2 W_i(k) W_j(k)\,, \tag{3.30}$$

where V is the box volume and $W_i(k)$ is the Fourier transform of the i-th radial shell

$$W_i(k) = \int \frac{\mathrm{d}^3 r}{V_i} j_0(kr) = \frac{r_{i,+}^3 W_{\rm th}(kr_{i,+}) - r_{i,-}^3 W_{\rm th}(kr_{i,-})}{r_{i,+}^3 - r_{i,-}^3}\,, \tag{3.31}$$

[1] The full covariance would include a trispectrum term (Scoccimarro et al. 1999), which we assume to be negligible (Grieb et al. 2016).

where $V_i = \frac{4\pi}{3}\left(r_{i,+}^3 - r_{i,-}^3\right)$ is the shell volume, $j_0(kr)$ is the zero-th order spherical Bessel function, and $W_{\rm th}(kr)$ is the Fourier-transform of the top-hat window function. Our model covariance therefore depends on two parameters $\theta = \{b, \alpha\}$. A simple choice for these parameters would be to use the bias we fit to the 2-point correlation function measurements $b \equiv \hat{b}$ and $\alpha = 0$.

Description of the Data

We take advantage of a very large set of $N_{\rm sims} = 10000$ mock halo catalogs obtained with the PINOCCHIO code (see Sect. 2.2.2). The mock catalogs are built from 1000^3 dark matter particles in a cubic box of side $L = 1500$, reproducing the set-up and adopting the cosmology of the Minerva N-body simulations (Grieb et al. 2016). The mass threshold is defined requiring that the large-scale amplitude of the PINOCCHIO catalogs power spectrum (including shot-noise) matches the amplitude of the same power spectrum measured in the Minerva simulations catalogs, the latter defined by a minimal mass of $M \simeq 1.12 \times 10^{13}\ h^{-1} M_\odot$. We refer the reader to Oddo et al. (2020) for a more detailed description of the mock halo catalog construction, that allows to reproduce the power spectrum and bispectrum variance within 10 percent (Oddo et al. 2020, 2021). The 2-point correlation function is measured using the standard Landy-Szalay estimator (Landy & Szalay 1993) as implemented in the CosmoBolognaLib code (Marulli et al. 2016), adapted, however, to account for the box periodic boundary conditions in the pair counting.

The numerical covariance is estimated directly from the mocks by applying the estimator of Eq. (3.8), with observable given by $\xi_{\rm h}(r)$. The numerical covariance obtained in this way has been compared with full simulations results, showing good agreement (but with a different definition of the mass threshold) in Lippich et al. (2019).

We should notice that the covariance model above does not account for the specific geometry of our distribution, that is the effect of the exact number of pairs in the case of a box with periodic boundary conditions (Philcox & Eisenstein 2019; Li et al. 2019). We therefore expect that the recovered value of the covariance model parameters accounts in part also for this neglected effect.

Results

In this section we outline the results of this test. The goal is to show that our model covariance is as reliable as the numerical one obtained from a very large set of simulations. The final test is therefore to demonstrate that cosmological parameters, in our case $\Omega_{\rm m}$ and σ_8, are recovered with the correct value and uncertainty using the model covariance. The procedure can be summarized as follows:

i) Build a set of numerical covariance matrices using Eq. (3.8) for varying number of simulations $N_{\rm sims} = 10000$, 1000, 100, 50, and 30.

ii) Build a model covariance with free parameters, following Eq. (3.30). The free parameters are the linear bias b and the deviation from Poisson shot noise α.

iii) Maximize the likelihood of Eq. (3.16) varying the free parameters, using the sets of C_n from point 1) to get a best-fit model covariance $\mathrm{C}(b_{\rm fit}, \alpha_{\rm fit})$.

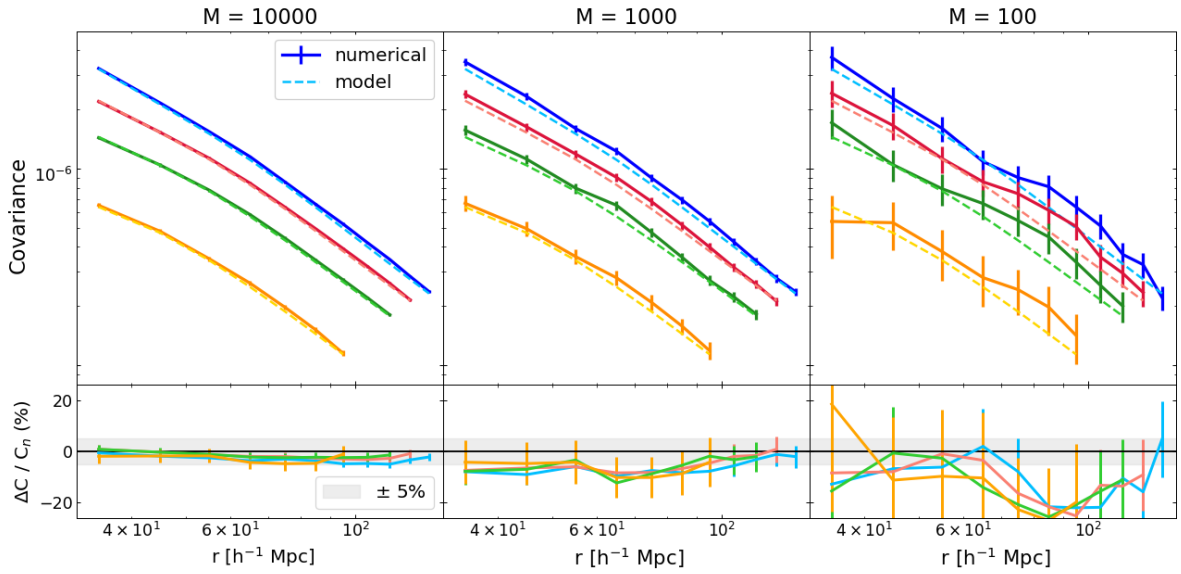

Figure 3.1: Comparison between the model C_ξ (dashed lines) and numerical (solid lines) covariance, computed with different number $N_{\rm sims}$ of simulations. Different colors represent different terms of the matrices: diagonal in blue, first off-diagonal in red, second off-diagonal in green and fourth off-diagonal in orange. In the bottom panels, percent residuals between numerical and model covariances.

.

iv) Verify the reliability of the model covariance matrix, and of all the numerical covariance matrices, for varying number of simulations.

We proceed then with details on the maximization procedure and the check of reliability of the model covariance. We also show results obtained by fixing the covariance parameters to the fit to the 2-point correlation function, C_ξ.

We fit our model covariance $\mathrm{C}(b,\alpha)$ using the technique described in Section 3.3.1. We perform the inference for b and α using the likelihood of Eq. (3.16). We assume flat priors for the two parameters, $b \in [0,5]$ and $\alpha \in [-1,1]$. We repeat the fit using several subsets of simulations $N_{\rm sims}$ = 10000, 1000, 100, 50, 30 to build the numerical covariance C_n. In Fig. 3.1, we show a comparison between the numerical and the model covariance matrices for three different subsets of simulations, $N_{\rm sims}$ = 10000, $N_{\rm sims}$ = 1000 and $N_{\rm sims}$ = 100. The error bars are given by the standard deviation computed on a set of $n = N_{\rm sims,tot}/N_{\rm sims}$ independent subsets of simulations, where $N_{\rm sims,tot}$ = 10000 is the total number of available simulations. In this case, we fix the model covariance to be C_ξ, i.e. fixing b to the value fit to the 2-point function measurements and $\alpha = 0$. As we decrease the number of simulations, the model deviates from the numerical covariance.

It is useful to show the posteriors resulting from the maximization of the likelihood, in the left panel of Fig. 3.2. As expected, as we use an increasing number of simulations, the contours shrink, but they are consistent with each other. Even with only 30 simulations we can broadly constrain the parameters well within the prior. Interestingly, the data prefer a non-zero value of the shot noise parameter, and a value of the bias that disagrees with the one we have fit to the 2-point correlation function (dashed line). This effect is distinguishable even with a very small number of simulations and it becomes very significant at $N_{\rm sims}$ = 10000 with an over 30 sigma tension between the standard Poisson shot noise and our measurement

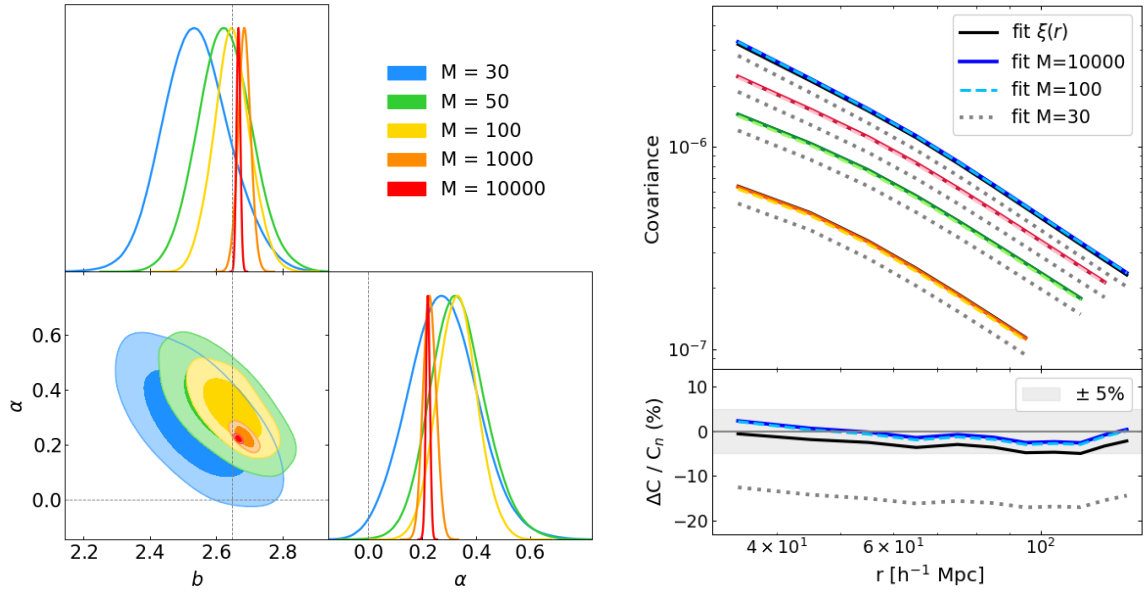

Figure 3.2: *Left Panel.* Contour plots at 68 and 95 per cent of confidence level for the covariance parameters, fitted over different numbers of simulations. The gray dashed lines represent the reference values, given by $\alpha = 0$ (Poissonian shot-noise) and bias fitted from the 2-point correlation function. *Right Panel.* Model covariances for the cases $N_{\rm sims} = 10000$, 100, 30 and $\xi(r)$ fit (respectively solid dark, dashed light, dotted gray and black lines). In the bottom panel, percent residuals with respect to the full numerical matrix. Color code as in Fig. 3.1.

of it. As mentioned, this is not necessarily reflecting a proper departure from the Poisson limit of the halo distribution shot-noise, but it can include additional systematics, e.g. geometry effects, and the incompleteness of the model.[2]

In Fig. 3.3 we plot the histogram of χ^2 values for the model covariances built from the subsets of simulations as described in Section 3.3.1. As a reference, we also calculate the histogram for the numerical covariance matrix using $N_{\rm sims} = 10000$ simulations and the model covariance where we fix the bias from the correlation function fit and $\alpha = 0$, C_ξ. All these candidate models for the covariance are compared to the theoretical χ^2 distribution for this setup, which has mean $\mu = 11$ and variance $\sigma^2 = 22$. We calculate the mean and variance of each histogram; their errors are estimated by bootstrap, i.e. by resampling the data and evaluating the confidence region from the bootstrap distribution of the resampled statistics. From this test it is clear that our model covariance agrees reasonably well with the theoretical curve already with only $N_{\rm sims} = 30$ simulations, even though with large error bars. On the other hand, the model covariance with fixed parameters is significantly away from the predicted distribution.

The final test is to show that from the clustering analysis of the 2-point correlation function we are able to correctly recover cosmological parameters from the simulations by using our model covariance. We consider a Gaussian likelihood for the observable, the 2-point correlation function of halos. The theoretical model is the one given in Eq. (3.29), where

[2] As a further check, we have fit b and α directly on power spectrum measurements performed on the same set of simulations. The fitted values are also in disagreement with our best-fit values found using our model covariance. This confirms that the discrepancy is explained by the incompleteness of the model covariance, rather than a true deviation from Poisson shot-noise.

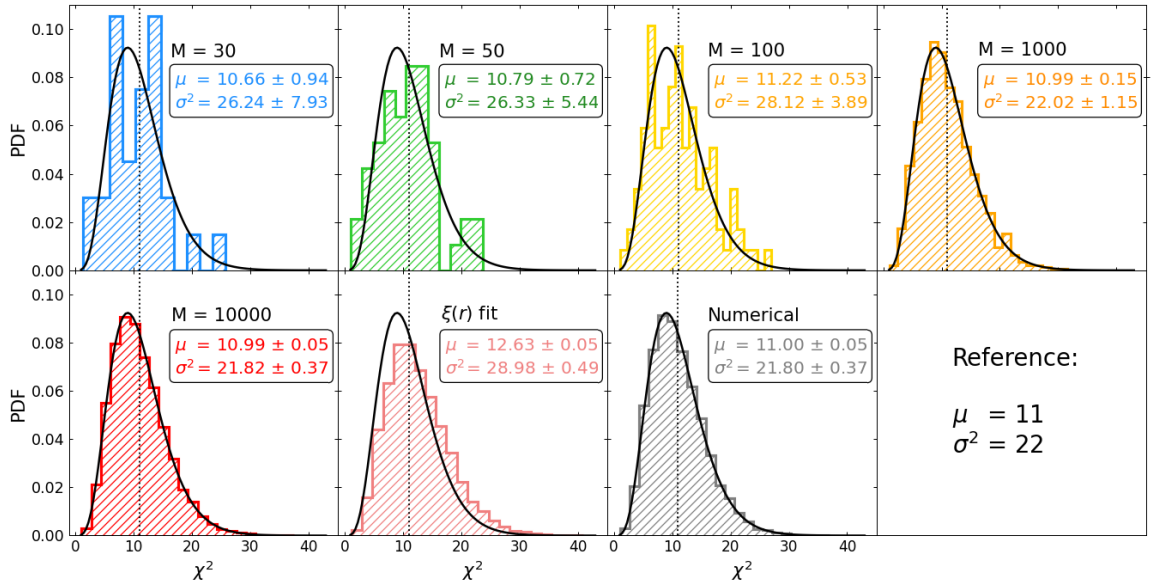

Figure 3.3: χ^2 distribution corresponding to the fitted parameters for different numbers of simulations (colored histograms), compared to the predicted distribution (black). In the bottom panels, comparison with the matrix with parameters fitted from $\xi(r)$ and the numerical matrix. The errors on the mean and the variance are computed with bootstrap method.

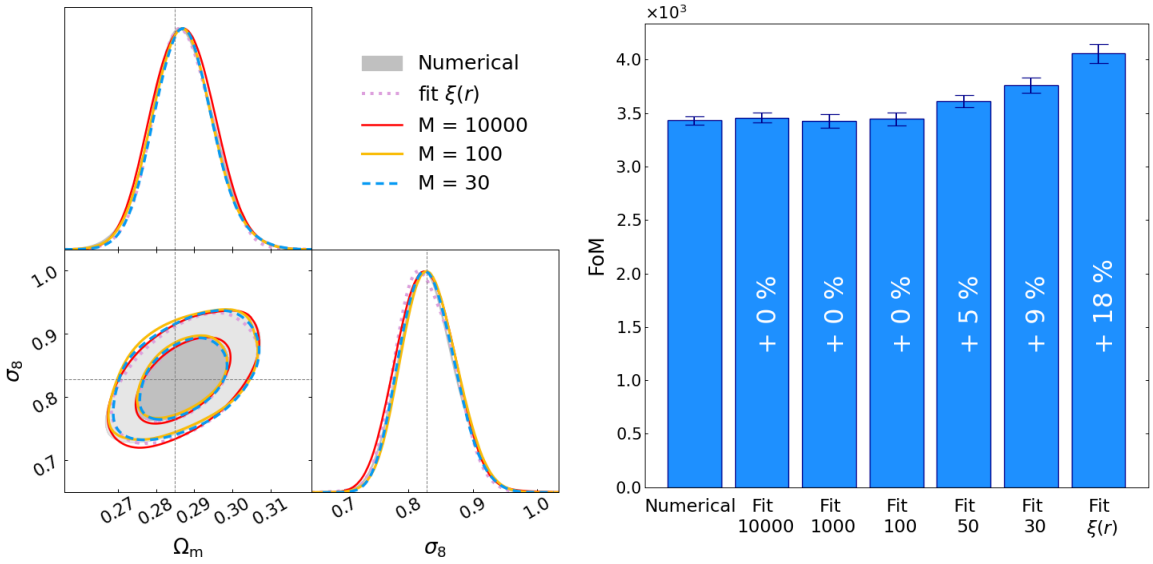

Figure 3.4: *Left Panel:* Contour plots at 68 and 95 per cent of confidence level for the cosmological parameters Ω_m and σ_8, computed with different covariance matrices: full numerical (gray), no-fit model (pink), $N_{sims} = 30$ fit (blue), $N_{sims} = 100$ fit (yellow), $N_{sims} = 10000$ fit (red). *Right Panel:* Figure of merit in the $\Omega_m - \sigma_8$ plane for different covariance cases: the numerical covariance matrix drawn from the full set of $N_{sims} = 10000$ simulation, our model covariance for varying N_{sims} where we use the best-fit values for b and α as found from the likelihood minimization, and the model covariance where we use b fit from the 2-point correlation function and $\alpha = 0$. The error bars are computed from an average of $n = 10$ realizations, as $\epsilon = \sigma/\sqrt{n}$.

we vary the linear bias and two cosmological parameters, $\Omega_{\rm m}$ and σ_8, which enter through the linear matter power spectrum. We choose the following flat priors for these parameters: $\{b, \Omega_{\rm m}, \sigma_8\} \in \{[0,5], [0.20, 0.35], [0.7, 0.9]\}$. As for the covariance, we use our model covariance set to the best-fit values of Fig. 3.2. Note that we allow the bias of the covariance model to be different to the bias in the correlation function model. This is because we expect the former to also play a role in absorbing the missing terms in the covariance model, and thus lose its physical meaning of bias. For comparison, we also consider the case in which covariance and correlation function biases are the same, i.e. C_ξ. All the cases are compared to the results with the full numerical covariance C_n. The results are shown in the left panel of Fig. 3.4. As expected, our model covariance with only $N_{\rm sims} = 30$ simulations does not bias the contours of the parameters with respect to the numerical one built from $N_{\rm sims} = 10000$ simulations. By eye, the fixed model covariance seems to be as good as the others, deviating by a small amount from the numerical one. To better evaluate the differences between the results, in the right panel of Fig. 3.4 we show the FoM for the resulting posteriors. To take into account the statistical uncertainty of the likelihood maximization process, we compute the figure of merit as the average over $n = 10$ realizations, with errors given by the standard error $\varepsilon = \sigma/\sqrt{n}$. Clearly, the figure of merit here is to be intended as an overall estimate of the parameters errors and it is relevant only in its departure from the fiducial value. A good covariance matrix would give the same FoM as numerical fit on 10,000 realizations: a higher FoM indicates errors that are too small, while a low FoM indicates errors that are too large. The result confirms that our model covariance works well already with $N_{\rm sims} = 30$, and provides a perfect match for $N_{\rm sims} = 100$ simulations. We also find a curious effect: using too few simulations provides a covariance matrix that not only varies from one set of 30 simulations to another, but one that is also systematically biased towards high FoM (underestimation of the error bars). With too few simulations, the numerical matrix turns out to be inaccurate, providing a biased fit of the model. As shown in left panel of Fig. 3.2, the covariance fitted from 30 simulations underestimates the true covariance; different results can be obtained from different subsets of simulations, as the data on which performing the fit can be biased in the opposite direction. The inaccuracy of such fit is confirmed by the FoM of Fig. 3.4.

Finally, we see that using a covariance where we fix the bias to the fitted value to the 2-point correlation function measurements and $\alpha = 0$, i.e. C_ξ, provides a $\sim 20\%$ underestimation of the error with respect to the numerical one, meaning that such a matrix is not accurate enough to allow for a proper estimation of cosmological constraints.

3.3.3 Test 2: Bispectrum

As a second test, we study the bispectrum, i.e. the three-point correlation function in Fourier space, on the same halo catalogs used for the first test. The motivation for choosing this observable as a test is twofold: first, it is an example where the covariance matrix can have very large dimensions. As compared to the power spectrum, where the covariance matrix is built from a data vector with typically $N \sim 20-50$ components, for the bispectrum the data vector may contain hundreds to thousands of triangles. Such a large data vector, and consequently covariance matrix, makes it very tricky to use the numerical covariance matrix as defined in Eq. (3.13). This is because we usually need $N_{\rm sims} \gg N$ to beat numerical noise, $N_{\rm sims}$ being the number of simulations and N the dimension of the data vector. Moreover, whenever the number of simulations is lower than the dimension of the data vector, the numerical covari-

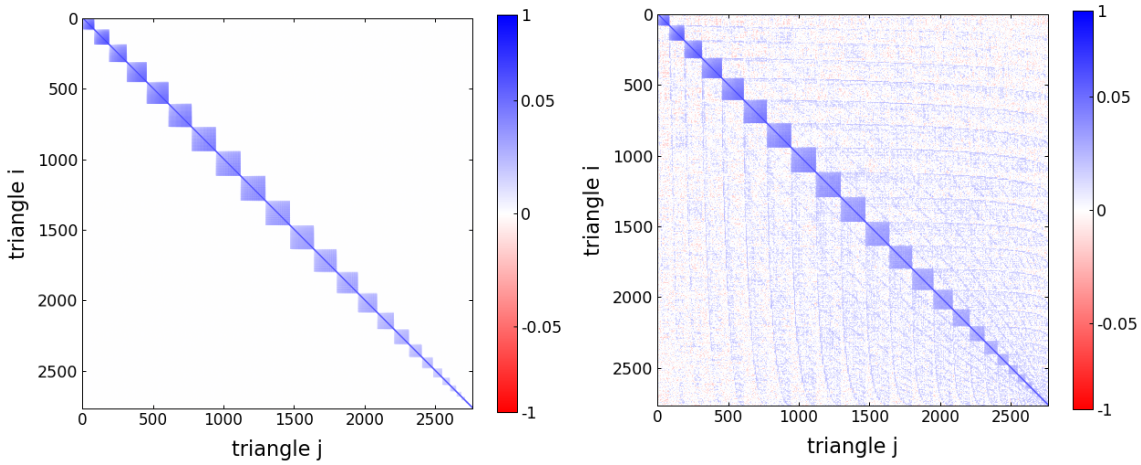

Figure 3.5: Cross-correlation matrix r_{ij} of the halo bispectrum covariance for the model covariance (left) and the numerical covariance computed on $N_{\rm sims} = 10000$ simulations (right).

ance matrix cannot be inverted. Secondly, it is a way of testing a more realistic scenario, as the modeling of the bispectrum is significantly more involved than the one for a 2-point function. In fact, as we will see, the model covariance we are going to use is knowingly incomplete, and our method will not be able to perform as well as a numerical covariance matrix drawn from $N_{\rm sims} = 10000$ simulations. It will show, however, that a fit with parameters can help in building a reliable covariance matrix, even if the model is incomplete, as compared to considering a diagonal Gaussian covariance matrix.

The bispectrum and its covariance

Let us first set the notation on the bispectrum. Differently than the previous example, we work in Fourier space, and the bispectrum is defined as

$$\langle \delta(\mathbf{k}_1)\delta(\mathbf{k}_2)\delta(\mathbf{k}_3)\rangle = \frac{\delta_K(\mathbf{k}_1+\mathbf{k}_2+\mathbf{k}_3)}{k_f^3} B(k_1,k_2,k_3), \tag{3.32}$$

where $\delta(\mathbf{k})$ is the discrete Fourier transform of the density contrast $\delta(\mathbf{x})$, δ_K is the Kronecker symbol (equal to unity when the argument vanishes, zero otherwise) and $k_f = 2\pi/L$ is the fundamental frequency of a cubic box of volume L^3. We measure the bispectrum for all the 10000 PINOCCHIO halo catalogs. We use unbiased estimators for the measurement of the bispectrum following the definition of Scoccimarro et al. (1998); Scoccimarro (2015). We implement a fourth-order density interpolation and the interlacing scheme described in Sefusatti et al. (2016). We divide k-modes into bins of width $\Delta k = k_f$ and up to a $k_{\rm max} = 0.12$ h/Mpc, for a total of 29 k-bins and 2766 triangles.

We consider the approximation for the bispectrum covariance given by[3] Sefusatti et al.

[3]The complete formula for the bispectrum covariance would read

$$C^B_{ij} = C^{B,(PPP)}_{ij} + C^{B,(BB)}_{ij} + C^{B,(PT)}_{ij} + C^{B,(P_6)}_{ij}, \tag{3.33}$$

where T and P_6 are the trispectrum and pentaspectrum, respectively. The "PT" term represents the product of the power spectrum and trispectrum. As explained below, we are approximating the PT term to be proportional to the BB term and neglect P_6. See Biagetti et al. (2022) for more details.

(2006); Biagetti et al. (2022)

$$C^B_{ij} = \alpha\, C^{B,(PPP)}_{ij} + \beta\, \delta^K_{k^i_3 k^j_3}\, C^{B,(BB)}_{ij}, \tag{3.34}$$

where α and β are free parameters and $\delta^K_{k^i_3 k^j_3}$ is a Kronecker symbol which is non-vanishing when the two triangles i and j have the smallest side in common, i.e. k^i_3 is equal to k^j_3. The first term, $C^{B,(PPP)}_{ij}$, is the Gaussian contribution, which we write down in the thin-shell approximation as

$$C^{B,(PPP)}_{ij} \simeq \frac{\delta_{ij}\, s_B}{k_f^3 N^i_{tr}}\, P(k^i_1)\, P(k^i_2)\, P(k^i_3), \tag{3.35}$$

where $s_B = 6, 2, 1$ is the symmetry factor accounting for the shape of the triangles (equilateral, isosceles and scalene, respectively) and N^i_{tr} is the number of fundamental triangles in the triangle bin $\left\{k^i_1, k^i_2, k^i_3\right\}$. The second term is defined as

$$C^{B,(BB)}_{ij} \simeq B_i\, B_j \left(\Sigma^{11}_{ij} + 8 \text{ perm.}\right), \tag{3.36}$$

where i and j indicate the triangle bins $\{k^i_1, k^i_2, k^i_3\}$ and $\{k^j_1, k^j_2, k^j_3\}$, respectively, B_i is the bispectrum for the triangle bin i and Σ^{ab}_{ij} is a mode-counting factor that depends again on the shape of the triangle. Both terms are computed using measurements of the power spectrum and bispectrum directly, without using any perturbative calculation. The resulting covariance has a block-diagonal structure, which we show in the left panel of Fig. 3.5 by plotting the cross-correlation matrix

$$r_{ij} = \frac{C_{ij}}{\sqrt{C_{ii} C_{jj}}}, \tag{3.37}$$

which helps in visualizing the importance of off-diagonal elements with respect to diagonal ones.

For comparison, we also plot the numerical covariance for $N_{\rm sims} = 10000$, in the right panel of the same figure. The numerical covariance shows a similar block diagonal structure as the modeled one. Indeed, these particular non-diagonal entries of the bispectrum covariance are the largest terms in the non-Gaussian covariance (Biagetti et al. 2022). Based on theoretical considerations (Barreira 2019; Biagetti et al. 2022), we expect that $\alpha \simeq 1$ and $\beta \simeq 2$. In particular, $\beta = 2$ assumes that the contribution due the product of the power spectrum and trispectrum of the field can be approximated by the term in Eq. (3.36), a good approximation for squeezed triangles, but not for generic shapes. In the numerical covariance, we can clearly see more structure outside the blocks, which Eq. (3.34) does not model.

Results

Having defined the model covariance for the bispectrum test, we can proceed with the same steps as done for the 2-point correlation function in the Section 3.3.2.

We maximize the likelihood of Eq. (3.16) varying α and β using sets of C_n for $N_{\rm sims} = 30$, 50, 100, 1000 and 10000 as in the previous test. We plot the contour plots for α and β in Fig. 3.6. Interestingly, the theoretical values do not fall within the contours for $N_{\rm sims} = 1000$ and $N_{\rm sims} = 10000$. In fact, this is not surprising, since the model covariance is an incomplete

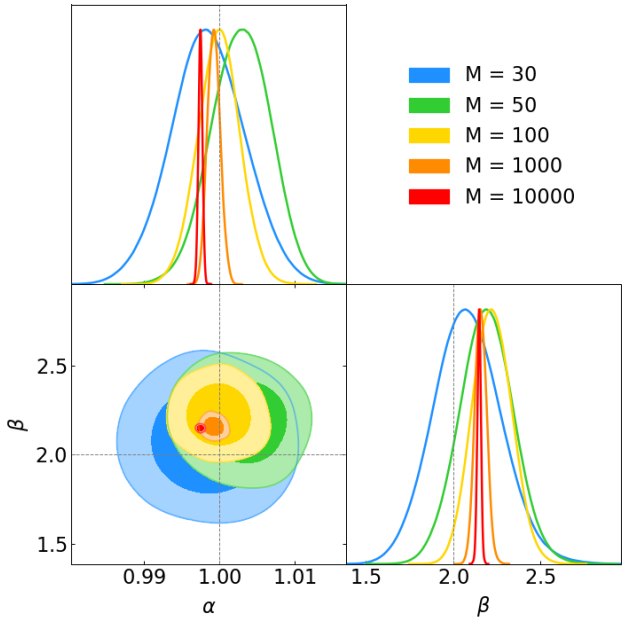

Figure 3.6: Same of left panel of Fig. 3.2 for the bispectrum covariance. The parameters α and β represent the amplitude of the Gaussian and (part of the) non-Gaussian covariance, respectively, as defined in Eq. (3.34).

model of the full covariance, which has non-zero elements also outside the block-diagonal structure modeled by Eq. (3.34). These non-zero elements might be sourced by a connected 6-point function, or by correlated noise. Even though these terms are small compared to the ones we model, when considering a large number of simulations they become significant with respect to sample noise and the fit tries to adapt shifting the central values of α and β.

Using the best-fit values for the α and β parameters obtained from maximizing the likelihood, we perform the χ^2 test introduced in the previous section in order to verify the performance of our model covariance. We show results in Fig. 3.7. Differently than for the 2-point correlation function, our model for the bispectrum covariance does not perform as well as the numerical covariance obtained from $N_{\rm sims} = 10000$ simulations. Indeed, even though the mean μ of the χ^2 distribution of our model covariance is in good agreement with the theoretical value of $\mu = 2766$ already at $N_{\rm sims} = 100$ simulations, the variance σ^2 is significantly off.[4] Again, we can expect this given that our model covariance is incomplete. Nevertheless, it is useful to point out that, in the absence of a theoretical prior on the free parameters, and a numerical covariance, this method would prove useful in building a good approximation of the true covariance. Indeed, given that the mean of the χ^2 is within the theoretical value, we expect that our model covariance does not bias strongly parameter estimation. For comparison, we compute the histogram also for the pure Gaussian covariance, i.e. a model covariance built fixing $\alpha = 1$ and $\beta = 0$, see Eq. (3.35). In this case, both the mean and the variance of the histogram are significantly off from the theoretical curve.

In order to further confirm that the failure of the χ^2 test is linked to the incompleteness of the model, we perform the following test: we calculate the numerical covariance matrix

[4]It is interesting to point out that even the numerical covariance does not fit perfectly well the reference χ^2. We attribute this fact to the actual likelihood of the bispectrum not being Gaussian, at this volume.

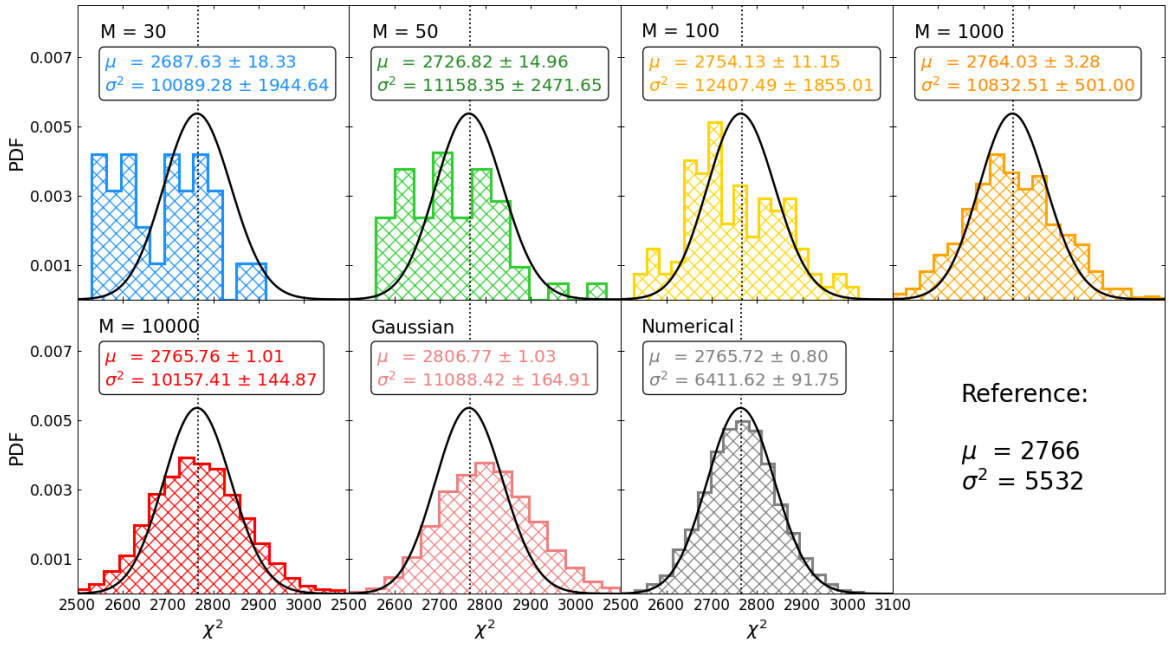

Figure 3.7: Same of Fig. 3.3, for the bispectrum covariance.

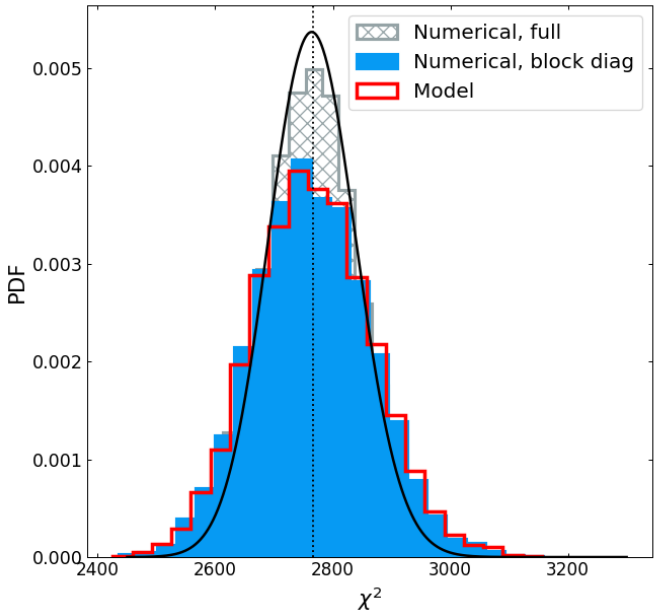

Figure 3.8: χ^2 distribution for the full numerical (gray), block-diagonal numerical (blue), and model (red) covariance.

where we only keep the block diagonals that are modeled by our model covariance, putting all other off-diagonal terms to zero. We then redo the χ^2 test using this numerical covariance and compare to the result that we got using the model covariance with $N_{\rm sims} = 10000$ simulations. We show the result of this test in Fig. 3.8. Indeed, if we only consider the blocks that we model in the numerical covariance, the χ^2 test gives a very similar result as for the model covariance.

Chapter 4

Cluster number counts results

In this chapter we describe the results of the covariance validation and likelihood analyses for the number counts, presented in Euclid Collaboration: Fumagalli et al. (2021). The aim of this work is to assess the contribution of shot-noise and sample variance to the statistical error budget expected for the *Euclid* photometric survey of galaxy clusters. The expectation is that the level of shot-noise error would decrease due to the large number of detected clusters, making the sample variance not negligible anymore. First, in Sect. 4.1, we describe and validate the analytical model of Hu & Kravtsov (2003) for the covariance matrix, which takes into account both sources of statistical error. Once we verified to have a correct description of the covariance, we move to the likelihood analysis (Sect. 4.2.2). We analyze the optimal redshift and mass binning scheme, which will ensure to extract the cosmological information in the best possible way. Then, we test the effects on parameter posteriors of different model assumptions: likelihood model, inclusion of sample variance and cosmology dependence.

4.1 Covariance matrix model

To describe the covariance associated to cluster number counts (Eq. 1.24), we consider the analytical model proposed by Hu & Kravtsov (2003) and validate its predictions against simulated data. For number counts, the total covariance is given by the sum of the shot-noise variance and the sample covariance,

$$C = C^{\rm SN} + C^{\rm SV} \,. \tag{4.1}$$

According to the model, such terms can be computed as

$$C^{\rm SN}_{abij} = \langle N \rangle_{ai} \, \delta_{ab} \, \delta_{ij} \,, \tag{4.2}$$

$$C^{\rm SV}_{abij} = \langle Nb \rangle_{ai} \, \langle Nb \rangle_{bj} \, S_{ab} \,, \tag{4.3}$$

where $\langle N \rangle_{ai}$ and $\langle Nb \rangle_{ai}$ are respectively the expectation values of number counts and number counts times the halo bias in the i-th mass bin and a-th redshift bin,

$$\langle N \rangle_{ai} = \Omega_{\rm sky} \int_{\Delta z_a} {\rm d}z \, \frac{{\rm d}V}{{\rm d}z \, {\rm d}\Omega} \int_{\Delta M_i} {\rm d}M \, \frac{{\rm d}n}{{\rm d}M}(M,z) \,, \tag{4.4}$$

$$\langle Nb \rangle_{ai} = \Omega_{\rm sky} \int_{\Delta z_a} {\rm d}z \, \frac{{\rm d}V}{{\rm d}z \, {\rm d}\Omega} \int_{\Delta M_i} {\rm d}M \, \frac{{\rm d}n}{{\rm d}M}(M,z) \, b(M,z) \,. \tag{4.5}$$

The term S_{ab} is the covariance of the linear density field between two redshift bins,

$$S_{ab} = D(z_a)\, D(z_b) \int \frac{\mathrm{d}^3 k}{(2\pi)^3}\, P_0(k)\, W_a(\mathbf{k})\, W_b(\mathbf{k}), \tag{4.6}$$

where $D(z)$ is the linear growth rate, $P_0(k)$ is the linear matter power spectrum at the present time, and $W_a(\mathbf{k})$ is the window function of the redshift bin, which depends on the shape of the volume probed. The window function for a redshift slice of a light cone is given in Costanzi et al. (2019) and takes the form

$$W_a(\mathbf{k}) = \frac{4\pi}{V_a} \int_{\Delta z_a} \mathrm{d}z\, \frac{\mathrm{d}V}{\mathrm{d}z} \sum_{\ell=0}^{\infty} \sum_{m=-\ell}^{\ell} (\mathrm{i})^\ell\, j_\ell[k\, r(z)]\, Y_{\ell m}(\hat{\mathbf{k}})\, K_\ell, \tag{4.7}$$

where $\mathrm{d}V/\mathrm{d}z$ and V_a are respectively the volume per unit redshift and the volume of the slice, which depend on cosmology. Also, in the above equation $j_\ell[k\, r(z)]$ are the spherical Bessel functions, $Y_{\ell m}(\hat{\mathbf{k}})$ are the spherical harmonics, $\hat{\mathbf{k}}$ is the angular part of the wave-vector, and K_ℓ are the coefficients of the harmonic expansion, such that

$$K_\ell = \frac{1}{2\sqrt{\pi}} \quad \text{for} \quad \ell = 0,$$
$$K_\ell = \sqrt{\frac{\pi}{2\ell+1}}\, \frac{P_{\ell-1}(\cos\theta) - P_{\ell+1}(\cos\theta)}{\Omega_{\mathrm{sky}}} \quad \text{for} \quad \ell \neq 0,$$

where $P_\ell(\cos\theta)$ are the Legendre polynomials.

The shot-noise and sample variance components described above are compared with the corresponding numerical matrices, namely $\hat{C}^{\mathrm{SN}}$ and $\hat{C}^{\mathrm{SV}}$, defined as

$$\hat{C}^{\mathrm{SN}}_{abij} = \hat{N}_{ia}\, \delta_{ab}\, \delta_{ij}, \tag{4.8}$$
$$\hat{C}^{\mathrm{SV}}_{abij} = \hat{C}_{abij} - \hat{C}^{\mathrm{SN}}_{abij}, \tag{4.9}$$

where $\hat{C}_{abij}$ is the total numerical matrix computed with the estimator of Eq. (3.8), and $\hat{N}_{ai}$ are the observed number counts in the a-th redshift bin and i-th mass bin.

4.1.1 Covariance model validation on spherical volumes

We test the Hu & Kravtsov (2003) model in the simple case of a spherically symmetric survey window function, to quantify the level of agreement with the numerical matrix, before applying it to the more complex geometry of light cones. The analytical model is simpler than the one described above, as in this case we consider only the correlation between mass bins at the fixed redshift of a PINOCCHIO snapshot. For the sample covariance, Eq. (4.3) becomes

$$C^{\mathrm{SV}}_{ij} = \langle Nb \rangle_i\, \langle Nb \rangle_j\, \sigma^2_R, \tag{4.10}$$

where the variance σ^2_R is given by Eq. (1.3), which contains the Fourier transform of the top-hat window function (Eq. 1.4).

The numerical matrix is obtained by computing spherical random volumes of fixed radius from the 1000 periodic boxes at a given redshift; the number of spheres was chosen in order to

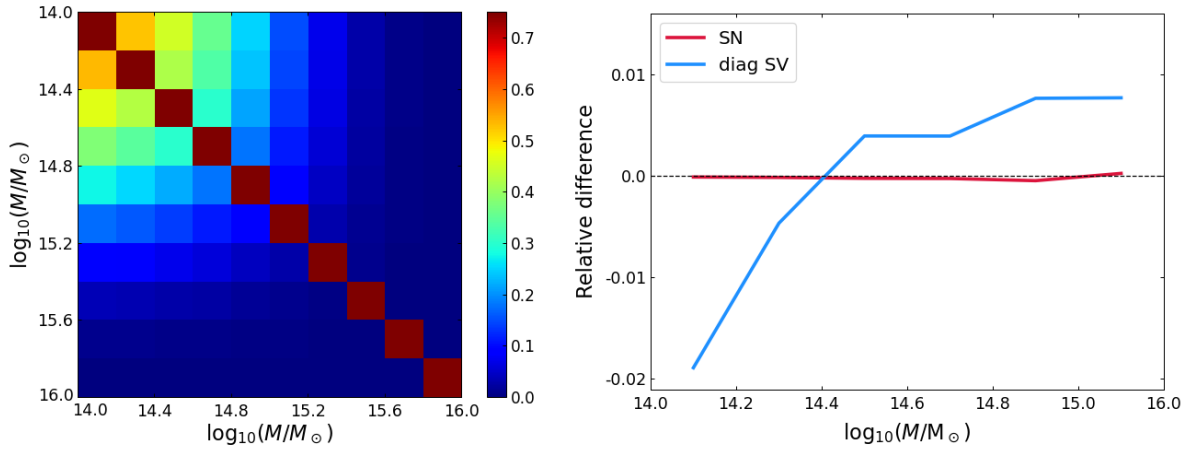

Figure 4.1: Normalized covariance from simulations (*upper triangle*) and analytical model (*lower triangle*), computed for 10^6 spheres of radius $R = 200\,h^{-1}$ Mpc at redshift $z = 0.506$, in 10 log-spaced mass bin in range $M = 10^{14} - 10^{16}\,M_\odot$. In the *left panel*, relative difference between simulations and model for the diagonal elements of the sample covariance matrix (blue) and for the shot-noise (red).

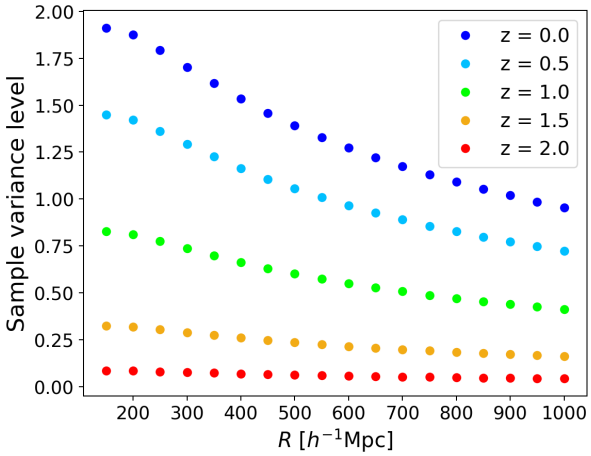

Figure 4.2: Sample variance level with respect to shot-noise, as a function of the filtering scale R, at low mass ($M = 10^{14}\,M_\odot$) and different redshifts.

obtain a high number of (statistically) non-overlapping sampling volumes from each box and thus depends on the radius of the spheres. The resulting covariance, computed by applying Eq. (3.8) to the whole set of sampling spheres, has been compared with the model, with filtering scale R equal to the radius of the spheres.

In Fig. 4.1 we show the resulting normalized matrices, which is defined as

$$R_{abij} = \frac{C_{abij}}{\sqrt{C_{aaii}\,C_{bbjj}}}\,. \tag{4.11}$$

The covariance is computed for $R = 200\,h^{-1}$ Mpc, with 10^3 spherical sub-boxes for each box, for a total of 10^6 samples. The redshift is $z = 0.506$, and we used 10 log-spaced mass bins in the range $M = 10^{14} - 10^{16}\,M_\odot$. For a better comparison, in the right panel we show the normalized difference between simulations and model, for the diagonal sample variance terms

and for shot-noise. We notice that the predicted variance is in agreement with the simulated one with a discrepancy less than 2 percent. We also notice a slight underestimation of the covariance predicted by the model at low masses and a slight overestimation at high masses. We ascribe this to the modeling of the halo bias, whose accuracy is affected by scatter at the few percent level.

In Fig. 4.2 we show the (maximum) sample variance contribution relative to the shot-noise level, as a function of the filtering scale, for different redshifts. The curves, predicted by the model, show that the level of sample variance is lower at high redshift, where the shot-noise dominates due to the small number of objects. Instead, at low redshift ($z < 1$) the sample variance level is even higher than the shot-noise one, and increase as the radius of the spheres decrease; this means that, at least at low redshift where the volumes of the redshift slices in the light cones are small, such contribution cannot be neglected, not to introduce systematics or underestimate the error on the parameter constraints.

4.1.2 Covariance model validation on the light cone

As described in Sect. 3.1, the first step of the validation process consists in the direct comparison of the analytical covariance with the numerical matrix. In Fig. 4.3 we show the normalized covariance matrix, obtained from simulation (upper triangle) and from the model (lower triangle). By looking at the numerical matrix (upper panel), it can be observed that the correlation induced by the sample variance is clearly detected in the block-diagonal covariance matrix (i.e., between mass bins), at least in the low-redshift range where the sample variance contribution is comparable to the shot-noise level. Instead, the off-diagonal and the high-redshift diagonal terms appear affected by the statistical noise, which completely dominates over the weak sample variance (anti-)correlation. In the lower panel we show the same matrix computed with the analytical model: by comparing the two results, we note that the covariance matrix derived from simulations is well reproduced by the analytical model, at least for the diagonal and the first off-diagonal terms, where the former is not dominated by statistical noise.

To ease the comparison between simulations and model and between the amount of correlation of the various components, in Fig. 4.4 we show the covariance from model and simulations for different terms and components of the matrix, as a function of redshift: in blue we show the sample variance diagonal terms (i.e., same mass and redshift bin, $C^{\rm SV}_{aaii}$), in red and orange the diagonal sample variance in two different mass bins ($C^{\rm SV}_{aaij}$ with respectively $j = i+1$ and $j = i+2$), in green the sample variance between two adjacent redshift bins ($C^{\rm SV}_{abii}$, $b = a+1$) and in gray the shot-noise variance ($C^{\rm SN}_{aaii}$). In the upper panel we show the components of the full covariance, in the central panel the covariance normalized with respect to the shot-noise term, and in the lower panel the normalized difference between model and simulations. Confirming what was noticed from Fig. 4.3, the block-diagonal sample variance terms are the dominant sources of error at low redshift, with a signal that rapidly decreases when considering different mass bins (blue, red and orange lines), while shot-noise dominates at high redshift. We also observe that the cross-correlation between different redshift bins produces a small anti-correlation, whose relevance however seems negligible; further considerations about this point will be presented in Sect. 4.2.2.

Regarding the comparison between model and simulations, the figure clearly shows that

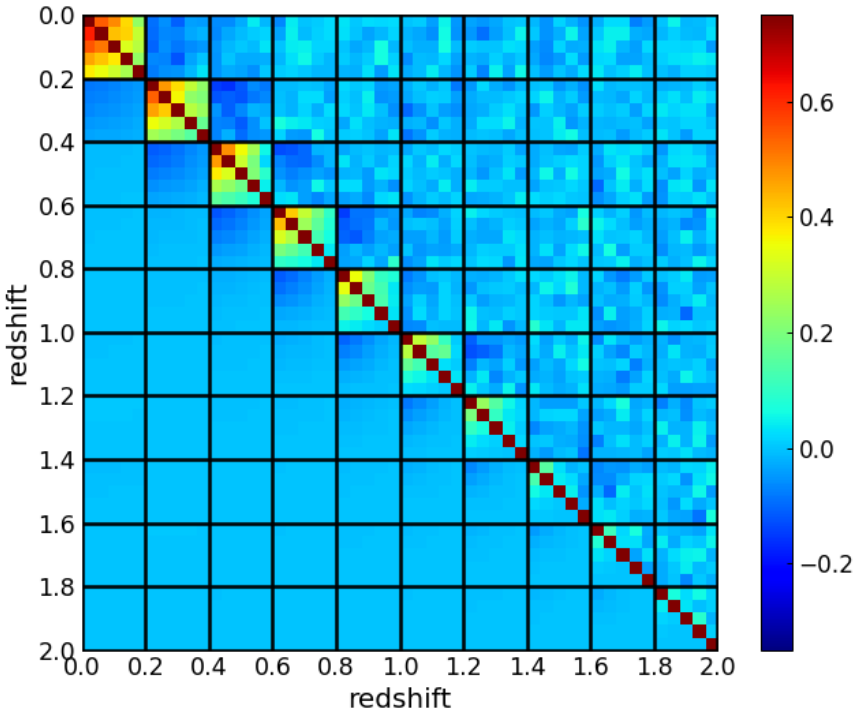

Figure 4.3: Normalized sample covariance between redshift and mass bins (Eq. 4.11), from simulations (*upper triangle*) and analytical model (*lower triangle*). The matrices are computed in the redshift range $z = 0-2$ with $\Delta z = 0.2$ and the mass range $= 10^{14} - 10^{16}\, M_{\odot}$, divided in 5 log-spaced bins. Black lines denote the redshift bins, while in each black square there are different mass bins.

the analytical model reproduces with good agreement the covariance from simulations, with deviations within the 10 percent level. Such agreement was expected, as the modes responsible for the sample covariance are generally very large, well within the linear regime in which the model operates. Part of the difference can be ascribed to the statistical noise, which produces random fluctuations in the simulated covariance matrix. We also observe, mainly on the block-diagonal terms, a slight underestimation of the correlation at low redshift and a small overestimation at high redshift, which are consistent with the under/overestimation of the T10 halo bias shown in the right panel of Fig. 2.3. Nevertheless, this discrepancy on the covariance errors has negligible effects on the parameter constraints, at this level of statistics. This comparison will be further analyzed in Sect. 4.2.2.

4.2 Cosmological parameter estimation

In this section we presents the results of the likelihood analysis. We first determine the best mass and redshift binning scheme for both the Poissonian and Gaussian likelihood functions. Then, we perform the likelihood analysis to assess the impact of the difference between the analytical and numerical covariance on the cosmological posteriors. Finally, we constrain the cosmological parameters $\Omega_{\rm m}$ and σ_8 with different covariance configurations, such as shot-noise versus sample covariance, full versus diagonal matrix, and cosmology dependent versus fixed covariance.

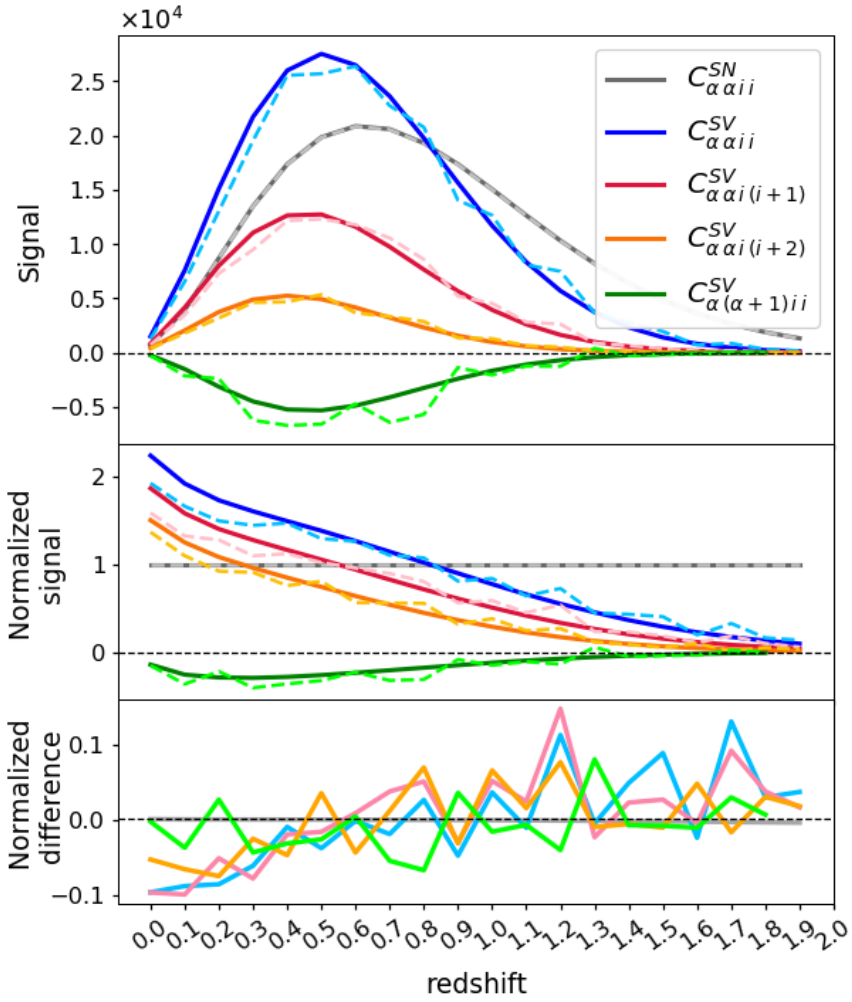

Figure 4.4: Covariance (*upper panel*) and normalized covariance (*central panel*) as predicted by the Hu & Kravtsov (2003) analytical model (solid lines) and by simulations (dashed lines) for different components: diagonal sample variance terms in blue, diagonal sample variance terms in two different mass bins in red and orange, sample variance between two adjacent redshift bins in green and shot-noise in gray. In the *lower panel*, residuals between analytical model and simulations. The matrices are computed in the redshift range $z = 0-2$ with $\Delta z = 0.1$ and the mass range $= 10^{14} - 10^{16}\, M_{\odot}$, divided in 5 log-spaced bins. The curves are represented as a function of redshift, in the first mass bin ($i = 1$).

4.2.1 Binning scheme

The optimal binning scheme should ensure to extract the maximum information from the data while avoiding wasting computational resources with an exceedingly fine binning: adopting too large bins would hide some information, while too small bins can saturate the extractable information, making the analyses unnecessarily computationally expensive. Such saturation occurs even earlier when considering the sample covariance, which strongly correlates narrow mass bins. Moreover, too narrow bins could undermine the validity of the Gaussian approximation due to the low occupancy numbers. This can happen also at high redshift, where the number density of halos drops fast.

To establish the best binning scheme for the Poissonian likelihood function, we analyze

the data assuming four redshift bin widths $\Delta z = \{0.03, 0.1, 0.2, 0.3\}$ and three numbers of mass bins $N_{\rm M} = \{50, 200, 300\}$. In the left panel of Fig. 4.5 we show the FoM as a function of Δz, for different mass binning. Since each result of the likelihood maximization process is affected by some statistical noise, the points represent the mean values obtained from 5 realizations (which are sufficient for a consistent average result), with the corresponding standard error. About the redshift binning, the curve increases with decreasing Δz and flattens below $\Delta z \sim 0.2$; from this result we conclude that for bin widths $\lesssim 0.2$ the information is fully preserved and, among these values, we choose $\Delta z = 0.1$ as the bin width that maximize the information. The change of the mass binning affects the results in a minor way, giving points that are consistent with each other for all the redshift bin widths. To better study the effect of the mass binning, we compute the FoM also for $N_{\rm M} = \{5, 500, 600\}$ at $\Delta z = 0.1$, finding that the amount of recovered information saturates around $N_{\rm M} = 300$. Thus, we use $N_{\rm M} = 300$ for the Poissonian likelihood case, corresponding to $\Delta \log_{10}(M/M_\odot) = 0.007$.

We repeat the analysis for the Gaussian likelihood (with full covariance), by considering the redshift bin widths $\Delta z = \{0.1, 0.2, 0.3\}$ and three numbers of mass bins $N_{\rm M} = \{5, 7, 10\}$, plus $N_{\rm M} = \{2, 20\}$ for $\Delta z = 0.1$. We do not include the case of a tighter redshift or mass binning, to avoid deviating too much from the Gaussian limit of large occupancy numbers. The result for the FoM is shown in the right panel of Fig. 4.5, from which we can state that also for the Gaussian case the curve starts to flatten around $\Delta z \sim 0.2$ and $\Delta z = 0.1$ results to be the optimal redshift binning, since for larger bin widths less information is extracted and for tighter bins the number of objects becomes too low for the validity of the Gaussian limit. Also in this case the mass binning does not influence the results in a significant way, provided that the number of binning is not too low. We decide to use $N_{\rm M} = 5$, corresponding to the mass bin widths $\Delta \log_{10}(M/M_\odot) = 0.4$. According to Eq. (3.10), since we use $N_S = 1000$ and $N_{\rm D} = 100$ (20 redshift bins and 5 mass bins), we correct the precision matrix by a factor of 0.90. Also, from Eq. 3.11 we obtain $f = 1.11$, meaning an 11 percent increase of parameter error bars due to sampling noise. However, since after the firsts off-diagonal terms the other elements are dominated by noise (see Sect. 4.1), we can set them to zero by decreasing this factor around unity.

4.2.2 Likelihood definition

We compare the three likelihood functions listed in Sect. 3.1, i.e., Poissonian, Gaussian with only shot-noise, and Gaussian with shot-noise and sample variance. The cosmological posteriors resulting from likelihood comparison are shown in Fig. 4.6. For the last case we compute the analytical covariance matrix at the input cosmology and compare it with the results obtained by using the covariance matrix from simulations. The corresponding FoM in the $\Omega_{\rm m} - \sigma_8$ plane is shown in Table 4.1. The first two cases look almost the same, meaning that a finer mass binning as the one adopted in the Poisson likelihood does not improve the constraining power compared to the results from a Gaussian plus shot-noise covariance. In contrast, the inclusion of the sample covariance (blue and black contours) produces wider contours (and smaller FoM), indicating that neglecting this effect leads to an underestimation of the error on the parameters. Also, there is no significant difference in using the covariance matrix from simulations or the analytical model, since the difference in the FoM is below the percent level. This result means that the level of accuracy reached by the model is sufficient to obtain an unbiased estimation of parameters in a survey of galaxy clusters having

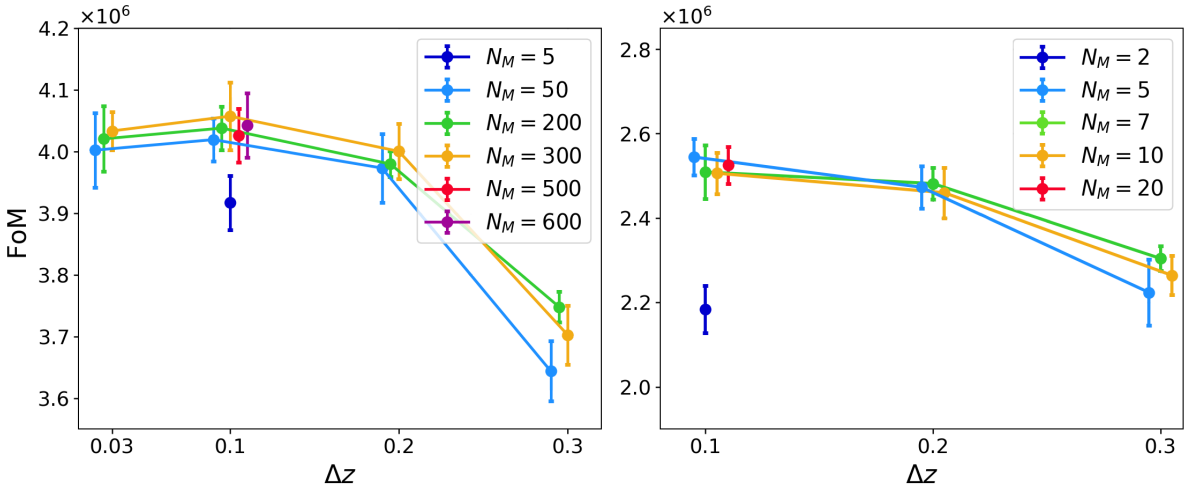

Figure 4.5: Figure of merit for the Poissonian likelihood (*left panel*) and Gaussian likelihood(*right panel*)as a function of the redshift bin widths, for different numbers of mass bins. The points represent the average value over 5 realizations and the error bars are the standard error of the mean. A small horizontal offset has been applied to make the comparison clearer.

sky coverage and cluster statistics comparable to that of the *Euclid* survey. According to this conclusion, we will use the analytical covariance matrix to describe the statistical errors for all following likelihood evaluations.

Having established that the inclusion of the sample variance has a non-negligible effect on parameter posteriors, we focus on the Gaussian likelihood case. In Fig. 4.7 we show the results obtained by using the full covariance matrix and only the block-diagonal of such matrix ($C_{ij\alpha\alpha}$), i.e. considering shot-noise and sample variance effects between masses at the same redshift but no correlation between different redshift bins. The resulting contours present small differences, as can be seen from the comparison of the FoM in Table 4.1: the difference in the FoM between the diagonal and full covariance cases is about half of the effect generated by the inclusion of the full covariance with respect the only shot-noise cases. This means that, at this level of statistics and for this redshift binning, the main contribution to the sample covariance comes from the correlation between mass bins, while the correlation between redshift bins produces a minor effect on the parameter posteriors. However, the difference between the two FoMs is not necessarily negligible: for three parameters, a ∼25% change in the FoM corresponds to a potential underestimate of the parameter error barby ∼10%. The Euclid Consortium is presently requiring for the likelihood estimation that approximations should introduce a bias in parameter error bars that is smaller than 10%, so as not to impact the first significant digit of the error. Because the list of potential systematics at the required precision level is long, one should avoid any oversimplification that alone induces such a sizable effect. The full covariance is thus required to properly describe the sample variance effect at the *Euclid* level of accuracy.

4.2.3 Cosmology-dependent covariance

We also investigate if there are differences in using a cosmology-dependent covariance matrix instead of a cosmology-independent one. In fact, the use of a matrix evaluated at a fixed

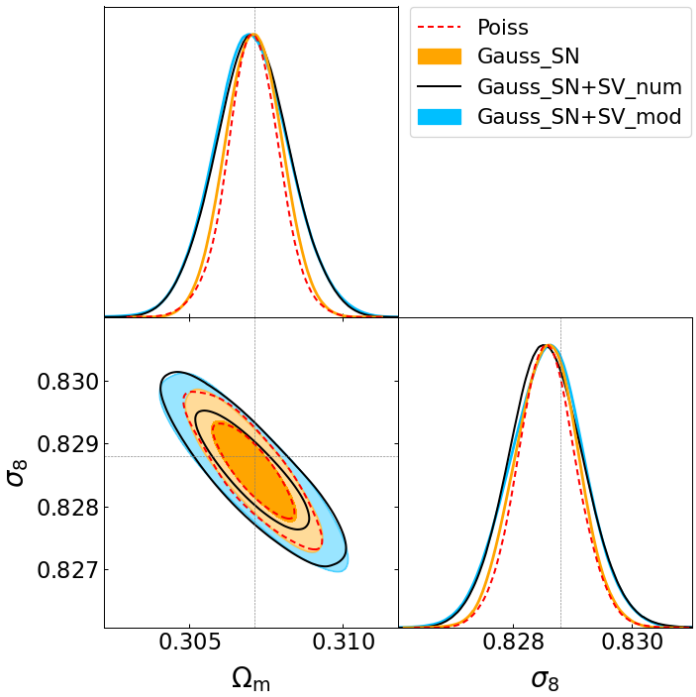

Figure 4.6: Contour plots at 68 and 95 percent of confidence level for the three likelihood functions: Poissonian (red), Gaussian with shot-noise (orange) and Gaussian with shot-noise and sample variance, with analytical (blue) and numerical (black) covariance. The gray lines represent the input values of parameters.

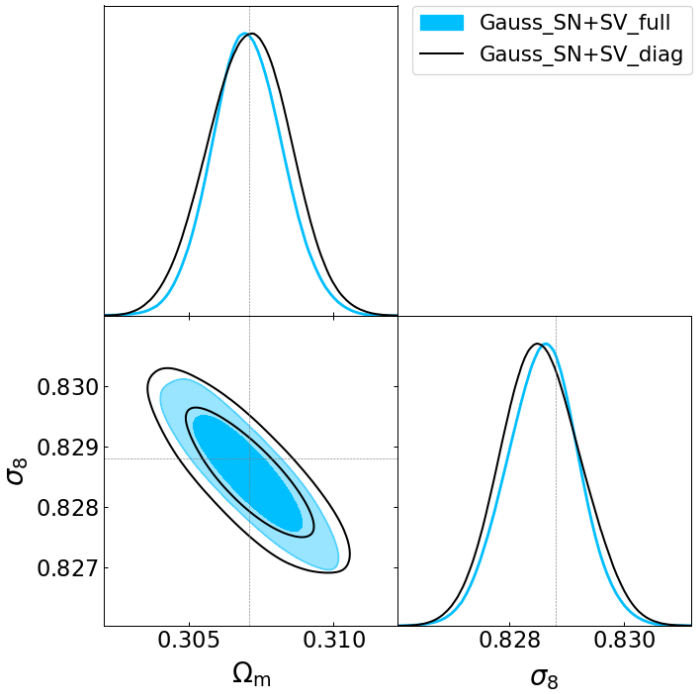

Figure 4.7: Same of Fig 4.6 for the Gaussian likelihood with full (blue) and block-diagonal (black) covariance.

Table 4.1: Figure of merit for the different likelihood and covariance cases. In the third column, percent difference with respect to the numerical Gaussian with full covariance case.

Case	FoM	ΔFoM / FoM$_{\rm num}$
Poissonian	4057193 ± 55001	+ 58 %
Gaussian, SN	4010045 ± 30740	+ 56 %
Gaussian, SN+SV	2561753 ± 34429	–
Gaussian, SN+SV, model	2549035 ± 24251	+ 0 %
Gaussian, SN+SV, model diag	1892933 ± 37907	– 26 %

cosmology can represent an advantage, by reducing the computational cost, but may bias the results. In Fig. 4.8 we compare the parameters estimated with a cosmology-dependent covariance (black contours), i.e., recomputing the covariance at each step of the MCMC process, with the posteriors obtained by evaluating the matrix at the input cosmology (blue contours), or assuming wrong values for $\Omega_{\rm m}$, $\log_{10} A_{\rm s}$ and σ_8, chosen in order to have departures from the fiducial values of the order of 2σ from Planck Collaboration VI. (2020). Specifically, we fix the parameter values at $\Omega_{\rm m} = 0.320$, $\log_{10} A_{\rm s} = -8.625$ and $\sigma_8 = 0.884$ for case *A* (orange contours) and $\Omega_{\rm m} = 0.295$, $\log_{10} A_{\rm s} = -8.685$ and $\sigma_8 = 0.776$ for case *B* (red contours). We notice, also from the FoM comparison shown in Table 4.2, that there is no appreciable difference between the first two cases. In contrast, when a wrong-cosmology covariance matrix is assumed we can find either tighter or wider contours, meaning that the effect of shot-noise and sample variance can be either under- or over-estimated. Thus, the use of a cosmology-independent covariance matrix in the analysis of real cluster abundance data might lead to under/overestimated parameter uncertainties at the level of statistic expected for *Euclid*. On the contrary, the use of a cosmology-dependent covariance does not affect the amount of information obtainable from the data compared to the input-cosmology case. An alternative way to include the cosmology dependence of the covariance is to perform an iterative likelihood analysis, in which a cosmology-independent covariance is updated in every iteration according to the maximum likelihood cosmology retrieved in the previous step (Eifler et al. 2009).

Table 4.2: Figure of merit for the covariance models of Fig. 4.8

Case	FoM	ΔFoM / FoM$_{\rm num}$
Gaussian, model, input cosmo	2540312 ± 55312	–
Gaussian, model, cosmo-dependent	2549035 ± 24251	+ 0 %
Gaussian, model, wrong cosmo A	1571553 ± 33840	– 38 %
Gaussian, model, wrong cosmo B	4526915 ± 135452	+ 78 %

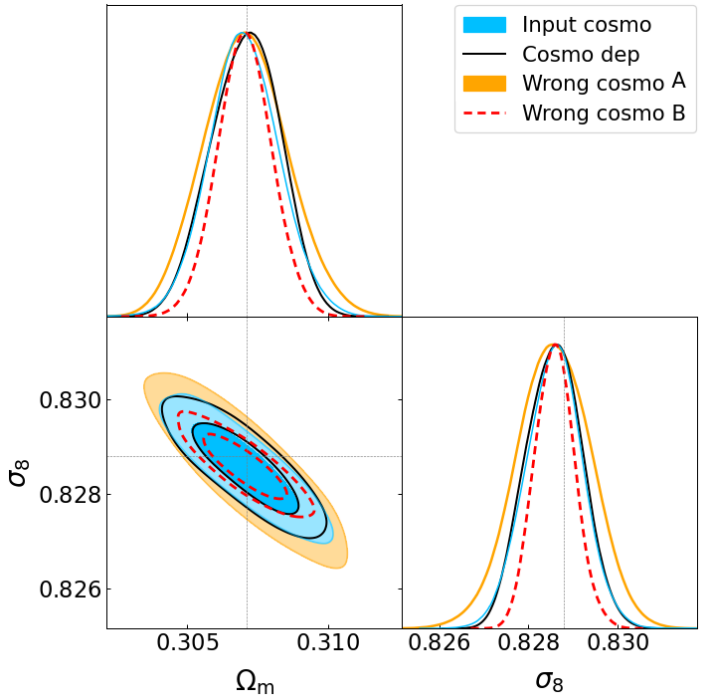

Figure 4.8: Contour plots at 68 and 95 per of cent confidence level for the Gaussian likelihood with: cosmology-dependent covariance matrix (black), covariance matrix fixed at the input cosmology (blue) and covariance matrices computed at two wrong cosmologies, one with $\Omega_m = 0.320$, $\log_{10} A_s = -8.625$, $\sigma_8 = 0.884$ (case A, orange) and one with $\Omega_m = 0.295$, $\log_{10} A_s = -8.685$, $\sigma_8 = 0.776$ (case B, red). The gray dotted lines represent the input values of parameters.

4.2.4 Sample covariance on different surveys

We repeated the likelihood comparison by mimicking other surveys of galaxy clusters, which differ in their volume sampled and their mass and redshift ranges. More specifically, we consider a *Planck*-like (Tauber et al. 2010) and an SPT-like (Carlstrom et al. 2011) cluster survey, both selected through the Sunyaev–Zeldovich effect, which represent two of the main currently available cluster surveys. We also analyze an eROSITA-like (Predehl 2014) X-ray cluster sample, an upcoming survey that, although not reaching the level of statics that will be provided by *Euclid*, will produce a much larger sample than current surveys.

The light cones have been extracted from our catalogs, by considering the properties (aperture, selection function, redshift range) of the three surveys, as provided by Bocquet et al. (2016, see Fig. 4 in their paper)[1]. For simplicity, we neglect the survey footprints, but consider a spherical window-function described by a fixed size opening angle.

The properties of the surveys are as follows:

SPT-like sample: we consider light cones with an area of 2500 deg^2, obtained by extracting a conical volume with an aperture of $\theta = 28.5°$ at the center of our *Euclid* light cones. The resulting catalogs contain $\sim$ 1100 halos with redshifts $z > 0.25$ and masses $M_{500c} \geq 3 \times 10^{14}\,M_\odot$. We analyze the redshift range $z = 0.25 - 1.5$ with bins of width $\Delta z = 0.2$

[1]Masses in the paper are defined at the overdensity $\Delta = 500$ with respect to the critical density; the conversion to virial masses has been performed with the python package `hydro_mc` (https://github.com/aragagnin/hydro_mc).

and the mass range $M_{500c} = 3\times10^{14} - 3\times10^{15}\,M_\odot$, divided in 10 bins for the Poissonian case and in 3 bins for the Gaussian case.

***Planck*-like sample:** we use the redshift-dependent selection function shown in the reference paper. Since the aperture of the *Planck* survey is about twice the size of the *Euclid* one, we stack together two light cones to obtain a *Planck*-like light cone; each of the 500 resulting samples contains ~ 650 objects. We consider the redshift range $z = 0-0.8$ with $\Delta z = 0.25$ and mass range $M_{\rm vir} = 10^{14} - 10^{16}\,M_\odot$; the number of mass bins varies for different redshift bins due to the redshift-dependent selection function, and it is chosen in order to have non-empty bins at each redshift (at least 10 objects per bin).

eROSITA-like sample: we select halos according to the redshift-dependent selection function given by $M_{500c}(z) \geq 2.3\,z \times 10^{14}\,\mathrm{M}_\odot$, with a mass cut at $7\times10^{13}\,\mathrm{M}_\odot$. We analyze the redshift range $z = 0-2$ with $\Delta z = 0.1$ and the mass range $M_{\rm vir} = 10^{14} - 10^{16}\,M_\odot$ with binning defined in order to have non-empty redshift bins, as for the *Planck* case. Also in this case, we stack together four PINOCCHIO light cones to create a full-sky eROSITA light cone, obtaining 250 samples containing $\sim 2\times10^5$ objects. For the purpose of this analysis we did not include any sensitivity mask, to account for the different depths of different surveyed area, due to the eROSITA scanning strategy.

In Fig. 4.9 we show the distribution of cluster masses of the three samples with their selection function, for comparison to the full *Euclid*-like catalog. For both SPT and *Planck*, despite the different selection functions that favor different mass and redshift ranges, the number of objects is low, so we expect shot-noise to be the main source of uncertainty. In contrast, the eROSITA sample contains a larger number of halos, which should lower the level of shot-noise and make the sample variance non-negligible.

In Fig. 4.10 we show the resulting average contours for the three samples, obtained with the Poissonian and Gaussian (full covariance) likelihood functions. for the *Planck* and SPT cases, the contours from the Gaussian case coincide with the Poissonian ones, confirming that for their survey properties, which produce a low number of objects, the shot-noise dominates over the sample variance. Thus, the use of the Poissonian likelihood still represents a good approximation that does not introduce significant differences at the level of statistics given by the present surveys. Moreover, no systematic effects related to uncertainties in the relation between mass and observable (integrated Compton-y parameter in this case), have been included in the analysis. Unlike *Euclid*, for these surveys such an uncertainty is expected to dominate the resulting uncertainty on the cosmological parameters (Bocquet et al. 2016), thus making the choice of the likelihood function conservative, since the posteriors would be larger and the effect of theoretical systematics less significant.

For the eROSITA case, we note that there is a large difference between the Poissonian and the Gaussian case, due to the inclusion of the sample variance effect. Such difference can be ascribed to the mass selection of the survey, which makes the Gaussian contours wider due to the fact that for an X-ray selection, the statistics of counts is dominated by low-redshift/low-mass objects distributed within a relatively small volume. This makes the contribution of sample variance becoming comparable to, or dominant over the shot-noise, and shows that in order to obtain cosmological constraints from the analysis of eROSITA number counts it is necessary to account for sample variance in order not to underestimate the error on parameters.

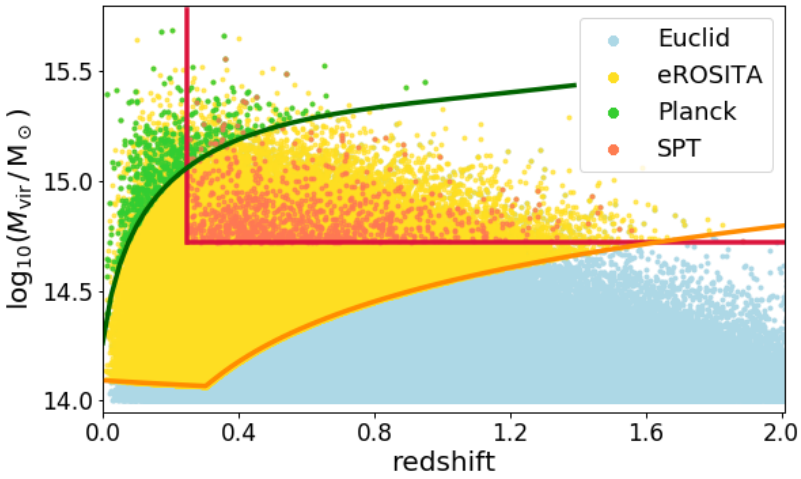

Figure 4.9: Mass distribution of the three samples extracted from a single light cone, with the respective selection functions: *Planck* in green, SPT in red and eROSITA in orange, overplotted to the full *Euclid* sample in blue.

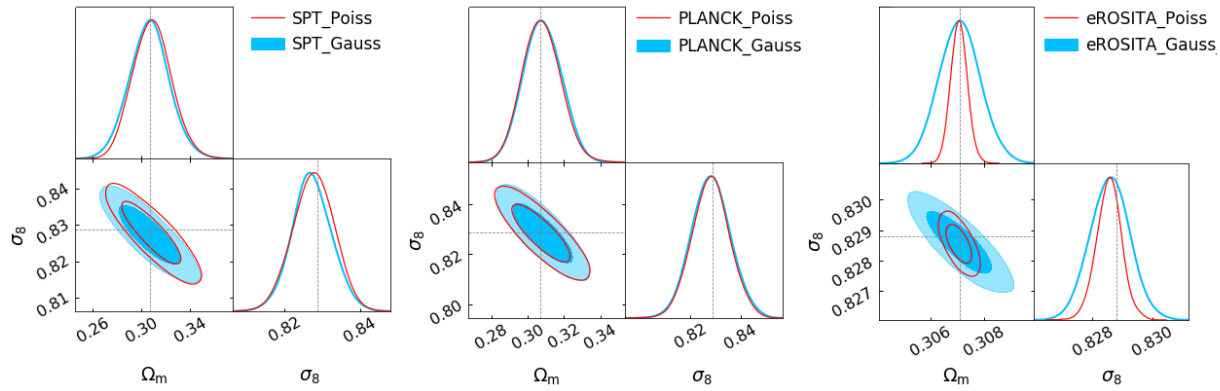

Figure 4.10: Contour plots at 68 and 95 percent of confidence level for the Poissonian (red) and Gaussian with full covariance (blue) likelihood for the SPT-like (*left*), *Planck*-like (*middle*), and eROSITA (*right*) samples samples. The gray dotted lines represent the input values of parameters.

Chapter 5

Cluster clustering results

This work, presented in Euclid Collaboration: Fumagalli et al. (2022), represents a second paper on a series, following Euclid Collaboration: Fumagalli et al. (2021). In this chapter, we validate a semi-analytical model for the covariance of the 2-point correlation function of clusters, by comparison with a numerical matrix. Since the final purpose is to apply this model covariance in the analysis of photometric data, we simply consider the real-space clustering. In fact, the redshift-space distortions of the monopole of the 2PCF are negligible with respect to the distortion produced by the photo-z uncertainties (Veropalumbo et al. 2014; Sereno et al. 2015; Lesci et al. 2022). Note that although *Euclid* will rely mainly on photometric data, their precision and accuracy should allow good estimation of 3D correlation functions. In fact, the mean redshift is expected to be known with an accuracy of $\sigma_{<z>} < 0.002\,(1+z)$, and precision of $\sigma_z < 0.05\,(1+z)$ (Laureijs et al. 2011). These estimates are comparable with the accuracy of surveys already used to study 3D cluster clustering (e.g., Sereno et al. 2015; Lesci et al. 2022).

We test the validity of a Gaussian model, with the addition of a low-order non-Gaussian term. We are interested in understanding whether such a simple model is suitable to describe the covariance for the future survey of galaxy clusters to be extracted from the *Euclid* photometric survey, estimating the impact of the missing high-order terms and of the shot-noise. Then, we focus our attention on the study of the cosmology-dependence of the covariance, to determine if this dependence can help to obtain a more precise estimate of the cosmological parameters. Lastly, we test the impact of mass binning on the cosmological constraints.

This chapter is structured as follows: in Sect 5.1 we describe the measurements of the 2PCF and the associated numerical covariance, and the analytical formalism to describe the 2PCF and its covariance. Then, in Sect. 5.2 we present the results of our analysis, concerning both the validation of the covariance model, and the likelihood forecasts to assess the impact of the covariance on the cosmological posteriors.

5.1 Covariance matrix model

Here we present the measurements and the theoretical predictions for the 2PCF and its covariance. In particular, we present an analytical model for the 2PCF covariance between radial and redshift bins (Sect. 5.1.3), and its extensions with the inclusion of mass binning (Sect. 5.1.4.

5.1.1 2-point correlation function measurements

We consider radial separations in range $r = 20 - 130\,h^{-1}$ Mpc. Such interval includes linear scales, where the bias is almost constant (Manera et al. 2010), plus the BAO peak. We consider all the halos above the mass threshold $M_{\rm vir} = 10^{14}\,M_\odot$, but it is straightforward to generalize the measurement formalism for the mass binning case.

To measure the 2PCF from simulations we use the Landy & Szalay (1993) estimator

$$\hat{\xi}^{as}_{\rm h} = \frac{{\rm DD}_{as} - 2{\rm DR}_{as} + {\rm RR}_{as}}{{\rm RR}_{as}}\,, \tag{5.1}$$

where ${\rm DD}_{as}$, ${\rm DR}_{as}$, ${\rm RR}_{as}$ are the number of pairs in the data-data, data-random and random-random catalogs, respectively, within the a-th redshift bin and s-th separation bin, normalized for the number of objects in the data and random catalogs, $N_{\rm R}$ and $N_{\rm D}$ (Kerscher et al. 2000). The random catalog has been built by randomly extracting objects from each mock and stacking them together, to obtain a catalog with $N_{\rm R} = 10\,N_{\rm D}$ objects randomly distributed inside the light cone volume. The measurement of the correlation function is performed with the `CosmoBolognaLib` package (Marulli et al. 2016).

In Fig. 5.1, we show the measured 2PCF in different redshift bins, as a function of the radial separation, averaged over the 1000 mocks and compared with the analytical prediction of Eq. (5.4). We associate to the average measured quantities an uncertainty given by the standard error on the mean, which is extremely small and thus not visible in the figure. The predicted 2PCF shows an agreement within 10 percent with the numerical one at almost all the separations and redshifts. The differences between the various redshift bins are ascribed to the non-perfect description of the halo bias, that is underestimated at high redshift and overestimated at low redshift. Such difference turns out to shift the cosmological posteriors with respect to the fiducial cosmology, indicating that an accurate description of the halo bias is fundamental to obtain unbiased constraints from the cluster clustering. Since the calibration of the halo bias is beyond the purpose of this paper, we simply compensate this inaccuracy by correcting the prediction for the 2PCF in the likelihood analysis with

$$\xi'_{\rm h}(\boldsymbol{\theta}) = \xi_{\rm h}(\boldsymbol{\theta})\frac{\langle\,\hat{\xi}_{\rm h}\,\rangle}{\xi_{\rm h}(\boldsymbol{\theta}_{\rm fiducial})}\,, \tag{5.2}$$

where $\langle\,\hat{\xi}_{\rm h}\,\rangle$ is the measured 2PCF averaged over the 1000 simulations, and $\boldsymbol{\theta}_{\rm fiducial}$ are the input parameters of the simulations. In this way, by construction, we provide an unbiased description of the 2PCF which contains the correct cosmology dependence.

In Fig. 5.1, we can also notice a smaller additional difference both at small separations and around the BAO scale, due to some non-linear effects. This confirms the correct choice of the radial range, which cannot be further extended to avoid introducing errors due to the limitations of a linear model.

We compute the numerical covariance matrix by using the estimator of Eq. (3.8). In the upper triangle of Fig. 5.2, we show the numerical correlation matrix (Eq. 4.11). The result shows a negligible cross-correlation between redshift bins, since the off-block diagonal terms of the matrix are only populated by noise consistent with zero signal. On the contrary, inside each redshift bin there is a significant non-diagonal correlation, especially at low redshift.

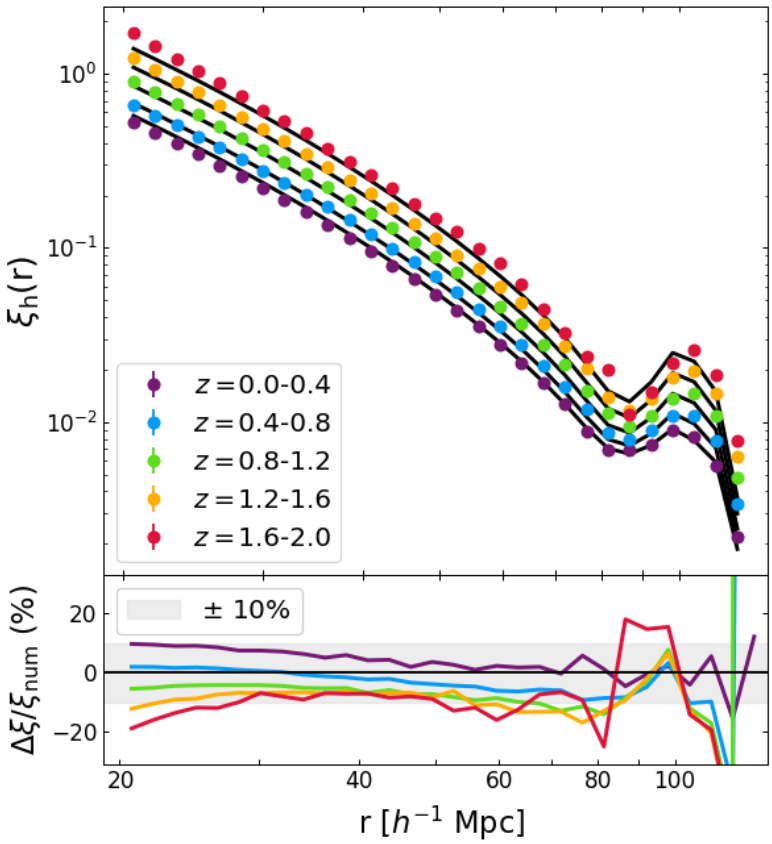

Figure 5.1: *Top panel:* measured (colored dots) and predicted (black lines) 2PCF of halos as a function of the radial separation, for different redshift bins. *Bottom panel:* percent residuals of the model with respect to the numerical function.

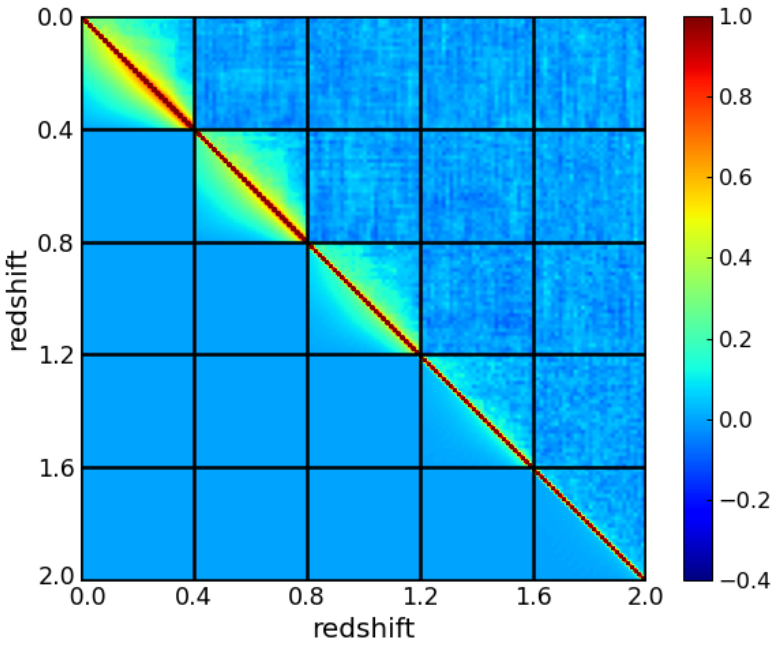

Figure 5.2: Numerical (upper triangle) and analytical (lower triangle) normalized covariance matrices.

5.1.2 2-point correlation function

The halo 2PCF is defined as the Fourier transform of the halo power spectrum; following Eqs. (1.11) and (1.22), we can write

$$\xi_{\rm h}(r,z\,|\,M) = \overline{b}^2(z\,|\,M) \int \frac{{\rm d}k\,k^2}{2\pi^2}\, P_{\rm m}(k,z)\, j_0(kr)\,, \tag{5.3}$$

where $P_{\rm m}(k,z)$ is the matter power spectrum, $j_0(kr)$ is the zero-order spherical Bessel function, r is the comoving radial separation, and $\overline{b}(z\,|\,M)$ is the effective linear bias of Eq. (2.11). For sake of simplicity, we validate our model considering halos with mass above a fixed threshold; in Sect. 5.1.4, we extend the discussion to the case with mass binning. As described in Sect. 1.1.2, we correct such prediction with the IR (Eq. 1.13), to correct for the broadening and the shift of the BAO peak.

The final expression for the real-space 2PCF of halos to be compared with observations is obtained by averaging Eq. (5.3) over the a-th redshift bin and s-th separation bin,

$$\xi_{\rm h}^{as} = \int \frac{{\rm d}k\,k^2}{2\pi^2} \left\langle \overline{b}\,\sqrt{P_{\rm m}(k)} \right\rangle_a^2 W_s(k)\,, \tag{5.4}$$

where $\langle\,\rangle_a$ indicates the average over the redshift bin:

$$\left\langle \overline{b}\,\sqrt{P_{\rm m}(k)} \right\rangle_a = \frac{\int_{\Delta z_a} {\rm d}z\, \frac{{\rm d}V}{{\rm d}z}\, \overline{n}(z)\, \overline{b}(z)\, \sqrt{P_{\rm m}(k,z)}}{\int_{\Delta z_a} {\rm d}z\, \frac{{\rm d}V}{{\rm d}z}\, \overline{n}(z)}\,, \tag{5.5}$$

where ${\rm d}V/{\rm d}z = \Omega_{\rm sky}\, {\rm d}V/{\rm d}\Omega\, {\rm d}z$ is the comoving volume per unit redshift and $\Omega_{\rm sky}$ is the survey area in steradians.[1] $W_s(k)$ represents the spherical shell window function, given by

$$W_s(k) = \int \frac{{\rm d}^3 r}{V_s}\, j_0(kr) = \frac{r_{s,+}^3 W_{\rm th}(kr_{s,+}) - r_{s,-}^3 W_{\rm th}(kr_{s,-})}{r_{s,+}^3 - r_{s,-}^3}\,, \tag{5.6}$$

where $W_{\rm th}(kr)$ is the top-hat window function, V_s is the volume of the s-th spherical shell, and $r_{s,-}$, $r_{s,+}$ are the extremes of the separation bin.

5.1.3 Covariance model

The 2PCF covariance can be obtained as the Fourier transform of the power spectrum covariance. The latter is defined as

$$C_P(\mathbf{k},\mathbf{k}') = \left\langle \left[\hat{P}(\mathbf{k}) - \langle\hat{P}(\mathbf{k})\rangle\right] \left[\hat{P}(\mathbf{k}') - \langle\hat{P}(\mathbf{k}')\rangle\right] \right\rangle\,, \tag{5.7}$$

where

$$\hat{P}(\mathbf{k}) = V\,|\delta_{\mathbf{k}}|^2 - \frac{1}{\overline{n}} \tag{5.8}$$

is the estimator for the halo power spectrum, such that $\langle\hat{P}(\mathbf{k})\rangle = P_{\rm h}(\mathbf{k})$. Here, V is the observed volume and $1/\overline{n}$ is the (Poissonian) shot-noise correction to the halo power spectrum $P_{\rm h}$.

[1] This expression is valid for a conical geometry survey; in more generic cases, the integral over the lightcone volume must take into account the geometry of the survey.

Substituting the power spectrum estimator in Eq. (5.7) we obtain the expression of the power spectrum covariance (Meiksin & White 1999; Scoccimarro et al. 1999)

$$
\begin{aligned}
C_P(\mathbf{k},\mathbf{k}') = \frac{(2\pi)^3}{V}\left[P_\mathrm{h}(k)+\frac{1}{\bar{n}}\right]^2\left[\delta^D(\mathbf{k}-\mathbf{k}')+\delta^D(\mathbf{k}+\mathbf{k}')\right] \\
+\frac{1}{V\bar{n}^2}\Big[P_\mathrm{h}(|\mathbf{k}-\mathbf{k}'|)+P_\mathrm{h}(|\mathbf{k}+\mathbf{k}'|)+2P_\mathrm{h}(k)+2P_\mathrm{h}(k')\Big] \\
+\frac{1}{V\bar{n}}\Big[B_\mathrm{h}(\mathbf{k},-\mathbf{k},0)+B_\mathrm{h}(0,\mathbf{k}',-\mathbf{k})+B_\mathrm{h}(\mathbf{k}+\mathbf{k}',-\mathbf{k},-\mathbf{k}') \\
+B_\mathrm{h}(\mathbf{k}-\mathbf{k}',-\mathbf{k},\mathbf{k}')+B_\mathrm{h}(\mathbf{k},\mathbf{k}'-\mathbf{k},-\mathbf{k}')+B_\mathrm{h}(\mathbf{k},-\mathbf{k}',\mathbf{k}')\Big] \\
+\frac{1}{V}T_\mathrm{h}(\mathbf{k},-\mathbf{k},\mathbf{k}',-\mathbf{k}')+\frac{1}{V\bar{n}^3},
\end{aligned}
\tag{5.9}
$$

where B_h and T_h are, respectively, the bispectrum and the trispectrum of halos, i.e., the three and four-point correlation functions in Fourier space. The first line represents the Gaussian covariance, while the other lines represent the non-Gaussian component. As motivated in Sect. 1.2.2, we do not consider the super-sample covariance.

By Fourier transforming Eq. (5.9) and integrating over separation and redshift bins (Cohn 2006), we obtain a model for the 2PCF covariance in the light cone

$$
\begin{aligned}
C_{asr} = \frac{2}{V_a}\int\frac{\mathrm{d}k\,k^2}{2\pi^2}\left[\left\langle\bar{b}^2P_\mathrm{m}(k)\right\rangle_a+\left\langle\frac{1}{\bar{n}}\right\rangle_a\right]^2 W_s(k)\,W_r(k) \\
+\frac{2}{V_a}\int\frac{\mathrm{d}k\,k^2}{2\pi^2}\left\langle\bar{b}^2P_\mathrm{m}(k)\right\rangle_a\left\langle\frac{1}{\bar{n}}\right\rangle_a^2\frac{W_r(k)}{V_s}\,\delta_{sr},
\end{aligned}
\tag{5.10}
$$

where s,r states for the two separation bins, while the a index is for the average over the redshift bin, and V_a is the volume of the redshift slice. The model in Eq. (5.10) is clearly a simplification of the full covariance matrix based on the following approximations:

- by considering large redshift slices ($\Delta z \gtrsim 0.2$), we assume the cross-correlation between redshift bins to be negligible, as verified from the numerical matrix;
- we neglect the contribution from higher-order correlation functions, only including the lowest order shot-noise contributions of the non-Gaussian covariance, in addition to the Gaussian part;
- we do not include the terms that contribute only at zero separation ($\propto \delta^\mathrm{D}(r_s),\delta^\mathrm{D}(r_r)$), since we consider larger scales;
- we do not account for the survey footprint, but consider a simplistic window-function described by a fixed size opening angle.

5.1.4 Mass binning

We now extend the formalism to take into account the mass binning instead of a simple mass threshold, in order to quantify the amount of information contained in the mass-dependence of the halo bias.

We rewrite Eq. (5.3) as

$$\xi_{\rm h}(r,z\,|\,M,M') = \overline{b}(z\,|\,M)\,\overline{b}(z\,|\,M') \int \frac{{\rm d}k\,k^2}{2\pi^2}\,P_{\rm m}(k,z)\,j_0(kr)\,, \tag{5.11}$$

and all the equations derived in Sect. 5.1.3 are modified according to this change. We obtain the binned 2PCF by integrating Eq. (5.11) over the s-th separation bin, a-th redshift bin, and between i-th and j-th mass bins. Note that now the integrals over mass (Eqs. 2.11 and 2.12) are performed between the edges of each mass bin. The final binned 2PCF takes into account both the auto-correlation inside a single mass interval, and the cross-correlation between halos belonging to two different mass bins

$$\xi_{\rm h}^{asij} = \int \frac{{\rm d}k\,k^2}{2\pi^2} \left\langle \overline{b}_i\,\sqrt{P_{\rm m}(k)} \right\rangle_a \left\langle \overline{b}_j\,\sqrt{P_{\rm m}(k)} \right\rangle_a W_s(k)\,, \tag{5.12}$$

Consequently, the covariance matrix is adapted to account for four kind of terms: auto-correlation between auto-2PCFs ($\propto \xi_{ii}^2$), auto-correlation between cross-2PCFs ($\propto \xi_{ij}^2$), cross-correlation between auto-2PCFs ($\propto \xi_{ii}\xi_{jj}$), and cross-correlation between cross-2PCFs ($\propto \xi_{ij}\xi_{kh}$), and reads as

$$C_{asr}{}^{ijkh} = \frac{C'_{asr}{}^{ikjh} + C'_{asr}{}^{ihjk}}{2}\,, \tag{5.13}$$

where

$$\begin{aligned} C'_{asr}{}^{ijkh} = \frac{2}{V_a} \int \frac{{\rm d}k\,k^2}{2\pi^2} &\left[\left\langle \overline{b}_i\,\overline{b}_j\,P_{\rm m}(k) \right\rangle_a + \left\langle \frac{\delta_{ij}}{\overline{n}_i} \right\rangle_a \right] \\ &\times \left[\left\langle \overline{b}_k\,\overline{b}_h\,P_{\rm m}(k) \right\rangle_a + \left\langle \frac{\delta_{kh}}{\overline{n}_k} \right\rangle_a \right] W_s\,W_r \\ + \frac{2}{V_a} \int \frac{{\rm d}k\,k^2}{2\pi^2} &\left\langle \overline{b}_i\,\overline{b}_k\,P_{\rm m}(k) \right\rangle_a \left\langle \frac{\delta_{ij}}{\overline{n}_i} \right\rangle_a \left\langle \frac{\delta_{kh}}{\overline{n}_k} \right\rangle_a \frac{W_s}{V_r}\delta_{sr}\,. \end{aligned} \tag{5.14}$$

Here the lower indexes a, s, r indicate, respectively, the redshift bin and the two separation bins, while the upper indexes i, j, k, h state for the mass bins. The terms $\overline{n}_i$ and $\overline{b}_i$ are defined as Eqs. (2.12) and (1.22), with integrals computed between the edges of each mass bin instead of the mass threshold.

5.2 Covariance model validation and likelihood forecasts

In this section we present the results of our analysis, concerning both the validation of the model, and the likelihood forecasts. In Sect. 5.2.1 we define the best binning in spatial separation and redshift to extract the cosmological information, while in Sect. 5.2.2 we compare the analytical and numerical matrices, introducing additional parameters to improve the agreement between the two covariances. In Sect. 5.2.3 we study the impact of the non-Gaussian term, and in Sect. 5.2.4 we investigate the effect of the cosmology-dependent matrix. In Sect. 5.2.5 we evaluate the impact of mass binning.

5.2.1 Binning scheme

Before starting the model validation, we are interested in defining the best binning scheme, to properly extract the cosmological information. To this purpose, we perform the likelihood analysis with different combinations of radial and redshift bin widths, for halos above the mass threshold $M_{\rm th} = 10^{14}\ M_\odot$; the mass binning scheme will be studied in Sec. 5.2.5. For this test, we consider only the covariance matrix extracted from numerical simulations, i.e. the reference covariance.

We divide the separation range in different number of bins: $N_{\rm r} = 20, 25, 30, 35$ log-spaced, plus $N_{\rm r} = 25$ linearly spaced, to test the effect of a different spacing. For the redshift binning, we test three bin widths, $\Delta z = 0.2, 0.4, 0.5$, which properly divide the whole redshift range. We do not consider thicker bins, to avoid the inclusion of non-negligible border effects in the pair count procedure.

In Fig. 5.3, we show the FoM for the different number of radial bins, as a function of the redshift bin width. To take into account the uncertainty in the inference process, we consider the average and the standard error computed over 5 realizations for each case. We do not observe a significant difference between the various Δz, since all the cases are statistically in agreement. About the radial binning, the FoM increases as the number of bins increases, suggesting a more efficient extraction of the information, and stabilizes around $N_{\rm r} = 30$, meaning that no more information can be extracted by further increasing the number of radial bins.

In the following analyses, we adopt the values $\Delta z = 0.4$ and $N_{\rm r} = 30$ log-spaced as our baseline redshift and radial bins choice. According to Eq. (3.10), by using $N_S = 1000$ and $N_{\rm D} = 150$ (5 redshift bins and 30 mass bins), we correct the precision matrix by a factor of 0.85. Also, from Eq. (3.11) we obtain $f = 1.17$. To reduce the sampling noise, as described in Sect. 4.1, we manually set to zero the cross-correlation between redshift bins in the numerical covariance, being dominated entirely by noise. The number of noise-affected bins in the matrix is reduced to $N_{\rm D} \sim N_{\rm r} = 30$, providing a correction factor for the inverse covariance of ~ 0.97 and a negligible increase of the parameter error bars ($f \sim 1.03$), allowing us to take the numerical results as reference for the model comparison.

5.2.2 Covariance comparison and parameter fit

In this section, we present the validation of the analytical model of Eq. (5.10), through the comparison with the numerical matrix. The two correlation matrices are represented, respectively, in the lower and upper triangle of Fig. 5.2. For a better comparison, in Fig. 5.4 we show the diagonal and two off-diagonal terms of the matrices as a function of the radial separation, in three redshift bins. We can see that the model (solid lines) correctly reproduces the reference values (shaded areas) only at low redshift, while at intermediate and high redshift it underestimates the numerical matrix by about 30 percent on the diagonal and by about 50 percent on the off-diagonal terms. We ascribe this difference to three factors:

- non-Poissonian shot noise: the Poissonian prediction does not properly describe the shot-noise affecting the halo power spectrum;
- inaccurate halo bias: the inaccuracy of the halo bias prediction propagates in the covariance model; [2]

[2]Note that the correction of Eq. (5.2) does not apply to the covariance prediction. However, this does not

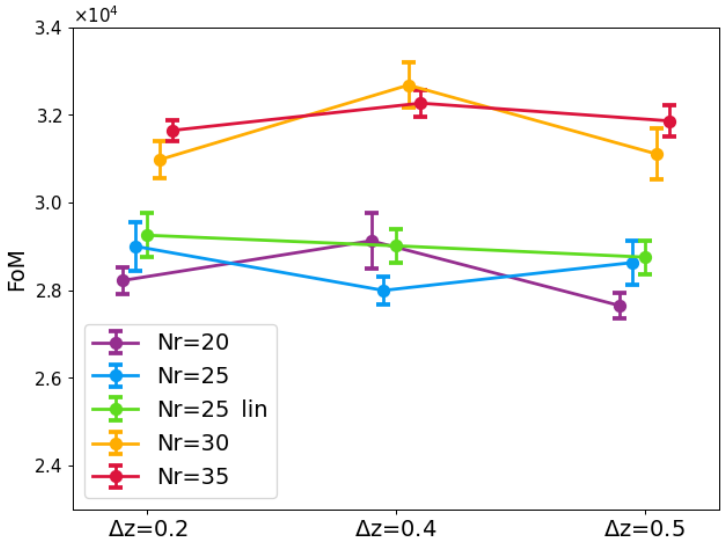

Figure 5.3: Figure of merit in the $\Omega_{\rm m}-\sigma_8$ plane for different numbers of radial bins, as a function of the redshift bin width. A small horizontal displacement has been applied to make the comparison clearer.

- lack of higher-order terms: the contribution of tri- and four-point functions is not negligible. This effect especially regards the terms weighted by $1/\bar{n}$, that would give a significant contribution at high redshift, where the shot noise increases.

We correct the inaccuracy of the predicted covariance by including some parameters in the model. More specifically, we modify Eq. (5.10) by adding three free parameters $\{\alpha,\beta,\gamma\}$

$$
\begin{aligned}
C_{asr} = \frac{2}{V_a}\int \frac{{\rm d}k\,k^2}{2\pi^2}\left[\left\langle(\beta\bar{b})^2 P_{\rm m}(k)\right\rangle_a + \left\langle\frac{1+\alpha}{\bar{n}}\right\rangle_a\right]^2 W_s(k)\,W_r(k) \\
+ \frac{2}{V_a}\int \frac{{\rm d}k\,k^2}{2\pi^2}\left\langle(\beta\bar{b})^2 P_{\rm m}(k)\right\rangle_a \left\langle\frac{1+\gamma}{\bar{n}}\right\rangle_a^2 \frac{W_r(k)}{V_s}\,\delta_{sr}\,,
\end{aligned}
\tag{5.15}
$$

where β corrects for the halo bias inaccuracy, and α and γ correct for the non-Poissonian nature of the shot-noise in the main and secondary term, respectively; the different weighting of the shot-noise correction should also account for the effect of higher-order terms. We fit such parameters from simulations in each redshift bin, assuming a constant value with scale and redshift in each slice. We adopted the method described in Fumagalli et al. (2022, see Sect. 3.3) to fit the free parameters α, β, and γ. In short, we constrain the covariance through the maximization of a Gaussian likelihood evaluated at the fiducial cosmology, with free covariance parameters. The best-fit covariance thus obtained is the one that best follows a χ^2 distribution with respect to the observed data. In the left panel of Fig. 5.5 we show the χ^2 distributions computed with respect to the measurements from the 1000 lightcones, for the three covariance matrices: numerical covariance in blue, analytical covariance in green and analytical covariance with fitted parameters in red. In Table 5.1 we report the mean and standard deviation for each distribution, with the corresponding 1σ uncertainties computed

affect our results, as we treat the bias in the 2PCF and the one in the covariance model as two different quantities.

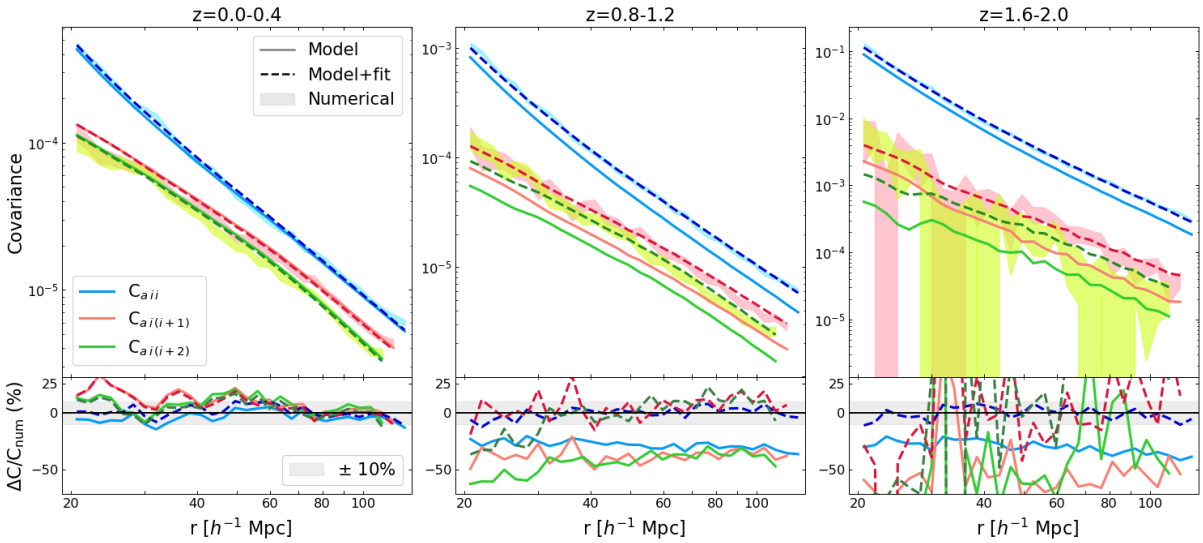

Figure 5.4: Numerical (shaded areas), analytical (solid lines), and analytical with fitted parameters (dashed lines) covariance matrices as a function of the radial separation, in three redshift bins (from the left to the right panels: $z = 0.0 - 0.4$, $z = 0.8 - 1.2$, $z = 1.6 - 2.0$). Different colors represent different components of the matrix: diagonal elements in blue, first off-diagonal elements in red and second off-diagonal elements in green. In the subpanels, percent residuals of the model covariance with respect the numerical matrix.

Table 5.1: χ^2distribution test values.

	mean	variance
Numerical	149.0 ± 0.5	255.0 ± 11.7
Model	195.0 ± 0.7	494.0 ± 22.8
Model + fit	152.0 ± 0.6	302.0 ± 13.9
Reference	150	300

Table 5.2: Power spectrum best-fit parameters.

Redshift	α	β
0.5	0.012 ± 0.010	0.987 ± 0.002
1.0	0.114 ± 0.004	1.006 ± 0.002
1.5	0.104 ± 0.002	1.013 ± 0.002
Reference	0	1

with the bootstrap technique. By construction, we expect the numerical matrix to perfectly follow the reference distribution. While this is true for the mean value, the variance differs by $\sim 4\sigma$ from the expected value; such discrepancy is ascribed to the noise in the numerical matrix that tightens the distribution. Anyway, since the errors are quite small, this distribution can be considered in good agreement with the expected one. Instead, the model of Eq. (5.10) produces a distribution that is several σ off the expectation, confirming that this model is not suitable for describing the covariance of data. Finally, the fitted matrix turns out to be in good agreement with the reference distribution, both for the mean value and the variance. This proves the goodness of our fit and ensures that the resulting model is able to correctly describe the covariance as well as, if not better than, the numerical matrix. Note that the fit was performed using all 1000 available simulations; despite of this, we verified that the fitting process provides consistent results even with only 100 simulations, confirming what was found in Sect. 3.3.

In Table 5.3, we show the best-fit values of the parameters in each redshift slice[3]: in most

[3]We show the value of best-fit parameters for general considerations. However, the value of these parameters

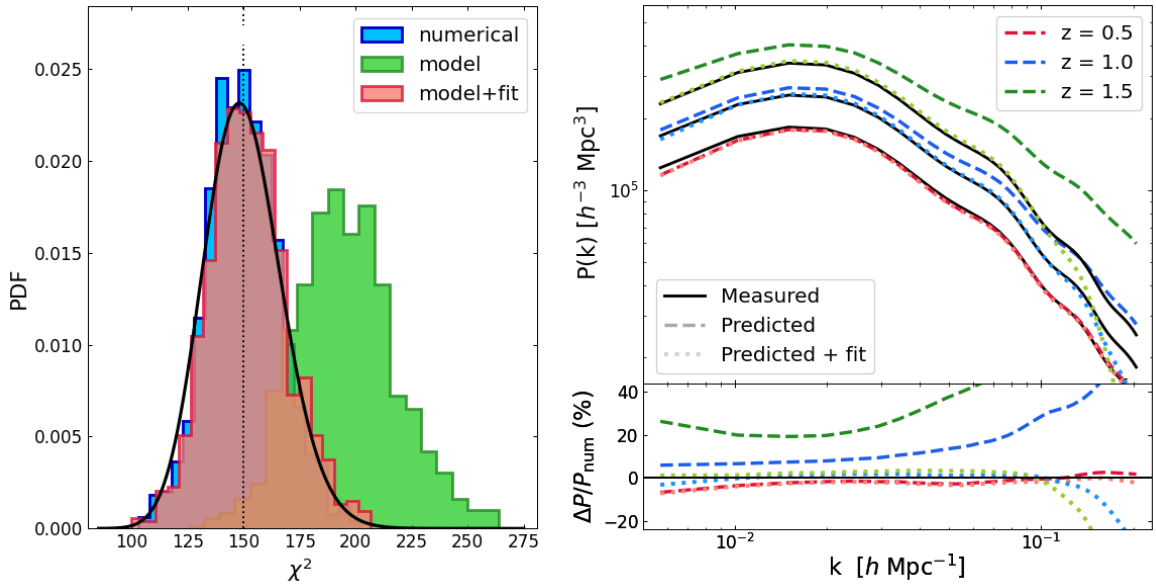

Figure 5.5: *Left panel:* χ^2 distribution for the numerical, analytical and analytical with fitted parameters covariance matrices. Reference distribution in black. *Right panel:* measured (black solid lines), predicted (darker dashed lines) and fitted (lighter dotted lines) halo power spectrum for boxes at three different redshifts. In the bottom panel, percent residuals of the predictions with respect to the numerical one.

of the cases the best-fit is not in agreement with the reference values. The correction of the halo bias is in line with the expectation (i.e., $\beta < 1$ at low redshift to correct an overestimated bias, and $\beta > 1$ at high redshift to correct an underestimated bias); anyway, at redshift $z \gtrsim 1$, the values of β overestimate the 2PCF correction of Eq. (5.2) by a factor from 5 to 30 percent depending on redshift. The shot-noise corrections also show conflicting results: the Gaussian term of the covariance seems to prefer a super-Poissonian shot-noise ($\alpha > 0$), while the non-Gaussian term is characterized by a sub-Poissonian shot-noise ($\gamma < 0$). Such contrasts suggest that the parameters actually absorb the effect of the wrong or missing terms of the covariance, instead of simply describing the halo bias correction or the deviation from the Poissonian prediction of the shot-noise.

To better explain the different values of these parameters with respect to their expectation, we study the power spectrum, i.e. the quantity that is both affected by bias and shot-noise. To avoid complications due to the redshift integration and the geometry of the survey, we measure the power spectrum from the 1000 cubical boxes described in Sect. 2.3. We consider three redshifts $z = 0.5, 1.0, 1.5$.

We compute the analytical total halo power spectrum as

$$P_{\rm h,tot}(k) = \bar{b}^2 P_{\rm m}(k) + \frac{1}{\bar{n}}, \tag{5.16}$$

where the matter power spectrum is calculated by means of the `CAMB` code (Lewis et al. 2000). We compare such quantity with the measured total power spectrum averaged over the 1000 boxes, for the three redshift values.

is not universal, but depends on the properties of the survey and must be fitted for each specific case.

Table 5.3: Best-fit values for the covariance model parameters introduced in Eq (5.15).

Redshift	α	β	γ
0.0 – 0.4	0.111 ± 0.008	0.979 ± 0.008	−0.027 ± 0.047
0.4 – 0.8	0.109 ± 0.008	1.055 ± 0.009	−0.083 ± 0.037
0.8 – 1.2	0.134 ± 0.008	1.181 ± 0.013	−0.129 ± 0.027
1.2 – 1.6	0.157 ± 0.008	1.270 ± 0.022	−0.199 ± 0.024
1.6 – 2.0	0.188 ± 0.008	1.460 ± 0.045	−0.263 ± 0.026
Reference	0	1	0

In the right panel of Fig. 5.5 we show the comparison of the measured and predicted power spectra (for a better comparison, we show the halo power spectrum, i.e. the total one minus the shot-noise): while at low redshift the two quantities are in agreement on almost all the scales, we can observe a clear deviation between the observed and predicted spectra that increases with redshift, up to more than 20 percent. We try to correct these discrepancies by fitting the two parameters $\{\alpha,\beta\}$, which account respectively for the correction to shot-noise and halo bias, directly from the power spectrum; the best-fit are shown in Table 5.2, and the resulting power spectra are shown in Fig 5.5 (dotted lines). We obtain an agreement of the fitted power spectra within 5 percent level at all the linear scales, at all redshifts. Nevertheless, the values deviate by several σ from the best-fit parameters found from the covariance fit in the corresponding redshift intervals (see Table 5.3). This confirms that the parameters in the covariance, in addition to correct for the wrong prediction of bias and shot-noise, also absorb the effect of the missing higher-order terms in the model.

The dashed lines in Fig. 5.4 show the predictions of the model modified by the introduction of the additional parameters. Now, the analytical covariance correctly describes the numerical results at all redshifts, with an accuracy of about 10 per cent. Note that even if the reference matrix on which the fit is performed is not perfectly accurate, due to sampling noise; this is not a problem for the fit process, which in fact allows the model to correctly reproduce the expected matrix without replicating that noise.

In Fig. 5.6, we show the posterior distributions resulting from the likelihood analysis with three different covariance configurations: numerical, model of Eq. (5.10) and model of Eq. (5.15) with the best-fit parameters shown in Table 5.3. As expected, the underestimated level of covariance provided by the original model translates in tighter posteriors with respect to the numerical case. On the contrary, the model corrected for the additional parameters recovers with good accuracy the result of the numerical matrix. The FoM obtained from these posteriors and the percent difference with respect to the numerical case are shown in Table 5.4: the addition of parameters decreases the deviation in the FoM from about 40 percent to only 5 percent.

5.2.3 Non-Gaussian covariance

We test here the effect of the low-order non-Gaussian term (i.e., second line in Eq. 5.10), to evaluate its impact with respect to the Gaussian covariance. In fig. 5.7 we compare the numerical matrix with the analytical model, with parameters fitted both from the full model (dashed lines), and from the Gaussian model, i.e., setting to zero the non-Gaussian term and

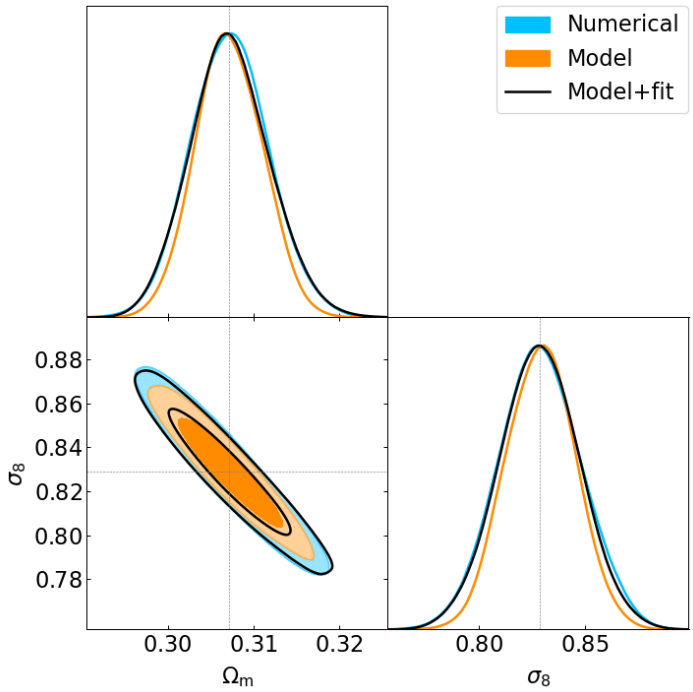

Figure 5.6: Contour plots at 68 and 95 percent of confidence level for the numerical (blue), analytical (orange) and analytical with fitted parameters (black) matrices. Dotted gray lines represent the fiducial cosmology.

fitting α and β (solid lines). Since such a term only contributes on the diagonal elements, we compare the variance in three different redshift bins. The figure clearly shows that the Gaussian model is unable to properly describe the numerical covariance, for two reasons: first, the non-Gaussian term gives a significant contribution at low scales, especially at high redshift, and neglecting this term leads to an underestimation of the diagonal terms by a factor up to 50 per cent. Second, the Gaussian model does not have enough degrees of freedom to provide a good fit and it is not able to absorb the effect of the missing terms, producing a wrong fit also at larger scales.

This differences in the Gaussian fit have an impact on the cosmological posteriors, with deviations in the FoM of about the 20 percent with respect to the numerical covariance case (see Table 5.4).

Since the importance of this term is mainly driven by the factor $\bar{n}^{-2}$ that grows with decreasing number of objects, we expect that the impact of this term increases when considering higher redshifts, as well as higher mass-limits. The same trend would apply to the bispectrum terms, due to the factor $\bar{n}^{-1}$, while the trispectum contribution should be less relevant, given the absence of such a factor.

5.2.4 Cosmology-dependent covariance

The impact of the cosmology dependence of the covariance in the likelihood analysis is a topic that has been largely discussed in literature. Several works (e.g. Krause & Eifler 2017; Eifler et al. 2009; Morrison & Schneider 2013; Blot et al. 2020; Euclid Collaboration: Fumagalli et al. 2021) have demonstrated that evaluating the covariance matrix at a wrong cosmol-

Table 5.4: Figure of merit for the different covariance cases. In the third column, percent difference with respect to the numerical case.

Case	FoM	ΔFoM / FoM$_{\rm num}$
Numerical	32681 ± 514	–
Model	45510 ± 413	+ 39 %
Model + fit	34307 ± 623	+ 5 %
Model + fit, Gauss	38855 ± 437	+ 19 %
Cosmo-dependent	86155 ± 670	+ 151 %

ogy would lead to a wrong estimation of the cosmological posteriors.

To avoid this, the correct way to perform the parameter inference from a Gaussian likelihood is to use a cosmology-dependent covariance, i.e., to recompute the matrix at each step of the MCMC process. The situation gets more complicated if the Gaussian likelihood is just an approximation of the true distribution of the data, as for the 2PCF. As pointed out by Carron (2013), in this case the use of a cosmology-dependent covariance may lead to a wrong estimation of the posteriors amplitude. To avoid this, one can use the iterative approach, which consists in running the MCMC with a fixed covariance computed at some fiducial cosmology, then using the best-fit parameters to construct a new covariance matrix and re-running the MCMC process. This can be iterated until convergence of the cosmological posteriors. It should be noted that, in the case of approximate likelihood, even this second method may not correctly estimate the posteriors amplitude.

Given this premise, we perform a simple test to establish which is the most correct method to extract the cosmological information from the 2PCF, with the likelihood and the covariance model proposed in this work. We analyze 100 light cones in two different ways: i) we apply the iterative method starting with a fiducial cosmology of $\Omega_{\rm m} = 0.30$ and $\sigma_8 = 0.77$, and verifying that a single step is sufficient to achieve convergence; ii) we use a cosmology-dependent covariance. The left and middle panel of Fig. 5.8 represents the result of the two analysis: dots are the best fit values for each light cone, compared to the mean contours obtained through Eq. (3.6). We can see the two cases exhibit a different best-fit distribution: analyzing the light cones with the cosmology-dependent covariance yields values that are more concentrated around the input cosmology, compared to the fixed covariance case, which instead presents a more scattered distribution. In both cases the individual values are in agreement with the mean distribution, making it difficult to determine which of the two analyses is more correct. Thus, for a better comparison, we compute the Deviance Information Criterion (DIC, Spiegelhalter et al. 2002) from the resulting posteriors, treating the problem as a model selection problem. The DIC is defined as

$$\mathrm{DIC}(m_i) = \langle \chi^2 \rangle + p_D \,, \tag{5.17}$$

with

$$p_D = \langle \chi^2 \rangle - \chi^2(\boldsymbol{\theta}_{\rm input}) \,. \tag{5.18}$$

Here $\chi^2 = -2 \ln \mathcal{L}(\mathbf{d}|m_i(\boldsymbol{\theta}), C)$ estimates the goodness of the fit and p_D is the Bayesian complexity, measuring the effective complexity of the model. The average is performed over the

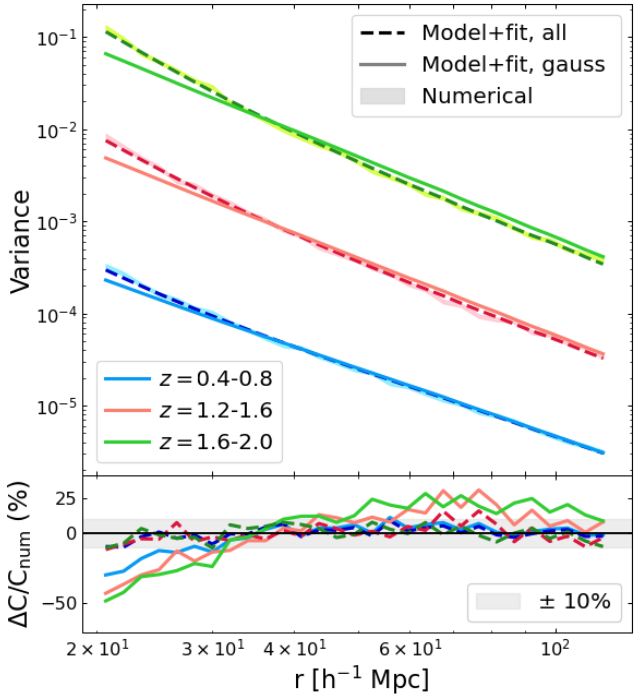

Figure 5.7: Variance as a function of the radial separation for three redshift bins, for the numerical matrix (shaded area), Gaussian analytical matrix (solid lines) and full analytical matrix (dashed lines, corresponding to the dashed lines of Fig. 5.4).

posteriors volume. Given two models $m_1(\boldsymbol{\theta})$ and $m_2(\boldsymbol{\theta})$, the difference $\Delta\text{DIC} = \text{DIC}(m_2) - \text{DIC}(m_1)$ is interpreted using the Jeffreys' scale presented in Grandis et al. (2016): $\Delta\text{DIC} = 0$ means that none of the two models is preferred, $-2 < \Delta\text{DIC} < 0$ that there is "no significant" preference for m_2, $-5 < \Delta\text{DIC} < -2$ a "positive" preference for m_2, $-10 < \Delta\text{DIC} < -5$ a "strong" preference for m_2, and $\Delta\text{DIC} < -10$ indicates a "decisive" preference for m_2. By defining $\Delta\text{DIC} = \text{DIC}_{\text{cosmo}} - \text{DIC}_{\text{bestfit}}$ for each of the 100 simulations, we obtain the distribution shown in the right panel of Fig. 5.8, characterized by a mean value $\langle\Delta\text{DIC}\rangle_{\text{sims}} = -11.5 \pm 1.6$. The analysis of the ΔDIC indicates that the model with cosmology-dependent covariance is statistically preferred over the iterative method.

To further explore the comparison between the fully cosmology-dependent likelihood analysis and the iterative method, we generate 100 synthetic light cones starting from a Gaussian distribution, with amplitude given by the covariance model at the input cosmology. In this way, we ensure that the Gaussian distribution is the true likelihood describing the data, and not just an approximation. The number of mocks was chosen so as to have enough statistics to compare the results. We repeat the analysis of the 100 light cones, finding a mean value $\langle\Delta\text{DIC}\rangle_{\text{synth}} = -13.7 \pm 2.1$, to be compared with the value from the analysis of the 100 PINOCCHIO mocks, i.e., $\langle\Delta\text{DIC}\rangle_{\text{sims}} = -11.5 \pm 1.6$. Moreover, by comparing the FoM of the cosmology dependent covariance and the iterative method, we obtain a mean variation of $\langle\Delta\text{FoM}\rangle_{\text{synth}} = 176 \pm 38\,\%$ for the synthetic catalogs, and $\langle\Delta\text{FoM}\rangle_{\text{sims}} = 142 \pm 33\,\%$ for the PINOCCHIO mocks. Both the DIC and the FoM analyses indicate that the two analysis are fully consistent. Although this result still does not define which posteriors are correct in case the true likelihood is unknown, it shows that at least for this particular analysis the narrowing of the posteriors does not primarily depends on some wrong approximation of the likelihood

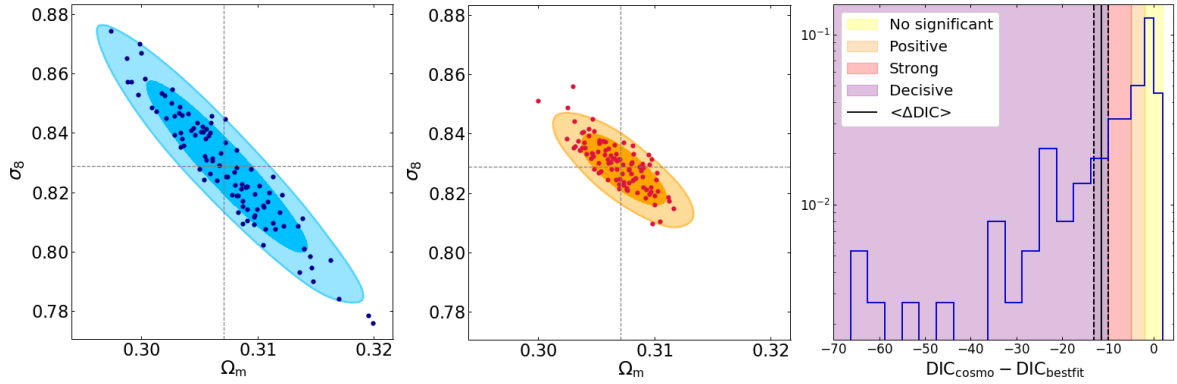

Figure 5.8: *Left and middle panels:* Contour plots at 68 and 95 percent of confidence level for input-cosmology covariance (blue), and the cosmology-dependent covariance (orange), obtained from the mean likelihood (Eq. 3.6). Dots are the best-fit values from 100 single light cones. Gray lines represent the input parameters. *Right panel:* ΔDIC distribution of the 100 light cones. Associated mean and error on the mean are highlighted as solid and dashed black lines. Colored regions represent the Jefferys' scale used to interpret the results.

function. In other words, when a Gaussian likelihood is assumed, it is possible to actually extract information from the cosmology dependence of the covariance.

After verifying that the use of the cosmology-dependence covariance is, from a statistical point of view, the most correct way to analyze the data, we study the impact on the (average) cosmological posteriors of a wrong-cosmology covariance and a cosmology-dependent covariance, with respect to the input covariance case. In Fig. 5.9 the posteriors obtained by fixing the covariance matrix at three different cosmologies. More specifically, we compare the input-parameter case ($\Omega_m = 0.307$, $\sigma_8 = 0.829$) with two choices of parameter combinations, i.e. $\Omega_m = 0.320$, $\sigma_8 = 0.775$ and $\Omega_m = 0.295$, $\sigma_8 = 0.871$, located approximately at the extremes of the 2σ contours of the input-cosmology posteriors, along the degeneracy direction (indicated by dots in the figure, with respect to the orange contours). Note that such deviations from the fiducial cosmology are comparable with the 2σ values from Planck Collaboration VI. (2020), which represents the state of the art in the cosmological constraints. We observe that using the covariance matrix computed at a wrong cosmology has a significative effect on the cosmological posteriors, with variations in the FoM of the order of $\sim 30 - 40\,\%$. We note that the recovered posterior distributions differ even if the two adopted cosmologies lie along the $\Omega_m - \sigma_8$ degeneracies. This result suggests that the cosmological dependence of the covariance matrix is different from that of the 2PCF.

To test this hypothesis we compare the derived posterior distribution on the cosmological parameters for the following three analyses:

i) We compute the covariance at the input cosmology and evaluate the expected 2PCF as a function of cosmological parameters. This case corresponds to the standard likelihood analysis with fixed covariance, where all the cosmological information is encapsulated in the expected value of $\xi(r, z)$.

ii) We evaluate the expected 2PCF at the fixed input cosmology, but let the covariance matrix vary as a function of cosmological parameters. In this way we evaluate the cosmology dependence of the covariance alone;

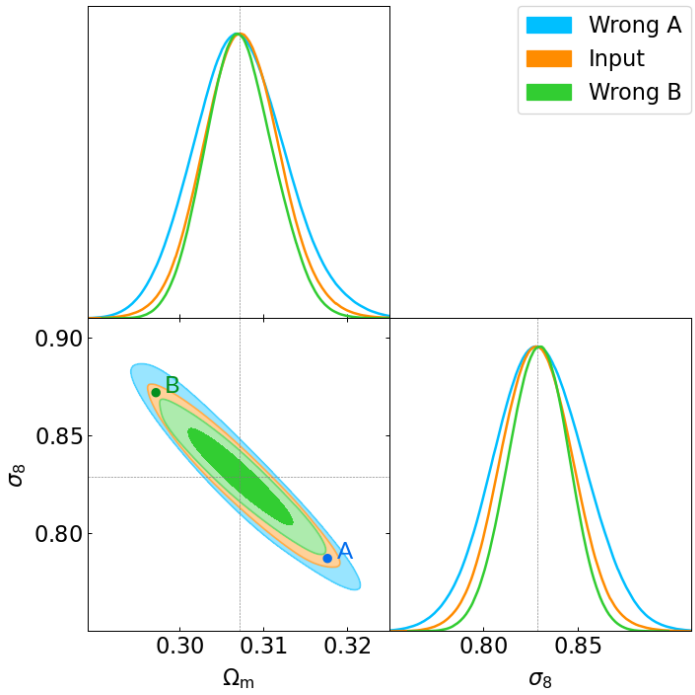

Figure 5.9: Contour plots at 68 and 95 percent of confidence level for input-cosmology covariance (orange), and two wrong-cosmology cases: A) $\Omega_m = 0.320$, $\sigma_8 = 0.775$ in blue, and B) $\Omega_m = 0.295$, $\sigma_8 = 0.871$ in green. Gray lines represent the input parameters.

iii) We compare the measured and expected clustering signal where both the mean value and its covariance matrix are varying as a function of cosmological parameters. This case corresponds to the full forward-modeling approach.

When adopting a cosmology-dependent covariance, we assume the fitted parameters α, β, and γ to be cosmology-independent. This limitation is due to the fact that we only have simulations for one cosmology on which perform the fit. The impact of such dependency will be verified in detail in future analyses. However, we expect that neglecting the cosmology dependence of these parameters would introduce a negligible error with respect to the one that we would introduce by not including these parameters at all.

Figure 5.10 clearly highlights a tilted degeneracy direction between Ω_m and σ_8 posteriors of cases *i*) and *ii*), indicating that covariance and 2PCF have a different cosmological dependencies (blue versus orange contours). As a result, by varying the cosmological parameters in both the quantities returns tighter constraints, with a FoM improved by about 150 percent with respect to the numerical case, which reflects the standard case *i*) likelihood analysis (see Table 5.4).

This different dependence on cosmology can be explained by noting that, unlike the mean value, the covariance of the 2PCF depends on the shot-noise, which is proportional to the inverse of the integrated mass function. Letting the cosmology vary also in the covariance thus makes it possible to extract all the information contained in the clustering of the clusters, and not only in the 2PCF itself.

For some additional considerations about the cosmology-dependence of the covariance, we repeat the test described above for the cluster number counts. As shown in Sect. 4.2.3 that the use of a fixed covariance in the likelihood analysis can bring an under/overestimation

of the FoM by more than 40 percent, if the cosmology at which the covariance is evaluated deviates from the fiducial values of an amount of 2σ from Planck Collaboration VI. (2020). Instead, there are not significant differences between the input and varying covariance cases, unlike the clustering case (Fig. 5.10). As shown by the posteriors in Fig. 5.11, for number counts the mean value is much more constraining than its covariance, making the degeneracy direction of the latter totally irrelevant. In this case, thus, the covariance only contributes as an estimation of the uncertainty, without adding further independent information.

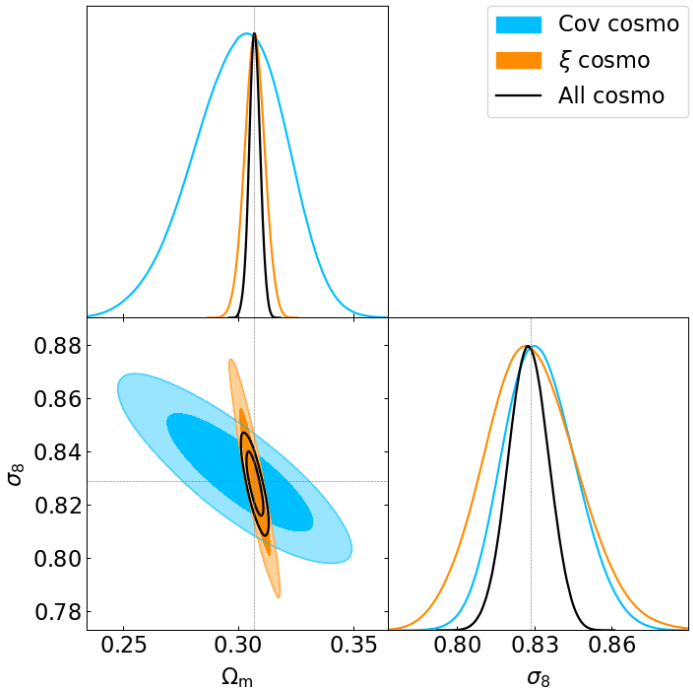

Figure 5.10: Contour plots at 68 and 95 percent of confidence level for: cosmology-dependent matrix and fixed mean value (blue), fixed covariance and cosmology-dependent mean value (orange), and cosmology-dependent mean value and covariance (black). Gray lines represent the input parameters.

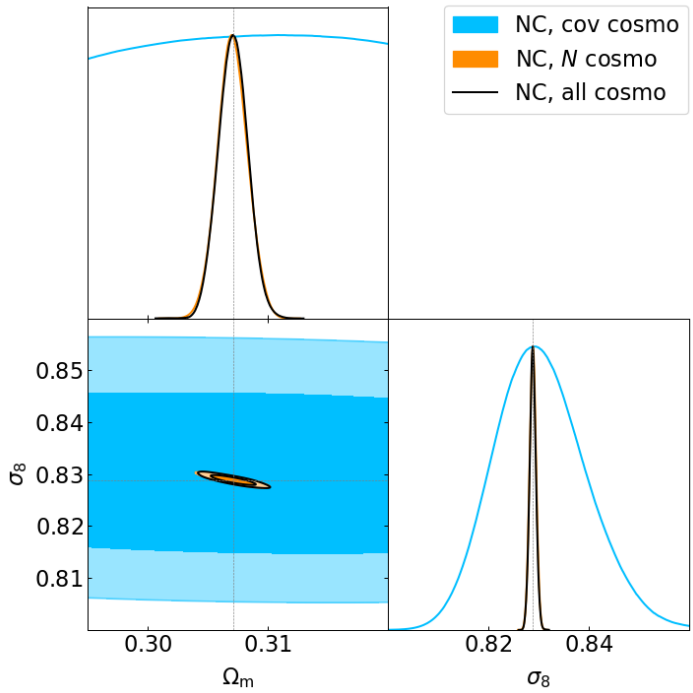

Figure 5.11: Same of Fig. 5.10 for cluster number counts.

5.2.5 Mass binning

We perform this analysis considering four redshift bins of width $\Delta z = 0.5$, to allow for more populated mass bins. We consider the case of two mass bins with cuts at $\log_{10} M/M_\odot = \{14.00, 14.15, 16.00\}$, three mass bins with cuts at $\log_{10} M/M_\odot = \{14.00, 14.05, 14.15, 16.00\}$ and four mass bins with cuts at $\log_{10} M/M_\odot = \{14.00, 14.05, 14.10, 14.20, 16.00\}$, chosen in order to have at least 4000 objects in each mass and redshift bin.

We show in Fig. 5.12 the posterior distribution from the three cases with mass binning, compared to the mass threshold case, while in Table 5.5 we report the corresponding FoMs. We observe an improvement in the FoM when considering the mass binning with respect of the mass-threshold case, indicating that the information included in the halo bias can be exploited to obtain tighter constraints on cosmological parameters. However, increasing the number of mass bins does not improve significantly the contours: this can be attributed to the closeness of the bins, characterized by a similar bias relation. On the other hand, selecting more distant bins implies having less populated intervals and therefore noisier quantities.

Once we have established the advantage of considering mass binning, we validate the corresponding covariance model presented in Eq. (5.14). For greater clarity, we consider the simplest two mass bins case; the cases with more mass bins are analogous. In Fig. 5.13 we show the diagonal components of the analytical matrix (solid lines), compared to the corresponding numerical terms (shaded areas). As in the mass threshold case, the model underestimates the expected covariance, with a difference in the FoM of about the 30 percent (see Table 5.5). Again, we correct this discrepancy by adding some covariance parameters, fitted for each mass and redshift bin, according to Eq. 5.15. When adding the parameters fitted from simulations, the discrepancy between numerical and analytical matrix drops to less than 5 percent on the FoM.

Finally, we test the effect of the cosmology-dependent covariance, following the analyses described in Sect. 5.2.4. In this case, the improvement in the cosmological posteriors is even higher than the mass threshold case, reaching a difference in the FoM of about 230 percent. This is due the mass-dependence of the shot-noise, that makes the covariance more constraining than the single mass threshold case.

Table 5.5: Figure of merit for the different mass binning cases. In the third column, percent difference with respect to the "Mass threshold" case in the upper part, and "2 mass bins" numerical case in the lower one.

Case	FoM	ΔFoM / FoM$_{\rm num}$
Mass threshold	29759 ± 554	–
2 mass bins	36555 ± 349	+ 23 %
3 mass bins	35243 ± 308	+ 18 %
4 mass bins	37160 ± 497	+ 25 %
Model	48500 ± 738	+ 33 %
Model + fit	37980 ± 543	+ 4 %
Cosmo-dependent	121921 ± 615	+ 230 %

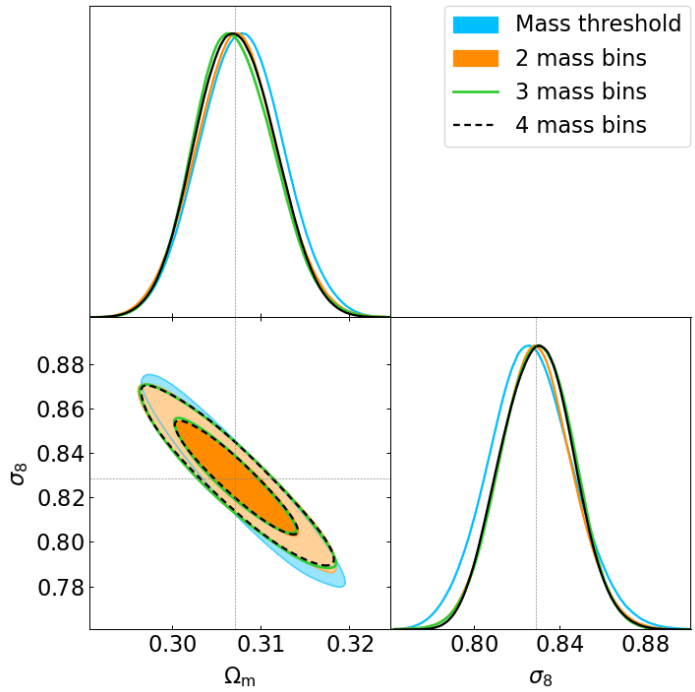

Figure 5.12: Contour plots at 68 and 95 percent of confidence level for three cases: no mass binning (blue), two mass bins (orange), and three mass bins (black). The numerical covariance is used.

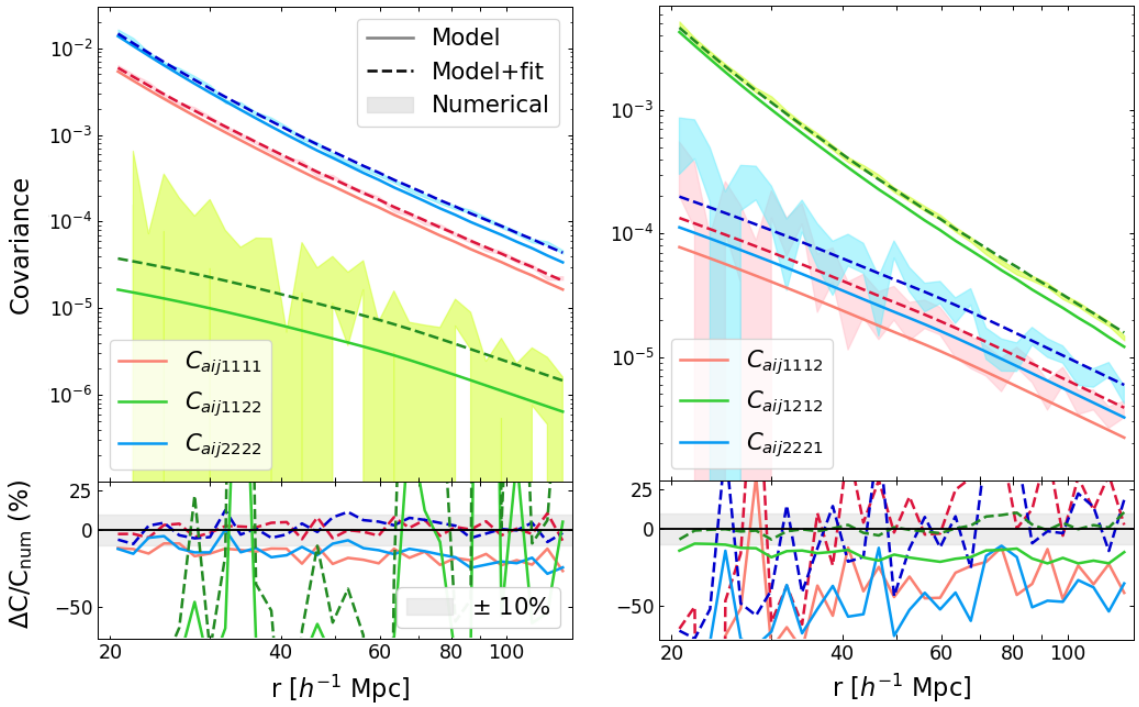

Figure 5.13: Numerical (shaded areas), analytical (solid lines), and analytical with fitted parameters (dashed lines) covariance matrices as a function of separation, in the redshift bin $z = 1.0 - 1.5$. Different colors represent the diagonal elements of different auto- and cross-correlation terms of the matrix.

Chapter 6

Combined number counts and clustering analysis

In this chapter we present the results of the covariance validation in observable space and of the joint number counts and clustering analysis. The first part consists in validating the covariance models in a more realistic scenario, achieved by including cluster richness through a richness-mass relation and observational uncertainties through selection functions (Sect. 6.1 and 6.2). In the second part, we forecast how the combination of cluster number counts and cluster clustering can improve the cosmological constraints at the level of accuracy expected for *Euclid* (Sect. 6.3)[1]. We show in Sect. 6.4 some applications of the number counts analysis, presented in Ragagnin et al. (2021) and Castro et al. (2020). Finally, in Sect. 6.5 we apply the whole pipeline to the SDSS redMaPPer cluster catalog in order to constrain cosmological parameters and determine if the addition of cluster clustering can actually improve the cosmological constraints in real data.

6.1 Observable space

Although the first steps of this analysis consist of validating covariances for mass-selected clusters, the analysis of real data requires the clusters to be selected through some observable property (see Sect. 1.2.2). Therefore, we introduce the richness, namely the number of galaxies contained in the cluster, as mass proxy.

We model the relation between the mass and true richness of a cluster as a log-normal distribution (see, e.g., Rozo et al. 2010; Saro et al. 2015; Costanzi et al. 2019)

$$P(\lambda|M,z) = \frac{1}{\lambda\sqrt{2\pi\sigma^2_{\ln\lambda}}}\exp\left[-\frac{(\ln\lambda - \langle\ln\lambda(M,z)\rangle)^2}{2\sigma^2_{\ln\lambda}}\right], \tag{6.1}$$

where the mean value and the scatter are obtained by fixing the scaling relation between richness and mass. In this work, we assume a scaling relation of the form

$$\langle\ln\lambda(M,z)\rangle = \ln(A_\lambda) + B_\lambda \ln\left(\frac{M}{3\times10^{14}\,h^{-1}\,M_\odot}\right) + C_\lambda \ln\left(\frac{1+z}{1+0.45}\right), \tag{6.2}$$

$$\sigma^2_{\ln\lambda}(M,z) = D^2_\lambda, \tag{6.3}$$

[1]The results in Sect. 6.2 and 6.3 have not been reviewed by the Euclid Consortium.

with parameters $A_\lambda = 52$, $B_\lambda = 0.9$, $C_\lambda = 0.5$, $D_\lambda = 0.15$ (Costanzi et al. 2021, adapted from M_{500c} to $M_{\rm vir}$).

In principle, Eq. (6.1) allows us to pass from the halo mass function to the richness counts:

$$\frac{\mathrm{d}n}{\mathrm{d}\lambda}(\lambda, z) = \int_0^\infty \mathrm{d}M \frac{\mathrm{d}n}{\mathrm{d}M} P(\lambda|M, z)\,. \tag{6.4}$$

However, both richness and redshift measurements are affected by additional scatter due to observational inaccuracy. The observed richness and redshift, respectively $\lambda^{\rm ob}$ and $z^{\rm ob}$, can be related to the true richness and redshift by means of selection functions, describing the probability for a cluster to be included in the sample. Following Abbott et al. (2020), we model the probability distributions $P(\lambda^{\rm ob}|\lambda, z)$ and $P(z^{\rm ob}|z, \lambda^{\rm ob})$ as

$$P(\lambda^{\rm ob}\,|\,\lambda) = \frac{1}{\sqrt{2\pi\sigma^2_{\lambda^{\rm ob}}(\lambda, z)}} \exp\left[-\frac{\left(\lambda^{\rm ob} - \lambda\right)^2}{2\sigma^2_{\lambda^{\rm ob}}(\lambda, z)}\right] \tag{6.5}$$

with scatter

$$\sigma^{\rm ob}_\lambda = (\lambda, z) = (0.9 + 0.1z)\,\lambda^{0.4} \tag{6.6}$$

and

$$P(z^{\rm ob}\,|\,z, \lambda^{\rm ob}) = \frac{1}{\sqrt{2\pi\sigma^2_{z^{\rm ob}}(z, \lambda^{\rm ob})}} \exp\left[-\frac{\left(z^{\rm ob} - z\right)^2}{2\sigma^2_{z^{\rm ob}}(z, \lambda^{\rm ob})}\right], \tag{6.7}$$

with scatter

$$\sigma_{z^{\rm ob}}(z, \lambda^{\rm ob}) = 0.005 + 0.025(z - 0.2) + 0.00025\frac{\langle\lambda^{\rm ob}\rangle}{50}\,. \tag{6.8}$$

The final prediction for the number counts in the i-th observed richness bin and in the a-th observed redshift bin is thus

$$N_{ai} = \Omega_{\rm sky} \int_0^\infty \mathrm{d}z\, \frac{\mathrm{d}V}{\mathrm{d}z\,\mathrm{d}\Omega}(z)\, n_i(z) \int_{\Delta z^{\rm ob}_a} \mathrm{d}z^{\rm ob} P(z^{\rm ob}\,|\,z, \Delta\lambda^{\rm ob}_i)\,, \tag{6.9}$$

where $\Omega_{\rm sky} = 2\pi(1 - \cos\theta)$ is the survey area, which is assumed to be independent on redshift, and

$$n_i(z) = \int_0^\infty \mathrm{d}M \frac{\mathrm{d}n}{\mathrm{d}M}(M, z) \int_{\Delta\lambda^{\rm ob}_i} \mathrm{d}\lambda^{\rm ob} \int_0^\infty \mathrm{d}\lambda\, P(\lambda^{\rm ob}\,|\,\lambda, z)\, P(\lambda\,|\,M, z)\,. \tag{6.10}$$

Analogously, the 2PCF in the a-th redshift, s-th separation bin, and i-th and j-th richness bins can be written as

$$\xi_{asij} = \int \frac{\mathrm{d}k\, k^2}{2\pi^2} \left\langle \overline{b}_i \sqrt{P_{\rm m}(k)} \right\rangle_a \left\langle \overline{b}_j \sqrt{P_{\rm m}(k)} \right\rangle_a W_s(k)\,, \tag{6.11}$$

where

$$\left\langle \overline{b}_i \sqrt{P_{\rm m}(k)} \right\rangle_a = \frac{1}{N_{ai}} \int_0^\infty \mathrm{d}z \frac{\mathrm{d}V}{\mathrm{d}\Omega\,\mathrm{d}z} n_i(z)\, b_i(z) \sqrt{P_{\rm m}(k, z)} \int_{\Delta z^{\rm ob}_a} \mathrm{d}z^{\rm ob} P(z^{\rm ob}\,|\,z, \Delta\lambda^{\rm ob}_i)\,, \tag{6.12}$$

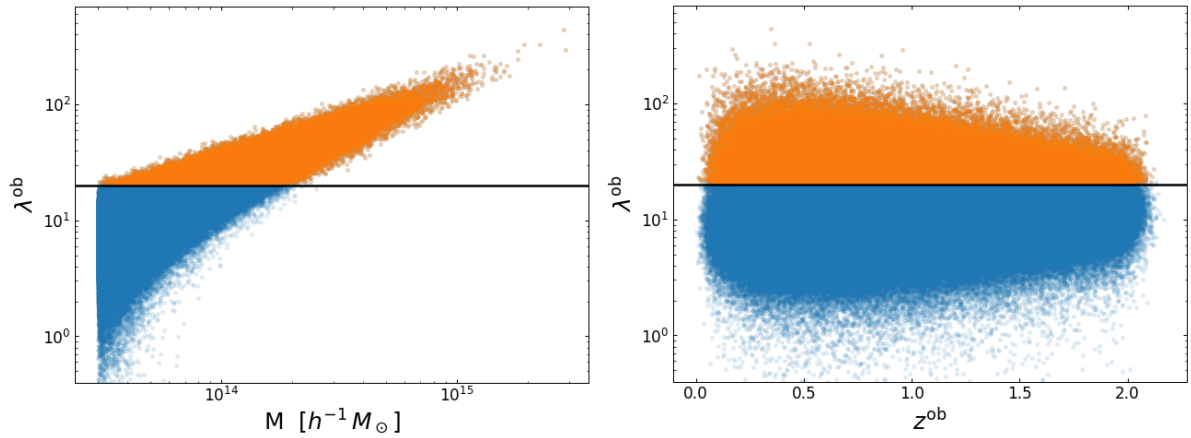

Figure 6.1: Observed richness distribution from a lightcone, as a function of mass (*left panel*) and observed redshift (*right panel*). Blue points represent the whole catalog, while orange points are the clusters selected above a richness threshold ($\lambda^{ob} = 20$, black horizontal line), chosen to ensure the completeness of the sample.

with

$$b_i(z) = \int_0^\infty \mathrm{d}M \frac{\mathrm{d}n}{\mathrm{d}M}(M,z)\, b(M,z) \int_{\Delta\lambda_i^{ob}} \mathrm{d}\lambda^{ob} \int_0^\infty \mathrm{d}\lambda\, P(\lambda^{ob}\,|\,\lambda,z)\, P(\lambda\,|\,M,z)\,. \tag{6.13}$$

Equations (6.9) and (6.11) substitute, respectively, Eqs. (1.24) and (5.11) for richness-selected surveys. The two analytical covariances of Eqs. (4.1) and (5.14) are modified according to these changes.

6.2 Covariance validation

Here we present the results of the covariance models validation in observable space. To perform the validation, we construct the dataset starting from the 1000 lightcones described in Sect. 2.3. For each mock, we assign a true richness to the halo masses through a log-normal distribution with mean and variance given by Eqs. (6.2) and (6.3). Then, we compute the observed richness and redshift for each halo, according to Eqs. (6.5) and (6.7). An example of the resulting sample is shown in Fig. 6.1: in the left panel we show the observed richness distribution as a function of the halo mass, while in the right panel we show the same distribution as a function of the observed redshift. To ensure the completeness of the catalogs, we apply a richness lower limit at $\lambda^{ob} = 20$. The resulting catalogs contain $\sim 2\times10^5$ objects in the redshift range $z = 0-2$. As in the previous analyses, we use these catalogs both for the covariance validation described in this section, and for the likelihood forecasts presented in Sect. 6.3.

6.2.1 Covariance models validation

We validate the two covariance models as described in the previous chapters. For the number counts we consider 10 redshift bins of width $\Delta z = 0.2$ and 5 richness bin composed by 4

log-spaced bins in $\lambda^{\rm ob} = 20-80$, plus a bin up to $\lambda^{\rm ob} = 300$. The binning scheme has been chosen in order to have at least 40 objects in each bin and to satisfy the results described in Sect. 4.2.1 for the optimal binning selection. Although they are always sub-dominant, the diagonal and off-diagonal terms of the sample covariance reach values comparable with the shot-noise level, in the low-mass/low-redshift range. The comparison is shown in the left panel of Fig. 6.2. We therefore expect this effect to be non-negligible also in observable space. As for the model validation, we confirm the 10 percent level of agreement between analytical model and numerical matrix. The good agreement between the two matrices can also be observed in the right panel of Fig. 6.2, showing the χ^2 distribution for the two covariances, compared to the expected distribution.

For cluster clustering, we consider 4 redshift bins of width $\Delta z = 0.5$, 30 log-spaced separation bins in range $r = 20-130\,h^{-1}$Mpc, and 3 richness bins $\lambda^{\rm ob} = \{20, 30, 300\}$. The binning scheme has been chosen according to the results presented in Sect. 5.2.1. Also in this case we confirm the results obtained for mass-selected clusters: the analytical model underestimates the numerical matrix, but the disagreement can be mitigated by fitting to simulations the three parameters $\{\alpha, \beta, \gamma\}$, as in Eq. (5.15). The results are shown in Fig. 6.3, where we compare the three matrices, i.e., the numerical, analytical and analytical with fitted parameters covariances: in the left panel we show the comparison of the diagonal elements of the analytical matrix with and without the fitted parameters (dashed and solid lines, respectively) with the numerical covariance, while in the right panel we show the χ^2 distribution for the three matrices.

As in previous analyses, we establish the impact of the difference between analytical and numerical matrix on cosmological posteriors. We perform the likelihood analysis by fixing the mass-observable relation parameters to assess the impact in the most stringent case; the difference will be comparable or smaller in the case where these parameters are left free, as this produces a broadening of the contours that absorbs, at least partially, the other sources of uncertainty. For both number counts and clustering, we find $\Delta\mathrm{FoM} \sim 3\,\%$ between the numerical and analytical covariances.

6.2.2 Covariance of number counts and clustering

Before starting with the joint number counts and clustering cosmological analysis, we need to verify if there is any covariance between the two observables. In the left panel of Fig. 6.4 we show the total correlation matrix, computed numerically for simulations. The two diagonal blocks correspond to the number counts and clustering auto-correlation matrices, while the off-diagonal blocks represent the cross-correlation matrix. Since such term is only dominated by noise, statistically consistent with zero, we can treat the two observables as independent quantities. As a further prove of this, we compute the number counts and clustering likelihoods for each light cone, and in the right panel of Fig. 6.4 we show their difference with respect to the log-likelihood averaged over the entire sample of simulations. We quantify the correlation by computing the Pearson correlation coefficient between the log-likelihood residuals. To this purpose, we assume that the residuals are Gaussian distributed around zero, with a covariance given by

$$C = \begin{pmatrix} \sigma^2_{\rm nc} & \rho\,\sigma_{\rm nc}\,\sigma_{\rm cl} \\ \rho\,\sigma_{\rm nc}\,\sigma_{\rm cl} & \sigma^2_{\rm cl} \end{pmatrix}, \tag{6.14}$$

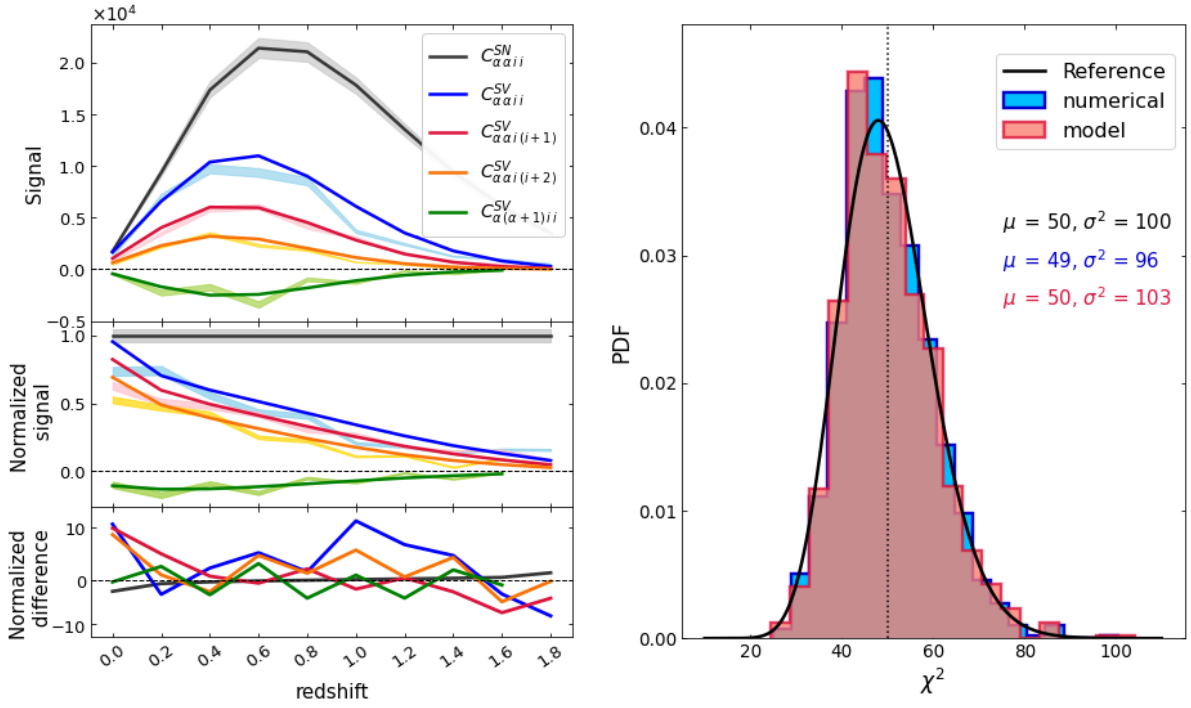

Figure 6.2: *Left panel:* same of fig. 4.4 for richness selected clusters. *Right panel:* χ^2 distribution for the numerical (blue) and analytical (red) covariance matrices. Reference distribution in black.

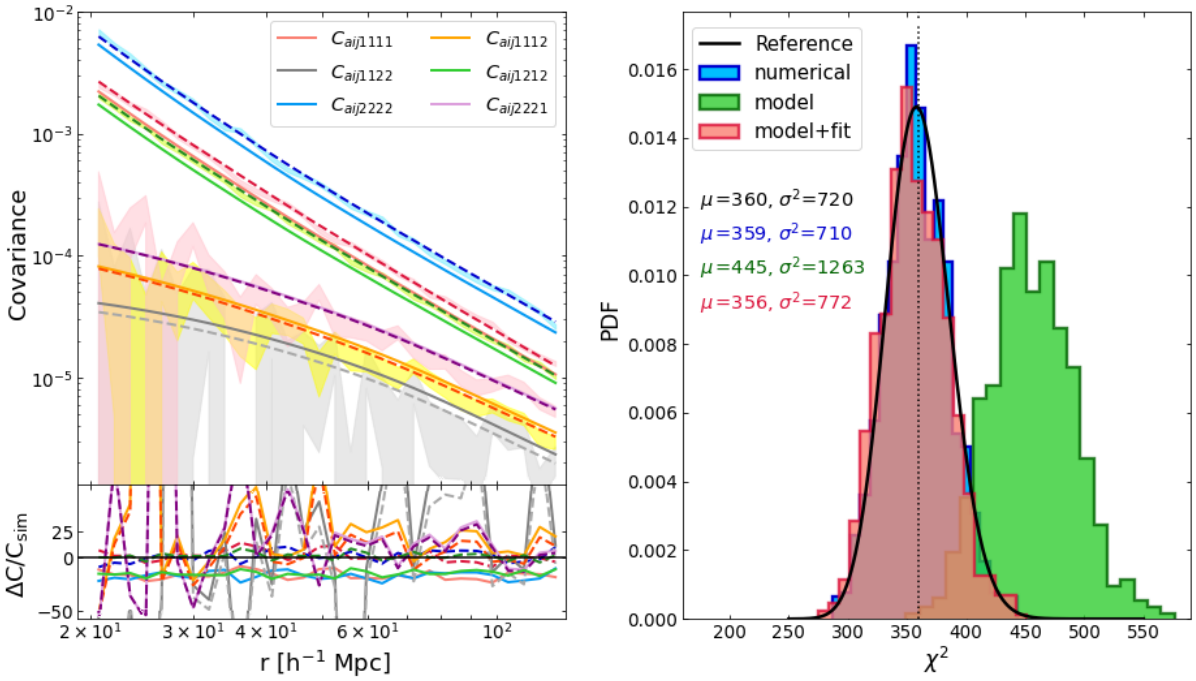

Figure 6.3: *Left panel:* same of Fig. 5.13 for richness selected clusters. *Right panel:* χ^2 distribution for the numerical (clue), analytical (green) and analytical with fitted parameters (red) covariance matrices. Reference distribution in black.

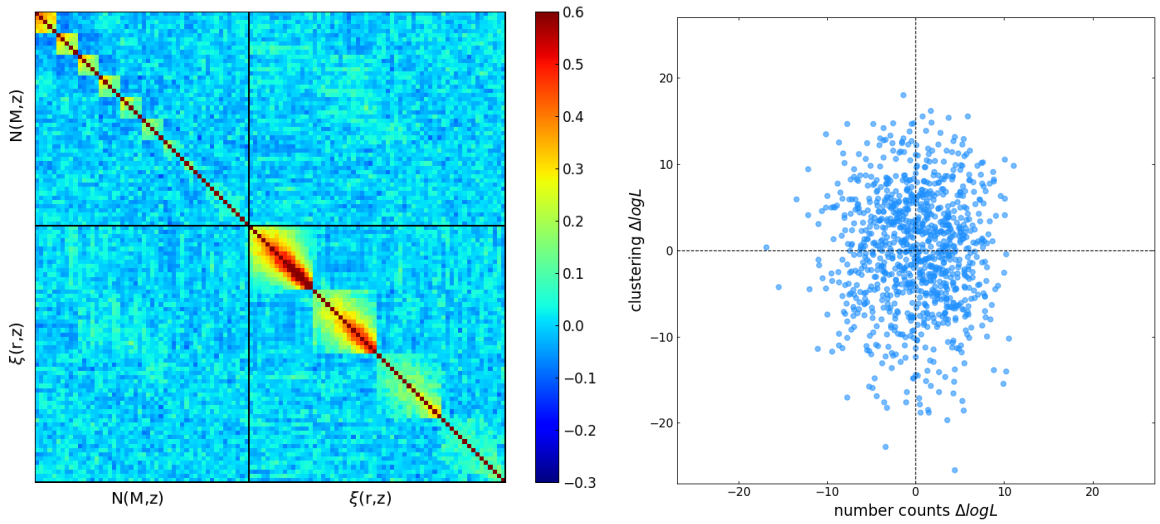

Figure 6.4: *Left panel:* normalized numerical covariance for number counts, clustering and cross-covariance. *Right panel:* log-likelihood residuals of the two observables with respect to the mean values.

where $\sigma_{\rm nc}$ and $\sigma_{\rm cl}$ are, respectively, the standard deviations computed from the number counts and clustering residuals, and ρ is the correlation coefficient. We fit the ρ parameter by maximizing a Gaussian likelihood, finding $\rho = -0.015 \pm 0.032$. The absence of correlation in the distribution of points confirms the absence of correlation between the two observables. The result is consistent with the result of Mana et al. (2013). Therefore, we will assume in the following that the total likelihood of the combined number counts and clustering probes is defined as the product of two Gaussian likelihood functions, one for each individual probe.

6.3 Cosmological parameter estimation

In this section we present the results concerning the likelihood forecasts for the number counts, clustering and their combined analyses. We explore the impact of three different choices for the prior distribution on the MoR parameters. We run all the analyses with the analytical cosmology-dependent covariances. Given the strong impact of cosmology-dependent covariance in the clustering analysis (see Sect. 5.2.4, in Sect. 6.3.2) we determine the impact of cosmo-dependent covariances in the combined analysis, and that of fixing the covariance matrix to a wrongly assumed input cosmology.

6.3.1 Impact of MoR's priors

We perform the likelihood forecasts by constraining the cosmological parameters $\Omega_{\rm m}$ and σ_8, plus the richness-mass relation parameters A, B, C, D contained in Eqs. (6.2) and (6.3). We use flat priors on cosmological parameters, equal to $\Omega_{\rm m} \in [0.2, 0.4]$ and $\sigma_8 \in [0.6, 1.0]$, and Gaussian priors on MoR parameters with amplitudes of 1, 3 and 5 %. The 5 % prior amplitude represents the current uncertainty on the richness-mass relations calibrated from observations, while the 3 and 1 % priors are chosen as optimistic estimations. We also consider the ideal case of 0 % uncertainty, corresponding to a statistically perfect knowledge of

Table 6.1: Figure of merit for the different prior amplitudes on richness-mass relation parameter. In the last column, percent difference with respect to the number counts case for each prior amplitude.

MoR prior	Probe	FoM	ΔFoM / FoM$_{NC}$
0 %	NC	1971760 ± 24660	–
	CL	81018 ± 231	−95 %
	NC + CL	2409898 ± 62519	+ 22 %
1 %	NC	186780 ± 4254	–
	CL	50875 ± 954	−72 %
	NC + CL	225765 ± 3593	+ 20 %
3 %	NC	39301 ± 708	–
	CL	22826 ± 839	−41 %
	NC + CL	64562 ± 1208	+ 64 %
5 %	NC	20572 ± 315	–
	CL	14766 ± 253	−28 %
	NC + CL	39052 ± 720	+90 %

the cluster masses. Although this does not perfectly match the mass-selected case, because of the intrinsic scatter, it allows us to remove the uncertainty given by the lack of knowledge of the mass-observable relation parameters.

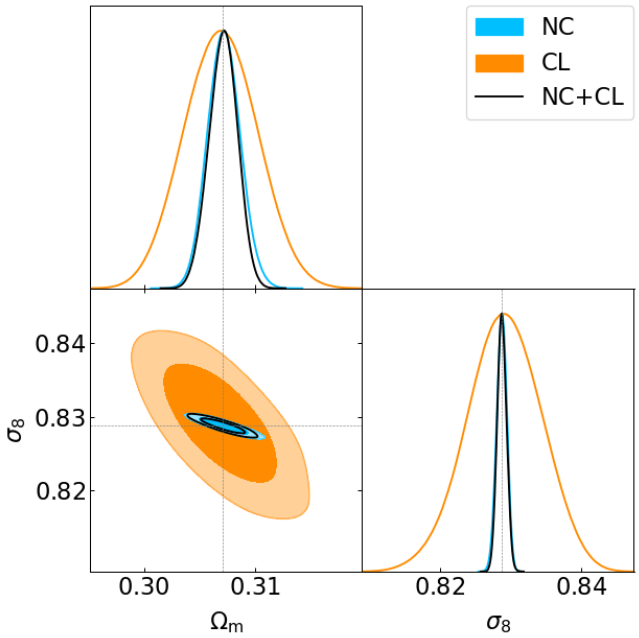

Figure 6.5: Contour plots at 68 and 95 percent of confidence level for number counts (blue), clustering (orange) and their joint (black) analysis for richness selected clusters, with MoR parameters fixed to the input values.

We study the impact of priors on parameter constraints for the number counts, clustering and joint analysis. In Figs. 6.5, 6.6, 6.7, 6.8 we show the posteriors for the number counts (NC, blue), clustering (CL, orange) and their combined (NC+CL, black) analyses, while in Table 6.1 we report the FoM of the various cases. For the 0 % prior case, the clustering is much less constraining, but nonetheless helps to improve the cosmological parameter constraints if combined with number counts, with an increase in the $\Omega_m - \sigma_8$ FoM of $\Delta\text{FoM} \sim 22\,\%$. When adding increasingly larger priors, the contours broaden due to the higher uncertainty. This broadening occurs to a greater extent on number counts than on clustering, making the combination of the two even more powerful for extracting the information, with an improvement of up to $\Delta\text{FoM} \sim 90\,\%$.

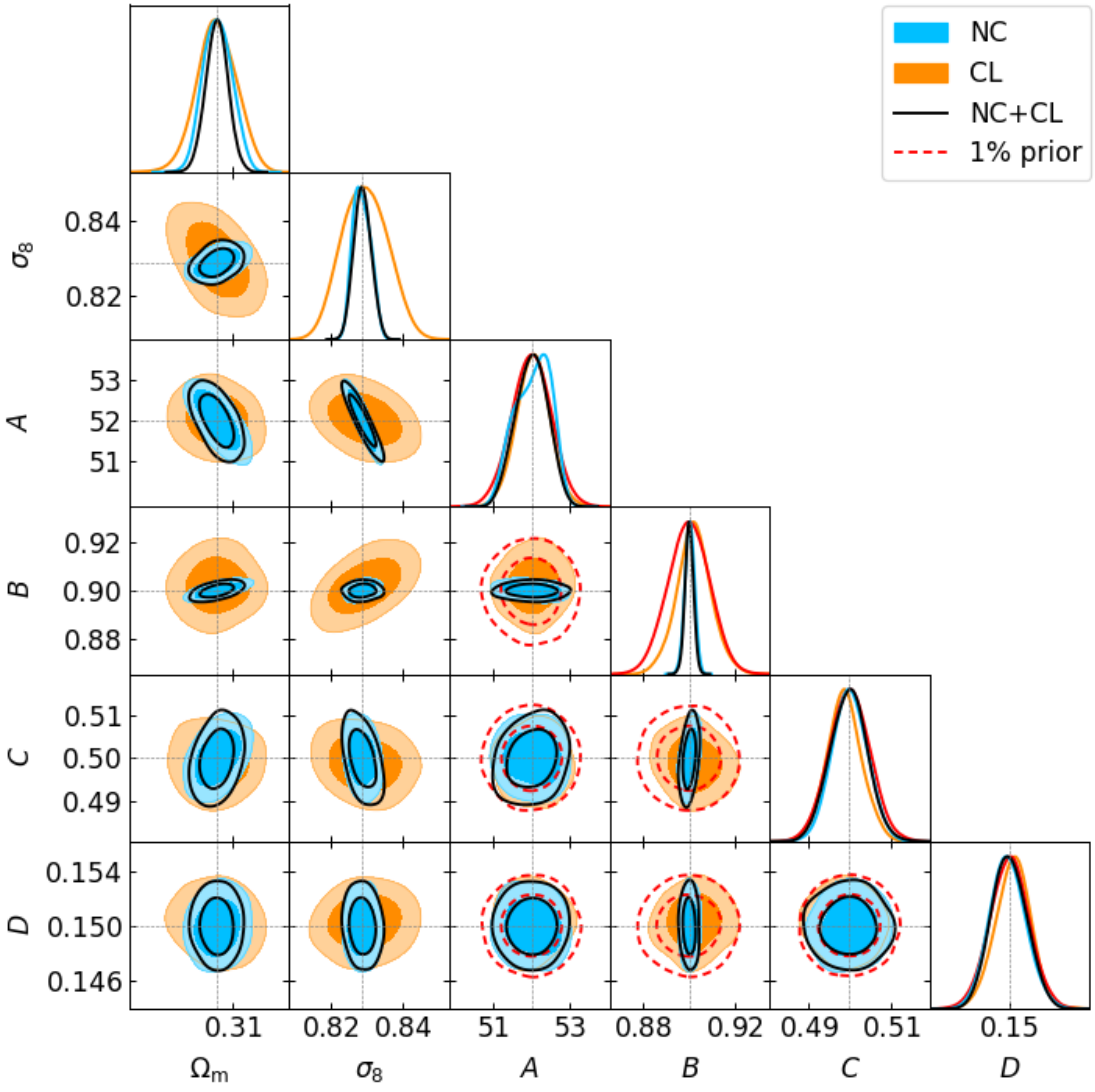

Figure 6.6: Contour plots at 68 and 95 percent of confidence level for number counts (blue), clustering (orange) and their joint (black) analysis for richness selected clusters. Red dashed lines represent the priors on richness-mass relation parameters, with 1 % amplitude.

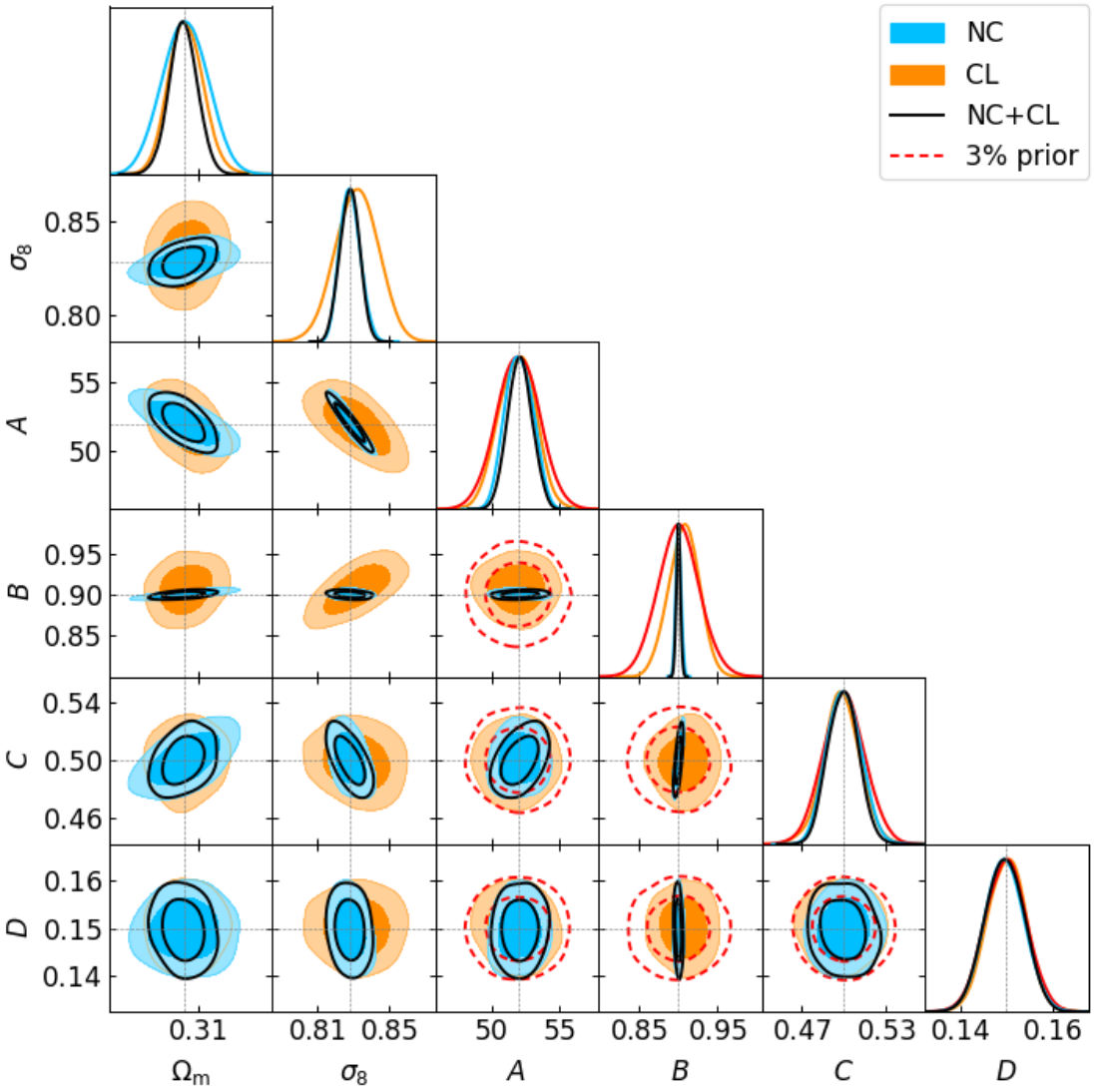

Figure 6.7: Same as Fig. 6.6 with 3 % prior amplitude.

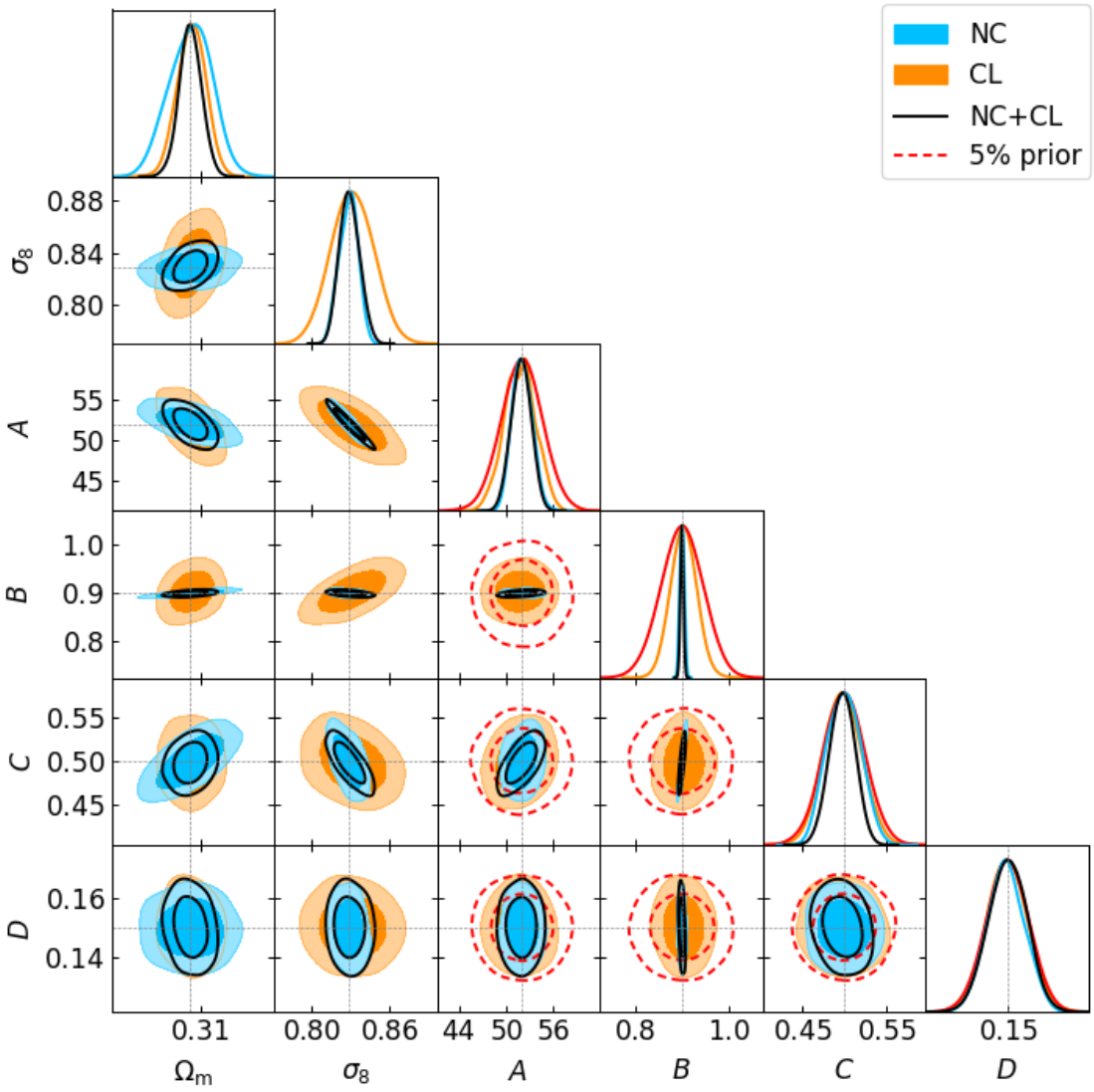

Figure 6.8: Same as Fig. 6.6 with 5 % prior amplitude.

6.3.2 Impact of cosmology-dependent covariances

In this section we assess the impact of fixing the covariance matrix at a wrong cosmology and of a cosmology-dependent covariance on the joint number counts and clustering analysis. We compare the results of the likelihood analysis by fixing the number counts and clustering covariance at the input cosmology and by considering cosmology-dependent matrices. We also compute the covariances at the two wrong cosmologies described in Sect. 5.2.4, i.e., $\Omega_m = 0.320$, $\sigma_8 = 0.775$ ("wrong A"), and $\Omega_m = 0.295$, $\sigma_8 = 0.871$ ("wrong B"). In Fig. 6.9 we show the resulting posteriors for the number counts and clustering combined analysis, obtained by fixing the mass-observable relation parameters. As expected, the use of wrong-cosmology covariances leads to under/overestimated posteriors on cosmological parameters, with a difference in the FoM of $\Delta\text{FoM}_A \sim +70\,\%$ and $\Delta\text{FoM}_B \sim -25\,\%$. On the contrary, the use of cosmology-dependent covariances provides almost the same posteriors of the input covariance case. The result seems to replicate the one obtained from the number counts

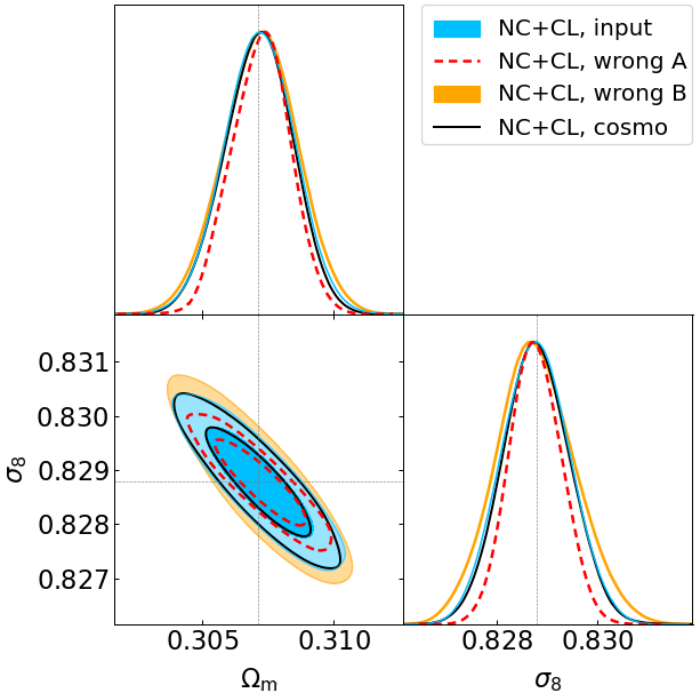

Figure 6.9: Contour plots at 68 and 95 percent of confidence level for the joint number counts and clustering analysis, with input-cosmology covariances (orange), cosmology-dependent covariances (black), and two wrong-cosmology cases: A) $\Omega_m = 0.320, \sigma_8 = 0.775$ in orange, and B) $\Omega_m = 0.295, \sigma_8 = 0.871$ in red. Gray lines represent the input parameters.

analysis (Fig. 4.8), while it does not show the improvement obtained by using the cosmology-dependent covariance in the clustering analysis (Fig. 5.10). This can be explained by the fact that cluster clustering is much less constraining with respect to number counts, so that the improvements coming from the fully cosmology-dependent analysis does not contribute significantly to the constraining power of the combined analysis.

We repeat the same analysis described above by setting the 5 % prior on mass-observable relation parameters; by doing so, we evaluate the impact of wrong covariances in the worst case. In Fig. 6.10 we can see that there is no significant difference between the various posteriors, with a FoM varying by less than 5 percent in all the three cases. Even if the clustering constraining power in this case is comparable to that from number counts, the broadening of the contours absorbs the effect of wrong covariances. In other words, the total error budget is at this point dominated by the uncertainty on the MoR.

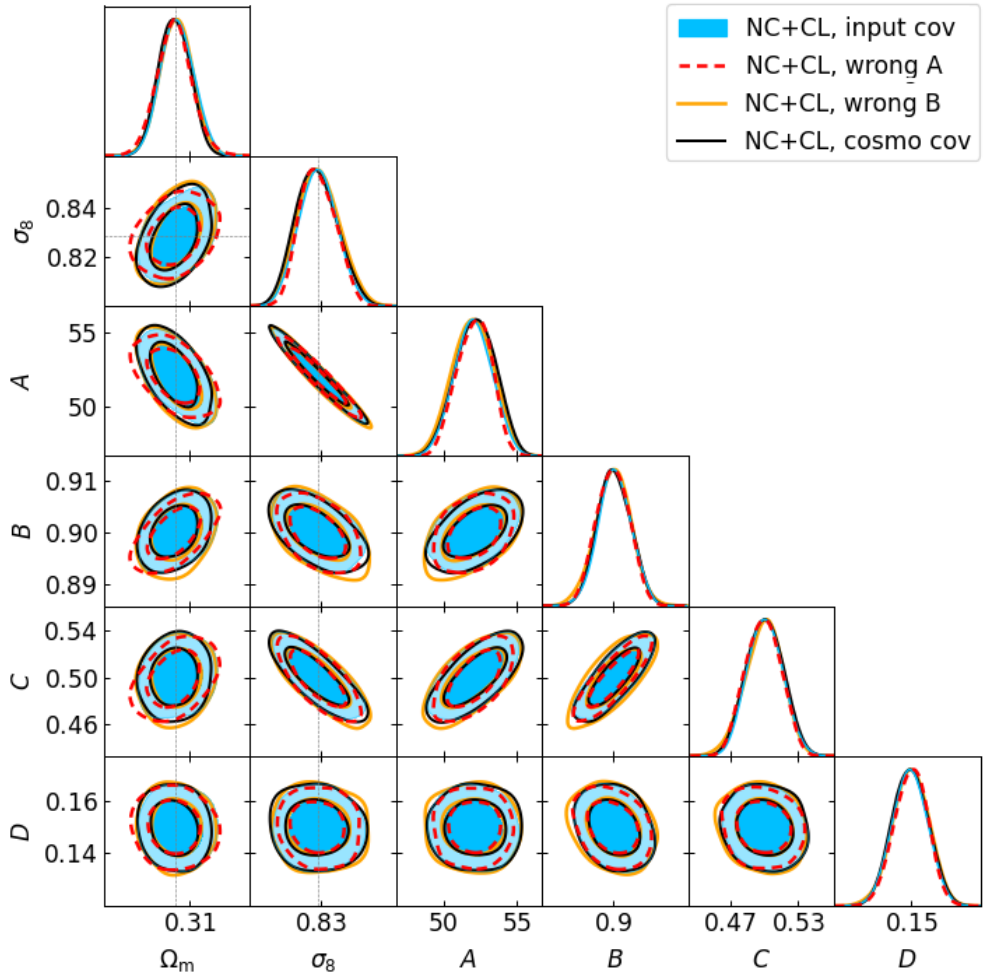

Figure 6.10: Same as Fig. 6.9 with 5 % amplitude of mass-observable relation priors.

6.4 Applications

We present here some applications of the number counts analysis, performed by using the analytical model covariance validated in this work.

6.4.1 Cosmology dependence of the HOD

We present here the first application, described in Ragagnin et al. (2021). We use the number counts likelihood analysis validated in this chapter to estimate the impact of a cosmology-dependent HOD (Halo Occupation Distribution, see, e.g., Kravtsov et al. 2004) on the cosmological parameter constraints. An HOD is the conditional probability distribution $P(N|M)$ that a halo of mass M has a galaxy abundance N. In the context of HOD, galaxy counting is separated into central N_c and satellite N_s abundances, so that $N = N_c + N_s$. In fact, central and satellite galaxies belong to two different populations as they experience different processes (Guzik & Seljak 2002), as shown by both observations (Skibba 2009) and numerical simulations (Wang et al. 2018). The satellite galaxy abundance distribution $P(N_s|M)$ is typically modeled with a Poisson distribution at each mass bin (Kravtsov et al. 2004) and its

average value should increase with halo mass; while the number of central galaxies N_c tends to unity asymptotically with respect to the galaxy mass selection threshold. The average $N_s - M$ relation can be described by a power law at high halo masses,

$$\langle N_s(M) \rangle \propto M^{\beta}. \tag{6.15}$$

Subhalo population is affected by the host halo accretion history (Giocoli et al. 2008) and HOD normalization has a mild evolution with redshift. The log-slope β plays a key role in galaxy formation efficiency and it is not yet well constrained.

In this section, we build an emulator, namely HODEmu[2], of satellite abundance based on cosmological parameters Ω_m, Ω_b, σ_8, h, and redshift z. We train our emulator using the *Magneticum*[3] hydrodynamic simulations that span 15 different cosmologies (labeled "Box1a/mr C1–C15"), each over 4 redshift slices between $z = 0-0.5$. Halos and their member galaxies are identified using, respectively, the FoF halo finder and an improved version of the subhalo finder SUBFIND (Springel et al. 2001) that takes into account the presence of baryons (Dolag et al. 2009). For each setup we fit normalization A, log-slope β and Gaussian fractional-scatter σ of the $N_s - M$ relation. The emulator is based on multi-variate output Gaussian Process Regression (GPR). The emulator predicts the number of satellites for a given cosmology, with an error within $\sim 20\%$.

To test the cosmology-dependence of the HOD on mock catalogs, we consider the richness. We recast Eq. (6.15) in terms of a richness-mass relation:

$$\langle \lambda(M) \rangle = A_\lambda \cdot \left(\frac{M}{M_p} \right)^{\beta_\lambda}, \tag{6.16}$$

with $A_\lambda = A_0 \cdot A_{\rm emu} = 72.4 \pm 0.7$ and $\beta_\lambda = \beta_0 \cdot \beta_{\rm emu} = 0.935 \pm 0.038$ (from table IV of Costanzi et al. 2021). Here, $A_{\rm emu}$ and $\beta_{\rm emu}$ are the predictions of the emulator and contain the dependence on cosmology, while A_0 and β_0 represent the cosmology-independent part of the total parameters.

To perform the analysis, we generate a simulated catalog of halo masses corresponding to the C8 simulation at redshift $z = 0$, following the D16 analytical mass function, with fluctuation assigned according to the covariance matrix validated in Sect. 4.1.1. This step ensures to have a proper description of the mass function, in order to obtain an unbiased estimation of parameters. We obtain a catalog with $\sim 2.8 \times 10^5$ objects, with virial masses above $M_{\rm vir} > 10^{13}\, M_\odot$, to which we assign richness by applying Eq. (6.16), plus a Poisson scatter. To ease the analysis, we neglect the intrinsic scatter of the HOD, which is subdominant with respect the Poisson one. In the end, we compute the number counts by considering five richness bins, between $\lambda = 30-300$, where the sample is complete in mass.

Then, we maximize a Gaussian likelihood to compare the mock "observed" number counts and the theoretical prediction, with covariance given by the model described and validated in Sect. 4.1.1, adapted to take into account richness-selected object according to the prescription described in this chapter. Since in this test we only aim to give an estimation of the impact of the cosmology-dependent HOD, we run a simplified MCMC process with only two free cosmological parameters, Ω_m and $\log_{10} A_s$ (and thus σ_8), neglecting the dependence of the HOD on Ω_b and h_0, and neglecting the redshift dependence.

Following the approach of Singh et al. (2020), we compare three different cases:

[2] https://github.com/aragagnin/HODEmu/

[3] www.magneticum.org

i) *no cosmo* case: we ignore the cosmology dependence of the HOD, so that $A_\lambda = A_0$ and $\beta_\lambda = \beta_0$. We assume flat uninformative priors both on Ω_m and $\log_{10} A_s$ and on A_λ and β_λ;

ii) *cosmo* case: we assume flat uninformative priors on Ω_m, $\log_{10} A_s$, A_0 and β_0, plus Gaussian priors on A_λ and β_λ, respectively given by $\mathcal{N}(72.4, 7.0)$ and $\mathcal{N}(0.935, 0.038)$. The cosmology-dependent parameters A_emu and β_emu are computed by the emulator at each step of the MCMC process, and, to take into account the emulator inaccuracy, we randomly extract a value from a Gaussian distribution with center in the emulator prediction and amplitude equal to $\sigma_{\log A_\mathrm{emu}} = 0.06$ and $\sigma_{\log \beta_\mathrm{emu}} = 0.09$;

iii) *cosmo + WL* case: we add the weak lensing (WL) cosmological dependence which affects the mass calibration in the real observations, to figure out whether the combination of the cosmology-dependent HOD with other cosmological probes could improve the parameter constraints. We model such dependence by modifying the prior on A_λ, which becomes a Gaussian prior with the same amplitude of the previous case, but centered on

$$A'_\lambda = A_\lambda - \ln 10^{\Delta(\Omega_\mathrm{m})} \tag{6.17}$$

with $\Delta(\Omega_\mathrm{m}) = \beta_\lambda \frac{\mathrm{d} \ln M_\mathrm{WL}}{\mathrm{d}\Omega_\mathrm{m}} (\Omega_\mathrm{m} - 0.3)$, where $\frac{\mathrm{d} \ln M_\mathrm{WL}}{\mathrm{d}\Omega_\mathrm{m}} = -0.68$ is the average value from table I of Costanzi et al. (2019).

In Fig. 6.11, we show the posterior distributions resulting from the three analysis. As expected, the marginalized posteriors recovered by the *cosmo* case are similar to the ones from the *no cosmo* case, but in addition the former is able to constrain the cosmology-dependent and cosmology-independent components of the richness-mass relation separately. This can represent an advantage, since the components of A_λ show stronger degeneracies with cosmological parameters with respect to the one of their combination; such degeneracies can be exploited when combined with other cosmological probes. On the contrary, this decomposition for β_λ does not present the same advantage, as the full parameter has a higher degeneracy with cosmological parameters with respects to its components.

The third case presents similar posteriors to the simple *cosmo* case; to better compare the differences, we quantify the accuracy of the parameter estimation by computing the FoM in the $\Omega_\mathrm{m} - \sigma_8$ plane. The result, shown in table 6.2, indicates that the use of the cosmology-dependent HOD allows us to obtain more constraining posteriors, further improved with the addition of the weak lensing information. To prove that the *cosmo+WL* result is not achieved only thanks to the addition of WL, we show also the FoM for the *no cosmo + WL* case, which has a constraining power similar to the simple *no cosmo* case. By comparing the FoM of the three cases, we obtain an improvement of about the 6 percent for the *cosmo* case and of about the 11 percent for the *cosmo + WL* case with respect the *no cosmo* one.

Table 6.2: Figure of merit in the $\Omega_m - \sigma_8$ plane for the three cases of Fig. 6.11, plus the *no cosmo + WL* case. In the right column, normalized differences with respect to the *no cosmo* case.

Case	FoM	ΔFoM/FoM$_{nc}$
no cosmo	980	-
no cosmo + WL	993	+ 1 %
cosmo	1044	+ 6 %
cosmo + WL	1088	+ 11 %

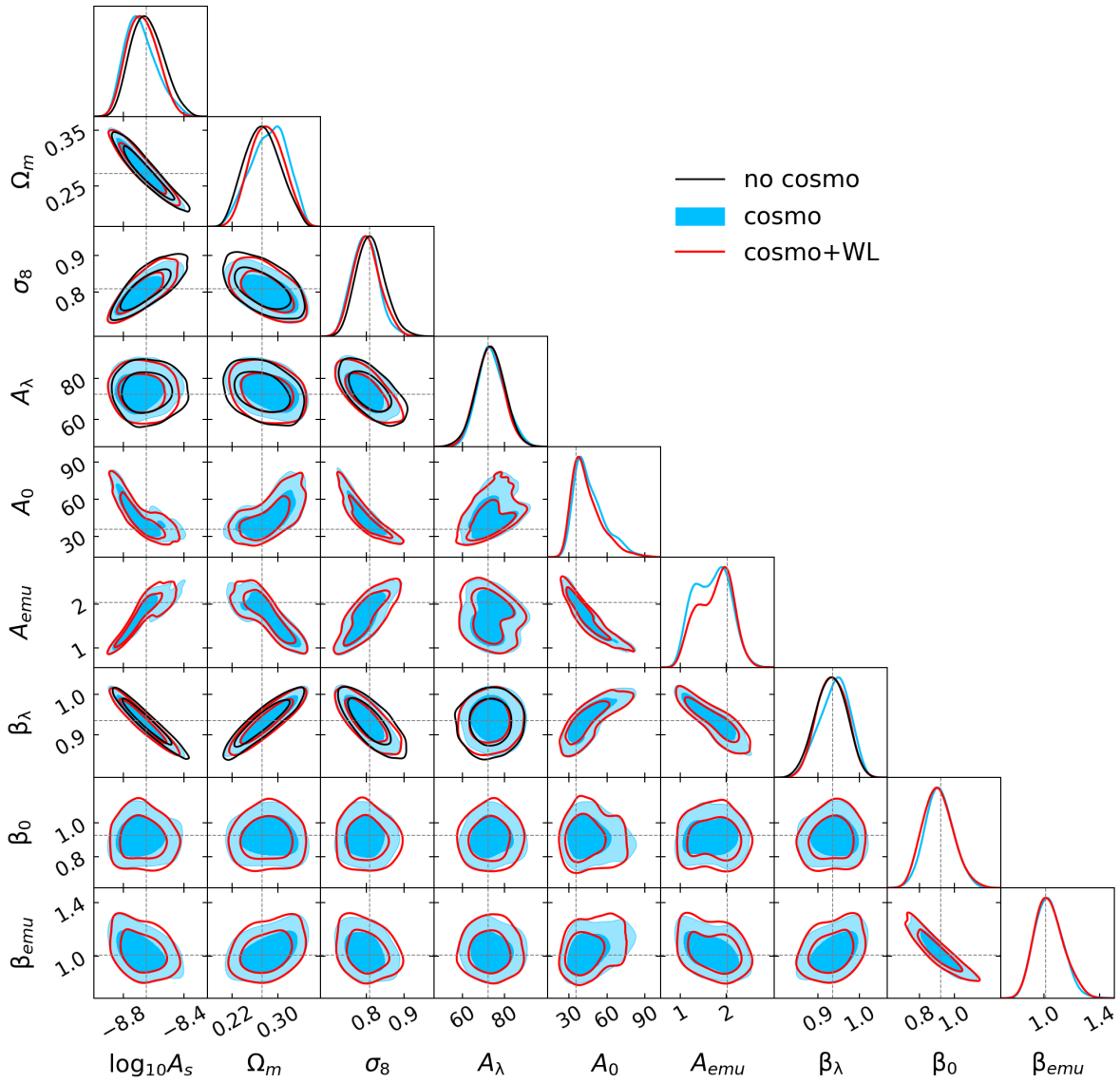

Figure 6.11: Contour plots at 68 and 95 percent of confidence level for the three cases: *no cosmo* (black), *cosmo* (blue) and *cosmo+WL* (red) contours. The grey dashed lines represent the input values of parameters.

6.4.2 Halo mass function calibration

The cluster number counts pipeline has also been applied in Euclid Collaboration: Castro et al. (2022), to forecast the impact of the halo mass function calibration on the cosmological posteriors. In this work, we propose a new calibration of the halo mass function, at the level of accuracy and precision required for the uncertainty in this quantity to be subdominant with respect to other sources of uncertainty in recovering cosmological parameters from Euclid cluster counts.

In our analysis, halos are defined as spherical overdensities with average enclosed density equal to $\Delta_{\rm vir}(z)$ times the background density, where $\Delta_{\rm vir}(z)$ is the non-linear density contrast of virialized structures as predicted by spherical collapse. We parameterize the halo mass function for a given cosmology at a given redshift according to the fitting function introduced by Bhattacharya et al. (2011),

$$f(\nu) = A(p,q)\sqrt{\frac{2a\nu^2}{\pi}}\mathrm{e}^{-a\nu^2/2}\left(1+\frac{1}{(a\nu^2)^p}\right)(\nu\sqrt{a})^{q-1}\,. \tag{6.18}$$

To satisfy the condition that all matter in the Universe is contained in halos, we impose the normalization

$$A(p,q) = \left\{\frac{2^{-1/2-p+q/2}}{\sqrt{\pi}}\left[2^p\,\Gamma\left(\frac{q}{2}\right)+\Gamma\left(-p+\frac{q}{2}\right)\right]\right\}^{-1}, \tag{6.19}$$

where Γ denotes the Gamma function. We write the parameters $\{a,p,q\}$ explicitly as functions of the matter power spectrum shape and background evolution,

$$a = a_R\,\Omega_{\rm m}^{a_z}(z) \tag{6.20}$$

$$p = p_1 + p_2\left(\frac{\mathrm{d}\ln\sigma}{\mathrm{d}\ln R}+0.5\right) \tag{6.21}$$

$$q = q_R\,\Omega_{\rm m}^{q_z}(z)\,. \tag{6.22}$$

where:

$$a_R = a_1 + a_2\left(\frac{\mathrm{d}\ln\sigma}{\mathrm{d}\ln R}+0.6125\right)^2 \tag{6.23}$$

$$q_R = q_1 + q_2\left(\frac{\mathrm{d}\ln\sigma}{\mathrm{d}\ln R}+0.5\right). \tag{6.24}$$

The model is calibrated against a suite of N-body simulations using a Bayesian approach that takes into account systematic errors arising from numerical effects in the simulation. We demonstrate the fitting function of Eq. (6.18) to be sub-percent accurate in reproducing results from 9 different variants of the ΛCDM model, including massive neutrinos cosmologies. The calibration process reported here does not take into account the uncertainties related to the astrophysics of baryons, whose impact will be studied in a forthcoming work.

After testing the convergence of the halo mass function predictions from different N-body codes, we quantify the effect of using different halo-finder algorithms, and how the resulting differences propagate to the cosmological constraints. We generate a synthetic cluster abundance data in the following way: we consider a *Euclid*-like light-cone covering 15 000 deg^2,

with redshift range $z = [0, 2]$. Optical richness λ is assigned to the halos according to the richness-mass relation $\langle \lambda | M_{\rm vir}, z \rangle$,

$$\langle \ln \lambda | M_{\rm vir}, z \rangle = \ln A_\lambda + B_\lambda \ln\left(\frac{M_{\rm vir}}{3\times 10^{14}\, M_\odot}\right) + C_\lambda \ln\left(\frac{E(z)}{E(z=0.6)}\right), \tag{6.25}$$

where $E(z)$ is defined by Eq. (1.27). We assume a richness range $\lambda = 20-2000$ and a log-normal scatter given by:

$$\sigma^2_{\ln\lambda|M_{\rm vir},z} = D^2_\lambda. \tag{6.26}$$

We use the following fiducial values for the parameters of Eqs. (6.25) and (6.26) $A_\lambda = 37.8$, $B_\lambda = 1.16$, $C_\lambda = 0.91$, $D_\lambda = 0.15$. These parameter values have been determined by converting the richness-mass relation presented by Saro et al. (2015) for M_{500c} (presented in their Table 2) to the virial mass definition, assuming that halos have a NFW profile (Navarro, Frenk, & White 1997) and mass-concentration relation given by Diemer & Joyce (2019). The adopted values are in agreement with the results presented by Castignani & Benoist (2016). Lastly, Poisson and sample variance fluctuations are added through a multivariate Gaussian distribution with amplitude given by the covariance model described in this chapter, with the only difference being the choice of the halo mass function (Eq. 6.18 instead of Eq.,2.7). We generate the synthetic data assuming the calibration from the ROCKSTAR (Behroozi et al. 2013) halo finder, and we compare the calibrations obtained by SUBFIND (Springel et al. 2001, 2021), VELOCIraptor (Elahi et al. 2019), and AHF (Knollmann & Knebe 2009), by performing a likelihood analysis. We constrain the cosmological parameters $\Omega_{\rm m}$ and σ_8, and the richness-mass relation parameters A_λ, B_λ, C_λ, D_λ, assuming flat priors on the cosmological parameters and Gaussian priors with amplitudes on the mass-observable parameters of 1, 3 and 5 percent. The likelihood sampling is performed with `zeus` (see Sect. 3.1).

In Table 6.3, we summarize the impact of the different halo finders on the inference of the marginalized cosmological parameters $\Omega_{\rm m}$ and σ_8. The impact of the different halo finders' calibrations is quantified using the index of inconsistency (IOI) (Lin & Ishak 2017), which is calculated as:

$$\mathrm{IOI} = \frac{\boldsymbol{\delta}^{\rm t}\, \boldsymbol{\Sigma}^{-1}\, \boldsymbol{\delta}}{2}, \tag{6.27}$$

where $\boldsymbol{\delta}$ is the two-dimensional difference vector between the best-fit and the assumed cosmological parameters $\{\Omega_{\rm m}, \sigma_8\} = \{0.30711, 0.8288\}$. Additionally, $\boldsymbol{\Sigma}$ is the covariance matrix between these parameters that we assume to be Gaussian distributed. In all cases, the tension in the $\Omega_{\rm m} - \sigma_8$ plane increases monotonically as the priors in the richness-mass relation tightens. For both VELOCIraptor and SUBFIND the tension goes from $\lesssim 1\sigma$ for 5 and 3 percent priors to $\lesssim 2\sigma$ when the prior tightens to 1 percent. The tension for the AHF case is $\lesssim 1\sigma$ for all priors considered.

In Table 6.3, we also summarize the impact of the systematic and statistical errors of our main (ROCKSTAR) calibration and one of the auxiliary calibrations (VELOCIraptor) on the marginalized uncertainties in the cosmological parameters $\Omega_{\rm m}$ and σ_8. We only consider one calibration of each group of halo finders, as this test is dominated by the number of simulations used in the mass function calibration. As the other halo finder all use the same number of simulations, equal to half of the set used for the ROCKSTAR calibration, they present very similar results. We compare the FoM change in the $\Omega_{\rm m} - \sigma_8$ plane obtained by fixing the halo mass function parameters to the calibrated values with the ones obtained

Table 6.3: Summary statistics for the forecast of the impact of different halo finders and calibration errors on *Euclid*'s cluster counts cosmological constraints on $\Omega_{\rm m}$ and σ_8. The index of inconsistency (IOI) quantifies the tension in the posteriors by using the ROCKSTAR calibration to create the synthetic data and either the VELOCIraptor, SUBFIND, or AHF calibration for the analysis. The relative difference of the FoM assesses the attenuation of cluster counts' constraining power if one marginalizes over the halo mass function parameters assuming the calibration chain as a prior. Errors for both statistics were estimated using bootstrap resampling.

Statistics	richness-mass relation priors	Analysis	Synthetic catalog	Value
IOI	1 %	VELOCIraptor (Fixed)	ROCKSTAR	1.66 ± 0.01
	3 %			0.77 ± 0.01
	5 %			0.65 ± 0.01
	1 %	SUBFIND (Fixed)	ROCKSTAR	1.70 ± 0.02
	3 %			0.84 ± 0.01
	5 %			0.61 ± 0.01
	1 %	AHF (Fixed)	ROCKSTAR	0.90 ± 0.02
	3 %			0.61 ± 0.01
	5 %			0.47 ± 0.00
$\frac{\Delta \mathrm{FOM}}{\mathrm{FOM}}$	1 %	ROCKSTAR (Marginalized)	ROCKSTAR	0.04 ± 0.05
	3 %			0.06 ± 0.04
	5 %			-0.01 ± 0.02
	1 %	VELOCIraptor (Marginalized)	VELOCIraptor	-0.09 ± 0.05
	3 %			0.00 ± 0.03
	5 %			-0.02 ± 0.03

by marginalizing over such parameters using a multi-variate Gaussian with covariance given by the fit uncertainties. We consider again 1, 3, and 5 percent priors on the richness-mass scaling relations. For ROCKSTAR, the statistical uncertainty only marginally affects the cosmological inference. For VELOCIraptor, we observe that the only significant impact happens for the 1 percent prior, where the FoM is overestimated by ~ 10 percent when the halo mass function parameters are left fixed.

Therefore, we conclude that differences in the halo mass function calibration associated with different choices of the halo finder propagate into systematic effects in the measurements of cosmological parameters that are comparable to the formal uncertainties in such parameters. Also, the residual uncertainties in the halo mass function parameters have a negligible impact on the corresponding cosmological constraints.

6.5 Cosmological constraints from the redMaPPer SDSS cluster survey

In this section we present preliminary results based on the application of the methodology described in this chapter to the Sloan Digital Sky Survey data release 8 (SDSS DR8, Aihara et al. 2011). This work is based on the analysis presented by Costanzi et al. (2019, hereafter DES18), who constrained cosmological and mass-observable relation parameters using cluster number counts and weak-lensing masses. We expand the DES18 analysis by including the cluster clustering, finding that the information contained in the real-space 2PCF can improve the constraints on both cosmological and richness-mass relation parameters.

6.5.1 Data and measurements

The dataset is composed by photometrically selected galaxy clusters identified in the SDSS DR8 with the redMaPPer cluster finding algorithm (Rykoff et al. 2014). The algorithm utilizes all five bands (*ugriz*) of the SDSS imaging to self-calibrate a model for red-sequence galaxies. This model is then used to identify galaxy clusters as red galaxy overdensities, while simultaneously estimating the probability that each red galaxy is a cluster member. The cluster richness is the sum of the membership probabilities over all the red galaxies within an empirically calibrated scale radius R_λ. We use the cluster richness λ as an observational mass-proxy, calibrating the relation between galaxy richness and cluster mass using weak lensing data and clustering data. Of the $\sim 14\,000\,\mathrm{deg}^2$ covered by SDSS DR8, the sample is restricted to the $\sim 10\,000\,\mathrm{deg}^2$ of high quality contiguous imaging defined by the Baryon Oscillation Spectroscopic Survey (BOSS) experiment (Dawson et al. 2013). The sample spans the redshift range $z = 0.1-0.3$ and contains clusters with richness threshold $\lambda \geq 20$. In numerical simulations this richness threshold ensures that 99% of the redMaPPer galaxy clusters can be unambiguously mapped to individual dark matter halos (Farahi et al. 2016). Differently from DES18, who used the v5.10 of the SDSS redMaPPer cluster catalog, we use the v6.3, for which the cluster random catalog is available. The observed number counts of v6.3 differ from the ones of v5.10 by less than 10 percent, and the parameter posteriors do not significantly change.

The weak lensing mass estimates employed in this analysis are a slight update of those presented in Simet et al. (2017), and rely on the shear catalog presented in Reyes et al. (2012). This catalog covers $\sim 9\,000\,\mathrm{deg}^2$ of the SDSS footprint and contains 39 million galaxies, corresponding to a source density of 1.2 gal/arcmin^2. Shear estimates were derived from the SDSS imaging using the re-Gaussianization algorithm of Hirata & Seljak (2003) and the appropriately calibrated responsivity to convert the measured shape distortions into shear estimates. The multiplicative shear bias appropriate for this catalog was characterized in Mandelbaum et al. (2012, 2013). The photometric redshifts for the sources in the shear catalog were obtained using the Zurich Extragalactic Bayesian Redshift Analyzer (ZEBRA, Feldmann et al. 2006), and the associated systematic uncertainties were calibrated in Nakajima et al. (2012).

The observed number counts and weak-lensing masses are described in DES18. Number counts are measured in five richness bins $\lambda^{\mathrm{ob}} = \{20, 27.9, 37.6, 50.3, 69.3, 140\}$ and a single redshift bin $z^{\mathrm{ob}} \in [0.1, 0.3]$. Weak lensing masses are measured in the same richness bins,

using the stacked weak lensing mass profiles of the clusters, assuming an NFW profile, and accounting for the effects of cluster miscentering, halo triaxiality, and projection effects. The cosmology dependence of weak lensing masses is modeled following Eq. (1.30); the slopes derived from fitting such an equation to the data are listed in Table 1 of DES18, and are used in our cosmological analysis to re-scale $\log_{10} M_{\rm WL}$ at each step of the MCMC.

The real-space 2PCF is computed by applying the Landy & Szalay (1993) estimator to the data and random catalogs with the CosmoBolognaLib code, as described in Sect. 5.1.1. We consider 30 log-spaced separation bins in the range $r = 20-130\,h^{-1}$ Mpc and, given the relatively low available statistics, we only consider a single richness bin.

Number counts and clustering and their covariances are modeled as described in Sect. 6.1, while weak-lensing masses are computed as

$$M_{ai}^{\rm WL} = \frac{1}{N_{ai}} \Omega_{\rm sky} \int_0^\infty {\rm d}z \, \frac{{\rm d}V}{{\rm d}z\,{\rm d}\Omega}(z) \langle M_i\, n_i \rangle(z) \int_{\Delta z_a^{\rm ob}} {\rm d}z^{\rm ob} P(z^{\rm ob}\,|\,z, \Delta\lambda_i^{\rm ob}) \,, \tag{6.28}$$

where

$$\langle M_i\, n_i \rangle(z) = \int_0^\infty {\rm d}M\, M \frac{{\rm d}n}{{\rm d}M}(M,z) \int_{\Delta\lambda_i^{\rm ob}} {\rm d}\lambda^{\rm ob} \int_0^\infty {\rm d}\lambda\, P(\lambda^{\rm ob}\,|\,\lambda,z)\, P(\lambda\,|\,M,z) \,. \tag{6.29}$$

To describe the halo mass function we use the model by Tinker et al. (2008), with the addition of two nuisance parameters to account for systematic effects:

$$\frac{{\rm d}n}{{\rm d}M}(M,z) = \frac{{\rm d}n_{\rm T08}}{{\rm d}M}(M,z)\,(s\,\log_{10}(M/M_0) + q) \,, \tag{6.30}$$

with $\log_{10}(M_0) = 13.8\,h^{-1}\,M_\odot$. According to the halo mass function, we use the halo bias model of Tinker et al. (2010).

We consider the three quantities as independent, with Gaussian likelihoods for number counts and clustering, and a log-normal likelihood for weak-lensing masses. While the absence of correlation between number counts and clustering has been demonstrated in Sect. 6.3, the independence of such observables and weak lensing masses is assumed by supposing that the dominant error sources for weak lensing masses do not affect the other observables (see DES18). However, the possible existence of correlations between richness and weak lensing masses is far from being excluded, and will be studied thoroughly in future works. We constrain cosmological, mass-observable and nuisance parameters listed in Table 3 of DES18, with priors reported in the third column of the mentioned table.

6.5.2 Preliminary results

We perform four analyses, testing all the possible combinations of the three cosmological probes: i) number counts and weak-lensing masses ("NC+$M_{\rm WL}$"), representing the standard analysis performed by DES18, ii) number counts and clustering ("NC + CL"), iii) clustering and weak-lensing masses ("CL+$M_{\rm WL}$"), and iv) number counts, clustering and weak-lensing masses ("NC+CL+$M_{\rm WL}$").

Firstly, we compare our "NC+$M_{\rm WL}$" results to the results by DES18. By comparing the blue contours in Fig 6.12 and the corresponding best fit values shown in table 6.4 with the results of DES18, it can be noticed that our results are slightly different from the ones of

DES18; this discrepancy is ascribed to numerical issues due to the use of a different code. However, the two result are fully consistent and do not present any addition bias. This consistency check ensures the absence of systematics in our analysis, confirming a good agreement between the two results.

In fig. 6.12 we show the cosmological posteriors obtained by the four analyses described above. It can be clearly observed a different degeneracy on parameters when the cluster clustering is included, where the role of cluster clustering is particularly important in constraining the total amount of matter (i.e., Ω_m). Although the "NC+CL" combination is not particularly constraining, cluster clustering turns out to be useful when combined with weak-lensing mass information (orange contours). As expected by the different degeneracies, the combination of the three observables provides the tightest posteriors (red contours), both for cosmological parameters and to constrain richness-mass relation. In Table 6.4 we list the best-fit values with 1σ uncertainty for each case.

In fig. 6.13, we show the observed quantities compared to the corresponding predictions, computed at the best-fit values listed in Table 6.4. The predictions poorly match with the observations when computed at the best-fit from the analysis without that observable. Part of the problem is related to the fact that the prediction takes into account only the best-fit and not the entire posterior. As seen in Fig. 6.12, the posteriors of the different observables are in all cases compatible with each other. The reason for the tension between the best-fit values is probably due to the presence of different systematics affecting the three quantities, and will be investigated more thoroughly in future work. In all the three cases, the "NC+CL+M_{WL}" best-fit presents a good agreement between the predicted and measured quantities.

The results obtained from this analysis, although preliminary, show that cluster clustering provides relevant information for constraining both scaling relations and cosmological parameters. This not only demonstrates the usefulness of combining different observables, but gives confidence that the pipeline created can be used in the *Euclid* perspective, where the available statistics will be even larger. Second, while the combined analysis of number counts and weak-lensing gives values of Ω_m lower than those obtained by other cosmological probes, clustering seems to be less affected by this bias. This could make clustering a relevant tool to verify the validation of weak-lensing calibration, as it is not affected by the same systematics

Table 6.4: Best-fit values with 1σ uncertainty for cosmological and mass-observable relation parameters for the four posteriors of Fig. 6.12.

Case	Ω_m	σ_8	$\log_{10} M_{min}$	$\log_{10} M_1$	α	σ_{intr}
NC+M_{WL}	$0.20^{+0.06}_{-0.04}$	$0.93^{+0.11}_{-0.10}$	$11.27^{+0.20}_{-0.19}$	$12.56^{+0.13}_{-0.15}$	$0.76^{+0.07}_{-0.06}$	$0.27^{+0.14}_{-0.11}$
NC+CL	$0.29^{+0.03}_{-0.03}$	$1.00^{+0.28}_{-0.18}$	$11.54^{+0.19}_{-0.15}$	$12.80^{+0.06}_{-0.08}$	$0.79^{+0.08}_{-0.09}$	$0.33^{+0.12}_{-0.15}$
CL+M_{WL}	$0.28^{+0.04}_{-0.03}$	$0.77^{+0.06}_{-0.06}$	$11.16^{+0.23}_{-0.25}$	$12.43^{+0.18}_{-0.19}$	$0.70^{+0.09}_{-0.07}$	$0.33^{+0.12}_{-0.15}$
NC+CL+M_{WL}	$0.27^{+0.03}_{-0.02}$	$0.82^{+0.05}_{-0.05}$	$11.40^{+0.19}_{-0.11}$	$12.74^{+0.03}_{-0.04}$	$0.86^{+0.03}_{-0.04}$	$0.27^{+0.15}_{-0.12}$

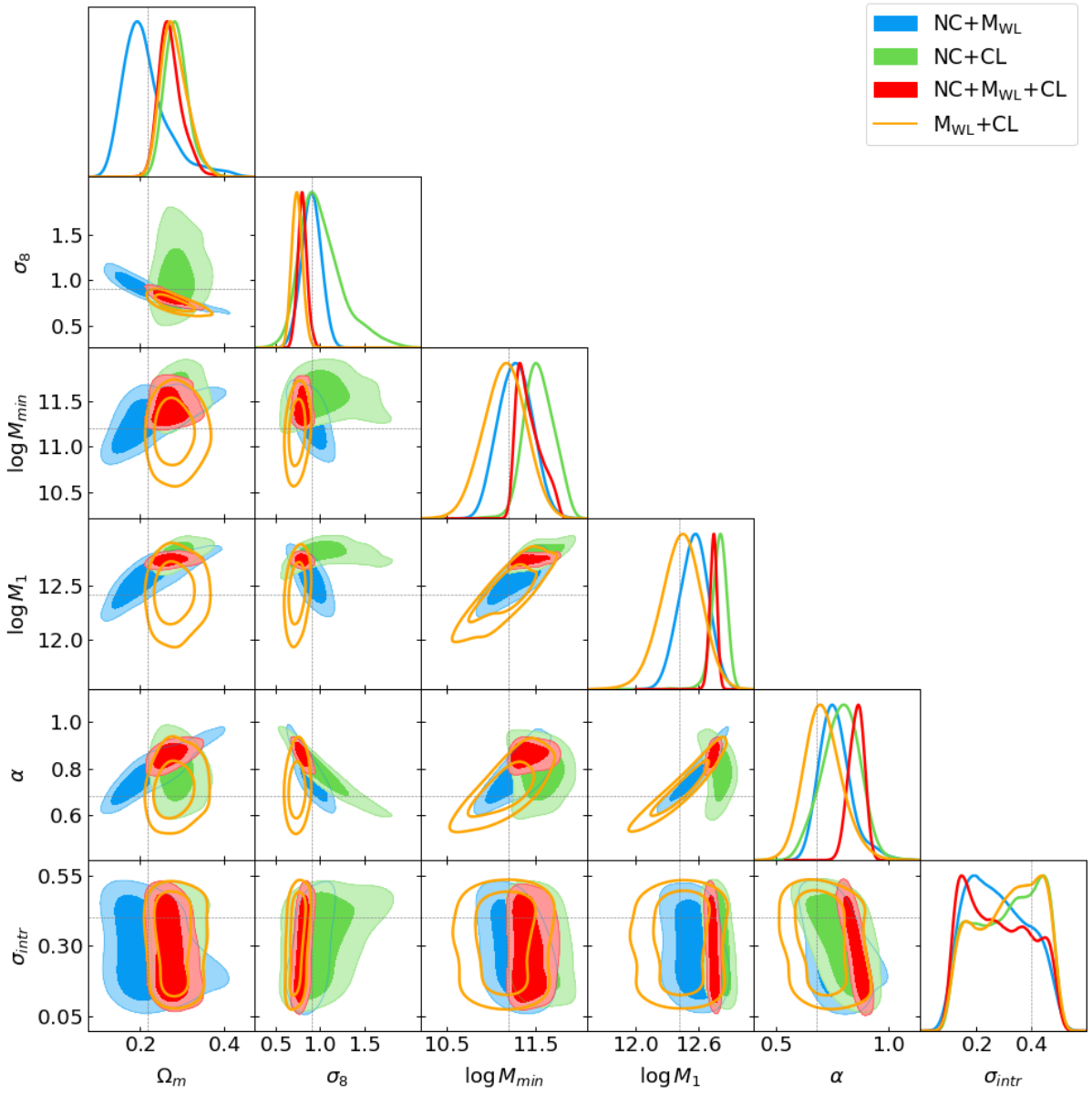

Figure 6.12: Contour plots at 68 and 95 percent of confidence level for number counts + weak lensing (NC+M$_{WL}$, blue), number counts + clustering (NC+CL, green), clustering + weak lensing (M$_{WL}$+CL, orange), and number counts + clustering+ weak lensing (NC+M$_{WL}$+CL, red) analyses. Gray dotted lines represent the best-fit values from DES18.

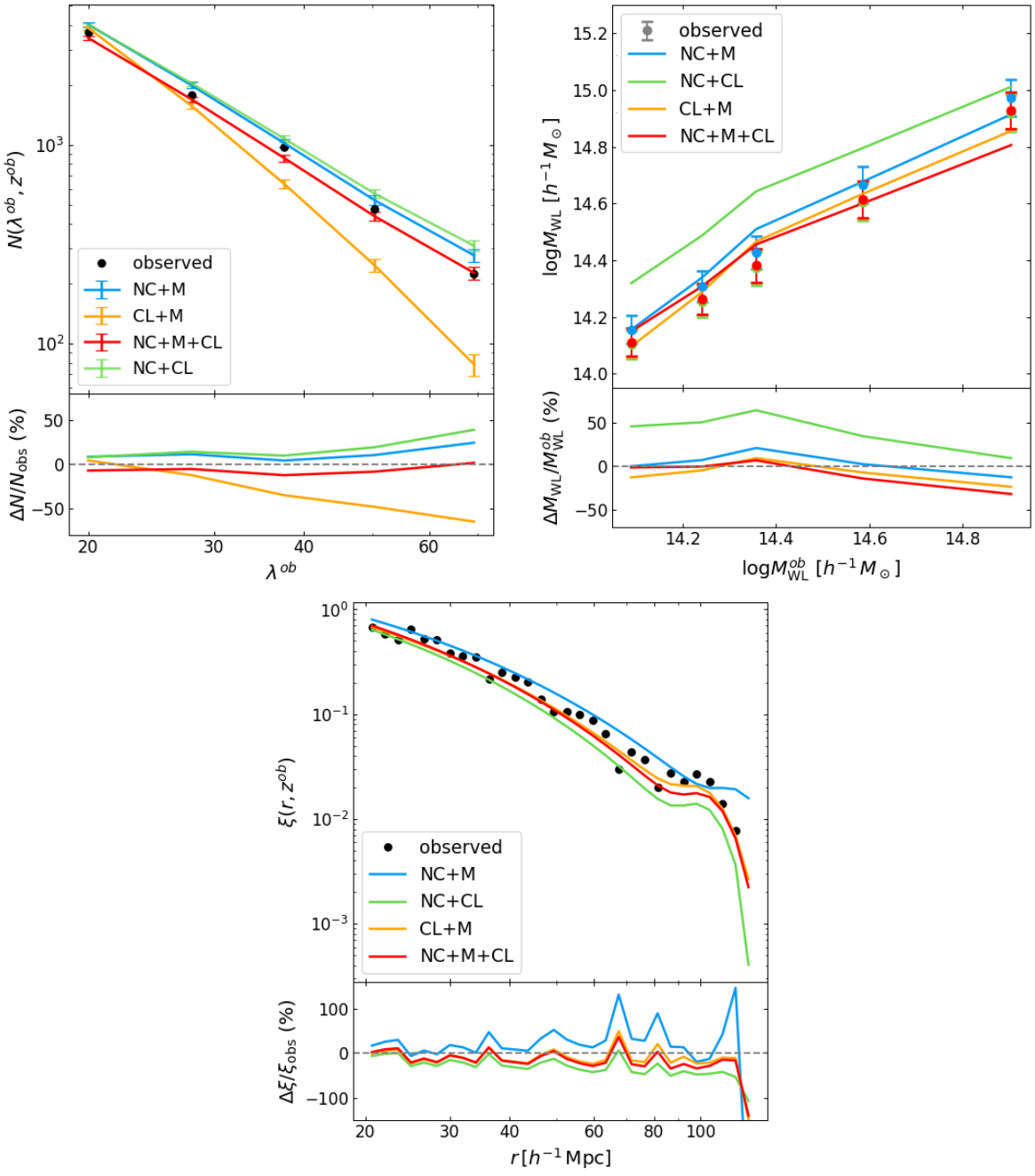

Figure 6.13: Observed number counts (*upper left*), weak-lensing masses (*upper right*), and 2PCF (*lower*), compared to the corresponding predicted quantities evaluated at the best-fit cosmologies of the contours in Fig. 6.12 (same color code).

Chapter 7

Discussion and conclusions

Galaxy clusters are extremely relevant cosmological structures, as they are characterized by properties that are sensitive to both the global geometry and the evolution of the large-scale structure of the Universe. The mass and spatial distribution of galaxy clusters, as well as their temporal evolution, exhibit a strong dependence on several cosmological parameters and are able to provide independent constraints that are complementary to those obtained from other purely geometric cosmological tests, such as the analysis of temperature anisotropies in the CMB and Type Ia supernovae. This makes galaxy clusters excellent cosmological probes for investigating the nature of the dark components of the Universe, such as dark matter and dark energy, and the behavior of gravity on a large scale, as well as information about the mass of neutrinos and the initial conditions of the matter density field.

In the next years, with the advent of new surveys that will observe large and deep areas of the sky, such as *Euclid*, the statistics available for the analysis of these observables will improve to such an extent that cosmological parameters can be constrained to unprecedented levels of precision. Given the level of precision expected for the analysis of these future catalogs, the estimation of parameters from observational data must necessarily be preceded by a study of systematics, whose contribution, if not accurately quantified, may alter the results and lead to erroneous conclusions regarding the nature of the components of the Universe. The main systematic error that can affect cluster cosmology is linked to the estimation of cluster masses, which must be carried out indirectly through mass proxies and calibration of scaling relations. Also the cluster detection process and a poor modeling of selection functions can introduce biases in the cosmological constraints. These factors must be carefully calibrated through the use of numerical simulations and/or observational data.

From a theoretical point of view, the main systematics can arise from the wrong modeling of shot-noise and sample variance effects, as well as the incorrect treatment of non-linear quantities or geometric effects, and from the calibration of halo mass function and halo bias. Such systematics must be taken into account in the cosmological analysis through the proper description of covariance matrices. In particular, the analysis of theoretical systematics is generally carried out through the use of catalogs produced with numerical simulations, in which the cosmological parameters assumed for the realization of the simulations themselves are known a priori: this makes it possible to determine whether the results obtained are correct or whether, on the contrary, there are systematic effects introducing biases into the analyses. The simulations used to carry out these analyses are produced using approximate methods that, unlike N-body simulations, are able to provide sufficiently high statistics to lower the

level of random errors and be able to give a correct estimate of systematic uncertainties. Such methods take advantage of the use of perturbative theories, such as the LPT and its first-order development, namely the Zel'dovich approximation, which allow particle displacements and the resulting formation of halos to be calculated more quickly and computationally less expensively than N-body simulations. In this thesis work, the analysis of the systematics has been carried out through the use of dark matter halo catalogs produced with the PINOCCHIO algorithm, consisting of 1000 light cones with area $\Omega_{\rm sky} = 10\,313$ deg^2 in the redshift interval $z = 0-2$. Masses were rescaled following the analytical mass function of D16, calibrated from numerical N-body simulations. We analyzed the mass distribution of dark matter halos, i.e. the number counts as a function of mass and redshift, and their clustering, described by the 2-point correlation function as a function of radial separation, redshift and mass. After validating the covariance models for the two observables, we forecast the impact of covariances on the cosmological constraints for both number counts and clustering analyses, and for their joint analysis.

In Chapter 3 we present a likelihood-based method for fitting the covariance matrix parameters from a small number of simulation. In this work, we have explored a two-step method to build a reliable and cheap covariance matrix. It is based on using two basic ingredients: an even imperfect model covariance with free parameters, and a χ^2-test. Upon successfully finding the best-fit values for the free-parameters for which the χ^2-test is passed, the methods provides a reliable covariance matrix having to run a small number of simulations, typically smaller than the data-vector itself. We have applied the method to two contexts, using the 2-point correlation function and the bispectrum of mock halo catalogs as observables. We employed knowingly incomplete models of the covariance with two free parameters in both cases. We have shown how to verify their reliability without relying on knowing the true covariance via a χ^2 test. In the case of the 2-point correlation function, using only 100 simulations, we are able to recover unbiased estimates of the cosmological parameters of the simulation. We found that our covariance matrix fit prefers a non-Poisson shot noise in our simple model. Since the effective shot noise is different when derived from covariance matrix compared to direct power spectrum fit, the most likely explanation is that we are detecting higher-order corrections. In the second example, using a non-Gaussian model for the bispectrum covariance we improve significantly with respect to a Gaussian covariance, but we are not able to match the numerical covariance drawn from $N_{\rm sims} = 10000$.

The main results of our analysis can be summarized as follows.

- As shown in Sect. 3.3.1 we find in both cases that the first moment of χ^2 is consistent with theoretical expectation. The second moment is correct for the case of correlation function, but too high in the case of bispectrum. There the wrong covariance matrix causes an extra excess on the χ^2 values with RMS of ~ 60, similar to intrinsic scatter from χ^2 distribution.

- The main strength of the method is that it can be applied to test a proposed covariance matrix even in the case where the number of simulated universes is not sufficient to generate even a positive-definite matrix. It relies on examining the consistency of χ^2 values derived from a model covariance matrix with theoretical expectation. A simple way of doing this is to measure mean and variance of realization χ^2 values, comparing these with expectation values for a χ^2 distribution. Even when the test is performed on

the same simulated realization used for fitting the covariance matrix, the result might be inconsistent if the covariance model is insufficiently flexible to describe the actual covariance. The results also quantify the badness of the covariance matrix by giving typical expected biases in χ^2 values.

- We also found that the adopted model can have intrinsic biases when fitting an insufficient number of simulations. For example, when fitting with only 30 simulations, the derived best-fit covariance matrix not only varies with sample variance but is systematically underestimated (see Fig. 3.2) for this subset of simulations. Investigating this effect further and developing covariance models that are unbiased (in the sense that they in average produce an unbiased covariance matrix) is left to future work.

In practice we have found that even covariance matrices that have a demonstrably biased χ^2 distributions often perform well enough in practical situations, giving cosmological parameters constraints that are acceptably biased with respect to the ideal case (See Fig. 3.4). This indicates that while our method allows for a proper propagation of covariance matrix uncertainties coming from sample variance on the number of realizations used into cosmological inferences, this might very rarely be used in practice. At the same time, the distribution of simulated χ^2 values might allow us to "recalibrate" the goodness of fit measures. In our bispectrum example, the fitted covariance matrix produces a distribution of χ^2 values which is too broad. This would allow us to better quantify the goodness of fit on the real data, which might be formally bad, but consistent with the distribution obtained with simulation with an imperfect covariance matrix.

While our test shows in principle the potential of our method, there are several more realistic setups where this method could prove to be crucial. For instance, it will be important to further test to what degree the fitting procedure can compensate for an incomplete modeling of the covariance and if approximate phenomenological terms can be added into covariance matrix model that absorb terms missing from the theory. A good testing ground for these tests is the galaxy/halo bispectrum framework we introduced in Section 3.3.3, since the covariance in this case has large off-diagonal terms for which we have only an incomplete model. We leave these tests to future work.

In Chapter 4 we presented the results of the number counts analysis. In this work we studied some of the theoretical systematics that can affect the derivation of cosmological constraints from the analysis of number counts of galaxy clusters from a survey having sky-coverage and selection function similar to those expected for the photometric *Euclid* cluster survey. One of the aims of this work was to understand if the inclusion of sample variance, in addition to the shot-noise error, could have some influence on the estimation of cosmological parameters, at the level of statistics that will be reached by the future *Euclid* catalogs. In this first part we only consider uncertainties which do not deal with observations, thus neglecting the systematics related to the mass estimation; however Köhlinger et al. (2015) state that for *Euclid* the mass estimates from weak lensing will be under control and, although there will be still additional statistical and systematic uncertainties due to mass calibration, the analysis of real catalogs will approach the ideal case considered here.

To describe the contribution of shot-noise and sample variance, we computed an analytical model for the covariance matrix, representing the correlation between mass and redshift bins as a function of cosmological parameters. Once the model for the covariance has been

properly validated, we moved to the identification of the more appropriate likelihood function to analyze cluster abundance data. The likelihood analysis has been performed with only two free parameters, $\Omega_{\rm m}$ and $\log_{10} A_{\rm s}$ (and thus σ_8), since the mass function is less affected by the variation of the other cosmological parameters.

The main results of our analysis can be summarized as follows.

- To include the sample variance effect in the likelihood analysis, we computed the covariance matrix from a large set of mock catalogs. Most of the sample variance signal is contained in the block-diagonal terms of the matrix, giving a contribution larger than the shot-noise term, at least in the low-mass/low-redshift regime. On the other hand, the anti-correlation between different redshift bins produces a minor effect with respect to the diagonal variance.

- In Sec. 4.1, we computed the covariance matrix by applying the analytical model by Hu & Kravtsov (2003), assuming the appropriate window function, and verified that it reproduces the matrix from simulations with deviations below the 10 percent accuracy; this difference can be ascribed mainly to the non-perfect match of the T10 halo bias with the one from simulations. However, we verified that such a small difference does not affect the inference of cosmological parameters in a significant way, at the level of statistic of the *Euclid* survey. Therefore we conclude that the analytical model of Hu & Kravtsov (2003) can be reliably applied to compute a cosmology-dependent, noise-free covariance matrix, without requiring a large number of simulations.

- In Sec. 4.2.1, we established the optimal binning scheme to extract the maximum information from the data, while limiting the computational cost of the likelihood estimation. We analyzed the halo mass function with a Poissonian and a Gaussian likelihood, for different redshift- and mass-bin widths and then computed the figure of merit from the resulting contours in $\Omega_{\rm m} - \sigma_8$ plane. The results show that, both for the Poissonian and the Gaussian likelihood, the optimal redshift bin width is $\Delta z = 0.1$: for larger bins, not all the information is extracted, while for smaller bins the Poissonian case saturates and the Gaussian case is no longer a valid approximation. The mass binning affects less the results, provided not to choose a too small number of bins. We decided to use $N_M = 300$ for the Poissonian likelihood and $N_M = 5$ for the Gaussian case.

- In Sec. 4.2.2, we included the covariance matrix in the likelihood analysis and demonstrated that the contribution to the total error budget and the correlation induced by the sample variance term cannot be neglected. In fact, the Poissonian and Gaussian with shot-noise likelihood functions show smaller error bars with respect to the Gaussian with covariance likelihood, meaning that neglecting the sample covariance leads to an underestimation of the error on parameters, at the *Euclid* level of accuracy. As shown in Sec. 4.2.4, this result holds also for the eROSITA survey, while it is not valid for present surveys like *Planck* and SPT.

- We verified that the anti-correlation between bins at different redshifts produces a minor, but non-negligible effect on the posteriors of cosmological parameters at the level of statistics reached by the *Euclid* survey. We also established that a cosmology-dependent covariance matrix is more appropriate than the cosmology-independent case,

which can lead to biased results due to the wrong quantification of shot-noise and sample variance.

One of the main results of the analysis presented here is that, for next generation surveys of galaxy clusters, such as *Euclid*, as well as for the latest currently available surveys like eROSITA, sample variance effects need to be properly included, becoming one of the main sources of statistical uncertainty in the cosmological parameters estimation process. The correct description of sample variance is guaranteed by the analytical model validated in this work.

In Chapter 5 we presented the results of the clustering analysis. In this work we validate a covariance model for the real-space 2-point correlation function of galaxy clusters in a survey that is comparable to that expected from the *Euclid* survey in terms of mass selection, sky coverage and depth. As for the number counts, in this first step we do not account here for the effect of selection functions and mass-observable relations.

We consider a Gaussian model plus the low-order non-Gaussian contribution, neglecting high-order terms. This choice is motivated since we expect the non-Gaussian terms to be minor corrections to the main Gaussian covariance. As such, great efforts to analytically calculate these complicated terms are not computationally justified. With this premise, we are interested in evaluating the impact of the approximations we made to compute this simple model, i.e. the absence of three- and four-point correlation functions, at the level of accuracy required for the future *Euclid* cluster catalogs.

We measure the 2PCF from the light cones with the Landy & Szalay (1993) estimator and compare the result with the theoretical prediction of Eq. (5.4), in the redshift range $z = 0-2$ and radial range $r = 20-130\,h^{-1}$ Mpc. We consider, in first place, halos more massive than $M_{\rm th} = 10^{14}\,M_\odot$. We quantify the differences between covariance matrices by performing a likelihood analysis with different covariance configurations, and evaluating their effect on the cosmological posteriors. To correct for the halo bias inaccuracy, we rescale the predicted 2PCF to the mean measured one, plus the cosmology dependence from theory. We constrain the parameters $\Omega_{\rm m}$ and σ_8, on which the cluster clustering is more strongly sensitive.

The main results of our analysis can be summarized as follows.

- In Sect. 5.2.1, we test different binning schemes, to properly extract the cosmological information. We find negligible differences when varying the width of redshift bins. We also observe a slight increase of the extracted information when increasing the number of radial bins, up to $N_{\rm r} \simeq 30$. We select the redshift bin width $\Delta z = 0.4$ and a number of radial log-spaced bins $N_{\rm r} = 30$, corresponding to $\Delta \log_{10}(r/h^{-1}\,{\rm Mpc}) = 0.028$;

- In Sect. 5.2.2, when comparing the analytical model of Eq. (5.10) with the numerical matrix, we find that the former underestimates the covariance at intermediate and high redshift by about 30 percent on the diagonal and more than 50 percent on the off-diagonal terms. We ascribe this difference to the absence of high-order non-Gaussian terms and to the inaccuracy of the Poissonian shot-noise assumption, as well as the residual inaccuracy of the assumed model for the halo bias;

- We correct the model by adding three parameters $\{\alpha, \beta, \gamma\}$, to correct for non-Poissonian shot-noise and halo bias prediction, as well as to absorb the effect of the missing

high-order terms (Eq. 5.15). The parameters are fitted from simulations following the method described in Sect. 3.3. We obtain an agreement within 10 percent with the numerical matrix at all the redshifts. It should be noted that, even if the missing terms are added analytically and a perfect description of the halo bias is provided, the exact value of shot-noise cannot be predicted. Correcting the model with such fitted parameters is therefore a well-motivated procedure;

- From the likelihood analysis we find a difference of about 40 percent between the the model and numerical FoMs. Such difference drops to about 5 percent when adding the fitted parameters to the model. This difference is considered to be negligible in more complete analyses (e.g. richness-selected catalogs), most likely to be absorbed by the broadening of the cosmological posteriors;

- In Sect. 5.2.3, we assess the relevance of the low-order non-Gaussian term, which turns out to be non-negligible at small scales, especially at high redshift;

- In Sect. 5.2.4, we find that, in this analysis, the likelihood with cosmology-dependent covariance is statistically preferred over the iterative method. Also, we find that evaluating the covariance at a fixed wrong cosmology can lead to an under/overestimated posterior's amplitude. Moreover, neglecting the cosmology-dependence of the covariance means losing the information contained in the shot-noise term. Such information is not contained directly in the 2PCF, but is nevertheless information that characterizes the clustering of clusters;

- In Sect. 5.2.5, we assess the cosmological information encoded in the shape of the halo bias by splitting our sample in mass bins, finding a significative improvement in the FoM compared to mass-threshold case. Such improvement is expected to be even more important for richness-selected halos, where this dependence can help to constrain the mass-observable relation parameters in addition to the cosmological ones.

Two main results emerge from this analysis. First, for cluster clustering a pure Gaussian model is not sufficient to correctly describe the covariance. This is due to the low number densities that characterize the spatial distribution of these objects, making non-Gaussian terms more important as the redshift and the mass threshold increase. Despite this, a simple semi-analytical model with parameters fitted from simulations permits to correct the inaccuracy of the model and give an accurate estimate of the errors associated with the 2PCF. Although this model still requires the use of simulations to fit the covariance parameters, the number of simulations is considerably lower than the number required to compute a good numerical matrix (approximately $O(10^2)$ instead of $O(10^3)$). Furthermore, the resulting matrix is completely noise-free and accounts for the dependence on cosmological parameters.

Second, the covariance of the 2PCF contains cosmological information that is not present in the mean value. Therefore, both quantities should be taken into account in constraining cosmological parameters, to correctly extract the information enclosed in the cluster clustering, especially when the mass binning is included. Note that this may require some care when performing a combined analysis of cluster number counts and cluster clustering, as the cosmological information contained in the 2PCF covariance is also contained in the number counts. We reserve to examine this issue in detail in a future dedicated work.

In this work we show how a simple semi-analytical model can be used to accurately describe the cluster clustering covariance matrix. However, the calibration of such model is not universal, but depends on the specific properties of the survey, such as geometry or mass and redshift range. The fit of the covariance parameters must then be performed for each survey, on appropriate simulations. Moreover, such parameters may contain a non-negligible dependence on cosmology whose impact is still to be quantified.

In Chapter 6 we present the results of the number counts and clustering joint analysis in observable space, and the application of the pipeline to real data. To this purpose, we assigned a richness to the halos in our lightcones, through a richness-mass relation. We also added observational uncertainties on richness and redshift, by means of selection functions. For each lightcone, we obtained a final sample with $\sim 10^5$ objects in the redshift range $z = 0$–2 and with richness $\lambda^{\rm ob} \geq 20$.

The main results of our analysis can be summarized as follows.

- In Sect. 6.2, we validated the two covariance models in observable space, confirming the results found for mass-selected objects, i.e., both the number counts and clustering covariances present a difference in the FoM below the 5 percent;
- In Sec. 6.2.2, we find negligible cross-correlation between number counts and clustering, with a cross-correlation coefficient $\rho = -0.015 \pm 0.032$, fully consistent with zero. This indicates that the two observables behave like independent quantities;
- In Sect. 6.3, we studied the effect of MoR prior on the parameter constraints, testing four priors' amplitudes equal to 5, 3, 1, and 0 %. In all the cases, clustering is less constraining than number counts, but the combination of the two observables provides tighter constraints than number counts alone, with an improvement in the FoM from 20 to 90 %, depending on the MoR uncertainty;
- In Sect. 6.3.2 we found that the impact of wrong cosmology/cosmology-dependent matrices is appreciable only if the uncertainly on the richness-mass relation parameter is low. In this case, since cluster clustering is much less constraining than number counts, the error in the posterior amplitude is driven by the covariance of number counts, while the cosmology-dependence of the clustering covariance does not impact the joint posteriors. When the uncertainty on the mass-observable relation is larger, the error made by fixing the covariance to a wrong cosmology ($\sim 2\sigma$ from Planck Collaboration VI. 2020) is absorbed by the broadening of the contours;
- In Sect. 6.4.1, we applied the number counts pipeline to assess the impact of a cosmology-dependent HOD, finding that such a dependence can improve the cosmological constraints of the 5% for number counts alone, and up to 10% when number counts are combined to weak-lensing information;
- In Sect. 6.4.2, we applied the number counts pipeline to forecast the impact of the halo mass function calibration on the cosmological posteriors. The statistical uncertainties on the halo mass function calibration presented in our analysis are significantly smaller than the expected accuracy for the mass-observational relation of *Euclid*. However, the

difference between the halo mass function of the halo-finders here studied is comparable to the expected accuracy for the mass-observational relation of *Euclid* and, as such, could lead to a biased inference of cosmological parameters;

- In Sect. 6.5, we applied the whole pipeline to the SDSS redMaPPer cluster catalog, repeating the analysis performed by DES18, with the addition of cluster clustering. We find that the inclusion of clustering can significantly break the parameter degeneracies, both for cosmological and mass-observable relation parameters. From the number counts, clustering and weak-lensing masses joint analysis we obtain $\Omega_{\rm m} = 0.27^{-0.03}_{-0.02}$ and $\sigma_8 = 0.81 \pm 0.05$.

The main result of this work is that cluster clustering actually helps to improve the constraining power of cluster number counts, despite the lower constraining power. This is true not only for future large surveys, as shown by our forecasts, but also for the currently available SDSS data, where the different degeneracies on parameters make cluster clustering a powerful tool to be combined with number counts and weak lensing. However, while the independence of number counts and clustering has been demonstrated by the absence of significant correlation between the two observables, the possible correlation of these observables with weak lensing masses has yet to be thoroughly investigated.

The results presented in this thesis work clearly demonstrate the importance of proper modeling of theoretical systematics. In fact, the inaccurate description of covariance matrices has a strong impact on the amplitude of cosmological posteriors, both in the case of number counts and clustering. We propose valuable models for (semi-)analytically predicting cosmology-dependent covariances. Also, we show the usefulness of cluster clustering as cosmological probes combined with number counts for future surveys like *Euclid*, as well as for the currently available SDSS data. We expect that the results of this analysis will have significant implications for the derivation of cosmological constraints from number counts and 2-point clustering statistics of the *Euclid* survey of galaxy clusters. Although this work was focused on preparation for the *Euclid* mission, these results can also be applied to other cluster surveys. In particular, the high statistics that characterizes the most recent and upcoming surveys such as KiDS, DES, Vera C. Rubin Observatory LSST[1], and eROSITa makes the accurate description of covariance matrices a key ingredient for unbiased estimation of cosmological parameters. At the same time, such catalogs will make it possible to measure cluster clustering with growing accuracy, making the combined analysis of cluster clustering and cluster counts increasingly powerful and competitive, as shown by the results of this work.

[1] https://www.lsst.org/

Acknowledgement

I would like to thank my supervisors, Alex Saro and Stefano Borgani, for following and helping me during my PhD course, without whom this doctoral experience would not have been so instructive. I would also like to thank all the people at the Trieste Observatory with whom I have collaborated and who have helped me over these three years: Matteo Biagetti, Matteo Costanzi, Pierluigi Monaco, Emiliano Sefusatti, and Anže Slosar. In particular, I thank Tiago Castro, for being an unofficial, but very supportive supervisor. Finally, I thank all the PhD students and postdocs for making these years so much enjoyable.

The Euclid Consortium acknowledges the European Space Agency and a number of agencies and institutes that have supported the development of *Euclid*, in particular the Academy of Finland, the Agenzia Spaziale Italiana, the Belgian Science Policy, the Canadian Euclid Consortium, the Centre National d'Etudes Spatiales, the Deutsches Zentrum für Luft- und Raumfahrt, the Danish Space Research Institute, the Fundação para a Ciência e a Tecnologia, the Ministerio de Economia y Competitividad, the National Aeronautics and Space Administration, the Netherlandse Onderzoekschool Voor Astronomie, the Norwegian Space Agency, the Romanian Space Agency, the State Secretariat for Education, Research and Innovation (SERI) at the Swiss Space Office (SSO), and the United Kingdom Space Agency. A complete and detailed list is available on the *Euclid* web site (`http://www.euclid-ec.org`).

Bibliography

Abbott, T. M. C. et al. 2020, Phys. Rev. D, 102, 023509

Adam, R. et al. 2019, A&A, 627, A23

Aguena, M. & Lima, M. 2018, Phys. Rev. D, 98, 123529

Aihara, H. et al. 2011, ApJS, 193, 29, [Erratum: ApJS 195, 26 (2011)]

Albrecht, A. et al. 2006, arXiv:0609591

Alcock, C. & Paczynski, B. 1979, Nature, 281, 358

Allen, S. W., Evrard, A. E., & Mantz, A. B. 2011, Ann. Rev. A&A, 49, 409

Anderson, T. 2003, An Introduction to Multivariate Statistical Analysis, Wiley Series in Probability and Statistics (Wiley)

Angulo, R., Baugh, C. M., Frenk, C. S., et al. 2005, MNRAS, 362, L25

Artis, E., Melin, J.-B., Bartlett, J. G., & Murray, C. 2021, A&A, 649, A47

Baldauf, T., Mirbabayi, M., Simonović, M., & Zaldarriaga, M. 2015, Phys. Rev. D, 92, 043514

Barreira, A. 2019, J. Cosmology Astropart. Phys., 03, 008

Bartelmann, M. & Schneider, P. 2001, Phys. Rep., 340, 291

Battye, R. A., Charnock, T., & Moss, A. 2015, Phys. Rev. D, 91, 103508

Behroozi, P. S., Wechsler, R. H., & Wu, H.-Y. 2013, ApJ, 762, 109

Bellagamba, F., Roncarelli, M., Maturi, M., & Moscardini, L. 2018, MNRAS, 473, 5221

Bernardeau, F., Colombi, S., Gaztanaga, E., & Scoccimarro, R. 2002, Phys. Rep., 367, 1

Bertschinger, E. 1998, Ann. Rev. Astron. Astrophys., 36, 599

Bhattacharya, S., Heitmann, K., White, M., et al. 2011, ApJ, 732, 122

Biagetti, M., Castiblanco, L., Noreña, J., & Sefusatti, E. 2022, J. Cosmology Astropart. Phys., 09, 009

Birkinshaw, M. 1999, Phys. Rep., 310, 97

Blot, L., Corasaniti, P.-S., Rasera, Y., & Agarwal, S. 2020, MNRAS, 500, 2532

Blot, L. et al. 2019, MNRAS, 485, 2806

Bocquet, S., Heitmann, K., Habib, S., et al. 2020, ApJ, 901, 5

Bocquet, S., Saro, A., Dolag, K., & Mohr, J. J. 2016, MNRAS, 456, 2361

Bocquet, S. et al. 2015, ApJ, 799, 214

Bocquet, S. et al. 2019, ApJ, 878, 55

Bond, J. R., Cole, S., Efstathiou, G., & Kaiser, N. 1991, ApJ, 379, 440

Bond, J. R. & Myers, S. T. 1996, ApJS, 103, 1

Borgani, S. & Guzzo, L. 2001, Nature, 409, 39

Borgani, S. & Kravtsov, A. 2011, Adv. Sci. Lett., 4, 204

Borgani, S., Plionis, M., & Kolokotronis, E. 1999, MNRAS, 305, 866

Bouchet, F. R., Colombi, S., Hivon, E., & Juszkiewicz, R. 1995, A&A, 296, 575

Bower, R. G., Lucey, J. R., & Ellis, R. S. 1992, MNRAS, 254, 601

Buchert, T. 1992, MNRAS, 254, 729

Buchner, J., Georgakakis, A., Nandra, K., et al. 2014, A&A, 564, A125

Carlstrom, J. E. et al. 2011, Publ. Astron. Soc. Pac., 123, 568

Carron, J. 2013, A&A, 551, A88

Castignani, G. & Benoist, C. 2016, A&A, 595, A111

Castro, T., Borgani, S., Dolag, K., et al. 2020, MNRAS, 500, 2316

Cataneo, M. & Rapetti, D. 2018, Int. J. Mod. Phys. D, 27, 1848006

Chevallier, M. & Polarski, D. 2001, Int. J. Mod. Phys. D, 10, 213

Chuang, C.-H., Kitaura, F.-S., Prada, F., Zhao, C., & Yepes, G. 2015, MNRAS, 446, 2621

Cohn, J. D. 2006, New A, 11, 226

Colavincenzo, M. et al. 2019, MNRAS, 482, 4883

Cole, S. & Kaiser, N. 1989, MNRAS, 237, 1127

Cole, S. et al. 2005, MNRAS, 362, 505

Costanzi, M., Villaescusa-Navarro, F., Viel, M., et al. 2013, J. Cosmology Astropart. Phys., 12, 012

Costanzi, M. et al. 2019, MNRAS, 488, 4779

Costanzi, M. et al. 2021, Phys. Rev. D, 103, 043522

Courtin, J., Rasera, Y., Alimi, J. M., et al. 2011, MNRAS, 410, 1911

Crocce, M., Fosalba, P., Castander, F. J., & Gaztanaga, E. 2010, MNRAS, 403, 1353

Cui, W., Borgani, S., & Murante, G. 2014, MNRAS, 441, 1769

Davis, M., Efstathiou, G., Frenk, C. S., & White, S. D. M. 1985, ApJ, 292, 371

Dawson, K. S. et al. 2013, , 145, 10

Despali, G., Giocoli, C., Angulo, R. E., et al. 2016, MNRAS, 456, 2486

Diemer, B. & Joyce, M. 2019, ApJ, 871, 168

Dodelson, S. & Schneider, M. D. 2013, Phys. Rev. D, 88, 063537

Dolag, K., Borgani, S., Murante, G., & Springel, V. 2009, MNRAS, 399, 497

Eifler, T., Schneider, P., & Hartlap, J. 2009, A&A, 502, 721

Eisenstein, D. J. & Loeb, A. 1995, ApJ, 439, 520

Eisenstein, D. J., Seo, H.-j., Sirko, E., & Spergel, D. 2007, ApJ, 664, 675

Eisenstein, D. J. et al. 2005, ApJ, 633, 560

Elahi, P. J., Cañas, R., Poulton, R. J. J., et al. 2019, PASA, 36, e021

Euclid Collaboration: Castro, T., Fumagalli, A., Angulo, R. E., et al. 2022, arXiv:2208.02174

Euclid Collaboration: Fumagalli, A., Saro, A., Borgani, S., et al. 2021, A&A, 652, A21

Euclid Collaboration: Fumagalli, A., Saro, A., Borgani, S., et al. 2022, arXiv:2211.12965

Euclid Collaboration: Scaramella, R. et al. 2022, A&A, 662, A112

Evrard, A. E. 1990, ApJ, 363, 349

Farahi, A., Evrard, A. E., Rozo, E., Rykoff, E. S., & Wechsler, R. H. 2016, MNRAS, 460, 3900

Feldman, H. A., Kaiser, N., & Peacock, J. A. 1994, ApJ, 426, 23

Feldmann, R. et al. 2006, MNRAS, 372, 565

Feroz, F., Hobson, M. P., & Bridges, M. 2009, MNRAS, 398, 1601

Friedrich, O., Seitz, S., Eifler, T. F., & Gruen, D. 2016, MNRAS, 456, 2662

Friedrich, O. et al. 2021, MNRAS, 508, 3125

Fumagalli, A., Biagetti, M., Saro, A., et al. 2022, arXiv:2206.05191

Giocoli, C., Tormen, G., & Bosch, F. C. v. d. 2008, MNRAS, 386, 2135

Gonzalez, A. 2014, in Building the Euclid Cluster Survey - Scientific Program, 7

Grandis, S., Rapetti, D., Saro, A., Mohr, J. J., & Dietrich, J. P. 2016, MNRAS, 463, 1416

Grieb, J. N., Sánchez, A. G., Salazar-Albornoz, S., & Dalla Vecchia, C. 2016, MNRAS, 457, 1577

Guzik, J. & Seljak, U. 2002, MNRAS, 335, 311

Hall, A. & Taylor, A. 2019, MNRAS, 483, 189

Hamilton, A. J. S. 1997, in Ringberg Workshop on Large Scale Structure

Handley, W. J., Hobson, M. P., & Lasenby, A. N. 2015, MNRAS, 450, L61

Hartlap, J., Simon, P., & Schneider, P. 2007, A&A, 464, 399

Heavens, A. 2009, arXiv:0906.0664

Heitmann, K. et al. 2016, ApJ, 820, 108

Heitmann, K. et al. 2019, ApJS, 245, 16

Hirata, C. M. & Seljak, U. 2003, Phys. Rev. D, 67, 043001

Hoekstra, H., Bartelmann, M., Dahle, H., et al. 2013, Space Sci. Rev., 177, 75

Hu, W. & Dodelson, S. 2002, Ann. Rev. A&A, 40, 171

Hu, W. & Kravtsov, A. V. 2003, ApJ, 584, 702

Huetsi, G. 2010, MNRAS, 401, 2477

Ishiyama, T. et al. 2021, MNRAS, 506, 4210

Jenkins, A., Frenk, C. S., Pearce, F. R., et al. 1998, ApJ, 499, 20

Jenkins, A., Frenk, C. S., White, S. D. M., et al. 2001, MNRAS, 321, 372

Johnston, D. E., Sheldon, E. S., Wechsler, R. H., et al. 2007, arXiv:0709.1159

Kaiser, N. 1986, MNRAS, 222, 323

Kaiser, N. 1987, MNRAS, 227, 1

Karamanis, M., Beutler, F., & Peacock, J. A. 2021, MNRAS, 508, 3589

Kerscher, M., Szapudi, I., & Szalay, A. S. 2000, ApJ, 535, L13

Kitaura, F.-S., Yepes, G., & Prada, F. 2014, MNRAS, 439, 21

Kitayama, T. & Suto, Y. 1996, ApJ, 469, 480

Knollmann, S. R. & Knebe, A. 2009, ApJS, 182, 608

Köhlinger, F., Hoekstra, H., & Eriksen, M. 2015, MNRAS, 453, 3107

Krause, E. & Eifler, T. 2017, MNRAS, 470, 2100

Kravtsov, A. & Borgani, S. 2012, Ann. Rev. A&A, 50, 353

Kravtsov, A. V., Berlind, A. A., Wechsler, R. H., et al. 2004, ApJ, 609, 35

Lacasa, F. & Kunz, M. 2017, A&A, 604, A104

Lacey, C. G. & Cole, S. 1993, MNRAS, 262, 627

Landy, S. D. & Szalay, A. S. 1993, ApJ, 412, 64

Lattanzi, M. & Gerbino, M. 2018, Front. in Phys., 5, 70

Laureijs, R. et al. 2011, arXiv:1110.3193

Lesci, G. F., Nanni, L., Marulli, F., et al. 2022, arXiv:2203.07398

Lewis, A., Challinor, A., & Lasenby, A. 2000, ApJ, 538, 473

Li, Y., Singh, S., Yu, B., Feng, Y., & Seljak, U. 2019, J. Cosmology Astropart. Phys., 01, 016

Lin, W. & Ishak, M. 2017, Phys. Rev. D, 96, 023532

Linder, E. V. 2005, Phys. Rev. D, 72, 043529

Lippich, M. et al. 2019, MNRAS, 482, 1786

Majumdar, S. & Mohr, J. J. 2004, ApJ, 613, 41

Maksimova, N. A., Garrison, L. H., Eisenstein, D. J., et al. 2021, MNRAS, 508, 4017

Mana, A., Giannantonio, T., Weller, J., et al. 2013, MNRAS, 434, 684

Mandelbaum, R., Hirata, C. M., Leauthaud, A., Massey, R. J., & Rhodes, J. 2012, MNRAS, 420, 1518

Mandelbaum, R., Slosar, A., Baldauf, T., et al. 2013, MNRAS, 432, 1544

Manera, M., Sheth, R. K., & Scoccimarro, R. 2010, MNRAS, 402, 589

Mantz, A. B. et al. 2015, MNRAS, 446, 2205

Marulli, F., Veropalumbo, A., & Moresco, M. 2016, Astron. Comput., 14, 35

Maturi, M., Bellagamba, F., Radovich, M., et al. 2019, MNRAS, 485, 498

McClintock, T., Rozo, E., Becker, M. R., et al. 2019, ApJ, 872, 53

Meiksin, A. & White, M. J. 1999, MNRAS, 308, 1179

Melchior, P. et al. 2017, MNRAS, 469, 4899

Miller, C. J., Nichol, R. C., & Batuski, D. J. 2001, ApJ, 555, 68

Mo, H. J. & White, S. D. M. 1996, MNRAS, 282, 347

Mohammad, F. G. & Percival, W. J. 2021, arXiv:2109.07071

Monaco, P. 1997, MNRAS, 287, 753

Monaco, P. 2016, Galaxies, 4, 53

Monaco, P., Sefusatti, E., Borgani, S., et al. 2013, MNRAS, 433, 2389

Monaco, P., Theuns, T., & Taffoni, G. 2002a, MNRAS, 331, 587

Monaco, P., Theuns, T., Taffoni, G., et al. 2002b, ApJ, 564, 8

Moresco, M., Veropalumbo, A., Marulli, F., Moscardini, L., & Cimatti, A. 2021, ApJ, 919, 144

Morrison, C. B. & Schneider, M. D. 2013, J. Cosmology Astropart. Phys., 11, 009

Moutarde, F., Alimi, J. M., Bouchet, F. R., Pellat, R., & Ramani, A. 1991, ApJ, 382

Munari, E., Monaco, P., Sefusatti, E., et al. 2017, MNRAS, 465, 4658

Murata, R., Nishimichi, T., Takada, M., et al. 2018, ApJ, 854, 120

Nakajima, R., Mandelbaum, R., Seljak, U., et al. 2012, MNRAS, 420, 3240

Narayan, R. & Bartelmann, M. 1996, in 13th Jerusalem Winter School in Theoretical Physics: Formation of Structure in the Universe

Navarro, J. F., Frenk, C. S., & White, S. D. M. 1996, ApJ, 462, 563

Navarro, J. F., Frenk, C. S., & White, S. D. M. 1997, ApJ, 490, 493

Nelson, D. et al. 2018 [[arXiv]1812.05609]

Norberg, P., Baugh, C. M., Gaztanaga, E., & Croton, D. J. 2009, MNRAS, 396, 19

O'Connell, R., Eisenstein, D., Vargas, M., Ho, S., & Padmanabhan, N. 2016, MNRAS, 462, 2681

Oddo, A., Rizzo, F., Sefusatti, E., Porciani, C., & Monaco, P. 2021, J. Cosmology Astropart. Phys., 11, 038

Oddo, A., Sefusatti, E., Porciani, C., Monaco, P., & Sánchez, A. G. 2020, J. Cosmology Astropart. Phys., 03, 056

Ondaro-Mallea, L., Angulo, R. E., Zennaro, M., Contreras, S., & Aricò, G. 2021, MNRAS, 509, 6077

Paech, K., Hamaus, N., Hoyle, B., et al. 2017, MNRAS, 470, 2566

Pearson, D. W. & Samushia, L. 2016, MNRAS, 457, 993

Percival, W. J., Friedrich, O., Sellentin, E., & Heavens, A. 2022, MNRAS, 510, 3207

Perlmutter, S. et al. 1999, ApJ, 517, 565

Philcox, O. H. E. & Eisenstein, D. J. 2019, MNRAS, 490, 5931

Planck Collaboration IX. 2020, A&A, 641, A9

Planck Collaboration VI. 2020, A&A, 641, A6, [Erratum: A&A652, C4 (2021)]

Planck Collaboration XVI. 2014, A&A, 571, A16

Pope, A. C. & Szapudi, I. 2008, MNRAS, 389, 766

Pratt, G. W., Arnaud, M., Biviano, A., et al. 2019, Space Sci. Rev., 215, 25

Predehl, P. 2014, Astronomische Nachrichten, 335, 517

Press, W. H. & Schechter, P. 1974, ApJ, 187, 425

Ragagnin, A., Fumagalli, A., Castro, T., et al. 2021, arXiv:2110.05498

Reyes, R., Mandelbaum, R., Gunn, J. E., et al. 2012, MNRAS, 425, 2610

Rozo, E., Rykoff, E. S., Becker, M., Reddick, R. M., & Wechsler, R. H. 2015, MNRAS, 453, 38

Rozo, E. et al. 2010, ApJ, 708, 645

Rykoff, E. S. et al. 2014, ApJ, 785, 104

Sahni, V. & Coles, P. 1995, Phys. Rep., 262, 1

Salopek, D. S. & Bond, J. R. 1990, Phys. Rev. D, 42, 3936

Salvati, L., Douspis, M., & Aghanim, N. 2020, A&A, 643, A20

Salvati, L. et al. 2022, ApJ, 934, 129

Saro, A. et al. 2015, MNRAS, 454, 2305

Sartoris, B., Borgani, S., Fedeli, C., et al. 2010, MNRAS, 407, 2339

Sartoris, B., Borgani, S., Rosati, P., & Weller, J. 2012, MNRAS, 423, 2503

Sartoris, B. et al. 2016, MNRAS, 459, 1764

Schellenberger, G. & Reiprich, T. H. 2017, MNRAS, 471, 1370

Schneider, P. 2006, in 33rd Advanced Saas Fee Course on Gravitational Lensing: Strong, Weak, and Micro, 269–451

Schuecker, P., Bohringer, H., Collins, C. A., & Guzzo, L. 2003, A&A, 398, 867

Scoccimarro, R. 2015, Phys. Rev. D, 92, 083532

Scoccimarro, R., Colombi, S., Fry, J. N., et al. 1998, ApJ, 496, 586

Scoccimarro, R. & Sheth, R. K. 2002, MNRAS, 329, 629

Scoccimarro, R., Zaldarriaga, M., & Hui, L. 1999, ApJ, 527, 1

Sefusatti, E., Crocce, M., Pueblas, S., & Scoccimarro, R. 2006, Phys. Rev. D, 74, 023522

Sefusatti, E., Crocce, M., Scoccimarro, R., & Couchman, H. 2016, MNRAS, 460, 3624

Sehgal, N., Bode, P., Das, S., et al. 2010, ApJ, 709, 920

Sellentin, E. & Heavens, A. F. 2016, MNRAS, 456, L132

Senatore, L. & Zaldarriaga, M. 2015, J. Cosmology Astropart. Phys., 02, 013

Sereno, M., Veropalumbo, A., Marulli, F., et al. 2015, MNRAS, 449, 4147

Sheth, R. K., Mo, H. J., & Tormen, G. 2001, MNRAS, 323, 1

Sheth, R. K. & Tormen, G. 2002, MNRAS, 329, 61

Simet, M., McClintock, T., Mandelbaum, R., et al. 2017, MNRAS, 466, 3103

Singh, P., Saro, A., Costanzi, M., & Dolag, K. 2020, MNRAS, 494, 3728

Skibba, R. A. 2009, MNRAS, 392, 1467

Slepian, Z. et al. 2017, MNRAS, 468, 1070

Spiegelhalter, D. J., Best, N. G., Carlin, B. P., & van der Linde, A. 2002, J. Roy. Statist. Soc. B, 64, 583

Springel, V., Pakmor, R., Zier, O., & Reinecke, M. 2021, MNRAS, 506, 2871

Springel, V., White, S. D. M., Tormen, G., & Kauffmann, G. 2001, MNRAS, 328, 726

Springel, V. et al. 2005, Nature, 435, 629

Sunayama, T., Park, Y., Takada, M., et al. 2020, MNRAS, 496, 4468

Takada, M. & Hu, W. 2013, Phys. Rev. D, 87, 123504

Tassev, S., Zaldarriaga, M., & Eisenstein, D. 2013, J. Cosmology Astropart. Phys., 06, 036

Tauber, J. A. et al. 2010, A&A, 520, A1

Taylor, A., Joachimi, B., & Kitching, T. 2013, MNRAS, 432, 1928

Tinker, J. L., Kravtsov, A. V., Klypin, A., et al. 2008, ApJ, 688, 709

Tinker, J. L., Robertson, B. E., Kravtsov, A. V., et al. 2010, ApJ, 724, 878

To, C. et al. 2021a, Phys. Rev. Lett., 126, 141301

To, C.-H. et al. 2021b, MNRAS, 502, 4093

Valageas, P., Clerc, N., Pacaud, F., & Pierre, M. 2011, A&A, 536, A95

Velliscig, M., van Daalen, M. P., Schaye, J., et al. 2014, MNRAS, 442, 2641

Verde, L., Treu, T., & Riess, A. G. 2019, Nature Astron., 3, 891

Veropalumbo, A., Marulli, F., Moscardini, L., Moresco, M., & Cimatti, A. 2014, MNRAS, 442, 3275

Villaescusa-Navarro, F. et al. 2020, ApJS, 250, 2

Vogelsberger, M., Marinacci, F., Torrey, P., & Puchwein, E. 2020, Nature Rev. Phys., 2, 42

Wadekar, D. & Scoccimarro, R. 2020, Phys. Rev. D, 102, 123517

Wang, E., Wang, H., Mo, H., et al. 2018, ApJ, 864, 51

Watson, W. A., Iliev, I. T., D'Aloisio, A., et al. 2013, MNRAS, 433, 1230

White, M. J. 2001, A&A, 367, 27

White, M. J. 2002, ApJS, 143, 241

White, M. J. & Kochanek, C. S. 2002, ApJ, 574, 24

Wu, H.-Y. et al. 2022, MNRAS, 515, 4471

Xu, X., Padmanabhan, N., Eisenstein, D. J., Mehta, K. T., & Cuesta, A. J. 2012, MNRAS, 427, 2146

Zeldovich, Y. B. 1970, A&A, 5, 84

Zhang, Y. & Annis, J. 2022, MNRAS, 511, L30